Efficient and Robust Topology Optimization of Compliant Mechanisms using Perturbed Geometrically Non-Linear Analysis

---

Master Thesis

Casper Kerkhove

Student ID: 4387961,
TU Delft, Department of Precision and Micro-systems Engineering (PME)

December 6, 2023

Preface

The present work is dedicated to the efficient and robust topology optimization of compliant mechanisms using geometrically non-linear structural analysis, continuing the efforts of Jasper Hoevenaars (2021). In addition to earning me my Master's degree in Mechanical Engineering at TU Delft, I hope my work serves a purpose in academia and the technological industry, making high-performance mechanism design more accessible. Although it is presented in a double-column paper format, it is unfortunately not yet condensed and refined enough to be published in a Journal. The style is maintained regardless, and the abstract covers more details on this work's goal, methodology, and findings, preceding the Paper body a few pages ahead.

While the present research is dedicated to efficient optimization, it mostly forced me to optimize my own efficiency and dedication within academic research. This resulted in a lengthy, painstaking process, teaching me what I can, cannot, and must not do, and how I can improve. Particularly managing my time and priorities has been, and remains, a primary learning goal, recognizing when certain parts are sufficiently elaborated or improved, while others are still lacking.

I would like to express my sincerest gratitude to Stijn Koppen for always taking his time to provide useful in-depth feedback and support. I would also like to thank Matthijs Langelaar for the same, and for presenting me with the opportunity to dive into the subjects that interest me the most, both before and after my graduation. I owe a lot of my academic growth to Jasper Hoevenaars as well, for raising such a high bar with his work preceding my own. Lastly, I am grateful to my family and friends who encouraged me throughout this process, and to those who have been or still are suffering the same fate at the long white tables at the Faculty of Industrial Design, for the shared support, wisdom, and coffee.

Casper Kerkhove,
TU Delft, Department of Precision and Micro-Systems Engineering (PME),
December 6, 2023.

Contents

1

Paper

Structural Topology Optimization using Bayesian-Enhanced Perturbed Non-Linear Analysis

Casper Kerkhove

TU Delft, Department of Precision and Micro-systems Engineering (PME)

December 6, 2023

Abstract The recent success of - and demand for - compliant mechanisms has increased rapidly within the micro-electromechanical systems-, aircraft-, spacecraft-, surgical-, and precision-instrument industries. Yet, even greater success may be achieved by overcoming the computational cost and instability of the mechanisms' design methodology. This involves large-scale topology optimization, geometrically non-linear structural analysis, and particularly integrating the latter into the former. Therefore, a novel framework is proposed that extends the powerful design freedom of topology optimization with most of the geometrically non-linear qualities, without as much of the computational ramifications. Utilizing a Bayesian-enhanced perturbed analysis, the equilibrium curve is locally approximated by an asymptotic expansion, satisfying the curve's higher-order geometric derivatives at the undeformed state. Each of the latter is recursively and efficiently obtained through a linear solve with the same, Cholesky-factorized stiffness matrix. Furthermore, a tensor reformulation and -decomposition of the four-noded bilinear element's Green-Lagrange strain energy model are successfully exploited. A tight error estimator is derived to govern the Bayesian analysis and balance approximation efficiency and accuracy during optimization. Design-sensitivities of this error-estimator and other design-dependent responses are analytically obtained through the adjoint method, and applied in a few classical density-based topology optimizations; While Bayesian-enhanced perturbed analysis required noticeably less computational effort compared to Newton-Raphson analysis under mildly non-linear conditions, it often resulted in practically identical performance improvements compared to linear analysis.

Keywords Topology Optimization • Compliant Mechanisms • Geometrically Non-Linear • Approximate Structural Analysis • Perturbation Analysis • Error Analysis • Bayesian Model Averaging • Tensor Formulation • Tensor Decomposition • Deformation Scaling

I Introduction

Mechanisms, or any means to transfer force, motion, or energy, have always been an essential part of all life, and have been evolving and optimizing as a result. The present work aims to continue this ancient trend using modern methodologies. First, the essence of mechanism design is introduced, followed by the involved challenges and a novel proposition.

I.1 Essence of Mechanism Design

For over four billion years, since well before humankind, countless structures have been emerging, interacting, transforming, and decaying. In some sense, pure odds govern these processes. However, these processes govern odds right back when they benefit a certain structure's chance of survival or reproduction (Miyata et al., 2020; Carroll, 2001), possibly affecting that of others. Competition ensues between increasingly more complex structures, their environment, and natural decay, continuously filtering out those with lower survivability. The coincidentally beneficial tendencies turn into necessities (Carroll, 2001), and the responsible mechanisms grow ever more functional and complex. Since at least 2.5 million years ago, humans have been complementing their relatively slowly evolving biological mechanisms and capabilities by actively designing external mechanisms, or tools (Ambrose, 2001). In turn, their society, culture, and even biology adapted to the fruits of this technological innovation, on which the species' survival, success, and comfort of life now rely more than ever.

Designing mechanisms manually, compared to natural evolution, requires a painstaking cycle of building, testing, and rebuilding, yielding initially rapid but ultimately bounded improvement. Nature has been fuelled by a near-limitless amount of material, energy, iterations, and time. This has been yielding mechanisms inspiring even advanced engineers to this day (Bejan, 2000), who rely on deduction and inference precisely because they cannot afford nature's exhaustive approach. However, this cognitive ability is a double-edged sword. While it allows engineers to bypass infinitely many arbitrary or inadequate designs, more often than not it limits them to designs they can comprehend. This forces engineers to compromise by

assuming or imposing simplified shapes[1], and approximate kinematic or structural behavior[2]. This affects attainable performance, either directly by excluding shapes or designs of possibly superior functionality, or indirectly through ill-informed design changes.

Compliant mechanisms have recently gained increasing recognition from engineers due to their outstanding potential compared to conventional mechanisms[3]. Conventional mechanisms function through the translation and rotation of multiple interacting rigid bodies, but compliant mechanisms through the deformation of a single elastic body. As a result, they do not require rotational or sliding joints, preventing friction, wear, and backlash[4], thus preventing noise and the need for lubrication. In turn, precision, accuracy, and durability may be increased. The typical low part count often allows for simplified production processes, reducing production time, cost, and waste correspondingly.[5] The overrepresentation of compliant structures in nature further testifies to their general effectiveness (Rus & Tolley, 2015). As a result, compliant mechanisms are gaining exponential academic and industrial interest, mainly within micro-systems and MEMS (micro-electromechanical systems) (Kota et al., 2001; MacHekposhti et al., 2018), aircraft (Kota et al., 2005), spacecraft (Merriam et al., 2013), soft robotics (Rus & Tolley, 2015), biomedical devices (Parenti-Castelli & Sancisi, 2013; Zhu et al., 2020), minimally invasive surgery (Lourdes Thomas et al., 2021), and precision instruments (Howell, 2013).

Designing compliant mechanisms especially poses challenges, many of which have yet to be overcome. Having technically infinitely many degrees of motion freedom, even simply shaped compliant mechanisms tend to feature complex structural behavior, requiring complex tools to model and predict. Designing is even more difficult as it additionally requires the inverse of this prediction, finding a shape that precisely features certain structural behavior. To remedy, state-of-the-art design approaches such as the FACT- (*Freedom and Constrained Topology-*, Yu et al., 2011) and PRB (*Pseudo-Rigid-Body-*, Howell, 2013) methods impose shape restrictions, respectively ensuring approximately linearized, or effectively localized deformations, both of which may be combined. Regardless, engineers tend to favor rigid-body mechanisms due to their inherent simplicity (Zhu et al., 2020), despite their flaws otherwise. Regardless, the attainable performance is limited. A means to design compliant mechanisms is desired, without the cognitive or numerical burden typical of structural complexity.

Fortunately, harnessing modern computational power may combine the best of nature's exhaustive approach with an engineer's intelligent approach, while minimally compromising the structural complexity, and thus performance. Typically, an efficient cycle of structural design, modeling, analysis, evaluation, and redesign is performed digitally, for many iterations. Here, the design quantifies the structure's shape or topology. Given a design, the model then *implicitly* defines kinematic and energetic behavior, often by relating forces and deformations. The structural analysis then aims to *explicitly* obtain this relation. Especially when non-linear, this relation poses a notorious bottleneck in the design cycle, as elaborated in the next subsection. Through user-defined metrics based on this relation, the evaluation then quantifies the structure's performance, feasibility, and how these change with its design. The cycle then repeats, redesigning for improved performance while respecting feasibility, until the design cannot be improved further. Throughout this cycle, however, some extent of simplification or approximation is unavoidable, as knowledge and resources will always be finite. The remainder of this introduction will briefly clarify this cycle, with emphasis on the analysis.

The structural model is a crucial component of the design cycle. It dictates the allowed complexity of the design's shape or topology, its structural behavior, and the corresponding challenges of its analysis. On those accounts, the *Finite Element Method* (FEM) has been widely adopted in order to efficiently and accurately model (Thompson & Walker, 1968; Williamson, 1980; Han et al., 2021), and design (Bendsøe & Kikuchi, 1988), compliant or elastic structures. Moreover, it provides a natural and convenient means to continuously define and model structures of intricate shapes and structural behavior, as an assembly of many small and simple elastic elements. This is notably exploited in the powerful, popularized, academically transparent[6] *density-based approach* (Sigmund, 2001; Andreassen et al., 2011) of topology optimization, on which the present work is based.

Topology optimization emerged as a powerful design tool over the past decades (Zhu et al., 2020), yielding innovative, high-performance designs that are difficult to obtain with conventional approaches (X. Zhang & Zhu, 2018). It has made great progress (C. Wang et al., 2021), being widely adopted in academia and

[1] For example, trusses feature simplified beams compared to the organic structures in nature

[2] Structural behavior can be characterized by the relation between load and deformation, often simplified through linearization.

[3] This is not to say that compliance had never been used by humans; For instance, the bow and arrow proved the archetypical hunting tool for tens of thousands of years (Cattelain, 1997).

[4] This is noted by Midha et al. (1992); Howell & Midha (1994); Sigmund (1997); Kota et al. (2005); Shuib et al. (2007); Merriam et al. (2013); Howell (2013); MacHekposhti et al. (2018); X. Zhang & Zhu (2018); Lourdes Thomas et al. (2021).

[5] Yet, structures that require additive manufacturing, often require increased production time and cost.

[6] C. Wang et al. (2021) notes the importance of academic transparency, and building upon existing codes, such the MATLAB-implementations of Sigmund (2001); Andreassen et al. (2011), in order to accelerate development of topology optimization.

industry (Han et al., 2021). It does not need to rely on the structural simplifications used in the FACT- (Yu et al., 2011) or Pseudo-Rigid-Body- (Howell, 2013) method, given an adequate means of non-linear structural modeling and analysis. The latter is especially challenging but potent when non-linear. This would extend the powerful design capabilities of topology optimization towards structures exploiting complex, non-linear structural behavior. Moreover, density-based topology optimization does not require an initially known design concept (X. Zhang & Zhu, 2018), and is well-suited for additive manufacturing (ZHU et al., 2021)[7]. If nothing else, the obtained topologies serve as valuable inspiration for novel, effective designs, even when translated into more conventional shapes and design methods (Han et al., 2021).

I.2 Challenge of Non-Linearity

Non-linearity is an often avoided but vital aspect of structural modeling within high-end structural design optimization. Certainly, a linear model and particularly its analysis are computationally much more robust, cheap, and easy to implement, and hence implemented in most topology optimizations (Han et al., 2021). Yet, mechanisms generally feature non-linearity in practice, even when modeled or intended linearly in theory. What is more, some mechanisms precisely derive their function from non-linearity. Notable examples are biomedical devices featuring multi-stability (Parenti-Castelli & Sancisi, 2013; Zhu et al., 2020), hand-held tools featuring near-zero actuation stiffness (Lourdes Thomas et al., 2021), non-linear path generators (Megaro et al., 2017) and frequency multipliers (MacHekposhti et al., 2018). In terms of attainable performance, designing structures without modeling non-linearity is therefore not only suboptimal but sometimes impossible. Despite the ongoing research on the structural analysis of large deflections and geometric non-linearity within topology optimization, such as Pedersen et al. (2001); Bruns & Tortorelli (2001); F. Wang et al. (2014); X. Zhang & Zhu (2018); Han et al. (2021); Debeurre et al. (2023), it remains a relatively unexplored, major challenge (X. Zhang & Zhu, 2018; Han et al., 2021; Chen et al., 2019a).

The *Newton-Raphson* approach (Crisfield, 1997; Bathe, 2016) remains the most widely adopted, but arguably lacking, state-of-the-art non-linear analysis method, within structural optimization (Buhl et al., 2000a; Bruns & Tortorelli, 2001; Pedersen et al., 2001; van Dijk et al., 2014; Chen et al., 2019a; Han et al., 2021), and without. It functions by sequentially solving the locally linearized or otherwise approximate structural equations.[8] Its popularity may be explained by the relative ease of implementation compared to alternatives (Haisler et al., 1972), in addition to its quadratic terminal convergence (Bruns & Tortorelli, 2001) leading to high accuracy (Haisler et al., 1972). Yet, the Newton-Raphson approach is often computationally expensive[9](Haisler et al., 1972; Azrar et al., 1993), and otherwise problematic in density-based topology optimization due to near-singularities and non-uniqueness. Due to low-density elements, the tangent stiffness matrix becomes ill- or even negatively conditioned, impeding convergence (Buhl et al., 2000a). While low conditioning may affect the numerical stability and accuracy of each iteration, negative conditioning denotes structural instability. Within low-density elements, ill-conditioning is often associated with inversion, or buckling (van Dijk et al., 2014) and non-uniqueness[10]. Ironically, these supposedly non-structural regions tend to affect the accuracy, stability, and efficiency of the structural analysis. This is particularly emphasized using Newton-Raphson analysis, aiming to locally linearize strongly non-linear phenomena, even when present in low-density, non-structural regions. This affects the accuracy and stability of the structural analysis and optimization as a whole.

Alternative approaches to non-linear structural analysis, include the under-acknowledged but promising *Perturbation*[11]- or *Asymptotic Numerical Method*[12] (ANM), or homotopy continuation[13] methods in general. The perturbation method was pioneered by Koiter (1945) and Turner et al. (1960), and then neatly formulated by (Thompson & Walker, 1968), predating[14] the very finite element analysis. Where the Newton-Raphson approach functions through multiple successive linear predictions and corrections, an asymptotic method generally functions through a single higher-order prediction, without correction. Ultimately, some

[7] Occasionally, however, topology optimization may be limited to more complex additive manufacturing methods (Liu et al., 2018). These often require manufacturing-oriented modifications of the optimization problem formulation and post-processing of the resulting topologies, currently demanding future research (ZHU et al., 2021; Liu et al., 2018).

[8] See Subsection II.3 for a brief explanation and review of state-of-the-art non-linear analysis methods.

[9] While a quasi-Newton approach reduces the cost per iteration by avoiding expensive updates of this matrix, it sacrifices quadratic convergence, possibly requiring disproportionately many iterations.

[10] In fact, the number of solutions to the structural equations increases exponentially versus the number of freedom degrees, as elaborated in Subsection II.4. This includes many inverted, buckled, or even complex solutions, only some of which are physically meaningful.

[11] For reference on Perturbation analysis, see Thompson & Walker (1968); Haisler et al. (1972); He (1998); Imazatène et al. (2001).

[12] This perturbation method is referred to as the Asymptotic Numerical Method by Damil & Potier-Ferry (1990); Azrar et al. (1993); Cochelin (1994); Cochelin, Damil, & Potier-Ferry (1994); Cochelin, Damil, & Potier-Ferry (1994); De Boer & Van Keulen (1997); Najah et al. (1998); Baguet & Cochelin (2002); Charpentier (2008); Ayane et al. (2019); El Kihal et al. (2022); Debeurre et al. (2023).

[13] For reference on homotopy analysis methods, see He (1998); Liao (2004, 2010); Agarwal et al. (2021).

[14] In fact, perturbation- or asymptotic methods have been applied to algebraic sets of equations since Poincare's *"three-body problem"*, published in 1892. Incidentally, minimizing Green-Lagrange strain energy amounts precisely to solving an algebraic set of equations.

curve asymptotically follows the equilibrium curve, by matching their local value up to some finite amount of geometric derivatives.[8] Often this amounts to a Taylor expansion using polynomials, or a Padé using rationals (Cochelin, Damil, & Potier-Ferry, 1994; Imazatène et al., 2001; El Kihal et al., 2022). In algebraic geometry, Laurent- or Puisseux expansions[15] are used precisely to analyze algebraic curves close to singularities.

The perturbation- or asymptotic methods may very well out-compete the Newton-Raphson, up to moderate non-linearity. Contrary to Haisler et al.'s conclusion (1972), perturbation techniques may be quite efficient, especially for many degrees of freedom. In order to obtain the necessary local derivatives of the equilibrium curve, the global non-linear (zeroth-order) structural equation is replaced by a set of local higher-order structural equations (Thompson & Walker, 1968). Each of these is, in fact, linear. Moreover, they can be solved efficiently using the same Cholesky-factorizable stiffness matrix, as will be shown in Section II.3. From the derivatives, a continuous, non-linear description of the equilibrium curve can be constructed, although inherently diverging as any other extrapolation (Demanet & Townsend, 2019). On the other hand, the information by which the extrapolation is constructed may be obtained further away from singularities, promoting numerical conditioning, hence stability and accuracy. Overall, perturbation methods have provided satisfactory solutions to moderately non-linear problems on multiple accounts, including (Thompson & Walker, 1968; Haisler et al., 1972; Najah et al., 1998; El Kihal et al., 2022), allowing posterior step-length specification along the equilibrium path, accurate estimation of the solution error, and occasionally more efficiency *and* stability than Newton-Raphson methods.

I.3 Plan of Attack

The main objective of this work is to extend the powerful design capabilities of topology optimization, with qualities of non-linear structural analysis, without as much of the computational cost and instability. The optimizer must be able to reach, and recognize, well-performing designs as much as possible. Therefore, neither complexity of shape and topology, nor structural behavior, should be compromised, with non-linear structural analysis of the latter being the bottleneck and core focus of this paper. Balancing its computational cost, accuracy, and robustness are priorities, using expensively obtained information to its fullest extent. However, knowing or being able to reliably estimate error, is absolutely vital to all the former[16]. Excessive error leads to ill-informed design changes, from which the optimizer may not recover. On the other hand, small errors may sometimes even be unattainable, or require disproportionate computational effort. Regardless, a good error estimator may guide the optimizer, having it avoid designs whose analysis can not become sufficiently accurate, while minimally compromising the desired non-linearity that inadvertently causes this error. Preferably, designs are achieved with superior accuracy or qualitative features compared to linear analysis, and superior efficiency compared to Newton-Raphson analysis.

The scope of this work is narrowed down such that the research and validation of the proposed methodology and its core features maintain clarity. At the same time, it maintains most of the generalizability towards other structural optimization frameworks or pure non-linear analysis settings. Formulating well-behaved responses based on strong non-linearities[17], such as post-buckling behavior or multi-stability, involves difficulties beyond structural analysis itself due to non-uniqueness and singularities. Hence, only mild non-linearities are considered, representing any large deflection within the structure's buckling loads. Furthermore, a two-dimensional density-based topology optimization setting is considered, assuming isotropic, linearly elastic material, and moderate deflections but small strains. Accordingly, four-noded, bilinear elements are employed using the Green-Lagrange strain measure and a Total Lagrangian formulation, as elaborated in Section III. The generality of the proposed methodology in Section III is discussed in Section VII.

In order to achieve efficient and stable structural topology optimization exploiting geometrically non-linear qualities, a novel methodology has been developed, centered on structural analysis. Utilizing a Bayesian-enhanced perturbed analysis, the equilibrium curve is stably extrapolated by an asymptotic expansion, satisfying the curve's higher-order geometric derivatives at the undeformed state. These derivatives are recursively and efficiently obtained through a linear solve with the same, Cholesky-factorized stiffness matrix[18]. Furthermore, a symbolic tensor reformulation and numerical tensor decomposition of the four-noded bilinear element's Green-Lagrange strain energy model significantly reduce the cost of any algebraic manipulation, aside from linear solves. In addition, a tight error estimator has been derived, facilitating Bayesian-enhanced structural analysis for

[15] These expansions generalize power series to fractional and negative exponents.

[16] Error can be easily overlooked as valuable information, as it seems to represent the opposite. In fact, it can be used to increase stability and accuracy for practically no additional cost, as demonstrated in this paper.

[17] Strong non-linearity of a solution refers to its non-uniqueness, or singularity of its derivative. By complement, mild non-linearity implies that the solution is unique and exists on the domain up to the nearest singularities.

[18] Note that exploitation of the repeated system matrix has been performed since Thompson & Walker (1968).

improved robustness and accuracy, and balanced computational cost and accuracy throughout the structural optimization. Finally, the design sensitivities of this error estimator and other design-dependent responses are analytically obtained through the adjoint method. The resulting methodology allows stable and efficient structural optimization, reliably predicting the true performance of designs due to prior specification of computational cost or error within the structural analysis. As a result, designs of superior performance or entirely new qualities may be obtained compared to using linear analysis, but lower cost compared to using Newton-Raphson analysis.

The contents of this paper are structured as follows. First, Section II covers the necessary preliminaries, starting with the adopted tensor-notation and -operations, and a generalized structural model to which the proposed and state-of-the-art non-linear analysis methods may be applied. These state-of-the-art methods are then briefly reviewed from a mathematical and numerical perspective, mainly comparing the Newton-Raphson procedure and perturbation analysis. Finally, the nature of the equilibrium curve is explored as an algebraic variety, given a polynomial structural model. On account of the former, a novel methodology is proposed in Section III. Here, the conceptual steps are elaborated in order to extend density-based topology optimization with an improved, stable, and efficient approximate structural analysis, referring to the Appendices for lengthy derivations. In order to validate the methodology, a selection of benchmark cases is then briefly justified and outlined, comparing linear, Newton-Raphson, and the novel Bayesian-enhanced perturbed structural analysis within density-based topology optimization. Aiming for a clean study of all separate components involved within the proposed perturbed analysis, regularization steps, and traditional counterparts for comparison, basic structural analysis is incrementally expanded towards fully-fledged topology optimization. The results are laid out and interpreted directly within Sections IV, V and VI. This somewhat unorthodox approach is adopted to maintain a logical, readable document despite the length and many validation stages. It also filters the obtained knowledge in preparation to its general discussion and the resulting conclusion in hyperref[sec:Discussion]Sections Section VII and VIII, considering the goals, major findings and limitations of the present work, relevant alternative works, and most importantly the course of future works.

II Preliminaries

Structural analysis forms a pivotal component of structural design optimization, relating the structural model's deformations to energy, stiffness and applied loads, ultimately characterizing the behavior and performance that are to be optimized. Especially a non-linear model and analysis pose great utility, yet greater challenges, that the methodology in Section III aims to overcome. First, however, preliminary context, relevance, and further justification is provided in this section. Subsection II.1 clarifies the adopted tensor-notation and -operations used in this paper. Then, Subsection II.2 elaborates the discrete, conservative, non-linear energy model in its most general form, pertaining to the proposed and other state-of-the-art non-linear analysis methods, within and even outside the area of structural analysis or engineering. Subsequently, Subsection II.3 reviews and categorizes these methods, their computational benefits, limitations, and other challenges regarding the optimization framework. Finally, Subsection II.4 briefly explores the nature of the implicit equilibrium relation through algebraic geometry, adding valuable insight into formulating a suitable method for its analysis.

II.1 Mathematical Notation

Due to the various higher-order multivariate derivatives and decomposition required for the perturbed structural analysis, a specialized notation is adopted to improve the readability and intuitiveness of the mathematical groundwork in this paper. Especially the symmetry that arises from repeated differentiation with respect to the same vector is exploited, yielding equations that can be understood from a univariate point of view, without as much of the complexities from multivariate calculus. To this end, the present subsection clarifies the adopted tensor notation, inner- and outer products, their higher-order generalizations, and finally multivariate differentiation.

Tensors belong to a subclass of hyper-matrices (Comon et al., 2008), i.e. multidimensional[19] or *multi-way* arrays of numbers, generalizing the concept of scalars, vectors, and matrices. Let a number, element, or component of some d-way array $\boldsymbol{A}$ be denoted as $A_{i_1 \cdots i_d}$, where positive integers $(i_1, \cdots, i_d)$ denote the element's index along each of the array's ways. Considering tensors in particular, their values often represent physical quantities that should be invariant to the chosen coordinate system, hence the tensor's transformative properties must obey certain rules. In most practical engineering applications, these algebraic objects represent multilinear relations between other scalars, vectors, or tensors[20]. Hence, they are often encoun-

[19] This use of the word dimension is regrettably common but confusing. In this paper, it refers to the *order* or amount of *ways* of the array. Each way then has an associated dimensionality, which is typically that of the physical coordinate space where this array holds meaning.

[20] In continuum elasto-mechanics, for example, some constituent four-way or fourth-order material tensor relates the two-way or second-order stress- and strain tensors (Bathe, 2016).

tered in algebraic - meaning polynomial - systems of equations, or as higher-order multivariate derivatives[21] of smooth functions such as in this paper.

Contractions or tensor-inner-products, denoted with operator $\bullet$, compactly describe weighed summations or multilinear maps. For example, consider a *scalar* $c \in \mathbb{R}$ resulting from the *first-order* contraction between vectors $\boldsymbol{a} \in \mathbb{R}^N$ and $\boldsymbol{b} \in \mathbb{R}^N$, whose dimensions must correspond:

$$c = \boldsymbol{a} \bullet \boldsymbol{b} \quad \Longleftrightarrow \quad c = \sum_{i=1}^{N} a_i b_i \,, \tag{II.1}$$

where a_i and b_i are the respective i^{th} components of $\boldsymbol{a}$ and $\boldsymbol{b}$, with integer index $i \in \mathbb{N}$ ranging from 1 to N. Next, consider a *vector* $\boldsymbol{c} \in \mathbb{R}^M$ resulting from the *second-order* contraction between three-way array $\boldsymbol{A} \in \mathbb{R}^{M \times N \times O}$ and two-way array (matrix) $\boldsymbol{B} \in \mathbb{R}^{N \times O}$:

$$\boldsymbol{c} = \boldsymbol{A} \underset{2}{\bullet} \boldsymbol{B} \quad \Longleftrightarrow \quad c_i = \sum_{j=1}^{N} \sum_{k=1}^{O} A_{ijk} B_{jk} \,. \tag{II.2}$$

Generally, contractions of arbitrary order extend towards matrices or tensors of arbitrary order, with arbitrary dimensionalities of each of their respective ways. As such, consider, the d^{th}-order contraction between some m-way $\boldsymbol{A} \in \mathbb{R}^{I_1 \times \cdots \times I_m}$ and some n-way $\boldsymbol{B} \in \mathbb{R}^{J_1 \times \cdots \times J_n}$, resulting in the $(m+n-2d)$-way $\boldsymbol{C} \in \mathbb{R}^{I_1 \times \cdots \times I_{m-d} \times J_{d+1} \times \cdots \times J_n}$, noting that $(I_{m-d}, \cdots I_m)$ must equal $(J_1, \cdots J_d)$:

$$\boldsymbol{C} = \boldsymbol{A} \underset{d}{\bullet} \boldsymbol{B} \quad \Longleftrightarrow \tag{II.3}$$

$$C_{i_1 \cdots i_{m-d}\, j_{d+1} \cdots j_n} = \sum_{j_1=1}^{J_1} \cdots \sum_{j_d=1}^{J_d} A_{i_1 \cdots i_{m-d}\, j_1 \cdots j_d} B_{j_1 \cdots j_d\, j_{d+1} \cdots j_n}$$

Tensor- or *Segre*-outer-products (Comon et al., 2008), denoted with operator $\otimes$, are more straightforwardly defined, and do not involve summation. Consider the outer-product between the same m- and n-way arrays $\boldsymbol{A}$ and $\boldsymbol{B}$ used for equation Equation II.3, now resulting in the $(m+n)$-way tensor $\boldsymbol{C}$:

$$\boldsymbol{C} = \boldsymbol{A} \otimes \boldsymbol{B} \quad \Longleftrightarrow \quad C_{i_1 \cdots i_m\, j_1 \cdots j_n} = A_{i_1 \cdots i_m} B_{j_1 \cdots j_m} \,. \tag{II.4}$$

By extension, a tensor-*outer-power* is adopted here, analogously to scalar-exponents. Consider some vector $\boldsymbol{a} \in \mathbb{R}^N$ raised to the d^{th} outer-power, hence resulting in a *symmetric* tensor $\boldsymbol{A} \in \text{Sym}\left(\mathbb{R}^{N^d}\right)$:

$$\boldsymbol{A} = \boldsymbol{a}^{\overset{d}{\otimes}} \equiv \underbrace{\boldsymbol{a} \otimes \boldsymbol{a} \otimes \cdots \otimes \boldsymbol{a}}_{d \text{ times}} \quad \Longleftrightarrow \quad A_{i_1 \cdots i_d} = a_{i_1} \cdots a_{i_d} \tag{II.5}$$

where $\text{Sym}\left(\mathbb{R}^{N^d}\right)$ denotes the subspace of $\mathbb{R}^{N^d}$ containing all symmetric tensors, whose elements do not change under any permutation of their indices. Both the tensor-outer-product and -power are convenient tools in compactly denoting and manipulating tensor decomposition, which greatly reduces the computational effort and memory transfer in order to perform the various higher-order contractions.

Let the dimensionality of $\mathbb{R}^{N^d}$ be denoted as $\dim\left(\mathbb{R}^{N^d}\right) = N^d$. Since any permutation of the indices of a d-way N-dimensional symmetric tensor $A_{i_1 \cdots i_d}$ yields the same tensor, its dimensionality $\dim\left(\text{Sym}\left(\mathbb{R}^{N^d}\right)\right)$ is substantially smaller. Its dimensionality is instead counted by the number of unique, unordered sets of integers ranging from 1 to N. Consider a tuple of strictly non-decreasing indices $(i_1 \cdots i_d)$, meaning $N \geqslant i_d \geqslant i_{d-1} \geqslant \ldots \geqslant i_1 \geqslant 1$. This may uniquely represent all possible permutations yielding the same $A_{i_1 \cdots i_d}$, by definition of its symmetry. The diagram in Figure II.1 may uniquely correspond to such a tuple, using N orbs and d dividers. Here, each of the indices is represented by a divider and the number of orbs to its left. Since indices may be equal but must be greater than zero, dividers may be adjacent but must remain to the right of the leftmost orb. Hence, there are effectively $(N-1)+d$ free objects in this diagram. The amount of its unique arrangements equals the amount of unique non-decreasing index tuples, hence the number of unordered sets of integers ranging from 1 to N, hence the dimensionality of $\text{Sym}\left(\mathbb{R}^{N^d}\right)$:

$$\dim\left(\text{Sym}\left(\mathbb{R}^{N^d}\right)\right) = \frac{((N-1)+1)!}{(N-1)!(d)!} = \binom{N-1+d}{d} \,. \tag{II.6}$$

When N is much larger than d, this means that $\dim\left(\text{Sym}\left(\mathbb{R}^{N^d}\right)\right) \approx \frac{1}{d!} \dim\left(\mathbb{R}^{N^d}\right)$.

Decomposition of a tensor may put its low theoretical dimensionality into practice, greatly reducing the required memory and floating-point operations involved in their numerical manipulations. In particular, the *Canonical Decomposition* (CP), as visualized in Figure II.2, of some symmetric d-way N-dimensional tensor $\boldsymbol{A} \in \text{Sym}\left(\mathbb{R}^{N^d}\right)$, redefines it as a sum of d^{th}-order outer-powers of possibly complex vectors $\boldsymbol{a}_r \in \mathbb{C}^N$:

[21] A higher-order multivariate derivative could be seen as a generalized extension of a Jacobian

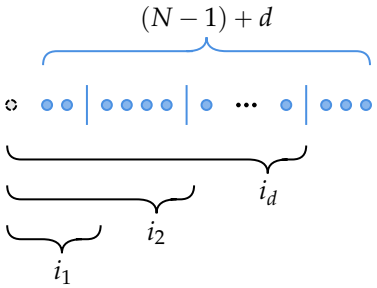

Figure II.1: Visualization of some d-tuple of indices where $N \geqslant i_d \geqslant i_{d-1} \geqslant \ldots \geqslant i_1 \geqslant 1$, uniquely representing all of the possible permutations yielding the same $A_{i_1 \cdots i_d}$ when symmetric.

$$\boldsymbol{A} = \sum_{r=1}^{R} \boldsymbol{a}_r^{\overset{d}{\otimes}} , \qquad \text{with} \quad R = \left\lceil \frac{1}{N} \binom{N-1+d}{d} \right\rceil , \tag{II.7}$$

where R denotes the *generic symmetric rank* of $\boldsymbol{A}$ (Comon et al., 2008).

Although a non-zero tensor may be of any positive rank, often still greater than N, it can be bounded by R. This arguably corresponds to the number of vectors $\boldsymbol{a}_r$ such that their collective amount of coefficients at least equals the dimensionality of $\boldsymbol{A}$. Yet, the rigorous proof for this generic rank is far from trivial, and finding a minimal rank, no less its CP decomposition, is *np-hard* (Comon et al., 2008). In addition, most contemporary methods are often ill-posed, regardless of choosing a full or even over-complete rank decomposition, or lower-rank approximation[22]. The custom strategy adopted in this work shall be elaborated in Section III and Appendix A.3.

Tucker decomposition may further reduce computational effort, essentially through a transformation of the tensors' coordinate bases, decreasing their dimensionality (but not their order), and possibly increasing their sparsity. Consider the Tucker decomposition, as visualized in Figure II.3, of the same symmetric d-way N-dimensional tensor $\boldsymbol{A}$ from Equation II.7 given transformation matrix $\boldsymbol{V} \in \mathbb{R}^{N \times \overline{N}}$:

$$\overline{\boldsymbol{A}} = \sum_{r=1}^{R} \left(\boldsymbol{V}^\top \bullet \boldsymbol{a}_r \right)^{\overset{d}{\otimes}} \quad \Longleftrightarrow \tag{II.8}$$
$$\overline{A}_{i_1 \cdots i_d} = V_{j_1 i_1} \cdots V_{j_d i_d} A_{j_1 \cdots j_d} ,$$

where $\overline{\boldsymbol{A}}$ is technically a projection of $\boldsymbol{A}$. However, Tucker decomposition becomes especially useful when a projection exists towards dimensionality $\overline{N}$ smaller than the original N, without loss of information, meaning linear operations on the tensor may be performed on its projection, the result of which may then be projected back. Notably, the very expensive CP decomposition may be preconditioned this way, significantly reducing its cost. Note that CP decomposition may be seen as a special kind of Tucker decomposition, both of which may coincide for second-order tensors, with diagonalization and spectral decomposition.

Multivariate derivatives are the final but most important concept elaborated here. They form the symmetric tensors as coefficients of the multivariate polynomial system of equations, governing structural behavior. Consider some scalar-valued function $\mathcal{E}(\boldsymbol{u})$ with vector-argument $\boldsymbol{u} \in \mathbb{R}^N$. Given that $\mathcal{E}(\boldsymbol{u})$ is smooth, its d^{th}-order derivative can be uniquely obtained and is denoted as:

$$\boldsymbol{A} = \frac{\partial^d \mathcal{E}(\boldsymbol{u})}{\partial \boldsymbol{u}^{\overset{d}{\otimes}}} \equiv \underbrace{\frac{\partial}{\partial \boldsymbol{u}} \cdots \frac{\partial}{\partial \boldsymbol{u}}}_{d \text{ times}} \mathcal{E}(\boldsymbol{u}) \quad \Longleftrightarrow \tag{II.9}$$
$$A_{i_1 \cdots i_d} = \frac{\partial^d \mathcal{E}\left([u_1, \ \ldots, \ u_N]^\top\right)}{\partial u_{i_1} \cdots \partial u_{i_d}} , \tag{II.10}$$

which exists in $\text{Sym}\left(\mathbb{R}^{N^d}\right)$, as the order of subsequent differentiations of $\mathcal{E}(\boldsymbol{u})$ versus the components of $\boldsymbol{u}$ is commutable due to smoothness, per *Clairout's theorem*. As a final remark, the mathematical relation among a set of higher-order derivative tensors, evaluated at the same point of some smooth scalar field, may especially be exploited during decomposition. To clarify, consider the basis of eigenvectors to the second-order derivative tensor. While it is generally unable to diagonalize (hence CP decompose) the derivative tensors of higher order than the second, a lot of the orthogonal properties are still able to greatly increase sparsity, and possibly reducing the effective dimension due to the field's invariance with respect to certain eigen-vectors. This notably applies to energy and translational deformation modes, as elaborated in Section III.

II.2 Discrete Structural Model

Kinematic transfer of energy is the intended purpose, hence defining characteristic, of a mechanical structure. Therefore, modeling the total energetic potential of such a structure and its interacting surroundings in terms of these kinematics is the starting point of structural analysis, before the structural behavior may be characterized or analyzed, consequently allowing the structure's shape or topology to be optimized.

In regard to modeling elasto-mechanical structures, Rayleigh-Ritz- or variational procedures are long-established and widely adopted tools (Thompson & Walker, 1968; Williamson, 1980; Han et al., 2021), such as most notably the *Finite Element Method* (FEM), developed by Courant (1943). In essence, the structure and interacting surroundings are considered as a single system, and its total energetic potential is mod-

[22] For literature on tensor-decomposition, see Kolda & Bader (2009); Battaglino et al. (2018); Comon & Luciani (2009); Brachat et al. (2010); Bernardi et al. (2013); Rabanser et al. (2017); Ge & Ma (2022), roughly ordered in terms of ascending complexity.

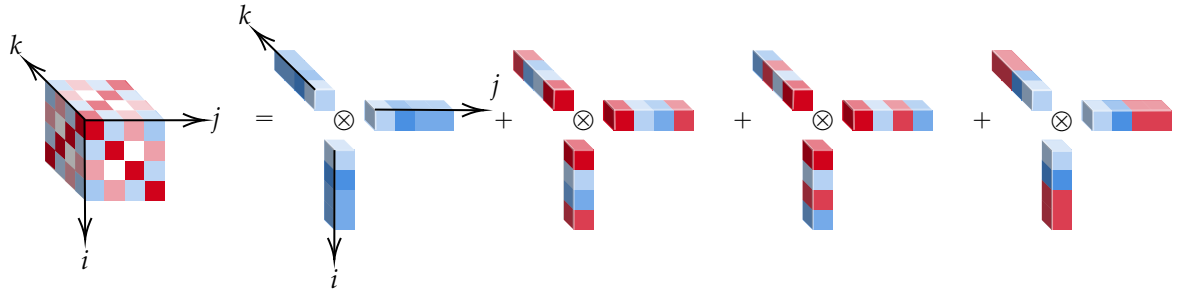

Figure II.2: *Canonical Polyadic* (CP) decomposition of some arbitrary tree-way four-dimensional symmetric tensor of symmetric rank 4.

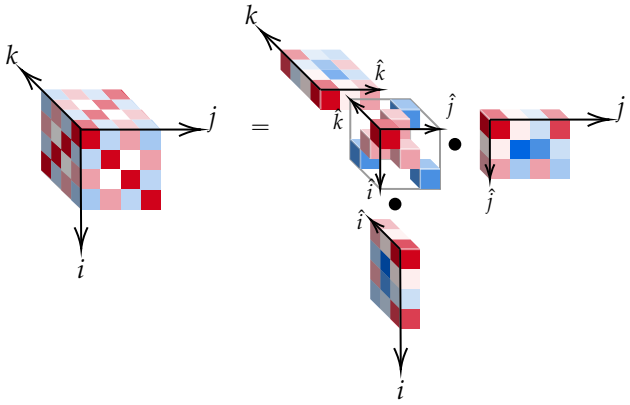

Figure II.3: *Tucker* decomposition of some arbitrary tree-way four-dimensional symmetric tensor of symmetric rank 4 and inner dimensionality 3 (i.e. nullity 1).

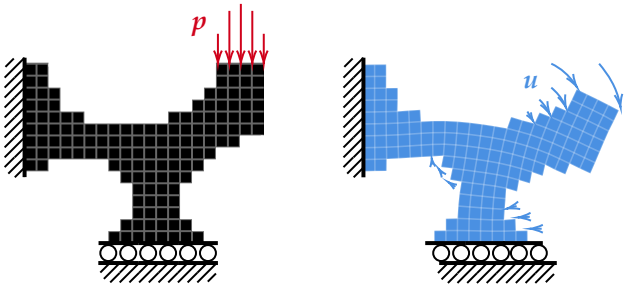

Figure II.4: Some arbitrary discrete conservative non-linear structural model, subjected to a load, a fixed- and a sliding contact. The true displacement field is approximately represented through a finite set of generalized quantities in *deformation vector* $\boldsymbol{u}$. Likewise, the true externally applied pressure field is approximately represented by a work-equivalent *applied force vector* $\boldsymbol{p}$.

eled to continuously depend on a finite amount of generalized coordinates representing the structure's deformation field and load variable[23], as illustrated in Figure II.4. In concrete mathematical terms, consider the total energetic potential $\mathcal{P}$ of a non-dynamical, conservative, discrete structural system in its most general form (Equation II.11). Here, $\mathcal{P}$ is a continuous, well-behaved function of some generalized N-dimensional kinematic freedom or *deformation vector* $\boldsymbol{u}$ and load-scalar λ, subjected to some applied force $\boldsymbol{p}$:

$$\mathcal{P}(\boldsymbol{u},\,\lambda) \equiv \mathcal{E}(\boldsymbol{u}) \;\underbrace{-\;\lambda \boldsymbol{p}\bullet\boldsymbol{u}}_{\mathcal{W}(\boldsymbol{u},\,\lambda)}\;, \qquad \text{with} \quad \begin{matrix}\boldsymbol{u}\in\mathbb{R}^N\,,\\ \lambda\in\mathbb{R}\,,\end{matrix} \tag{II.11}$$

where $\mathcal{E}$ represents the internally stored elastic energy, and $\mathcal{W}$ the externally exerted work, hence negative load-potential.

The characteristic of an elasto-mechanical structure may be interpreted as the way its deformation, energy, reactant force, stiffness, or other derived quantities change with the imposed boundary conditions. Any such quantity is implicitly, although not necessarily uniquely[24], defined through minimization of the energetic potential $\mathcal{P}(\boldsymbol{u},\,\lambda)$ (Equation II.11) with respect to its free deformations[25] $\boldsymbol{u}$:

$$\mathcal{C} \equiv \left\{ (\boldsymbol{u},\,\lambda)\in\mathbb{R}^{N+1} \;\middle|\; \frac{\partial\mathcal{P}(\boldsymbol{u},\,\lambda)}{\partial\boldsymbol{u}} = \boldsymbol{0} \right\}\,, \tag{II.12}$$

defining the structure's characteristic equilibrium curve. This is the central object of non-linear structural analysis, as will be covered next in Subsection II.3.

Some important remarks can be made on the equilibrium curve's continuity. Indeed, $\mathcal{C}$ is a one-dimensional subspace of $\mathbb{R}^{N+1}$, as there are N imposed equations within an $(N+1)$-dimensional space. Moreover, in all but a finite amount of points, its smoothness may be verified through the duly elaborated perturbation method. Here, bounded geometric derivatives can be uniquely obtained through recursive sets of linear equations. While the branch that passes through the origin is defined as the main

[23] See Appendix A for a detailed derivation concerning the proposed density-based framework in Section III.

[24] This statement pertains to solutions of any non-linear system of equations, which may yield any amount of roots including zero or infinite.

[25] Note that all physical systems naturally tend to their most likely state, where entropy is maximized and the flow of energy is in equilibrium everywhere.

branch, $\mathcal{C}$ often features numerous bifurcations, additional branches, isolated curves, or even points, satisfying equilibrium within the structural model. However, most of these are precisely non-physical artifacts of the structural model, arising where it fails to accurately predict reality. At any rate, at least the main branch may be parametrically described versus some *arc-* or *path* variable a (Thompson & Walker, 1968), up to the nearest singularities or discontinuities within $\mathcal{C}$ and up to a bijection[26] with respect to a:

$$(\forall a \in \mathbb{R}) \quad \left(\tilde{\boldsymbol{u}}(a),\ \tilde{\lambda}(a)\right) \in \mathcal{C} \ . \tag{II.13}$$

Although all definitions are now in place to understand and perform state-of-the art non-linear analysis methods (Subsection II.3), some useful physical interpretations and alternative definitions will be discussed in the remainder of this subsection. Particularly, the higher-order displacement derivatives of the elastic energy $\mathcal{E}(\boldsymbol{u})$ provide key utility and insight into perturbation- and algebraic analysis methods discussed in Subsections II.3 and II.4, respectively. Incidentally, the reformulation generalizes the classical internal force- and tangent stiffness matrix adopted in Bathe (2016).

The energy's *first* displacement-derivative defines the structure's surjective *internal force* vector function $\boldsymbol{f}(\boldsymbol{u})$:

$$\boldsymbol{f}(\boldsymbol{u}) \equiv \frac{\partial \mathcal{E}(\boldsymbol{u})}{\partial \boldsymbol{u}} \ , \tag{II.14}$$

which is named appropriately, as it should equal the externally applied force $\lambda \boldsymbol{p}$ for equilibrium. As such, the *residual force* $\boldsymbol{r}(\boldsymbol{u})$ defines the extent of *in-equilibrium*, thus error between both forces:

$$\boldsymbol{r}(\boldsymbol{u},\ \lambda) \equiv -\frac{\partial \mathcal{P}(\boldsymbol{u},\ \lambda)}{\partial \boldsymbol{u}} = \lambda \boldsymbol{p} - \boldsymbol{f}(\boldsymbol{u}) \ . \tag{II.15}$$

Moving on, the energy's *second* displacement-derivative defines the structure's instantaneous, or *tangent stiffness* matrix function $\boldsymbol{\mathcal{K}}(\boldsymbol{u})$:

$$\boldsymbol{\mathcal{K}}(\boldsymbol{u}) \equiv \frac{\partial \boldsymbol{f}(\boldsymbol{u})}{\partial \boldsymbol{u}} \equiv \frac{\partial^2 \mathcal{E}(\boldsymbol{u})}{\partial \boldsymbol{u}^{\overset{2}{\otimes}}} \ , \tag{II.16}$$

where, to clarify, the $(i,j)^{\text{th}}$ component of $\boldsymbol{\mathcal{K}}(\boldsymbol{u})$ may be interpreted as $\mathcal{E}(\boldsymbol{u})$ differentiated with respect to the i^{th}, and then again to the j^{th} component of $\boldsymbol{u}$. This quantity plays a key role in any practical non-linear structural analysis method. Notably, when polynomial strain- and material models are used to define conservative elastic energy $\mathcal{E}(\boldsymbol{u})$, it may be reformulated without loss of accuracy, as a multivariate polynomial

[26] Any non-linear one-to-one correspondence between a and an alternative parameter, or even a surjection, do not change the shape of the curve that is being traced.

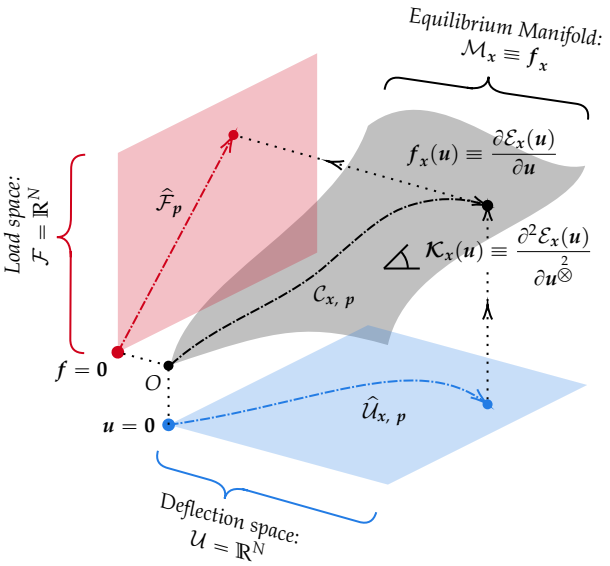

Figure II.5: Visualization of the equilibrium manifold $\mathcal{M} \subset \mathbb{R}^{2N}$, containing all equilibria simply as the graph of the internal force function $\boldsymbol{f}_x(\boldsymbol{u})$, parameterized by design $\boldsymbol{x}$. Structural analysis often involves seeking displacements $\widehat{\mathcal{U}}_{x,\,p}$ such that $\boldsymbol{f}_x(\widehat{\mathcal{U}}_{x,\,p}) = \widehat{\mathcal{F}}_p \equiv \text{Span}\{\boldsymbol{p}\}$.

of finite degree, or finite multivariate MacLaurin series:

$$\mathcal{E}(\boldsymbol{u}) = \sum_{k=0}^{d} \frac{1}{k!} \left. \frac{\partial^k \mathcal{E}(\boldsymbol{u})}{\partial \boldsymbol{u}^{\overset{k}{\otimes}}} \right|_{\boldsymbol{u}=\boldsymbol{0}} \bullet_k \boldsymbol{u}^{\overset{k}{\otimes}} \ . \tag{II.17}$$

This multivariate polynomial reformulation, or tensorial reformulation, will be particularly useful for the proposed methodology in Section III, if the symmetric coefficient tensors, being the derivatives of $\mathcal{E}(\boldsymbol{u})$, are successfully decomposed. Appendix A contains a detailed elaboration of the reformulation and decomposition as used within the proposed methodology.

Finally, all structural model definitions elaborated in this section are preferably smoothly related to some *design vector* $\boldsymbol{x}$, typically governing the structure's shape, topology, or local density. Through this quantity, the equilibrium curve thus structural behavior can then incrementally be manipulated in order to optimize the design's performance. Figure II.5 compactly visualizes all mentioned definitions, with subscripts emphasizing dependence on both design $\boldsymbol{x}$ and $\boldsymbol{p}$. In addition, the equilibrium curve $\mathcal{C}$ may be considered as a subspace or section of the *equilibrium manifold* $\mathcal{M}$, containing all equilibrium configurations for any possible applied load $\boldsymbol{p}$. Effectively, $\mathcal{M}$ is the graph of $\boldsymbol{f}(\boldsymbol{u})$.

II.3 Non-Linear Structural Analysis

Given the structure's non-linear energetic model (Equation II.11) and implicitly defined equilibrium curve (Equation II.12), structural analysis exclusively deals with the challenge of explicitly finding or approximat-

ing this curve, by solving its governing set of non-linear equations. This has been a subject of considerable interest for over multiple decades (Haisler et al., 1972). Notably, most state-of-the-art methods that deal with non-linear problems tend to leverage the advantageous properties of linear problems. These include the existence and uniqueness of their solutions, which may hence be found robustly and efficiently. Generally, however, solving non-linear equations is an old[27], notoriously difficult problem transcending the field of engineering, for which many methods are being rapidly developed relatively recently (He, 1998). Hence, a wide variety of suitable methods exist beyond the default choices within structural analysis. This subsection mainly compares the most widely adopted but arguably lacking *Newton-Raphson* approach, and the under-acknowledged but promising *Perturbation Method*, both of which generalize beyond the otherwise limited linear analysis.

Computational effort, accuracy, and stability are the main challenges and hence first priorities of structural analysis within structural optimization, given sufficient ease of implementation. Here, stability refers to an algorithm's capability to consistently yield, or converge to, a unique output that smoothly varies with its input over a large domain. Within gradient-based design optimization, unstable or strongly input-dependent responses may yield ill-informed or chaotic design changes, slowing down or even preventing convergence entirely. Rather than curating instability through additional implementations, it is most preferably avoided in the first place. Furthermore, *strong* non-linearity is considered as the local non-uniqueness of some relation or set of solutions, causing ill-conditioned or even singular derivatives[28]. While the latter compromises the efficiency, accuracy, and stability of almost any contemporary method of non-linear analysis, the non-uniqueness poses additional challenges to formulating a well-behaved response, deemed beyond the scope of this work. In terms of direct practical use, as well as a future extension towards the strongly non-linear domain, much value is to be gained by first considering small deformations within the *mildly* non-linear domain[29]. This ensures uniqueness, allowing for more elementary responses, and also promotes efficiency and stability of the structural analysis and -optimization as a whole.

Returning to the task of non-linear structural analysis, recall the equilibrium curve $\mathcal{C}$ as the set of solutions to the non-linear equilibrium equations (II.12), or equivalently the roots of the non-linear residual equations (II.15):

$$\mathcal{C} = \left\{ (\boldsymbol{u},\ \lambda) \in \mathbb{R}^{N+1} \;\middle|\; \underbrace{\lambda \boldsymbol{p} - \boldsymbol{f}(\boldsymbol{u})}_{\boldsymbol{r}(\boldsymbol{u},\ \lambda)} = \boldsymbol{0} \right\}, \tag{II.18}$$

Haisler et al. (1972) distinguished the majority of the non-linear analysis methods into two classes. The first class *I* comprises the inherently diverging, incremental, extrapolative methods. The incremental stiffness method, being one of the oldest, is equivalent to the forward integration of the equilibrium equation in differential form:

$$\boldsymbol{\mathcal{K}}(\boldsymbol{u})\mathrm{d}\boldsymbol{u} = \boldsymbol{p}\mathrm{d}\lambda\ , \tag{II.19}$$

inherently leading to drift from $\mathcal{C}$. To remedy, higher-order generalizations such as *Modified Euler* or *Runge-Kutta* can be applied, all of which are approximately equivalent to successive perturbation methods, aiming to predict neighboring solutions on $\mathcal{C}$, given readily obtained solutions. The second class *II* comprises the self-correcting, usually interpolative methods, to which the following is a notable exception. Moreover, the Newton-Raphson approach has remained most successful due to its relative ease of implementation, low amount of tunable parameters[30], and particularly its high accuracy and robustness when faced with strongly non-linear problems (Thompson & Walker, 1968; Haisler et al., 1972). However, technically it is a class *I* method incorporated with corrective steps, meaning a more sensible distinction is in order.

Homotopy, prediction, and correction are predominant state-of-the-art non-linear solution strategies, often complementing each other in hybrid schemes. Homotopy[31] methods often use some bijective relation, mapping the challenging non-linear equations that govern the original solution into an equivalent but less challenging set of non-linear, or sometimes even linear equations. Then, the corresponding solution is mapped back to the original solution space. Of course, this inverse map poses another non-linear problem of its own, typically requiring previously described methods. Within non-linear structural analysis, homotopy is generally difficult to use but certainly very promising. For instance, it may bypass the small-parameter requirement inherent to most perturbation methods (He, 1998; Liao, 2004, 2010). In fact, based on the present work it is strongly recommended to extend the proposed perturbation method with algebraic-geometric analysis, using some rational homotopy. Here, it is assumed that there exists a bi-rational map between some true polynomial solution curve within the projective load-deflection space, and the original load-

[27] A famous example dates back to Zu's *"n-body problem"* (1885) which can be recast into a set of algebraic differential equations, akin to the structural equilibrium equations adopted in Section III.

[28] Examples of strong non-linearity are buckling, multi-stability, or zero-stiffness.

[29] The mildly non-linear domain is defined here to extend from the undeformed state up to the first strong non-linearity

[30] Tunable parameters refer to parameters specific to the method of analysis, rather than the model that is analyzed.

[31] For reference on homotopy analysis methods, see He (1998); Liao (2004, 2010); Agarwal et al. (2021).

deflection space. This shall be further clarified in Subsection II.4 and Subsection VII.4.

Regardless, the remainder of this work mainly focuses on prediction and correction, more particularly *Newton-Raphson* (**NR**) and *Perturbation* (**P**) analysis, for several reasons. As duly argued and demonstrated, basic **P** (*Perturbation*) analysis can readily outcompete **NR** (*Newton-Raphson*) analysis in terms of effort, accuracy, and stability, under realistic conditions. Furthermore, it forms a necessary but solid stepping stone towards an improved algebraic geometric variant employing homotopy, suggested as future work (Subsection VII.4).

NR analysis aims to curate error through multiple linear implicit prediction- and explicit correction steps. Alternatively, the asymptotic- or **P** analysis aims to prevent error through a single high-order prediction, without correction. More precisely, a non-linear prediction barely facilitates correction, as this would pose a correspondingly non-linear problem similar to the original equilibrium equations.

For mathematical clarification, consider the approximate residual $\widetilde{\boldsymbol{r}}(a)$ as a function of path variable a along some implied prediction towards, or explicit prediction along, the equilibrium curve $\mathcal{C}$:

$$\widetilde{\boldsymbol{r}}(a) \equiv \boldsymbol{r}\Big(\widetilde{\boldsymbol{u}}(a),\ \widetilde{\lambda}(a)\Big) \ . \tag{II.20}$$

The first-order prediction within **NR** differs from the higher-order prediction within **P** regarding imposed accuracy, respectively requiring $\widetilde{\boldsymbol{r}}(a+\Delta a)$ to equal:

$$\begin{aligned} (\mathbf{NR}) \qquad & \widetilde{\boldsymbol{r}}(a) + \frac{\mathrm{d}\widetilde{\boldsymbol{r}}(a)}{\mathrm{d}a}\Delta a && = \ \boldsymbol{\mathcal{O}}(\Delta a^2) \ , \\ (\mathbf{P}) \qquad & \widetilde{\boldsymbol{r}}(a) + \sum_{k=1}^{n} \frac{1}{k!}\frac{\mathrm{d}^k\widetilde{\boldsymbol{r}}(a)}{\mathrm{d}a^k}\Delta a^k && = \ \widetilde{\boldsymbol{r}}(a) + \boldsymbol{\mathcal{O}}(\Delta a^{n+1}) \ , \end{aligned} \tag{II.21}$$

where $\boldsymbol{\mathcal{O}}(g(\Delta a))$ denotes limit behavior being upper-bounded by $\boldsymbol{M}\cdot g(\Delta a)$ for some finite $\boldsymbol{M} \in \mathbb{R}^N$. In other words, with respect to a preceding step, **NR** aims to correct the current residual up to a second-order error, by solving for the first-order prediction $(\widetilde{\boldsymbol{u}}(a),\ \widetilde{\lambda}(a))$ satisfying zeroth-order equilibrium, meaning towards $\mathcal{C}$. On the other hand, some n^{th}-order **P** aims to prevent increased residual up to an $(n+1)^{\text{st}}$-order error, by constructing an n^{th}-order prediction $(\widetilde{\boldsymbol{u}}(a),\ \widetilde{\lambda}(a))$ satisfying first-, up to n^{th}-order equilibrium, parallel to $\mathcal{C}$. Hence, the following respective sets of structural equations are successively imposed until some desired error criterion is met:

$$\begin{aligned} (\mathbf{NR}) \qquad & \widetilde{\boldsymbol{r}}(a_k) + \frac{\mathrm{d}\widetilde{\boldsymbol{r}}(a_k)}{\mathrm{d}a_k}\,(a_{k+1}-a_k) = \boldsymbol{0} \\ & \qquad\qquad \text{s.t.} \quad \ell\Big(\widetilde{\boldsymbol{u}}(a_{k+1}),\ \widetilde{\lambda}(a_{k+1})\Big) = 0 \ , \\ (\mathbf{P}) \qquad & \frac{\mathrm{d}^k\widetilde{\boldsymbol{r}}(a)}{\mathrm{d}a^k} = \boldsymbol{0} \qquad \text{s.t.} \quad \ell\Big(\widetilde{\boldsymbol{u}}(a),\ \widetilde{\lambda}(a)\Big) = 0 \ , \end{aligned} \tag{II.22}$$

where $\ell(\boldsymbol{u},\lambda)$ denotes a generalized step-length metric, such that the newly introduced, otherwise indeterminate path variable a may be resolved.

As a simplified example, consider a load-controlled analysis initiated from the undeformed state, meaning $\lambda = \widetilde{\lambda}(a) \equiv a$, $\boldsymbol{u} = \widetilde{\boldsymbol{u}}(a) = \widetilde{\boldsymbol{u}}(\lambda)$ and $\lambda = 0 \Leftrightarrow \boldsymbol{u} = \boldsymbol{0}$. Starting with **NR**, Equation II.22 reduces to the following recursive sequence zeroth-order residuals, implicitly defining a sequence of zeroth-order displacement solutions $\boldsymbol{u}_k$, for $k = 1,\ \ldots,\ n$:

$$\underbrace{\boldsymbol{r}(\boldsymbol{u}_{k-1},\ \lambda)}_{\boldsymbol{r}_{k-1}} + \underbrace{\left.\frac{\partial \boldsymbol{r}(\boldsymbol{u},\ \lambda)}{\partial \boldsymbol{u}}\right|_{\boldsymbol{u}=\boldsymbol{u}_{k-1}}}_{-\boldsymbol{\mathcal{K}}(\boldsymbol{u}_{k-1})} \bullet (\boldsymbol{u}_k - \boldsymbol{u}_{k-1}) = \boldsymbol{0} \ , \tag{II.23}$$

with $\boldsymbol{u}_0 \equiv \boldsymbol{0}$. More explicitly, this sequence then equals:

$$\begin{aligned} & \boldsymbol{u}_0 \equiv \boldsymbol{0} \ , && (\mathbf{NR}) \\ & \boldsymbol{u}_1 = \Big[\boldsymbol{\mathcal{K}}(\boldsymbol{0})\Big]^{-1} \bullet (\lambda \boldsymbol{p}) \ , \\ & \boldsymbol{u}_2 = \boldsymbol{u}_1 + \Big[\boldsymbol{\mathcal{K}}(\boldsymbol{u}_1)\Big]^{-1} \bullet \Big(\lambda \boldsymbol{p} - \boldsymbol{f}(\boldsymbol{u}_1)\Big) \ , \\ & \quad \vdots \\ & \boldsymbol{u}_n = \boldsymbol{u}_{n-1} + \underbrace{\Big[\boldsymbol{\mathcal{K}}(\boldsymbol{u}_{n-1})\Big]^{-1}}_{-\left.\frac{\partial \boldsymbol{u}}{\partial \boldsymbol{r}}\right|_{\boldsymbol{u}=\boldsymbol{u}_{n-1}}} \bullet \underbrace{\Big(\lambda \boldsymbol{p} - \boldsymbol{f}(\boldsymbol{u}_{n-1})\Big)}_{\boldsymbol{r}(\boldsymbol{u}_{n-1},\ \lambda)} \ . && (\text{II.24}) \end{aligned}$$

The linear prediction- and correction steps within such a **NR** sequence of displacement solutions are schematically visualized in Figure II.6, for a single degree of freedom.

Moving on to **P**, Equation II.22 reduces to the following recursive sequence of incrementally higher-order residual derivatives, implicitly defining a sequence of incrementally higher-order displacement derivatives $\boldsymbol{u}^{(k)}$, for $k = 1,\ \ldots,\ n$:

$$\begin{aligned} \underbrace{\left.\frac{\mathrm{d}^k\widetilde{\boldsymbol{r}}(\lambda)}{\mathrm{d}\lambda^k}\right|_{\lambda=0}}_{\boldsymbol{r}^{(k)}} = \underbrace{\left.\frac{\partial \boldsymbol{r}(\boldsymbol{u},\ \lambda)}{\partial \boldsymbol{u}}\right|_{\boldsymbol{u}=\boldsymbol{0}}}_{-\boldsymbol{\mathcal{K}}(\boldsymbol{0})} \bullet \underbrace{\left.\frac{\mathrm{d}^k\widetilde{\boldsymbol{u}}(\lambda)}{\mathrm{d}\lambda^k}\right|_{\lambda=0}}_{\boldsymbol{u}^{(k)}} \\ + \boldsymbol{\mathcal{R}}^{(k)}\left(\boldsymbol{u}^{(1)},\ \boldsymbol{u}^{(2)},\ \ldots,\ \boldsymbol{u}^{(k-1)}\right) = \boldsymbol{0} \ , \end{aligned} \tag{II.25}$$

with $\boldsymbol{u}^{(0)} \equiv \boldsymbol{0}$. The expression for $\boldsymbol{r}^{(k)}$ is obtained by recursively applying the product- and chain rule, where $\boldsymbol{\mathcal{R}}^{(k)}$ denotes the resulting multilinear form, excluding the first RHS-term which contains the $\boldsymbol{u}^{(k)}$ that is yet to be solved at the k^{th} perturbation iteration. Alternatively, a closed-form expression for $\boldsymbol{r}^{(k)}$ may be obtained using *Faá di Bruno*'s generalized chain rule. Moreover, when $\boldsymbol{r}(\boldsymbol{u}, \lambda)$ is some low-order multivariate polynomial versus $\boldsymbol{u}$, a much less complicated closed-form expression for $\boldsymbol{r}^{(k)}$ may be obtained using *Leibniz* generalized product-rule. This is notably the case given the quadratic strain model within the proposed methodology in Section III, where this differentiation step is elaborated in more detail. More explicitly, the sequence of Equation II.25 then equals:

$$
\begin{aligned}
&\boldsymbol{u}^{(0)} \equiv \boldsymbol{0} \,, && (\mathbf{P}) \\
&\boldsymbol{u}^{(1)} = \Big[\boldsymbol{\mathcal{K}}(\boldsymbol{0})\Big]^{-1} \bullet (\boldsymbol{p}) \,, \\
&\boldsymbol{u}^{(2)} = \Big[\boldsymbol{\mathcal{K}}(\boldsymbol{0})\Big]^{-1} \bullet \left(-\frac{\partial^2 \boldsymbol{f}(\boldsymbol{u})}{\partial \boldsymbol{u}^{\overset{2}{\otimes}}}\bigg|_{\boldsymbol{u}=\boldsymbol{0}} \overset{2}{\bullet} \left(\boldsymbol{u}^{(1)}\right)^{\overset{2}{\otimes}} \right) \,, \\
&\quad \vdots \\
&\boldsymbol{u}^{(n)} = \Big[\boldsymbol{\mathcal{K}}(\boldsymbol{0})\Big]^{-1} \bullet \boldsymbol{\mathcal{R}}^{(n)} \left(\boldsymbol{u}^{(1)}, \boldsymbol{u}^{(2)}, \dots, \boldsymbol{u}^{(n-1)}\right) \,.
\end{aligned}
\tag{II.26}
$$

The linear and higher order predictions constructed from such a **P** sequence of displacement derivatives are schematically visualized in Figure II.6, for a single degree of freedom.

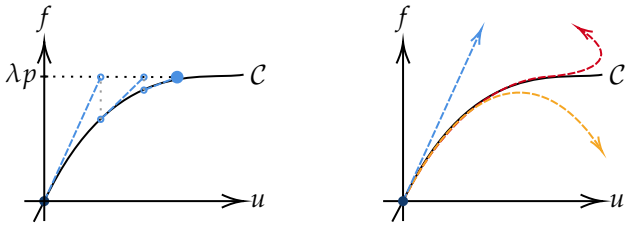

Figure II.6: Schematic visualization of a linear predictor-corrector (Newton-Raphson-) method (**left**) and high-order predictor (Perturbation-) method (**right**).

In different ways, **NR** and **P** analysis generalize beyond linear analysis, to which they are effectively identical only at their respective first iterations. This can be seen by comparing Equation II.24 and II.26. To clarify, both $\boldsymbol{u}_1$ and $\boldsymbol{u}^{(1)}\lambda$ equal $\lambda \boldsymbol{K}^{-1}\boldsymbol{p}$, for $\boldsymbol{K} \equiv \boldsymbol{\mathcal{K}}(\boldsymbol{0})$. Then, from their respective second iterations and onward, they feature separate strengths and weaknesses.

Starting with utility, **NR** and **P** analysis respectively converge towards a point and a continuous interval on the equilibrium curve $\mathcal{C}$ (Figure II.6). This respectively yields isolated zeroth-order information, or distributed higher-order information on $\mathcal{C}$. When structural performance has been user-defined to depend on distributed or higher-order equilibrium information, rather than isolated zeroth order, **P** analysis may efficiently suit the needs through a single local expansion, where **NR** analysis may require several converged points. Some examples are path-generation, multi-stability (Parenti-Castelli & Sancisi, 2013), and frequency multiplication (MacHekposhti et al., 2018).

More generally concerning accuracy, not only the domain but also the rate of convergence differs between **NR** and **P** analysis, excluding their respective zeroth and first iterations where both methods, their errors, and rates are still identical. **NR** has been known to feature quadratic terminal convergence (Bruns & Tortorelli, 2001), even when it initially diverges. On the other hand, **P** typically features (sub)-linear convergence, or (super)-linear divergence, as shown in Appendix B and verified in Subsection IV.1. When using a Taylor expansion, this phenomenon may be characterized by the radius of convergence. Beyond the radius, predictions tend to get exponentially worse versus the order, and polynomially worse versus the path parameter, while the exact opposite happens towards the expansion point within the radius. In that sense, **NR** can handle larger step lengths, and ultimately converges much faster. With each new error roughly equal to the previous error squared, a doubly exponential convergence is obtained. Table II.1 and Figure II.7 give an indication of the relative normed errors using **NR** and **P** analysis, based on their estimators derived in Appendix B.

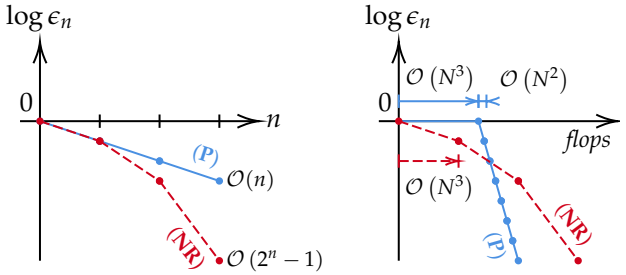

Figure II.7: Schematic convergence of the relative normed error ϵ_n versus the amount of structural solves n (**left**) and corresponding amount of floating-point operations (*flops*) (**right**), comparing the Newton-Raphson approach (**NR**) and perturbation method (**P**). Here, N denotes the structure's number of freedom degrees.

In terms of total computational cost given some desired accuracy, **P** analysis may still outcompete **NR** analysis. While **NR** has an exponentially accelerating convergence rate, it also has a higher iteration cost. Comparing their sequence of iterations, meaning Equation II.24 to II.26, it can be seen that **NR** requires an updated system matrix $\boldsymbol{\mathcal{K}}(\boldsymbol{u}_k)$ each iteration, in order to maintain quadratic convergence and robustness. On the other hand, **P** uses the same $\boldsymbol{\mathcal{K}}(\boldsymbol{0})$, which can be exploited through a prior Cholesky-factorization. Al-

n		0	1	2	3	4	5
$\widetilde{\epsilon}_n$	**(P)**	1	ϵ_L	ϵ_L^2	ϵ_L^3	ϵ_L^4	ϵ_L^5
$\widetilde{\epsilon}_n$	**(NR)**	1	ϵ_L	ϵ_L^3	ϵ_L^7	ϵ_L^{15}	ϵ_L^{31}

Table II.1: Relative displacement error estimator $\widetilde{\epsilon}_n$ where n denotes the number of structural solves, or iterations, for perturbed analysis **(P)**, and Newton-Raphson analysis (**NR**). Note that $\epsilon_L \equiv \epsilon_1$ is identically obtained after a single Newton-Raphson iteration, and a first-order perturbation, both of which are then equivalent to linear analysis.

though the latter requires a heavier calculation than a single **NR** iteration, both involve a number of floating-point operations (*flops*) of the order $\mathcal{O}(N^3)$, given N degrees of freedom[32]. However, for every following iteration, **P** now requires roughly $\mathcal{O}(N^2)$ flops per iteration. Especially for large N this initial investment repays itself, allowing **P** to temporarily overtake **NR** due to its superior initial convergence rate in terms of accuracy to cost, or flops. It must be noted, however, that the right-hand-side vector $\boldsymbol{R}^{(n)}$ also super linearly increases in cost versus n due to nested applications of the chain- and product-rule. This may become problematic without having access to decomposed element-tensors. Fortunately, these need to be obtained only once for a single element of a given type and material model, as shown in Appendix A.3.

Further concerning computational efficiency and robustness, some step length of load-scalar λ or path-variable a can be continuously varied *after* **P** analysis has been performed[33]. Conversely, **NR** analysis requires the step length to be determined before the analysis, meaning the sequence must restart if it diverges. In fact, **NR** is much more likely to suffer from an ill-conditioned stiffness matrix, especially near load limits (Bruns & Tortorelli, 2001). The radius of convergence and error for **P** analysis can accurately be estimated, such as derived in Appendix B.2. As a result, a feasible or even optimal step length is practically determined by the method itself, rather than the user (Azrar et al., 1993). It facilitates automated control over cost and accuracy, and rapid automatic continuation of $\mathcal{C}$ (Azrar et al., 1993; Cochelin, Damil, & Potier-Ferry, 1994) when using multiple expansions. This is to bypass the diminishing returns of accuracy over cost, and the limited radius of convergence for a single expansion. Effectively, **P** then becomes an accelerated or higher-order **NR** method, or some confluent Runge-Kutta method. Still incapable of correction steps, it does not require them nearly as much as basic **NR** regardless.

[32]Note that for sparse systems, this order of floating-point operations is slightly lower for both the solve, and the factorization.

[33]This has been verified by Cochelin (1994); Cochelin, Damil, & Potier-Ferry (1994); Cochelin, Damil, & Potier-Ferry (1994); De Boer & Van Keulen (1997); Azrar et al. (1993); El Kihal et al. (2022).

To summarize, **NR** analysis is easier to implement, features quadratic convergence, and is one of the most accurate methods up to date. However, it may only yield a point on the equilibrium curve, requires a predetermined step length, becomes unstable near load limits, and requires system matrix updates each iteration. **P** analysis overcomes all of these drawbacks, yielding a continuous or asymptotic approximation of the equilibrium curve, facilitating an optimal automatic step length, and retains a relatively well-conditioned sequence of structural solves. However, it may be more difficult to implement, requiring the construction and possibly decomposition of higher-order element-tensors, featuring only linear convergence at best, albeit at the same initial rate as **NR**. Nevertheless, it does not require system matrix updates, facilitating Cholesky factorization and significantly more efficient solves. Overall, **P** incidentally features superior efficiency, utility and robustness compared to **NR**, at least within the radius of convergence. Currently, the size of this radius and high-order prediction divergence beyond it, are the most prominent limitations.

Various promising attempts have been made to increase the radius of convergence and robustness of **P** analysis, to which the choice of parameterization $(\widetilde{\boldsymbol{u}}(a),\ \widetilde{\lambda}(a))$ has been found highly significant (Thompson & Walker, 1968; Cochelin, 1994; De Boer & Van Keulen, 1997; Najah et al., 1998). Rather than the most elementary choices of MacLaurin or Taylor expansions, rationals have been adopted, or more precisely Padé extrapolants (Najah et al., 1998; Cochelin, Damil, & Potier-Ferry, 1994; Cochelin, Damil, & Potier-Ferry, 1994; De Boer & Van Keulen, 1997; Ayane et al., 2019; El Kihal et al., 2022), yielding significantly increased radii and a natural means to control limit behavior for large a, by balancing the numerator and denominator degrees. Oddly, the greatly increased effectiveness has been described as mysterious (Najah et al., 1998). However, from an algebraic geometrical perspective, this should not be entirely unexpected as some true parameterization of the solution has been proven to exist, given an algebraic set of structural equations, as elaborated in the next subsection. Furthermore, spurious poles of rational perturbation methods have been found problematic to its accuracy and robustness (Cochelin, 1994; De Boer & Van Keulen, 1997; El Kihal et al., 2022). A *vectorial* Padé extrapolant has been adopted (El Kihal et al., 2022) to reduce the risk of such poles, simply by imposing the same denominator for all components tracing the curve. Again, this seems to be an unnoticed remarkable consistency with the parametric form of algebraic curves. By coincidence, the proposed Bayesian-enhanced perturbation method in Section III effectively yields a vectorial Padé extrapolant without poles, through the very attempt to minimize error and divergence, and optimize robustness. Perhaps this is less coincidental than it seems,

and the powerful capabilities of vectorial rationals shall be demonstrated from both the analytical (Subsection II.4), and a stochastic (Appendix C) perspective, regardless.

II.4 Algebraic Structural Analysis

By strategically using prior information on the nature of the structural equilibrium curve, unnecessary complexity, thus computational effort and potential instability, become avoidable during its analysis. Particularly, the algebraic nature of the structural equations and corresponding solutions are exploited here. Although ultimately a perturbation-based methodology has been developed and validated, the present subsection provides valuable insight into its validity, and more importantly, a foundation for future extensions towards possibly superior algebraic geometric variants.

When the structural model and corresponding non-linear equations are found to be algebraic, meaning polynomial, much can be revealed about the existence, smoothness, and degree of the set, or manifold, containing all solutions. This set belongs to the class of algebraic varieties, and is covered by an extensive amount of literature[36]. Again, recall the equilibrium curve $\mathcal{C}$ as the set of solutions to the non-linear residual equations (II.15):

$$\mathcal{C} = \left\{ \; (\boldsymbol{u},\, \lambda) \in \mathbb{R}^{N+1} \;\middle|\; \underbrace{\lambda \boldsymbol{p} - \boldsymbol{f}(\boldsymbol{u})}_{\boldsymbol{r}(\boldsymbol{u},\, \lambda)} = \boldsymbol{0} \right\}, \qquad \text{(II.27)}$$

where the residual $\boldsymbol{r}(\boldsymbol{u},\, \lambda)$ has now been reformulated, without loss of accuracy, into its full MacLaurin series. This is due to the polynomial strain- and linear material model, as adopted in the methodology, and elaborated in Appendix A.

$$\boldsymbol{r}(\boldsymbol{u},\, \lambda) \;\equiv\; \lambda \boldsymbol{p} \;-\; \overbrace{\boldsymbol{K} \bullet \boldsymbol{u}}^{\text{Linear FEM}} \;\underbrace{-\; \tfrac{1}{2} \boldsymbol{S} \underset{2}{\bullet} \boldsymbol{u}^{\overset{2}{\otimes}} \;-\; \tfrac{1}{6} \boldsymbol{Q} \underset{3}{\bullet} \boldsymbol{u}^{\overset{3}{\otimes}}}_{\text{Geometrically non-linear FEM}}, \qquad \text{(II.28)}$$

where $\boldsymbol{K}(\boldsymbol{x}) \in \mathrm{Sym}\big(\mathbb{R}^{N^2}\big)$, $\boldsymbol{S}(\boldsymbol{x}) \in \mathrm{Sym}\big(\mathbb{R}^{N^3}\big)$ and $\boldsymbol{Q}(\boldsymbol{x}) \in \mathrm{Sym}\big(\mathbb{R}^{N^4}\big)$ represent the second-, third- and fourth-order partial displacement derivatives of $\mathcal{E}(\boldsymbol{u};\, \boldsymbol{x})$ versus $\boldsymbol{u}$, evaluated at $\boldsymbol{u} = \boldsymbol{0}$, being two-, three- and four-way N-dimensional symmetric tensors[34]. As a result, $\mathcal{C}$ can be regarded an *algebraic curve* of degree up to 3^N, as argued next.

[34] As duly elaborated in Section III, numerical operations involving these N-dimensional tensors can be efficiently mediated using their decomposed, 8-dimensional contributions on the element level, assuming 8 degrees of freedom per structural element.

Given some fixed load-scalar λ in the multivariate *cubic* system of Equation II.28, one can express three solutions for a single component of $\boldsymbol{u}$ in terms of the remaining, unresolved $N-1$ components. For each of these solutions, one can express another three solutions for a second component in terms of the remaining $N-2$ unresolved ones, yielding nine so far. Doing this for all components theoretically yields an astronomically high total of 3^N solutions, most of which are spurious, complex-valued, or otherwise unphysical. [35] By the same reasoning, given any fixed component of $\boldsymbol{u}$ and solving for the remaining $N-1$ components of $\boldsymbol{u}$ and single component of λ yields 3^N solutions

Through algebraic geometry[36], the nature of the curve $\mathcal{C}$ (Equation II.12) is directly revealed as an algebraic variety which, under certain conditions, can be rationally parameterized. To clarify - leaving the rigorous proof to the literature[36] - some $N+1$ rational functions versus some path- or *arc* variable $a \in \mathbb{R}$ may perfectly trace $\mathcal{C}$, excluding a finite amount of points:

$$\begin{cases} \widetilde{\boldsymbol{u}}(a) = \dfrac{\boldsymbol{U}(a)}{Z(a)} \\ \widetilde{\lambda}(a) = \dfrac{\Lambda(a)}{Z(a)} \end{cases} \quad : \quad \boldsymbol{f}\big(\widetilde{\boldsymbol{u}}(a)\big) = \widetilde{\lambda}(a) \boldsymbol{p} \;, \qquad \text{(II.29)}$$

with the components of $\boldsymbol{U}(a)$, $\Lambda(a)$, and $Z(a)$ being univariate polynomials of degree up to 3^N. This can be verified by substituting $\widetilde{\boldsymbol{u}}(a)$ and $\widetilde{\lambda}(a)$ into Equation II.28, equating it to $\boldsymbol{0}$ for equilibrium, and then multiplying everything by $Z(a)^3$ to obtain an algebraic equation again:

$$\begin{aligned} \boldsymbol{K} \bullet \Big(Z(a)^2 \boldsymbol{U}(a) \Big) + \tfrac{1}{2} \boldsymbol{S} \underset{2}{\bullet} \Big(Z(a) \boldsymbol{U}(a)^{\overset{2}{\otimes}} \Big) \\ + \tfrac{1}{6} \boldsymbol{Q} \underset{3}{\bullet} \Big(\boldsymbol{U}(a)^{\overset{3}{\otimes}} \Big) = \Big(Z(a)^2 \Lambda(a) \Big) \boldsymbol{p} \;, \end{aligned} \qquad \text{(II.30)}$$

where the role of denominator $Z(a)$ now becomes apparent: *homogenizing* (Sendra et al., 2008) the polynomial system of Equation II.30, meaning all polynomial terms of are now of equal degree versus a, although most importantly the left- and right-hand-side are, which would not be possible without the denominator $Z(a)$. Note that the homogenized system can be compactly rewritten simply by recollecting terms:

[35] This is a very rough illustration of *Bézout's Theorem*, stating that the amount of zeros of a multivariate polynomial equals the product its components' degrees (Hartshorne, 2013).

[36] For relevant literature on algebraic geometry and rational parameterization, see Sendra et al. (2008), Hartshorne (2013), and Wurm et al. (2005).

$$\boldsymbol{A} \underset{3}{\bullet} \boldsymbol{Y}(a)^{\overset{3}{\otimes}} = \boldsymbol{0} \,, \qquad \text{with} \quad \boldsymbol{Y}(a) \equiv \begin{bmatrix} \boldsymbol{U}(a) \\ \Lambda(a) \\ Z(a) \end{bmatrix} \in \mathbb{R}^{N+2} \,, \tag{II.31}$$

where $\boldsymbol{A} \in \mathrm{Sym}\left(\mathbb{R}^{(N+2)^4}\right)$ denotes the 4-way symmetric tensor of the homogenized system, within the projective load-deflection space $\mathbb{R}^{N+2}$. Furthermore, $\boldsymbol{A}$ is a linear combination of the original structural system tensors $\boldsymbol{K}$, $\boldsymbol{S}$, $\boldsymbol{Q}$, and applied load $\boldsymbol{p}$.

The exceedingly high degree of 3^N for the individual univariate polynomials may roughly be explained through the previously argued amount of solutions given some fixed component of $\boldsymbol{u}$ or λ. Considering each of the curve's $N+1$ components separately, its value must occur up to 3^{N-1} or 3^N times, accounting for complex solutions and multiplicity; The $3^{N\text{th}}$ degree numerators $\boldsymbol{U}(a)$ and $\Lambda(a)$ facilitate exactly that, while the denominator $Z(a)$ of the same degree ensures the homogeneity and existence of a solution to Equation II.30 for all but a finite amount of $a \in \mathbb{R}$.

Bifurcations are also worth addressing from the algebraic geometrical perspective, as they are linked to structural instability, element inversion, but most notably predict a reduced effective degree of the equilibrium curve's main branch. The residual force $\boldsymbol{r}(\boldsymbol{u},\ \lambda) = \lambda \boldsymbol{p} - \boldsymbol{f}(\boldsymbol{u})$ may be considered as the curve's *defining* polynomial, which in turn may be factored out repeatedly until they become irreducible. In this case, each of these irreducible factors defines a separate, potentially isolated branch, or even singular point (*acnode*), whose degrees sum up to that of the total curve. Where multiple of these curves coincide, the total defining polynomial becomes *multiply* zero, hence the same amount of its derivatives minus one becomes zero. Equivalently, the residual remains zero along multiple (not necessarily independent) directions, being null-vectors of $\partial \boldsymbol{r} / \partial [\boldsymbol{u}^\top,\ \lambda]^\top$. Given the well-documented existence of structural bifurcations, the main branch of interest is of a much lower degree than 3^N, although most likely still impractically large.

In conclusion, each branch of the equilibrium curve in $\mathbb{R}^{N+1}$ may be perfectly traced by a continuous rational parameterization of finite, yet impractically large degree. On the other hand, an equivalent projective equilibrium curve in $\mathbb{R}^{N+2}$ may be perfectly traced by a polynomial parameterization of the same degree. Moreover, polynomials have an infinite radius of convergence, whereas traditional perturbation methods are often bottle-necked by a finite, small radius of convergence. An infinite radius remarkably guarantees global convergence of the approximation towards the considered equilibrium branch. At any rate, the smoothness within each equilibrium branch, and possibly the form of their finitely complex analytical parameterization, are valuable even to basic perturbation analysis. Moreover, they are valuable to the formulation and validation of an adequate structural topology optimization methodology based on perturbation analysis, as proposed in the next Section III.

III Methodology

A novel methodology is proposed here, extending structural topology optimization with efficient and robust geometrically non-linear analysis. Subsection III.1 gives a general overview, summarizing conceptual steps and justification behind its formulation and implementation. Then, Subsection III.2, and the optional but strongly recommended Subsection III.3, elaborate the adopted structural design model exploiting a tensor reformulation and decomposition, facilitating the structural analysis proposed in Subsection III.4. Here, a Bayesian approach is taken based on error estimation, improving the robustness and accuracy of perturbed non-linear analysis, which readily overcomes many other limitations of Newton-Raphson analysis within density-based topology optimization. Then, the bridge towards optimization is formulated in Subsection III.5, covering regularization and the adjoint design sensitivity analysis. Lastly, a validation strategy and corresponding study cases are mapped out in Subsection III.6, through which the analysis and topology optimization results in Section IV and V are obtained. Ultimately, the state-of-the-art Newton-Raphson (NR), Perturbed (P) and novel Bayesian-enhanced perturbed (B) analyses are compared, all of which are identical to Linear (L) analysis for a single iteration, but distinctively generalize beyond it.

III.1 General Overview

Harnessing the modern computational cycle of structural design, modeling, analysis, evaluation, and redesign, the methodology is mostly based on the two-dimensional density-based topology optimization Matlab-code `top99.m` (Sigmund, 2001), its numerically optimized `top88.m` (Andreassen et al., 2011), and the Method of Moving Asymptotes (MMA, Svanberg, 1987), for several reasons. The duly clarified overview can be seen in Figure III.2. In addition to its powerful design freedom argued in Section I and Subsection II.2, building upon existing and accessible codes accelerates future development, as suggested by C. Wang et al. (2021). A more detailed account is provided in Subsection III.2. Ultimately, some continuous *design-vector* $\boldsymbol{x}$ governs the structural design, as visualized in Figure III.1, using a density-based finite element model.

Consider some design $\boldsymbol{x}$, an applied *load-vector* $\boldsymbol{p}$ scaled by some continuous load variable λ, and other structural boundary conditions. Traditional structural

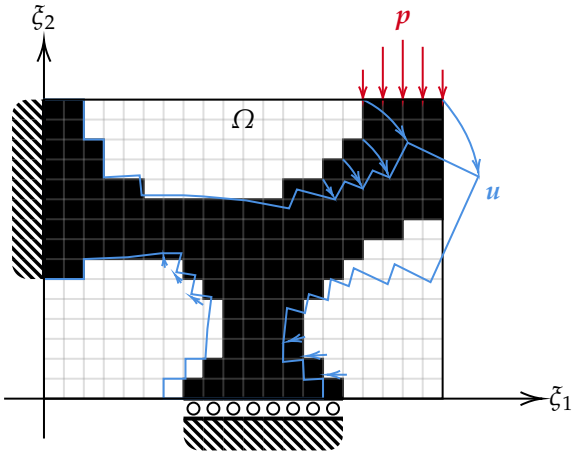

Figure III.1: Some arbitrary density-based structural design defined through $\boldsymbol{x}$, on design domain Ω over global coordinates $(\xi_1,\ \xi_2)$. The main goal of this work is to efficiently but accurately obtain displacement $\boldsymbol{u}$ given certain boundary conditions and applied force $\lambda \boldsymbol{p}$, versus $\lambda \in [0,\ 1]$.

analysis then aims to relate the resulting *displacement-vector* $\boldsymbol{u}$ to the former, by solving a set of minimum-potential, i.e. structural equilibrium equations, as covered in the following subsections. The equilibrium curve $\mathcal{C}$ then denotes all possible solutions over a continuous range of λ, visualized in Figure III.3.

Rather than facing the drawbacks of solving the original zeroth-order equilibrium equations at various non-zero loads or λ, the *Perturbed* analysis in Subsection III.4 involves solving various higher-order equilibrium equations at zero load and displacement. This implicitly defines the geometric derivatives of $\mathcal{C}$ at the undeformed state, or likewise those of some parameterization $(\boldsymbol{u},\ \lambda) = \big(\widetilde{\boldsymbol{u}}(a),\ \widetilde{\lambda}(a)\big)$. Here, a denotes the path variable along this parametric curve, that hence asymptotically approximates $\mathcal{C}$ in the neighborhood of the undeformed state, where $a = 0$. Intuitively, the matching initial derivatives between the parametric and true curve ensures that $\big(\widetilde{\boldsymbol{u}}(a),\ \widetilde{\lambda}(a)\big)$ features no initial error, velocity, acceleration, up to a finite amount of higher-order equivalents, away from the equilibrium curve $\mathcal{C}$ as a is increased above 0. Note that the present methodology adopts a load-controlled parameterization, meaning $(\boldsymbol{u},\ \lambda) = \big(\widetilde{\boldsymbol{u}}(\lambda),\ \lambda\big)$, conforming the scope being limited to mild-nonlinearities, as argued in Section I.

Without going into too much detail on the perturbed analysis, an error estimator of the higher-order prediction can benefit robustness and accuracy twofold. Originally, an elementary MacLaurin extrapolant was constructed from the obtained higher-order derivatives:

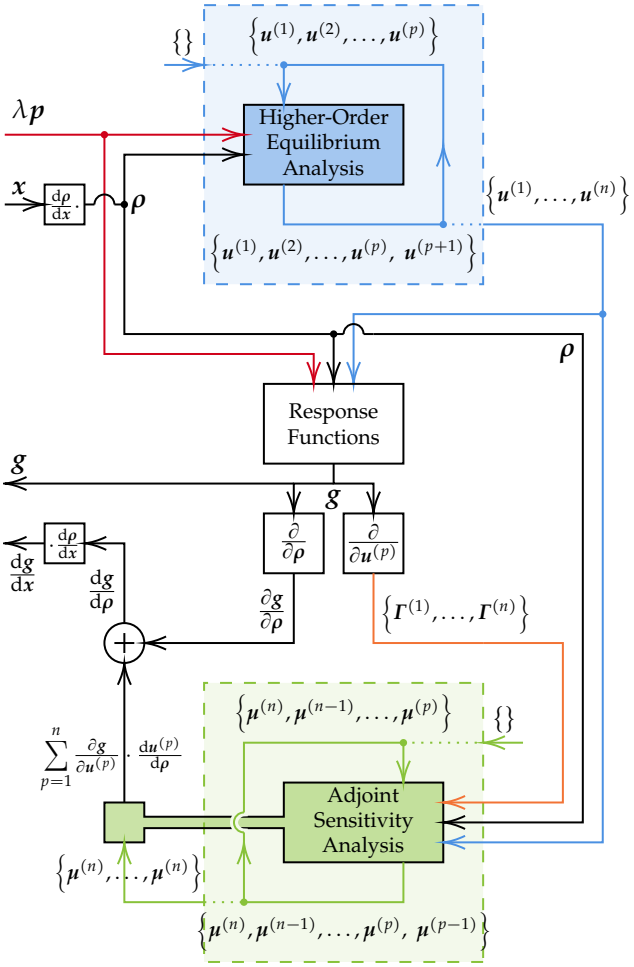

Figure III.2: Topology optimization function-chain for perturbed structural analysis and adjoint sensitivity analysis. Note the analogy between the structural displacement-derivatives $\boldsymbol{u}^{(p)}$ and adjoint solutions $\boldsymbol{\mu}^{(p)}$, and likewise between the external load $\lambda \boldsymbol{p}$ and adjoint load $\boldsymbol{\Gamma}^{(p)} \equiv \partial \boldsymbol{g} / \partial \boldsymbol{u}^{(p)}$.

$$\widetilde{\boldsymbol{u}}_n(\lambda) \equiv \sum_{p=1}^{n} \frac{1}{p!} \boldsymbol{u}^{(p)} \lambda^p \ , \qquad \text{where} \quad \boldsymbol{u}^{(p)} \equiv \frac{\mathrm{d}^p \boldsymbol{u}}{\mathrm{d}\lambda^p}\bigg|_{\lambda=0} \ . \tag{III.1}$$

Technically, one could implement the perturbed analysis as is. However, Taylor series in particular (Powell, 1964; Cochelin, 1994), or any other extrapolation (Demanet & Townsend, 2019), is generally bound to ultimately diverge. As a result, dependent responses and their design sensitivities become inaccurate, which may quickly destabilize the topology optimization unless this divergence is directly or indirectly controlled. Since stable control requires feedback, hence a normed estimator of this inaccuracy, or error $\widetilde{\epsilon}_n(\lambda)$, was derived. Firstly, this can guide the optimizer by ensuring sufficient accuracy of the analysis, and justification of the optimized design. Secondly, it facilitates an

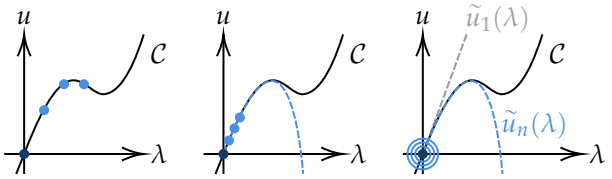

Figure III.3: Equilibrium curve $\mathcal{C}$ (black) and solutions resulting from various methods (blue). **Left:** converged equilibrium points. **Center:** exact curve-fit $\widetilde{\boldsymbol{u}}(\lambda)$ to $n > 1$ converged equilibrium points close to the origin. **Right:** exact k^{th}-degree curve-fit $\widetilde{\boldsymbol{u}}_k(\lambda)$ to exact equilibrium derivatives at the origin, respectively supplied with $k = 1$ and $k = n$ derivatives.

improved extrapolant or prediction, and corresponding error estimator, simply by averaging all $\widetilde{\boldsymbol{u}}_p(\lambda)$ and $\widetilde{\epsilon}_p(\lambda)$ for $p = 1, \ldots, n$, in a way that continuously minimizes the aggregate error estimator given any λ. Hence, every last drop of information is squeezed out of the painstakingly obtained higher-order derivatives $\boldsymbol{u}^{(p)}$. This process, referred to as *Bayesian Model Averaging* (Hoeting et al., 1999), incidentally yields a rational-, or more specifically a vectorial Padé-type (El Kihal et al., 2022) extrapolant, of superior robustness and accuracy, but without the spurious poles encountered in other attempts at rational perturbation analysis (Cochelin, Damil, & Potier-Ferry, 1994; De Boer & Van Keulen, 1997; El Kihal et al., 2022).

For future reference, a simplified overview of the topology optimization function chain is depicted in Figure III.2, omitting the Bayesian-enhanced high-order prediction. While most of the symbols and processes are duly elaborated in more detail, they can be briefly described as follows. Some design $\boldsymbol{x}$ is regularized or filtered into a corresponding set of densities $\boldsymbol{\rho}$. Combined with the applied load $\lambda \boldsymbol{p}$, the n^{th}-order equilibrium analysis loop is performed, incrementally yielding higher-order derivatives of equilibrium-satisfying displacements $\boldsymbol{u}$ versus λ, denoted with superscript (p) for $p = 1, \ldots, n$. Then, the user-defined responses $\boldsymbol{g}$, and corresponding analytical first-order partial derivatives, are evaluated as a direct function of $\boldsymbol{\rho}$ and the various $\boldsymbol{u}^{(p)}$. This respectively yields the responses density-derivatives, and the *adjoint forces* $\boldsymbol{\Gamma}^{(p)}$ for $p = 1, \ldots, n$, simply named due to their analogy with $\lambda \boldsymbol{p}$ in the following loop. The adjoint sensitivity analysis loop is then performed analogously to the equilibrium analysis loop, incrementally yielding the *adjoint solutions* $\boldsymbol{\mu}^{(p)}$ for $p = n, \ldots, 1$. Due to this loop, ultimately the derivatives of $\boldsymbol{g}$ versus $\boldsymbol{x}$ are obtained, without explicitly having to calculate those of $\boldsymbol{u}^{(p)}$ and $\boldsymbol{\mu}^{(p)}$ for $p = 1, \ldots, n$. Finally, the responses and their design derivatives are fed into the *Method of Moving Assymptotes* (MMA) (Svanberg, 1987), producing an updated design $\boldsymbol{x}$, after which the cycle repeats.

III.2 Density-Based Structural Model

A foundational component of the structural design cycle is the structural model and corresponding set of assumptions, implicitly defining the kinematic and energetic behavior as evaluated by some user-defined performance metric. Conforming to the two-dimensional density-based finite element approach argued in Subsection I.3, II.2, and III.1, the presented methodology is based on the effective and accessible `top99.m` (Sigmund, 2001) and `top88.m` (Andreassen et al., 2011). Further considering frictionless compliant mechanisms, the simplistic yet accurate geometric non-linearity (Buhl et al., 2000a; Pedersen et al., 2001; Han et al., 2021) is modeled using the *Green-Lagrange* strain measure and *Total Lagrangian Formulation* (Bathe, 2016; Chapter 6), based on a displacement field bi-linearly interpolated between each 4-noded element's nodes, each of which hence has 8 degrees of freedom. The material for each element is modeled uniformly isotropic and linearly elastic, depending only on its effective *Young*'s modulus E, *Poisson*'s contraction coefficient ν, and the chosen out-of-plane stress- or strain condition[37]. Finally, the structural model is reformulated as an exact multivariate polynomial without loss of accuracy, facilitating its local reversion, or inversion, through perturbed analysis, in addition to prior element domain integration, and otherwise increased numerical efficiency.

The structural design is modeled through the total energetic potential of a density-controlled, frictionless finite element model, subjected to conservative loads, kinematic constraints, and possibly other boundary conditions. By subdividing some overall design domain Ω (Figure III.1) into some M element or voxel domains, the structure's shape, topology, and behavior are defined through a regular grid of tiny structural elements of varying elasticity. Design vector $\boldsymbol{x} \in \mathbb{R}^M$ then contains for each element a continuous scalar between zero and one, controlling these stiffnesses.

Concretely, before elaborating on the element level, *total energetic potential* $\mathcal{P}(\boldsymbol{u},\ \lambda;\ \boldsymbol{x})$ denotes the continuous, well-behaved function of some generalized N-dimensional kinematic freedom or *deformation vector* $\boldsymbol{u} \in \mathbb{R}^N$, subjected to some *applied load vector* $\boldsymbol{p} \in \mathbb{R}^N$ scaled by *load variable* $\lambda \in \mathbb{R}$, typically within $[0, 1]$, given some design $\boldsymbol{x}$:

$$\mathcal{P}(\boldsymbol{u},\ \lambda;\ \boldsymbol{x}) \equiv \mathcal{E}(\boldsymbol{u};\ \boldsymbol{x}) \ - \ \underbrace{\lambda \boldsymbol{p} \bullet \boldsymbol{u}}_{\mathcal{W}(\boldsymbol{u},\ \lambda)} \ , \tag{III.2}$$

where $\mathcal{E}(\boldsymbol{u};\ \boldsymbol{x})$ represents the internally stored elastic energy, and $\mathcal{W}(\boldsymbol{u},\ \lambda)$ the externally exerted work, hence negative load potential. As duly elaborated, $\mathcal{E}(\boldsymbol{u};\ \boldsymbol{x})$ is simply modeled as the sum of element con-

[37] Commonly, either zero out-of-plane stress or strain is chosen for two-dimensional structural designs.

tributions.

In the end, the design's structural behavior is characterized by the equilibrium relation, meaning the deformations that minimize total potential, given a design variable $\boldsymbol{x}$ and the applied boundary conditions. Equivalently, it is characterized by zero inequilibrium, or *residual force* $\boldsymbol{r}(\boldsymbol{u},\ \lambda;\ \boldsymbol{x})$, defined as:

$$\boldsymbol{r}(\boldsymbol{u},\ \lambda;\ \boldsymbol{x}) \equiv \lambda \boldsymbol{p} - \boldsymbol{f}(\boldsymbol{u};\ \boldsymbol{x}) \ , \tag{III.3}$$

$$\overbrace{-\frac{\partial \mathcal{P}(\boldsymbol{u},\ \lambda;\ \boldsymbol{x})}{\partial \boldsymbol{u}}} \qquad \overbrace{\frac{\partial \mathcal{E}(\boldsymbol{u},\ \lambda;\ \boldsymbol{x})}{\partial \boldsymbol{u}}}$$

where $\boldsymbol{f}(\boldsymbol{u};\ \boldsymbol{x})$ defines the surjective[38] *internal force* vector function. Given some design $\boldsymbol{x}$, the *equilibrium curve* $\mathcal{C}_{\boldsymbol{x}}$ that is ultimately sought-after or approximated during structural analysis, then compactly denotes the set of equilibrium solutions, or residual roots, relating applied forces to deformations as:

$$\mathcal{C}_{\boldsymbol{x}} \equiv \left\{ \ (\boldsymbol{u},\ \lambda) \in \mathbb{R}^{N+1} \ : \ \underbrace{\lambda \boldsymbol{p} - \boldsymbol{f}(\boldsymbol{u};\ \boldsymbol{x})}_{\boldsymbol{r}(\boldsymbol{u},\ \lambda;\ \boldsymbol{x})} = \boldsymbol{0} \ \right\} . \tag{III.4}$$

In order to facilitate perturbed analysis, the structural model is recast into an algebraic, tensorial, or equivalently multivariate polynomial form without loss of accuracy, pertaining to $\mathcal{P}(\boldsymbol{u}_e;\ \boldsymbol{x})$, thus $\mathcal{E}(\boldsymbol{u};\ \boldsymbol{x})$, and all of its derivatives versus $\boldsymbol{u}$. More precisely, the element contributions that sum up to $\mathcal{E}(\boldsymbol{u};\ \boldsymbol{x})$ are reformulated into their respective MacLaurin expansions about their undeformed state, exploiting the low-degree polynomial nature of the adopted Green-Lagrange strain measure.[39] Ultimately, perturbed analysis involes higher-order path derivatives of the equilibrium equation (III.4) defining $\mathcal{C}_{\boldsymbol{x}}$, hence higher-order displacement derivatives of $\mathcal{E}_e(\boldsymbol{u}_e;\ \boldsymbol{x})$ through the chain rule. To this end, the remainder of this subsection covers the structural assembly and element tensor reformulation. Computational concerns regarding the involved contractions of these tensors are addressed in Subsection III.5, being an optional but strongly recommended step of the methodology. Furthermore, details on regularization, such as material penalization, density filtering and deformation scaling, are left to Subsection III.5.

Assembly effectively connects all individual 8-degrees-of-freedom structural element models to one another, forming the overall N-degree-of-freedom structural model. It generalizes the way that the elastic energy and deformation of the overall structure straightforwardly relate to those of its elements. To clarify, the internally stored elastic energy $\mathcal{E}(\boldsymbol{u};\ \boldsymbol{x})$ equals the sum over element contributions:

$$\mathcal{E}(\boldsymbol{u};\ \boldsymbol{x}) = \sum_{e=1}^{M} \mathcal{E}_e(\boldsymbol{u}_e;\ \boldsymbol{x}) \ , \tag{III.5}$$

$$\text{where} \quad \boldsymbol{u}_e = \mathbb{A}_e \boldsymbol{u} \quad \text{and} \quad \mathbb{A}_e \equiv \frac{\partial \boldsymbol{u}_e}{\partial \boldsymbol{u}} \ ,$$

where $\boldsymbol{u}_e \in \mathbb{R}^8$ denotes the deformation of the structure's e^{th} element, simply being a partition of the structure's global deformation $\boldsymbol{u} \in \mathbb{R}^N$ according to the degree of freedom connectivity visualized in Figure III.4. *Assembly matrix* $\mathbb{A}_e \in \{0,\ 1\}^{8 \times N}$ represents this partition, constructed purely from ones and zeros.

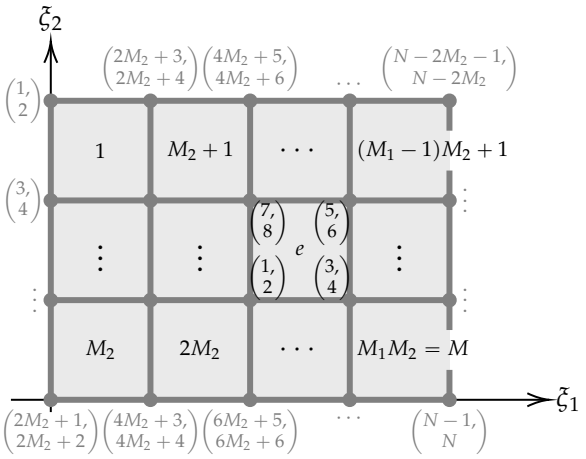

Figure III.4: Element numbers $e = 1,\ \ldots,\ M$, global degree-of-freedom indices $i = 1,\ \ldots,\ N$ and local degree-of-freedom indices $i = 1,\ \ldots,\ 8$ for some e^{th} element of an M_2-by-M_1 voxel-grid structure. Adapted from Sigmund (2001) and Andreassen et al. (2011).

Extending assembly to higher-order derivatives of Equation III.5 such as force and stiffness, the purpose of this seemingly unwieldy definition or interpretation of $\mathbb{A}_e$ will become apparent. Namely, in a conservative system, the internal force vector $\boldsymbol{f}(\boldsymbol{u};\ \boldsymbol{x}) \in \mathbb{R}^N$ and tangent stiffness matrix $\boldsymbol{\mathcal{K}}(\boldsymbol{u};\ \boldsymbol{x}) \in \text{Sym}\left(\mathbb{R}^{N^2}\right)$ equal the respective first- and second-order partial derivatives of $\mathcal{E}(\boldsymbol{u};\ \boldsymbol{x})$ versus $\boldsymbol{u}$. Applying the chain rule $\frac{\partial}{\partial \boldsymbol{u}} = \frac{\partial \boldsymbol{u}_e}{\partial \boldsymbol{u}}^{\top} \bullet \frac{\partial}{\partial \boldsymbol{u}_e}$ respectively once and twice, using $\frac{\partial \boldsymbol{u}_e}{\partial \boldsymbol{u}} = \mathbb{A}_e$, yields:

$$\boldsymbol{f}(\boldsymbol{u};\ \boldsymbol{x}) \equiv \frac{\partial \mathcal{E}(\boldsymbol{u};\ \boldsymbol{x})}{\partial \boldsymbol{u}} = \sum_{e=1}^{M} \mathbb{A}_e^{\top} \bullet \underbrace{\frac{\partial \mathcal{E}_e(\boldsymbol{u}_e;\ \boldsymbol{x})}{\partial \boldsymbol{u}_e}}_{\boldsymbol{f}_e(\boldsymbol{u}_e;\ \boldsymbol{x})} , \tag{III.6}$$

[38] A surjective function maps its domain *onto* its image, meaning multiple inputs may correspond to the same output.

[39] Notably, the MacLaurin reformulation of total potential originally inspired this work's earlier attempt of multivariate polynomial reversion, later found to be equivalent to perturbed analysis (Thompson & Walker, 1968) and the asymptotic numerical method (Cochelin, 1994).

$$\boldsymbol{\mathcal{K}}(\boldsymbol{u};\ \boldsymbol{x}) \equiv \frac{\partial^2 \mathcal{E}(\boldsymbol{u};\ \boldsymbol{x})}{\partial \overset{2}{\boldsymbol{u}^{\otimes}}} = \sum_{e=1}^{M} \mathbb{A}_e^{\top} \bullet \underbrace{\frac{\partial^2 \mathcal{E}_e(\boldsymbol{u}_e;\ \boldsymbol{x})}{\partial \overset{2}{\boldsymbol{u}_e^{\otimes}}}}_{\boldsymbol{\mathcal{K}}_e(\boldsymbol{u}_e;\ \boldsymbol{x})} \bullet \mathbb{A}_e \ , \tag{III.7}$$

with element e's internal force vector $\boldsymbol{f}_e(\boldsymbol{u}_e;\ \boldsymbol{x}) \in \mathbb{R}^8$ and tangent stiffness matrix $\boldsymbol{\mathcal{K}}_e(\boldsymbol{u}_e;\ \boldsymbol{x}) \in \mathrm{Sym}\left(\mathbb{R}^{8^2}\right)$.

Generalizing the derivatives beyond force and stiffness, the MacLaurin reformulation of $\mathcal{E}_e(\boldsymbol{u}_e;\ \boldsymbol{x})$ is obtained. Specifically, a multivariate quartic description of $\mathcal{E}_e(\boldsymbol{u}_e;\ \boldsymbol{x})$ results from the quadratic Green-Lagrange strain measure:

$$\begin{aligned} \mathcal{E}_e(\boldsymbol{u}_e;\ \boldsymbol{x}) \ \equiv \ & \overbrace{\tfrac{1}{2}\boldsymbol{K}_e(\boldsymbol{x}) \underset{2}{\bullet} \overset{2}{\boldsymbol{u}_e^{\otimes}}}^{\text{Linear FEM}} \\ & \underbrace{+ \ \tfrac{1}{6}\boldsymbol{S}_e(\boldsymbol{x}) \underset{3}{\bullet} \overset{3}{\boldsymbol{u}_e^{\otimes}} \ + \ \tfrac{1}{24}\boldsymbol{Q}_e(\boldsymbol{x}) \underset{4}{\bullet} \overset{4}{\boldsymbol{u}_e^{\otimes}}}_{\text{Geometrically non-linear FEM}} , \end{aligned} \tag{III.8}$$

where $\boldsymbol{K}_e(\boldsymbol{x}) \in \mathrm{Sym}\left(\mathbb{R}^{8^2}\right)$, $\boldsymbol{S}_e(\boldsymbol{x}) \in \mathrm{Sym}\left(\mathbb{R}^{8^3}\right)$ and $\boldsymbol{Q}_e(\boldsymbol{x}) \in \mathrm{Sym}\left(\mathbb{R}^{8^4}\right)$ are respectively treated and obtained as the second-, third- and fourth-order partial displacement derivatives of $\mathcal{E}_e(\boldsymbol{u}_e;\ \boldsymbol{x})$ versus $\boldsymbol{u}_e$, given $\boldsymbol{u}_e = \boldsymbol{0}$, being two-, three- and four-way 8-dimensional symmetric tensors[40]. Appendix A.2 elaborates the detailed reformulation.

On the structural level, the reformulation of Equation III.8 is entirely analogous, omitting the subscript e. The structural tensors become $\boldsymbol{K}(\boldsymbol{x}) \in \mathrm{Sym}\left(\mathbb{R}^{N^2}\right)$, $\boldsymbol{S}(\boldsymbol{x}) \in \mathrm{Sym}\left(\mathbb{R}^{N^3}\right)$ and $\boldsymbol{Q}(\boldsymbol{x}) \in \mathrm{Sym}\left(\mathbb{R}^{N^4}\right)$, exponentially sparser in that order. Surely, $\boldsymbol{K}(\boldsymbol{x})$ may need to be assembled on the structural level, being involved in structural solves of the perturbation analysis. On the other hand, although the assembled $\boldsymbol{S}(\boldsymbol{x})$ and $\boldsymbol{Q}(\boldsymbol{x})$ are mathematically convenient to work with, implementing them as such is incredibly inefficient and fortunately unnecessary, as shown in Subsection III.4.

III.3 Structural Tensor Decomposition

Tensor decomposition is an optional but strongly recommended step regarding numerical efficiency. It renders the potentially problematic but unavoidable structural MacLaurin, or tensorial reformulation even superior to its canonical form proposed by Bathe (2016). Without decomposition, it is especially taxing when applied to perturbed analysis, compared to Newton-Raphson analysis. To clarify, due to the recursive application of the product rule, perturbed analysis requires a super-linearly increasing amount of force-like evaluations and corresponding tensor contractions versus the perturbation order, as shown in Subsection III.4. To remedy, the involved tensors themselves are also reformulated and implemented as their near-minimal decompositions on the element level, more than sufficiently addressing the associated computational concerns. The ultimate goal is only to reduce the required effort on force-like evaluations, up to the point where the associated structural solves or other overhead calculations become dominant.

More specifically, a single representative element is formulated, and a *Canonical Polyadic* (CP) decomposition[41] is constructed from the corresponding tensors, such that it and its decomposition may be cheaply related to those of all other elements, given that their model linearly relates to the representative model. While CP decomposition is a highly non-convex, ill-posed, incredibly expensive problem even for a single element, as further elaborated in Appendix A.3, its result may be stored and extensively recycled or cheaply transformed forever. In this appendix, it is also shown that evaluating the structure's internal force and tangent stiffness becomes a few times more efficient, comparing the decomposed tensor formulation to Bathe's (2016) canonical formulation. The tensor reformulation already factors the structural model's deformation dependence out of the domain integrations involved in the discretization of the structural continuum equations, elaborated in Appendix A.2. Additionally, through decomposition, a nearly minimal amount of storage and floating point operations is now required when evaluating force, stiffness, or any other related force-like derivatives.

Considering the mathematics and implementation of tensor decomposition, recall that $\boldsymbol{S}_e(\boldsymbol{x})$ and $\boldsymbol{Q}_e(\boldsymbol{x})$ respectively denote the third- and fourth-order partial displacement derivatives of $\mathcal{E}_e(\boldsymbol{u}_e;\ \boldsymbol{x})$ versus $\boldsymbol{u}_e$ given $\boldsymbol{u}_e = \boldsymbol{0}$. Then, defining the representative structural element of the adopted quadrilateral type and particular material model $\boldsymbol{D}$, let $\widehat{\mathcal{E}}_{\boldsymbol{D}}(\widehat{\boldsymbol{u}})$ denote its internally stored elastic energy in terms of its displacement $\widehat{\boldsymbol{u}} \in \mathbb{R}^8$ in some natural or local coordinate frame. Any $\mathcal{E}_e(\boldsymbol{u}_e;\ \boldsymbol{x})$ can then be linearly related to this one, as:

$$\mathcal{E}_e(\boldsymbol{u}_e;\ \boldsymbol{x}) = c_e(\boldsymbol{x}) \cdot \widehat{\mathcal{E}}_{\boldsymbol{D}}\Big(\boldsymbol{B}_e(\boldsymbol{x}) \bullet \boldsymbol{u}_e\Big) \ , \tag{III.9}$$

where the linear operators $c_e(\boldsymbol{x}) \in \mathbb{R}$ and $\boldsymbol{B}_e(\boldsymbol{x}) \in \mathbb{R}^{8\times 8}$ may be non-linear functions of $\boldsymbol{x}$ themselves, as placeholders for any density scaling and linear displacement or coordinate mapping, or otherwise linear transformation of the current element's energy model. Correspondingly, any $\boldsymbol{S}_e(\boldsymbol{x})$ and $\boldsymbol{Q}_e(\boldsymbol{x})$ may be respectively related to the same $\widehat{\boldsymbol{S}}_{\boldsymbol{D}}$ and $\widehat{\boldsymbol{Q}}_{\boldsymbol{D}}$. Moreover, the same applies to their respective decompositions, equal to Equation III.10 for $d = 3$ and $d = 4$. A preferably (nearly) minimal symmetric tensor rank R_d (Comon

[40] The reader is referred back to Subsection II.1 and II.2 for more details on the tensor notation and structural model.

[41] For a visualization of Canonical Polyadic decomposition, see Figure II.2.

et al., 2008) is often assumed or guessed prior to the numerically decomposing such a d-way tensor:

$$\left.\frac{\partial^d \widehat{\mathcal{E}}_{\boldsymbol{D}}(\widehat{\boldsymbol{u}})}{\partial \widehat{\boldsymbol{u}}^{\overset{d}{\otimes}}}\right|_{\widehat{\boldsymbol{u}}=\boldsymbol{0}} \equiv \sum_{r=1}^{R_d} \widehat{\boldsymbol{a}}_r^{\overset{d}{\otimes}}, \tag{III.10}$$

$$\text{hence} \quad \left.\frac{\partial^d \mathcal{E}_e(\boldsymbol{u}_e;\, \boldsymbol{x})}{\partial \boldsymbol{u}_e^{\overset{d}{\otimes}}}\right|_{\boldsymbol{u}_e=\boldsymbol{0}} = c_e(\boldsymbol{x}) \cdot \sum_{r=1}^{R_d} \left(\boldsymbol{B}_e(\boldsymbol{x}) \bullet \widehat{\boldsymbol{a}}_r\right)^{\overset{d}{\otimes}}, \tag{III.11}$$

where $\widehat{\boldsymbol{a}}_r \in \mathbb{R}^8$ for $r = 1, \ldots, R_d$ are scaled eigenvectors or otherwise orthogonal vectors when $R_d \leqslant \dim(\mathbb{R}^8) = 8$ (Sturmfels, 2016; Rabanser et al., 2017), but most often they are no eigenvectors, and cannot even be orthogonal when $R_d > \dim(\mathbb{R}^8) = 8$. While they may certainly still hold some physical meaning, this is irrelevant in the present work, where they are purely intended to reduce memory usage and floating point operations during tensor contractions.

Some practical remarks regarding the decomposition and rank of $\widehat{\boldsymbol{S}}_{\boldsymbol{D}}$ and $\widehat{\boldsymbol{Q}}_{\boldsymbol{D}}$ are in order before moving on to the perturbed analysis in Subsection III.4. Assuming a lower-than-true rank ultimately facilitates too little information or coefficients to capture the original tensor, resulting in a numerically inexact approximation. On the other hand, assuming a higher rank does not affect the numerical exactness, but actually improves the odds and speed by which a decomposition may be found, especially when the true rank is generic, being the highest possible rank an arbitrary tensor of given dimensionality and order may obtain. Then again, overestimating the rank directly increases the memory storage and number of floating point operations involved in all future contractions, diminishing the very purpose of this decomposition. As such, during CP decomposition of $\widehat{\boldsymbol{Q}}_{\boldsymbol{D}}$ the assumed rank was chosen equal to its true rank when sub-generic, and increased by one when generic, as minimal generic decompositions were practically impossible to find otherwise. Ultimately, the following decomposition forms are assumed and successfully implemented in the methodology, given the generic case:

$$\widehat{\boldsymbol{Q}}_{\boldsymbol{D}} = \sum_{r=1}^{21+1} \widehat{\boldsymbol{q}}_r^{\overset{4}{\otimes}}, \qquad \widehat{\boldsymbol{S}}_{\boldsymbol{D}} = \sum_{r=1}^{21+1} \widehat{\boldsymbol{s}}_r \otimes \widehat{\boldsymbol{q}}_r^{\overset{2}{\otimes}}, \tag{III.12}$$

where $\widehat{\boldsymbol{q}}_r \in \mathbb{R}^8$ and $\widehat{\boldsymbol{s}}_r \in \mathbb{R}^8$ denote the factors shared among the decompositions of $\widehat{\boldsymbol{Q}}_{\boldsymbol{D}}$ and $\widehat{\boldsymbol{S}}_{\boldsymbol{D}}$. This promotes efficiency by allowing future contractions to be factored out or recycled among both, as shown in Subsection III.4. Furthermore, the generic rank of a four-way *six*-dimensional symmetric tensor is 21, argued from Equation II.7. This is effectively the case for the four-way 8-dimensional $\widehat{\boldsymbol{Q}}_{\boldsymbol{D}}$, due to the energy's two-dimensional translational invariance, as exploited in its *Tucker Decomposition* visualized in Figure II.3, and elaborated in Appendix A.3 (Rabanser et al., 2017). In this work, Tucker decomposition preconditions the CP decomposition process, greatly reducing its cost but ultimately not affecting the decompositions used during structural analysis. While tensor decomposition software is freely available (Bader & Kolda, 2007), a custom approach is presented in Appendix A.3. Admittedly, many sufficient means or assumed forms of decomposition are available, and the reader is advised to experiment beyond the somewhat arbitrary decomposition choices made in this work.

III.4 Perturbed Structural Analysis

The most challenging yet pivotal component of the structural design cycle is non-linear structural analysis, explicitly obtaining the equilibrium relation between load and displacement, as implicitly defined by the previously elaborated model. From this relation, structural performance may ultimately be measured and optimized. Here, a novel means of perturbed analysis is proposed to efficiently and robustly predict this non-linear equilibrium relation, in four steps. Intuitively, while the internal and applied external forces naturally equal zero at the undeformed state, they are imposed to *change* equally, and their subsequent instantaneous changes of changes likewise. While in general a basic implementation of such an asymptotic approach cannot prevent ultimate divergence from the true relation, it can be postponed or attenuated through duly elaborated modifications. To improve the readability of this subsection, functional dependence on the design $\boldsymbol{x}$ is omitted, as the analysis method itself does not vary with it. The four steps are first briefly summarized and then elaborated.

The first step is higher-order structural analysis, avoiding the drawbacks of obtaining distant equilibrium data, through concentrated equilibrium data at the undeformed state. Here, a set of incrementally higher-order derivatives of the equilibrium equation is recursively solved, yielding the equilibrium curve's exact geometric derivatives of corresponding orders. The second step involves higher-order equilibrium prediction, where a continuous curve is parameterized such that it matches the obtained derivatives. In this work, a straightforward MacLaurin extrapolation is considered, explicit in terms of load variable λ to accommodate the mildly non-linear scope. More importantly, it facilitates a tight error estimator in the third step, facilitating an extent of control over the true error as done in the fourth and final step. In fact, a whole family of extrapolations is constructed in the second step, matching up to incrementally higher-order derivatives, each of which has its own error versus λ. The fourth step of *Bayesian Model Averaging* (Hoeting et al., 1999) is then simply to take a weighted average of these ex-

trapolations, such that the aggregate error estimation is minimized and incidentally less than that of any individual extrapolation for any λ. The remainder of this subsection elaborates on these four steps.

The first step of higher-order structural analysis is quite literally derived from the original zeroth-order equilibrium equation. Consider the N-degree-of-freedom structure and its MacLaurin-reformulated residual equation, whose roots, i.e. zeros, define equilibrium:

$$\boldsymbol{r}(\boldsymbol{u},\ \lambda) \equiv \lambda \boldsymbol{p} - \boldsymbol{K} \bullet \boldsymbol{u} - \tfrac{1}{2}\boldsymbol{S} \underset{2}{\bullet} \boldsymbol{v} - \tfrac{1}{6}\boldsymbol{Q} \underset{3}{\bullet} \boldsymbol{w} \ , \qquad \text{(III.13)}$$

$$\text{where} \quad \boldsymbol{v} \equiv \boldsymbol{u}^{\overset{2}{\otimes}} \ ,$$

$$\text{and} \quad \boldsymbol{w} \equiv \boldsymbol{u}^{\overset{3}{\otimes}} \ ,$$

where substitutions $\boldsymbol{v}$ and $\boldsymbol{w}$ will be convenient later on. Also note that the structural tensors $\boldsymbol{K}$, $\boldsymbol{S}$ and $\boldsymbol{Q}$ are constant with respect to $\boldsymbol{u}$, being higher-order energy derivatives at $\boldsymbol{u} = \boldsymbol{0}$.

Considering the load-controlled analysis versus λ, the aim is to obtain some $\boldsymbol{u} = \widetilde{\boldsymbol{u}}(\lambda)$ that asymptotically satisfies equilibrium. To clarify, strictly equating the residual $\boldsymbol{r}\big(\widetilde{\boldsymbol{u}}(\lambda),\ \lambda\big)$ to zero over a finite interval, implicitly equates all of its derivatives to zero at any point on that interval, simply because the derivatives of a zero-valued function must then also be zero. Conversely, equating up to a finite amount of its derivatives to zero at one particular point, only ensures that $\boldsymbol{r}\big(\widetilde{\boldsymbol{u}}(\lambda),\ \lambda\big)$ asymptotically stays zero near that point, through whatever smooth prediction $\widetilde{\boldsymbol{u}}(\lambda)$ this condition is met. Regardless, such high-order predictions may have multiple distinct advantages over a linear prediction, or an iterative prediction-correction approach such as Newton-Raphson, as readily discussed in Subsection II.3 and later demonstrated in Section V.

Concretely, $\boldsymbol{r}\big(\widetilde{\boldsymbol{u}}(\lambda),\ \lambda\big)$ and all of its higher-order derivatives are equated to $\boldsymbol{0}$ at the undeformed state, meaning $\lambda = 0$. Incidentally, this implies the higher-order derivatives of $\widetilde{\boldsymbol{u}}(\lambda)$ at $\lambda = 0$ due to the chain rule. Denoting some p^{th}-order derivative versus λ given $\lambda = 0$ with superscript (p), the higher-order residual equations are then defined for $p = 0,\ 1,\ \ldots,\ n$:

$$\boldsymbol{r}^{(p)} \equiv \lambda^{(p)}\boldsymbol{p} - \boldsymbol{K} \bullet \boldsymbol{u}^{(p)} - \tfrac{1}{2}\boldsymbol{S} \underset{2}{\bullet} \boldsymbol{v}^{(p)} - \tfrac{1}{6}\boldsymbol{Q} \underset{3}{\bullet} \boldsymbol{w}^{(p)} \equiv \boldsymbol{0} \ , \qquad \text{(III.14)}$$

where $\lambda^{(p)}$ equals 1 for $p = 1$, and zero otherwise. Less trivially, $\boldsymbol{v}^{(p)}$ and $\boldsymbol{w}^{(p)}$ can be obtained using *Leibniz's generalized product rule*[42]:

$$\boldsymbol{v}^{(p)} = \frac{\mathrm{d}^p}{\mathrm{d}a^p}\left(\boldsymbol{u} \otimes \boldsymbol{u}\right)\Big|_{a=0} = \sum_{q=0}^{p} \binom{p}{q} \boldsymbol{u}^{(q)} \otimes \boldsymbol{u}^{(p-q)} \ ,$$

$$\boldsymbol{w}^{(p)} = \frac{\mathrm{d}^p}{\mathrm{d}a^p}\left(\boldsymbol{v} \otimes \boldsymbol{u}\right)\Big|_{a=0} = \sum_{q=0}^{p} \binom{p}{q} \boldsymbol{v}^{(q)} \otimes \boldsymbol{u}^{(p-q)} \ . \qquad \text{(III.15)}$$

with $\boldsymbol{u}^{(0)} = \boldsymbol{0}$ denoting the undeformed state by definition. As a result, $\boldsymbol{v}^{(p)}$ and $\boldsymbol{w}^{(p)}$ respectively become nonzero for $p \geqslant 2$ and $p \geqslant 3$, but most importantly, exclusively depend on all $\boldsymbol{u}^{(q)}$ for $q \leqslant p-1$ and $q \leqslant p-2$. Hence, $\boldsymbol{u}^{(p)}$ can be isolated, yielding the desired derivatives in the recursive form:

$$\boldsymbol{K} \bullet \boldsymbol{u}^{(p)} = \lambda^{(p)}\boldsymbol{p} \ \underbrace{- \left(\tfrac{1}{2}\boldsymbol{S} \underset{2}{\bullet} \boldsymbol{v}^{(p)} + \tfrac{1}{6}\boldsymbol{Q} \underset{3}{\bullet} \boldsymbol{w}^{(p)}\right)}_{\boldsymbol{\mathcal{R}}^{(p)}\left(\boldsymbol{u}^{(1)},\ \boldsymbol{u}^{(2)},\ \ldots,\ \boldsymbol{u}^{(p-1)}\right)} \ , \qquad \text{(III.16)}$$

where $\boldsymbol{\mathcal{R}}^{(p)}$ denotes some multilinear form, just to indicate the linear dependence of $\boldsymbol{u}^{(p)}$ on all $\boldsymbol{u}^{(q)}$ for $q = 1,\ \ldots,\ p-1$. More explicitly:

$$\begin{aligned}
\boldsymbol{u}^{(0)} &= \boldsymbol{0} \ , \\
\boldsymbol{u}^{(1)} &= \boldsymbol{K}^{-1} \bullet \boldsymbol{p} \ , \quad \big\} \quad \text{Linear FEM} \\
\boldsymbol{u}^{(2)} &= \boldsymbol{K}^{-1} \bullet \left(-\boldsymbol{S} \underset{2}{\bullet} \boldsymbol{u}^{(1)^{\overset{2}{\otimes}}}\right) \ , \\
\boldsymbol{u}^{(3)} &= \boldsymbol{K}^{-1} \bullet \left(-3 \cdot \boldsymbol{S} \underset{2}{\bullet} \left(\boldsymbol{u}^{(1)} \otimes \boldsymbol{u}^{(2)}\right) - \boldsymbol{Q} \underset{3}{\bullet} \boldsymbol{u}^{(1)^{\overset{3}{\otimes}}}\right) \ , \\
&\ \ \vdots \\
\boldsymbol{u}^{(n)} &= \boldsymbol{K}^{-1} \bullet \left(-\tfrac{1}{2}\boldsymbol{S} \underset{2}{\bullet} \boldsymbol{v}^{(n)} - \tfrac{1}{6}\boldsymbol{Q} \underset{3}{\bullet} \boldsymbol{w}^{(n)}\right) \ . \qquad \text{(III.17)}
\end{aligned}$$

Notably, the entire sequence is solved through the same, symmetric stiffness matrix $\boldsymbol{K}$. This facilitates efficiency through Cholesky factorization, provided the invested factorization cost does not outweigh the reduced solution cost.

Before moving on to the second step, concerns regarding the large structural tensor contractions are addressed, by performing those contractions on the explicit assembly of decomposed elemental tensors. Specifically, consider the bracketed term of Equation III.16, which can be rewritten as an assembly of element contributions. Taking the p^{th}-order derivative of the force assembly equation (III.6) with $\boldsymbol{u} = \widetilde{\boldsymbol{u}}(\lambda)$, evaluated at $\lambda = 0$, and substituting it into Equation III.16 then yields:

[42] The resulting expression after repeatedly differentiating a binary product, hence repeatedly applying the product-rule, may be illustrated by Pascal's triangle, or alternatively be argued from a combinatorics' perspective.

$$\left(\tfrac{1}{2}\boldsymbol{S} \underset{2}{\bullet} \boldsymbol{v}^{(p)} + \tfrac{1}{6}\boldsymbol{Q} \underset{3}{\bullet} \boldsymbol{w}^{(p)}\right) = \sum_{e=1}^{M} \mathbb{A}_e^{\top} \bullet \left(\tfrac{1}{2}\boldsymbol{S}_e \underset{3}{\bullet} \boldsymbol{v}_e^{(p)} + \tfrac{1}{6}\boldsymbol{Q}_e \underset{3}{\bullet} \boldsymbol{w}_e^{(p)}\right) \tag{III.18}$$

where subscript e denotes the element e's equivalent with respect to any previously defined vectors or tensors in this subsection, now concerning 8 dimensions along each tensor's ways. Next, applying the decomposition proposed in Equation III.12, in addition to Leibniz's generalized product rule stated in Equation III.15, then yields:

$$\begin{aligned}\boldsymbol{S}_e \underset{2}{\bullet} \boldsymbol{v}_e^{(p)} &= \sum_{r=1}^{22} \boldsymbol{s}_{re} \underbrace{\left(\boldsymbol{q}_{re}^{\overset{2}{\otimes}} \underset{2}{\bullet} \boldsymbol{v}_e^{(p)}\right)}_{(\mathrm{qqv})_{re}^{(p)}} \\ &= \sum_{r=1}^{22} \boldsymbol{s}_{re} \sum_{q=1}^{p} \binom{p}{q} \underbrace{\left(\boldsymbol{q}_{re} \bullet \boldsymbol{u}_e^{(q)}\right)}_{(\mathrm{qu})_{re}^{(q)}} \underbrace{\left(\boldsymbol{q}_{re} \bullet \boldsymbol{u}_e^{(p-q)}\right)}_{(\mathrm{qu})_{re}^{(p-q)}}\end{aligned} \tag{III.19}$$

$$\begin{aligned}\boldsymbol{Q}_e \underset{3}{\bullet} \boldsymbol{w}_e^{(p)} &= \sum_{r=1}^{22} \boldsymbol{q}_{re} \left(\boldsymbol{q}_{re}^{\overset{3}{\otimes}} \underset{3}{\bullet} \boldsymbol{w}_e^{(p)}\right) \\ &= \sum_{r=1}^{22} \boldsymbol{q}_{re} \sum_{q=1}^{p} \binom{p}{q} \underbrace{\left(\boldsymbol{q}_{re}^{\overset{2}{\otimes}} \underset{2}{\bullet} \boldsymbol{v}_e^{(q)}\right)}_{(\mathrm{qqv})_{re}^{(q)}} \underbrace{\left(\boldsymbol{q}_{re} \bullet \boldsymbol{u}_e^{(p-q)}\right)}_{(\mathrm{qu})_{re}^{(p-q)}}\end{aligned} \tag{III.20}$$

where vectors $\boldsymbol{s}_{re} \in \mathbb{R}^8$ and $\boldsymbol{q}_{re} \in \mathbb{R}^8$ respectively denote (one of the) factors of the r^{th} term of the e^{th} element's decomposed structural tensors. But most importantly, note the repeated use of scalars $(\mathrm{qu})_{re}^{(p)}$ and $(\mathrm{qqv})_{re}^{(p)}$ for $r = 1, \ldots, 22$, then $e = 1, \ldots, M$ and finally $p = 1, \ldots, n$. The contractions they originate from dominate the overall calculation, but they can be stored in some 22 by M by n array, allowing them to be cheaply recycled many times over.

Given the efficiently obtained higher-order derivatives of the equilibrium curve, the second step involves constructing a smooth prediction or extrapolation $\widetilde{\boldsymbol{u}}(\lambda)$ that matches them. For several reasons, a MacLaurin extrapolation is considered. In fact, the whole family of p^{th} order expansions is considered for $p = 1, \ldots, n$, as their computational cost is negligible compared to the expensively obtained derivatives $\boldsymbol{u}^{(p)}$ for $p = 1, \ldots, n$:

$$\widetilde{\boldsymbol{u}}_p(\lambda) \equiv \sum_{q=1}^{p} \frac{\boldsymbol{u}^{(q)} \lambda^q}{q!} \,. \tag{III.21}$$

Its simplicity and transparency allow a more thorough understanding of the proposed method. This may create a stepping stone towards future extensions using a parametric formulation $(\boldsymbol{u}, \lambda) = \left(\widetilde{\boldsymbol{u}}(a), \widetilde{\lambda}(a)\right)$ or algebraic varieties rather than plain power series. Moreover, it facilitates the third step where its error is estimated, which may not have been so easy using alternative formulations. Formulating the approximate structural analysis through an explicit power series allows for some useful assumptions and simplifications on the convergence rate and conditions that affect it.

Moving on to the final two steps, fewer ramifications of error are suffered when its estimation is properly exploited. Hence, the error of the MacLaurin expansions is estimated with respect to the true equilibrium curve they intend to predict or approximate. Merely a scalar-valued indication of how accurate one expansion is compared to the others, given some λ, facilitates a superior aggregate of these predictions, explained duly.

As argued, the third step involves a scalar-valued family of error estimators corresponding to the family of MacLaurin expansions versus λ. The particular choice of defining true error may impact its estimatability. Hence, exploiting Taylor's theorem and some properties of geometric series as performed in Appendix B.2, the true, relative, normed displacement error is considered for $p = 1, \ldots, n$, as:

$$\epsilon_p(\lambda) \equiv \frac{\left|\widetilde{\boldsymbol{u}}_p(\lambda) - \boldsymbol{u}(\lambda)\right|}{\left|\boldsymbol{u}(\lambda)\right|} \,, \tag{III.22}$$

whose corresponding estimators have been derived in Appendix B.2 for $p = 1, \ldots, n$, as:

$$\widetilde{\epsilon}_p(\lambda) \equiv \left(\frac{\lambda}{\overline{\lambda}_n}\right)^p \,, \quad \text{with} \quad \overline{\lambda}_n \equiv \left(n! \frac{|\boldsymbol{u}^{(1)}|}{|\boldsymbol{u}^{(n)}|}\right)^{\frac{1}{n-1}} \,, \tag{III.23}$$

which is incidentally similar to the error estimator used by Cochelin (1994), Cochelin, Damil, & Potier-Ferry (1994), and other related works adopting a polynomial asymptotic numerical method of structural analysis. Here, $\overline{\lambda}_n$ may be interpreted as an estimator for the *radius of convergence* $\overline{\lambda}$. Further properties of this estimator will be discussed and exploited in the fourth and final step, yielding a superior aggregate prediction.

As a side note, while the facilitated control of a displacement-based error estimator may be tight over the true displacement error, it may be loose on the residual force. Depending on the desired structural performance, this might be problematic. To clarify, when the displacement error of fixed magnitude aligns with stiffer tangent eigendeformations, greater residual forces may be observed. However, residual evaluations and especially their design sensitivities are much more expensive, hence future work on its estimation is advised when cheap but tight control over them is desired.

While not one MacLaurin prediction of the nonlinear equilibrium relation is superior everywhere, all of them do provide *some* value everywhere, and may even be superior at least somewhere. To clarify, inspecting the estimator (III.23) suggests an exponentially decreasing and increasing error versus p, respectively, for $\lambda < \overline{\lambda}$ and $\lambda > \overline{\lambda}$. Hence, higher-order predictions are respectively superior and inferior to lower-order predictions. Even worse, the perturbed analysis suffers an exponentially increasing prediction error versus p for some fixed $\lambda > \overline{\lambda}$, and p^{th}-order increasing error versus λ everywhere. When trusting only the highest order prediction, this divergence may severely destabilize the topology optimization when the design dependent $\overline{\lambda}$ even slightly drops below some λ considered within the structural performance evaluation.

As the fourth and final step, all predictions are aggregated into a superior prediction through weighted averaging. This Bayesian average (Hoeting et al., 1999) extracts the most value out of all predictions everywhere, and hence additional value out of the expensively obtained derivatives in the first step. In somewhat of a nuanced or smooth selection process, the relative influence of all individual predictions on the aggregate increases respectively with their estimated local accuracy, as derived in Appendix C. Admittedly based on coarse observations and ignorance to some extent, it was assumed that the respective vector-valued displacement errors are uncorrelated and unbiased. In such a case, errors have the tendency to partially cancel out when averaged, especially when these errors are equal in magnitude. Otherwise, the largest error will simply dominate, wasting the accuracy of the other predictions. As shown in Appendix C, weighting all predictions corresponding to their inverse squared normed local errors, expectedly equalizes their relative error contribution, optimizing cancelation and minimizing the aggregate's error everywhere. In other words, this aggregate prediction generally ensures either maximal convergence or minimal divergence, versus both λ and n everywhere.

Concretely, the Bayesian-enhanced equilibrium predictor $\widetilde{\widetilde{\boldsymbol{u}}}_n(\lambda)$ is defined as:

$$\widetilde{\widetilde{\boldsymbol{u}}}_n(\lambda) \equiv \sum_{p=1}^{n} \omega_p(\lambda) \widetilde{\boldsymbol{u}}_p(\lambda) \equiv \frac{\sum_{p=1}^{n} \left(\frac{1}{\widetilde{\epsilon}_p(\lambda)} \right)^2 \widetilde{\boldsymbol{u}}_p(\lambda)}{\sum_{p=1}^{n} \left(\frac{1}{\widetilde{\epsilon}_p(\lambda)} \right)^2} , \tag{III.24}$$

with the MacLaurin predictor $\widetilde{\boldsymbol{u}}_p(\lambda)$ defined as in Equation III.21 and its error estimator $\widetilde{\epsilon}_p(\lambda)$ as in Equation III.23. Furthermore, weights $\omega_p(\lambda)$ for $p = 1, \ldots, n$ have been derived such that their sum evaluates to 1, and the Bayesian-enhanced predictor's error estimator $\widetilde{\widetilde{\epsilon}}_n(\lambda)$, also referred to as Bayesian error, is minimized for all $\lambda \in \mathbb{R}$:

$$\widetilde{\widetilde{\epsilon}}_n(\lambda) \equiv \sqrt{\frac{1}{\sum_{p=1}^{n} \left(\frac{1}{\widetilde{\epsilon}_p(\lambda)} \right)^2}} , \tag{III.25}$$

which may notably be recognized as the smooth minimum of $\widetilde{\epsilon}_p(\lambda)$ for all $p = 1, \ldots, n$.

Regarding numerical implementation, a stable and efficient reformulation of this rational Bayesian-enhanced predictor $\widetilde{\widetilde{\boldsymbol{u}}}_n(\lambda)$ and its error estimator $\widetilde{\widetilde{\epsilon}}_n(\lambda)$ could be made as follows:

$$\widetilde{\widetilde{\boldsymbol{u}}}_n(\lambda) = \underbrace{[\widetilde{\boldsymbol{u}}_1(\lambda), \ldots, \widetilde{\boldsymbol{u}}_n(\lambda)]}_{\widetilde{\boldsymbol{U}}_n(\lambda)} \underbrace{\begin{bmatrix} \omega_1(\lambda) \\ \vdots \\ \omega_n(\lambda) \end{bmatrix}}_{\boldsymbol{\omega}_n(\lambda)} , \tag{III.26}$$

where the substitution $\beta \equiv \lambda / \overline{\lambda}$ results in the following compact reformulation for the MacLaurin predictors $\widetilde{\boldsymbol{U}}_n(\lambda) \in \mathbb{R}^{N \times n}$, weights $\boldsymbol{\omega}_n(\lambda) \in \mathbb{R}^n$, and Bayesian error $\widetilde{\widetilde{\epsilon}}_n(\lambda) \geqslant 0$ for all $\lambda \in \mathbb{R}$:

$$\widetilde{\boldsymbol{U}}_n(\lambda) \equiv \left[\overline{\lambda} \boldsymbol{u}^{(1)}, \frac{\overline{\lambda}^2}{2!} \boldsymbol{u}^{(2)}, \ldots, \frac{\overline{\lambda}^n}{n!} \boldsymbol{u}^{(n)} \right] \begin{bmatrix} \beta & \beta & \cdots & \beta \\ & \beta^2 & \cdots & \beta^2 \\ & & \ddots & \vdots \\ & & & \beta^n \end{bmatrix} ,$$

$$\begin{bmatrix} \widetilde{\widetilde{\epsilon}}_n(\lambda)^2 \\ \hdashline \boldsymbol{\omega}_n(\lambda) \end{bmatrix} = \begin{bmatrix} \beta^{2n} \\ \hdashline \beta^{2n-2} \\ \beta^{2n-4} \\ \vdots \\ 1 \end{bmatrix} \frac{1 - \beta^2}{1 - \beta^{2n}} , \qquad \text{with} \quad \beta \equiv \frac{\lambda}{\overline{\lambda}} . \tag{III.27}$$

In some sense, one could define the Bayesian error estimator $\widetilde{\widetilde{\epsilon}}_n(\lambda)^2 \equiv w_0(\lambda)$, or the MacLaurin error estimator $\widetilde{\epsilon}_p(\lambda)^2 \equiv \beta^{-2p}$. The combined expression for $\boldsymbol{\omega}_n(\lambda)$ and $\widetilde{\widetilde{\epsilon}}_n(\lambda)$ is obtained using the identity $(1-a)\sum_{p=1}^{n} a^p = \left(1 - a^{p+1}\right)$ for geometric series, for any $a \in \mathbb{C}$. Additionally, β is factored in and out, in such a way that the resulting expression has no artificial zero-pole cancelation at $\lambda = 0 \Leftrightarrow \beta = 0$. Otherwise, the expression cannot be evaluated at this point, or suffers inflated floating point errors close to this point. All remaining poles are the complex n^{th}-order roots of unity, meaning the prediction suffers no spurious poles for *real* $\lambda \in \mathbb{R}$. An elaborate derivation can be found in Appendix C.

In conclusion, the Bayesian-enhanced equilibrium predictor $\widetilde{\widetilde{\boldsymbol{u}}}_n(\lambda)$ is a rational but stable vector function of type $(2n-1)$ over $(2n-2)$, parameterized purely by

the set of exact higher-order derivatives $\boldsymbol{u}^{(1)}, \ldots, \boldsymbol{u}^{(n)}$ obtained in the first step. Due to the shared denominator among all components of $\tilde{\tilde{\boldsymbol{u}}}_n(\lambda)$ and its limit behavior as $\lambda \to 0$, it classifies as a vectorial Padé (El Kihal et al., 2022), albeit without its typical downside of spurious poles (Cochelin, 1994; Cochelin, Damil, & Potier-Ferry, 1994; De Boer & Van Keulen, 1997). More importantly, for $|\lambda|$ larger than the radius of convergence $\overline{\lambda}$, $\tilde{\tilde{\boldsymbol{u}}}_n(\lambda)$ *does not* diverge beyond $\tilde{\boldsymbol{u}}_1(\lambda)$. As a result, a higher-order n for $\tilde{\tilde{\boldsymbol{u}}}_n(\lambda)$ maximally improves its accuracy within the radius of convergence $\overline{\lambda}$, without worsening the divergence elsewhere. Especially at $\lambda = \overline{\lambda}$, where $\tilde{\epsilon}_p(\lambda)$ is equal for all $p = 1, \ldots, n$, optimal cancelation yields an aggregate error reduced by a factor $\sqrt{n}$. Overall, while divergence versus λ cannot be prevented, its rate is bounded below that of the linear predictor. What is more, divergence versus n is successfully eliminated. Given a fixed set of derivatives, compared to a plain MacLaurin predictor, the proposed Bayesian-enhanced predictor should improve the odds of the topology optimization to recover from inaccurate responses and sensitivities, and perhaps decrease the odds of derailing in the first place.

III.5 Topology Optimization Formulation

At last, the structural design optimization cycle is closed by a means to evaluate the performance and performance sensitivity with respect to the structure's current design, including some essential regularization modifications. Technically, this evaluation can be based directly on the density-based design, its model, and analysis. However, convergence of the analysis or overall design may be either poor, or prone toward unphysical or unmanufacturable results. All of these issues may be unwanted artifacts of the chosen models, formulations, and method-specific parameters, and sometimes sensitively or unpredictably so. Regularization aims to remedy this, yielding physical, repeatable and representative results, which is not only practically but academically desirable. Given the proposed methodology, integrating a novel means of structural analysis into an established density-based topology optimization routine, a minimal set of regularization steps is justified, and the resulting optimization problem is concretely formulated in negative null form.

Regarding traditional density-based topology optimization, the established regularization techniques of density filtering, and material scaling and penalization are adopted, as summarized within Figure III.5. Ultimately they aim to remedy a chain of issues caused by allowing a continuous range of densities between solid and void, representing the presence or absence of material. While this so-called *design relaxation* (Sigmund & Petersson, 1998) is certainly a powerful approach to facilitate gradient-based optimization, it results in an ill-posed formulation. Even worse, while design optimality may generally involve intermediate densities, their physical interpretation, no less modeling or manufacturing, poses ongoing challenges of its own (Bendsøe & Kikuchi, 1988; de Buhan et al., 2017).

An effective, practical solution to avoid intermediate densities is *Solid-Isotropic Material Penalization* (SIMP, Bendsøe (1989); Zhou & Rozvany (1991); Sigmund (2001)), penalizing these intermediate densities yielding manufacture black-and-white designs. In addition, a minimum density prevents the structural equations from becoming singular, i.e. prevents zero stiffness, infinite compliance, and a diverging analysis hence optimization. Furthermore, it prevents sensitivities corresponding to void elements from vanishing, meaning the direction in which this density may be increased again remains defined. Yet, the optimizer is able to circumvent material penalization through black-and-white checkerboard patterns (Sigmund & Petersson, 1998). While this remarkable, unintended exploitation of homogenization effectively results in intermediate densities on a larger scale, the overall physical model and its manufacturing remain problematic. Considering geometric non-linearity, single-noded hinges may also be severely exploited for their unphysically infinite rotational compliance (Buhl et al., 2000a). To remedy both checkerboarding and these hinges, local weighted averaging of neighboring element densities, called density filtering (Sigmund, 2001; Andreassen et al., 2011), is employed.

Regarding the proposed perturbation analysis, and to the benefit of Newton-Raphson analysis, a simple density-based deformation scaling is formulated and implemented here. It diminishes the extent of non-linearity and resulting issues of the structural model, especially addressing numerical issues caused by low-density elements, while minimally affecting the physically relevant portion of the model. Similar to F. Wang et al.'s (2014) approach, each element's structural model is exponentially more linearized the closer it gets to void or zero density, while solid elements remain practically unaffected.

The remainder of this subsection shall mostly elaborate on the mathematical details of all mentioned regularization steps, in preparation for the assembled structural optimization formulation. Starting from a representative element's energy model in decomposed tensorial form, here referred to as the *natural* form, the mapped and regularized contributions are ultimately assembled into the gradient-based optimization formulation. An overview of the adopted regularization steps is visualized in Figure III.5, and the duly elaborated mathematical relations of each regularized element's energy model with respect to their common natural form are summarized in Equation III.28, III.29 and III.30.

Recall the representative element's energy model

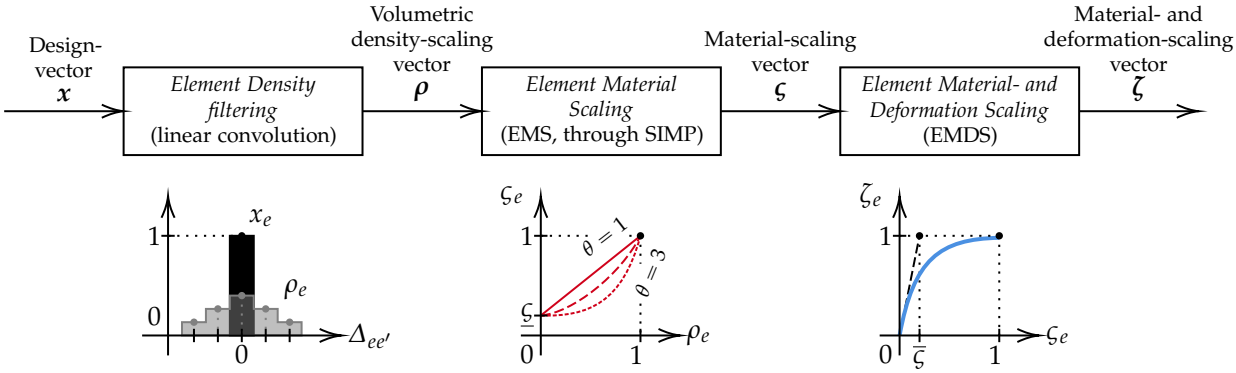

Figure III.5: Regularization function-chain, filtering the design vector $\boldsymbol{x}$ into the density vector $\boldsymbol{\rho}$, and mapping it to the material scaling vector $\boldsymbol{\varsigma}$ and EMDS vector $\boldsymbol{\zeta}$, as defined in III.30 and III.31. Recall that SIMP refers so *Solid-Isotropic Material Penalization* (Bendsøe, 1989; Zhou & Rozvany, 1991; Sigmund, 2001).

in decomposed, tensorial form, introduced in Subsection III.3. Ultimately, all regularized elements and their decompositions may be related through linear coordinate transformations, given the same material model $\boldsymbol{D}$ but not necessarily the same initial geometry. Let the representative *natural* form $\widehat{\mathcal{E}}_{\boldsymbol{D}}(\widehat{\boldsymbol{u}})$ in terms of natural coordinates and displacements $\widehat{\boldsymbol{u}} \in \mathbb{R}^8$ be denoted as:

$$\widehat{\mathcal{E}}_{\boldsymbol{D}}(\widehat{\boldsymbol{u}}) \equiv \frac{1}{2}\widehat{\boldsymbol{K}} \underset{2}{\bullet} \widehat{\boldsymbol{u}}^{\overset{2}{\otimes}} + \frac{1}{6}\widehat{\boldsymbol{S}} \underset{3}{\bullet} \widehat{\boldsymbol{u}}^{\overset{3}{\otimes}} + \frac{1}{24}\widehat{\boldsymbol{Q}} \underset{4}{\bullet} \widehat{\boldsymbol{u}}^{\overset{4}{\otimes}} , \quad \text{(III.28)}$$

$$\text{recalling that} \quad \widehat{\boldsymbol{S}}_{\boldsymbol{D}} = \sum_{r=1}^{22} \widehat{\boldsymbol{s}}_r \otimes \widehat{\boldsymbol{q}}_r^{\overset{2}{\otimes}} ,$$

$$\widehat{\boldsymbol{Q}}_{\boldsymbol{D}} = \sum_{r=1}^{22} \widehat{\boldsymbol{q}}_r^{\overset{4}{\otimes}} .$$

Exploiting the shared coordinate map from natural to each element's local coordinates due to the regular voxel grid, the geometrically mapped *null* form $\mathcal{E}_0(\boldsymbol{u}_e)$ in terms of local coordinates and displacements $\boldsymbol{u}_e \in \mathbb{R}^8$ is obtained as:

$$\mathcal{E}_0(\boldsymbol{u}_e) \equiv \det(\boldsymbol{J}) \cdot \widehat{\mathcal{E}}_{\boldsymbol{D}}(\boldsymbol{J}^{-1} \bullet \boldsymbol{u}_e) , \quad \text{(III.29)}$$

$$\text{with coordinate mapping :} \quad \boldsymbol{J} \equiv \frac{\partial \boldsymbol{u}_e}{\partial \widehat{\boldsymbol{u}}} = \frac{L_e}{2}\boldsymbol{I} ,$$

where Jacobian $\boldsymbol{J} \in \mathbb{R}^{8\times 8}$ is shared by all square elements of equal length L_e. This relation is a result of the domain-integration and -differentiation that defines the natural form, as shown in Appendix A.1. Ultimately, each element's *regularized* form $\mathcal{E}_e(\boldsymbol{u}_e;\ \boldsymbol{x})$ in terms of the same local coordinates and displacements $\boldsymbol{u}_e \in \mathbb{R}^8$, is linearly related to the same null form, as summarized in Equation III.30 and visualized earlier in Figure III.5:

$$\mathcal{E}_e(\boldsymbol{u}_e;\ \boldsymbol{x}) \equiv \frac{\varsigma_e}{\zeta_e^2} \cdot \mathcal{E}_0(\zeta_e \cdot \boldsymbol{u}_e) , \quad \text{(III.30)}$$

$$\text{with density filtering :} \quad \rho_e \equiv \frac{\partial \rho_e}{\partial \boldsymbol{x}} \bullet \boldsymbol{x} ,$$

$$\text{EMS / SIMP :} \quad \varsigma_e \equiv \underline{\varsigma} + (1 - \underline{\varsigma}) \cdot \rho_e^{\theta} ,$$

$$\text{EMDS :} \quad \zeta_e \equiv 1 - \exp\left(-\frac{\varsigma_e}{\overline{\varsigma}}\right) ,$$

Briefly, element e's volumetric density scalar ρ_e, material scalar ς_e, and mixed deformation, or EMDS scalar ζ_e are respectively obtained after density filtering, material penalization, and the custom *Element Material and Deformation* (EMDS) scaling. Furthermore, $\underline{\varsigma}$ may be recognized as each element's *void density*, or more appropriately named, minimum stiffness scalar or *void stiffness*. Then, θ denotes the material penalization exponent, typically between 1 and 3, causing an artificial reduction of specific stiffness ς_e/ρ_e. Finally, $\overline{\zeta}$ is defined as the *EMDS threshold*, below which values of ζ_e noticeably start to linearize the element's internal force model, being the displacement-gradient of its energy model.

In more detail, the density filtering prevents checkerboarding, single-noded hinges or otherwise unwanted or unphysical element-scale features through local weighted density averaging. This effective linear map from design vector $\boldsymbol{x} \in \mathbb{R}^M$ to density vector $\boldsymbol{\rho} \in \mathbb{R}^M$ is implemented as the convolution filter proposed by Sigmund (2001):

$$\rho_e = \frac{\sum_{\Delta_{ee'} \leqslant \overline{\Delta}} \left(\overline{\Delta} - \Delta_{ee'}\right) x_e}{\sum_{\Delta_{ee'} \leqslant \overline{\Delta}} \overline{\Delta} - \Delta_{ee'}} \quad \Longleftrightarrow \quad \boldsymbol{\rho} = \boldsymbol{H}\boldsymbol{x} , \quad \text{(III.31)}$$

with filter radius $\overline{\Delta}$ in m, euclidean distance $\Delta_{ee'}$ between elements e and e' in m, and $\boldsymbol{H} \equiv \frac{\partial \boldsymbol{\rho}}{\partial \boldsymbol{x}}$ compactly denoting the linear map from design-vector $\boldsymbol{x}$ to volu-

metric density-vector $\boldsymbol{\rho}$.

In order to obtain the fully assembled, regularized, decomposed tensorial form of the structure's energy model, consider the following geometrically mapped, but not yet regularized elemental, tensorial null form:

$$\mathcal{E}_0(\boldsymbol{u}_e) = \frac{1}{2}\boldsymbol{K}_0 \underset{2}{\bullet} \boldsymbol{u}_e^{\overset{2}{\otimes}} + \frac{1}{6}\boldsymbol{S}_0 \underset{3}{\bullet} \boldsymbol{u}_e^{\overset{3}{\otimes}} + \frac{1}{24}\boldsymbol{Q}_0 \underset{4}{\bullet} \boldsymbol{u}_e^{\overset{4}{\otimes}} \,, \tag{III.32}$$

where the elemental null tensors $\boldsymbol{K}_0$, $\boldsymbol{S}_0$ and $\boldsymbol{S}_0$ can be expressed in terms of their natural counterparts $\widehat{\boldsymbol{K}}$, $\widehat{\boldsymbol{S}}$ and $\widehat{\boldsymbol{S}}$:

$$\begin{aligned}
&\boldsymbol{K}_0 \equiv \det\big(\boldsymbol{J}\big) \cdot \boldsymbol{J}^{-\top} \bullet \widehat{\boldsymbol{K}}_{\boldsymbol{D}} \bullet \boldsymbol{J}^{-1} \,, \\
&\boldsymbol{S}_0 = \sum_{r=1}^{22} \boldsymbol{s}_{r0} \otimes \boldsymbol{q}_{r0}^{\overset{2}{\otimes}} \,, \qquad \boldsymbol{s}_{r0} \equiv \det\big(\boldsymbol{J}\big)^{\frac{1}{2}} \cdot \boldsymbol{J}^{-1} \bullet \widehat{\boldsymbol{s}}_r \,, \\
&\boldsymbol{Q}_0 = \sum_{r=1}^{22} \boldsymbol{q}_{r0}^{\overset{4}{\otimes}} \,, \qquad \boldsymbol{q}_{r0} \equiv \det\big(\boldsymbol{J}\big)^{\frac{1}{4}} \cdot \boldsymbol{J}^{-1} \bullet \widehat{\boldsymbol{q}}_r \,.
\end{aligned} \tag{III.33}$$

To verify, one can write out this decomposed null form obtaining its relation to the natural form in Equation III.28. It must be noted that Jacobian $\boldsymbol{J}$ technically depends on the material coordinates, over which must be integrated to obtain the currently discussed discretized element energy. However, when the dependence of $\boldsymbol{J}$ and $\det(\boldsymbol{J})$ over the material coordinates is constant, they can factored out of the element domain integral. Within the field of finite elements, regular coordinate maps are defined precisely to result in a constant Jacobian, meaning any combination of translation, rotation, constant shear, and axial scaling. Moreover, the adopted density-based structural framework involves a grid of perfectly square elements, resulting in an identical, constant Jacobian for all elements with respect to their natural form.

The local *regularized* form, as ultimately used when modeling, analyzing and evaluating the structure, is defined as:

$$\mathcal{E}_e(\boldsymbol{u}_e;\, \boldsymbol{x}) = \frac{1}{2}\boldsymbol{K}_e \underset{2}{\bullet} \boldsymbol{u}_e^{\overset{2}{\otimes}} + \frac{1}{6}\boldsymbol{S}_e \underset{3}{\bullet} \boldsymbol{u}_e^{\overset{3}{\otimes}} + \frac{1}{24}\boldsymbol{Q}_e \underset{4}{\bullet} \boldsymbol{u}_e^{\overset{4}{\otimes}} \,, \tag{III.34}$$

where the regularized elemental tensors $\boldsymbol{K}_e$, $\boldsymbol{S}_e$ and $\boldsymbol{S}_e$ can be expressed in terms of the null tensors $\boldsymbol{K}_0$, $\boldsymbol{S}_0$ and $\boldsymbol{S}_0$:

$$\boldsymbol{K}_e = \varsigma_e \boldsymbol{K}_0, \quad \boldsymbol{S}_e = \frac{\varsigma_e}{\zeta_e}\boldsymbol{S}_0, \quad \boldsymbol{Q}_e = \frac{\varsigma_e}{\zeta_e^2}\boldsymbol{Q}_0 \,, \tag{III.35}$$

which are notably dependent on $\boldsymbol{x}$ through the regularization scalars ρ_e, ς_e and ζ_e. While this relation from the null form to each element's regularized form can be used to explicitly obtain all corresponding tensor decompositions, this would be inefficient and unnecessary.

The structural topology optimization is cast into negative null form, ultimately feeding all responses and their design sensitivities into the gradient-based optimization method of *Moving Asymptotes* (MMA, Svanberg (1987)). Here, M variables within the design vector $\boldsymbol{x}$ are sought in $[0,\ 1]$, such that some user-specified performance metric is minimized and (in)equality constraints are satisfied, all of which depend either directly on $\boldsymbol{x}$ or indirectly through structural equations. More concretely, the optimization problem is formulated in negative null form as:

$$\underset{\boldsymbol{x}}{\text{minimize}} \quad g(\boldsymbol{x},\, \boldsymbol{u}_{\boldsymbol{x}}) \,, \tag{III.36a}$$

$$\begin{aligned}
\text{subject to} \quad & \overset{\leqslant}{\boldsymbol{g}}(\boldsymbol{x},\, \boldsymbol{u}_{\boldsymbol{x}}) \leqslant \boldsymbol{0} \,, \\
& \overset{=}{\boldsymbol{g}}(\boldsymbol{x},\, \boldsymbol{u}_{\boldsymbol{x}}) = \boldsymbol{0} \,, \\
& \boldsymbol{R}_{\boldsymbol{x}} = \boldsymbol{0} \,,
\end{aligned} \tag{III.36b}$$

$$\text{and} \quad \boldsymbol{x} \in [0,\ 1]^M \,,$$

$$\begin{aligned}
\text{where} \quad & \boldsymbol{u}_{\boldsymbol{x}} = \widetilde{\widetilde{\boldsymbol{u}}}\big(\lambda;\, \boldsymbol{U}_{\boldsymbol{x}}\big) \in \mathbb{R}^N \,, \\
& \boldsymbol{U}_{\boldsymbol{x}} \equiv \Big[\boldsymbol{u}_{\boldsymbol{x}}^{(1)},\, \ldots,\, \boldsymbol{u}_{\boldsymbol{x}}^{(n)}\Big] \in \mathbb{R}^{N\times n} \\
& \boldsymbol{R}_{\boldsymbol{x}} \equiv \Big[\boldsymbol{r}_{\boldsymbol{x}}^{(1)},\, \ldots,\, \boldsymbol{r}_{\boldsymbol{x}}^{(n)}\Big] \in \mathbb{R}^{N\times n} \,, \\
& \boldsymbol{M}_{\boldsymbol{x}} \equiv \Big[\boldsymbol{\mu}_{\boldsymbol{x}}^{(1)},\, \ldots,\, \boldsymbol{\mu}_{\boldsymbol{x}}^{(n)}\Big] \in \mathbb{R}^{N\times n} \,,
\end{aligned} \tag{III.36c}$$

where subscript $\boldsymbol{x}$ denotes the quantity's (in)direct dependence on $\boldsymbol{x}$, and the newly introduced *adjoint* solutions in $\boldsymbol{M}_{\boldsymbol{x}}$ are clarified next. Note that the condition $\boldsymbol{R}_{\boldsymbol{x}} = \boldsymbol{0}$ is readily satisfied within the higher-order structural equilibrium analysis at the undeformed state:

$$\boldsymbol{r}_{\boldsymbol{x}}^{(p)} \equiv \lambda^{(p)}\boldsymbol{p} - \boldsymbol{K}_{\boldsymbol{x}} \bullet \boldsymbol{u}_{\boldsymbol{x}}^{(p)} - \tfrac{1}{2}\boldsymbol{S}_{\boldsymbol{x}} \underset{2}{\bullet} \boldsymbol{v}_{\boldsymbol{x}}^{(p)} - \tfrac{1}{6}\boldsymbol{Q}_{\boldsymbol{x}} \underset{3}{\bullet} \boldsymbol{w}_{\boldsymbol{x}}^{(p)} \equiv \boldsymbol{0} \tag{III.37}$$

However, the explicit inclusion of a set of satisfied constraints, and a corresponding set of higher-order adjoint solutions $\boldsymbol{M}_{\boldsymbol{x}}$ may ultimately be exploited to cancel out an otherwise expensive sensitivity calculation as elaborated next.

The so-called *Adjoint* Formulation (Bendsøe & Kikuchi, 1988) casts some original response $g(\boldsymbol{x},\, \boldsymbol{u}_{\boldsymbol{x}})$ into its *Lagrange* form $\mathcal{L}_{\boldsymbol{x}}$, with multipliers in $\boldsymbol{M}_{\boldsymbol{x}}$ and inherently satisfied constraints in $\boldsymbol{R}_{\boldsymbol{x}}$:

$$\mathcal{L}_{\boldsymbol{x}} \equiv g(\boldsymbol{x},\, \boldsymbol{u}_{\boldsymbol{x}}) + \underbrace{\sum_{p=1}^{n} \boldsymbol{\mu}_{\boldsymbol{x}}^{(p)} \bullet \boldsymbol{r}_{\boldsymbol{x}}^{(p)}}_{\boldsymbol{M}_{\boldsymbol{x}} \underset{2}{\bullet} \boldsymbol{R}_{\boldsymbol{x}} = 0} \,, \quad \begin{cases} g(\boldsymbol{x},\, \boldsymbol{u}_{\boldsymbol{x}}) = \mathcal{L}_{\boldsymbol{x}} \,, \\ \dfrac{\mathrm{d}g(\boldsymbol{x},\, \boldsymbol{u}_{\boldsymbol{x}})}{\mathrm{d}\boldsymbol{x}} = \dfrac{\mathrm{d}\mathcal{L}_{\boldsymbol{x}}}{\mathrm{d}\boldsymbol{x}} \end{cases} \tag{III.38}$$

This effectively adds zero to the original response, regardless of how $\boldsymbol{M}_{\boldsymbol{x}}$ is chosen in $\mathbb{R}^{N\times M}$, which shall

precisely be exploited in calculating its sensitivity:

$$\frac{\mathrm{d}\mathcal{L}_{\boldsymbol{x}}}{\mathrm{d}\boldsymbol{x}} = \frac{\partial g(\boldsymbol{x},\, \boldsymbol{u}_{\boldsymbol{x}})}{\partial \boldsymbol{x}} + \frac{\partial g(\boldsymbol{x},\, \boldsymbol{u}_{\boldsymbol{x}})}{\partial \boldsymbol{u}_{\boldsymbol{x}}} \bullet \frac{\partial \widetilde{\widetilde{\boldsymbol{u}}}(\lambda;\, \boldsymbol{U}_{\boldsymbol{x}})}{\partial \boldsymbol{U}_{\boldsymbol{x}}} \underset{2}{\bullet} \frac{\mathrm{d}\boldsymbol{U}_{\boldsymbol{x}}}{\mathrm{d}\boldsymbol{x}}$$
$$+ \boldsymbol{M}_{\boldsymbol{x}} \underset{2}{\bullet} \frac{\partial \boldsymbol{R}_{\boldsymbol{x}}}{\partial \boldsymbol{x}} + \boldsymbol{M}_{\boldsymbol{x}} \underset{2}{\bullet} \frac{\partial \boldsymbol{R}_{\boldsymbol{x}}}{\partial \boldsymbol{U}_{\boldsymbol{x}}} \underset{2}{\bullet} \frac{\mathrm{d}\boldsymbol{U}_{\boldsymbol{x}}}{\mathrm{d}\boldsymbol{x}}\,, \tag{III.39}$$

where the second line technically equates to zero, containing all sensitivity contributions of the adjoint term $\boldsymbol{M}_{\boldsymbol{x}} \underset{2}{\bullet} \boldsymbol{R}_{\boldsymbol{x}} = 0$. The utility of the adjoint term now becomes apparent by choosing or defining the adjoint solutions in $\boldsymbol{M}_{\boldsymbol{x}}$ such that the second term of both lines annihilate. This bypasses the need to calculate and contract with the very expensive design-sensitivity of displacement derivatives in $\boldsymbol{U}_{\boldsymbol{x}}$:

$$\left(\forall \frac{\mathrm{d}\boldsymbol{U}_{\boldsymbol{x}}}{\mathrm{d}\boldsymbol{x}} \in \mathbb{R}^{N\times n\times M}\right) \tag{III.40}$$
$$\left(\frac{\partial g(\boldsymbol{x},\, \boldsymbol{u}_{\boldsymbol{x}})}{\partial \boldsymbol{u}_{\boldsymbol{x}}} \bullet \frac{\partial \widetilde{\widetilde{\boldsymbol{u}}}(\lambda;\, \boldsymbol{U}_{\boldsymbol{x}})}{\partial \boldsymbol{U}_{\boldsymbol{x}}} + \boldsymbol{M}_{\boldsymbol{x}} \underset{2}{\bullet} \frac{\partial \boldsymbol{R}_{\boldsymbol{x}}}{\partial \boldsymbol{U}_{\boldsymbol{x}}}\right) \underset{2}{\bullet} \frac{\mathrm{d}\boldsymbol{U}_{\boldsymbol{x}}}{\mathrm{d}\boldsymbol{x}} = \boldsymbol{0}\,,$$

which means that for $p = n, n-1, \ldots, 1$:

$$\underbrace{\frac{\partial g(\boldsymbol{x},\, \boldsymbol{u}_{\boldsymbol{x}})}{\partial \boldsymbol{u}_{\boldsymbol{x}}} \bullet \frac{\partial \widetilde{\widetilde{\boldsymbol{u}}}(\lambda;\, \boldsymbol{U}_{\boldsymbol{x}})}{\partial \boldsymbol{u}_{\boldsymbol{x}}^{(p)}}}_{\boldsymbol{\Gamma}_{\boldsymbol{x}}^{(p)\top}} + \sum_{q=1}^{n} \boldsymbol{\mu}_{\boldsymbol{x}}^{(q)} \bullet \underbrace{\frac{\partial \boldsymbol{r}_{\boldsymbol{x}}^{(q)}}{\partial \boldsymbol{u}_{\boldsymbol{x}}^{(p)}}}_{-\boldsymbol{K}_{\boldsymbol{x}}^{(q,p)}} = \boldsymbol{0}\,, \tag{III.41}$$

where $\boldsymbol{\Gamma}_{\boldsymbol{x}}^{(p)}$ defines the adjoint force, and $\boldsymbol{K}_{\boldsymbol{x}}^{(q,p)}$ the adjoint stiffness. The resulting recursive adjoint equation yielding the adjoint solution $\boldsymbol{\mu}^{(p)}$ is remarkably similar to the recursive higher-order structural equation yielding displacement derivatives $\boldsymbol{u}^{(q)}$:

$$\boldsymbol{K}_{\boldsymbol{x}} \bullet \boldsymbol{\mu}_{\boldsymbol{x}}^{(p)} = \boldsymbol{\Gamma}_{\boldsymbol{x}}^{(p)} - \sum_{q=p+1}^{n} \boldsymbol{K}_{\boldsymbol{x}}^{(q,p)} \bullet \boldsymbol{\mu}_{\boldsymbol{x}}^{(q)} \tag{III.42}$$

where it has readily been used that $\boldsymbol{K}_{\boldsymbol{x}}^{(q,p)}$, defined as $-\partial \boldsymbol{r}_{\boldsymbol{x}}^{(q)}/\partial \boldsymbol{u}_{\boldsymbol{x}}^{(p)}$, equals $\boldsymbol{K}_{\boldsymbol{x}}$ when $p = q$, and **zero** when $p > q$. This can be seen from Equation III.37, recalling that $\boldsymbol{v}_{\boldsymbol{x}}^{(p)}$ and $\boldsymbol{w}_{\boldsymbol{x}}^{(p)}$ only depend on $\boldsymbol{u}_{\boldsymbol{x}}^{(q)}$, respectively for $q \leqslant p-1$ and $q \leqslant p-2$. However, obtaining $\boldsymbol{K}_{\boldsymbol{x}}^{(q,p)}$ for $p < q$ is less obvious, and hence derived in Appendix D.6, yielding:

$$\boldsymbol{K}_{\boldsymbol{x}}^{(q,p)} = \binom{q}{p} \left(\boldsymbol{S}_{\boldsymbol{x}} \bullet \boldsymbol{u}^{(q-p)} + \frac{1}{2} \boldsymbol{Q}_{\boldsymbol{x}} \underset{2}{\bullet} \boldsymbol{v}^{(q-p)}\right)\,. \tag{III.43}$$

Note that this adjoint stiffness matrix $\boldsymbol{K}_{\boldsymbol{x}}^{(q,p)}$ for $p < q$ does not need to be assembled before contracting with the adjoint solution $\boldsymbol{\mu}_{\boldsymbol{x}}^{(q)}$. Moreover, the bracketed elemental decompositions of $\boldsymbol{S}_{\boldsymbol{x}}$ and $\boldsymbol{Q}_{\boldsymbol{x}}$ should already have been contracted with $\boldsymbol{u}_{\boldsymbol{x}}^{(r)}$ and $\boldsymbol{v}_{\boldsymbol{x}}^{(r)}$ for all $r = 1, \ldots, n$ during the higher-order structural analysis, which can hence be recycled. The adjoint force $\boldsymbol{\Gamma}_{\boldsymbol{x}}^{(p)}$ can then also be obtained explicitly, as derived for pure MacLaurin-based perturbed analysis in Appendix D.2, and for Bayesian-enhanced analysis in Appendix D.4. Finally, the higher-order residual's design sensitivity $\partial \boldsymbol{r}_{\boldsymbol{x}}^{(p)}/\partial \boldsymbol{x}$ can then be assembled from its regularized elemental contributions in decomposed tensorial form, as:

$$\frac{\partial \boldsymbol{r}_{\boldsymbol{x}}^{(p)}}{\partial \boldsymbol{x}} = \sum_{e=1}^{M} \mathbb{A}_e^{\top} \bullet \frac{\mathrm{d}\boldsymbol{r}_e^{(p)}}{\mathrm{d}\rho_e} \bullet \frac{\partial \rho_e}{\partial \boldsymbol{x}}\,, \tag{III.44}$$
$$\text{with} \quad \frac{\mathrm{d}\boldsymbol{r}_e^{(p)}}{\mathrm{d}\rho_e} = -(\varsigma_e)' \boldsymbol{K}_0 \bullet \boldsymbol{u}_e^{(p)}$$
$$- \left(\frac{\varsigma_e}{2\zeta_e}\right)' \boldsymbol{S}_0 \underset{2}{\bullet} \boldsymbol{v}_e^{(p)} - \left(\frac{\varsigma_e}{6\zeta_e^2}\right)' \boldsymbol{Q}_0 \underset{3}{\bullet} \boldsymbol{w}_e^{(p)}\,,$$

where $(\circ)'$ denotes the derivative operation $\frac{\mathrm{d}(\circ)}{\mathrm{d}\rho_e}$.

To summarize, while some generic user-defined responses $g(\boldsymbol{x},\, \boldsymbol{u}_{\boldsymbol{x}})$ of the current structural design $\boldsymbol{x}$ can straight-forwardly be obtained as it is defined, its design sensitivity can be efficiently obtained through the adjoint formulation:

$$\frac{\mathrm{d}g(\boldsymbol{x},\, \boldsymbol{u}_{\boldsymbol{x}})}{\mathrm{d}\boldsymbol{x}} = \frac{\partial g(\boldsymbol{x},\, \boldsymbol{u}_{\boldsymbol{x}})}{\partial \boldsymbol{x}} + \sum_{p=1}^{n} \boldsymbol{\mu}_{\boldsymbol{x}}^{(p)} \bullet \frac{\partial \boldsymbol{r}_{\boldsymbol{x}}^{(p)}}{\partial \boldsymbol{x}}\,. \tag{III.45}$$

Here, the adjoint solution $\boldsymbol{\mu}_{\boldsymbol{x}}^{(p)}$ is recursively obtained through Equation III.42 for $p = n, n-1, \ldots, 1$. The adjoint stiffness is obtained through Equation D.6.1. Then, the contraction $\boldsymbol{K}_{\boldsymbol{x}}^{(q,p)} \bullet \boldsymbol{\mu}_{\boldsymbol{x}}^{(q)}$could be efficiently obtained through the assembly of decomposed elemental tensor forms, similarly to Equation III.18, using III.19 and III.20. The adjoint force $\boldsymbol{\Gamma}_{\boldsymbol{x}}^{(p)}$ is then obtained using Appendix D.2 or D.4. Finally, the higher-order residual sensitivity $\partial \boldsymbol{r}_{\boldsymbol{x}}^{(q)}/\partial \boldsymbol{x}$, is then obtained through Equation III.44. For a final overview of the structural optimization routine, see Figure III.2.

III.6 Validation Strategy

Recalling the main goal of this work - extending structural topology optimization with efficient, sufficiently accurate, and robust geometrically non-linear analysis - a validation strategy is argued and outlined here. The proposed Bayesian-enhanced perturbed analysis (B) is validated and compared with Newton-Raphson (NR) and linear analysis (L), particularly in terms of the old challenges it overcomes and the new ones it presents within the context of density-based non-linear structural analysis and its structural optimization.

The general approach of the validation strategy is to consider study cases of incremental complexity in terms of scale, non-linearity, and likeness to a practical density-based setting, working from structural analysis of fixed designs in the first part (Section IV), towards large-scale compliance minimization in the second part (Section V), and finally practical topology optimization exploiting rather than suppressing compliance in the third part (Section VI). This is done to isolate and study aspects, properties, or effects of each method, and any parameters that govern the case study's non-linearity, regularization, element resolution, and the analysis method itself otherwise. More specifically, a set of case parameters is systematically swept over in each case study, while a set of performance quantifiers is measured, pertaining to the goals as set for the proposed methodology. Recalling that Newton-Raphson (NR), Perturbed (P), and the novel Bayesian-enhanced perturbed (B) analysis are technically identical to Linear (L) analysis up to their first iteration ($n = 1$, $\#S = 1$), the remainder of this work shall investigate their different limitations and benefits from their second iteration and onwards.

The first part of the validation concerns pure non-linear, load-controlled structural analysis of a loaded C-shaped compliant structure (*C-Beam*), comparing the standard Newton-Raphson and linear analysis to the proposed perturbed MacLaurin and Bayesian-enhanced analysis. For several reasons, a C-Beam of approximately fixed geometrical shape, material model, and boundary conditions is considered, up to a scalar variation of the applied load and a duly argued set of other case parameters. Not only can the results obtained here be compared to the literature from which it is inspired (Yoon & Kim, 2005; van Dijk et al., 2014), but more importantly, many of the features and obstacles encountered in density-based topology optimization can be emulated.

Particularly, the effects of void and filtered density elements and thin structural features under compression can be investigated. This is known to cause problems for Newton-Raphson analysis (Buhl et al., 2000a; Pedersen et al., 2001; Yoon & Kim, 2005; van Dijk et al., 2014), leading to excessively deformed or inverted void elements, impeded or slowed convergence, or even intermediate divergence of solid regions, risking unphysical or unexpected solutions. Overall, accuracy, efficiency, and robustness are affected by it. Furthermore, incrementally higher element resolutions can be, as typical within the density-based setting. This tends to emphasize the mentioned issues related to low densities, and disproportionately increases the cost of structural assembly and solves on its own. Lastly, material- and displacement scaling and density filtering are investigated, as they are regarded here as the minimal but essential set of regularization steps regarding perturbed and Newton-Raphson analysis within density-based topology optimization.

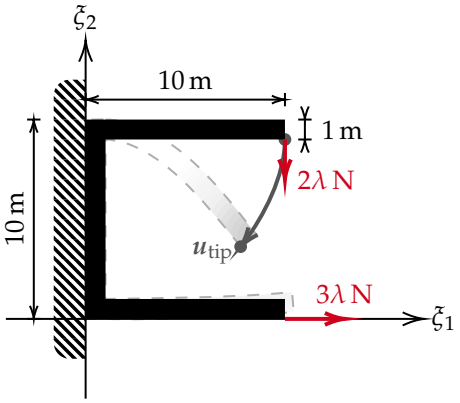

Figure III.6: Geometry, material and boundary conditions of the C-shaped compliant beam structure (C-Beam), as studied in the next section. An isotropic, linear elastic material is assumed, with Young's Modulus $E = 1000\,\text{GPa}$ and Poisson's ratio $\nu = 0.3$ under plane-stress condition, in accordance with Yoon & Kim (2005), van Dijk et al. (2014).

Concretely, consider the following problem definition, case parameters, and performance quantifiers regarding the loaded C-Beam study case. The geometry, material, and boundary conditions of the loaded C-Beam are defined in Figure III.6, with two applied nodal forces scaled by the load variable λ in accordance with Yoon & Kim (2005) and van Dijk et al. (2014). Next, the case parameters that are systematically swept over are listed in Table III.1. Finally, the performance of each analysis method given all other case parameters is mostly quantified through its normed, relative displacement error ϵ and convergence rate versus n and λ, where n in this case generalizes to the amount of solves. Here, the analysis result $\boldsymbol{u}^*$ of a specific method given a certain λ, n, or termination criterion, is compared to the Newton-Raphson result $\boldsymbol{u}$ that has converged up to a normed, relative residual of 10^{-10}, occasionally without voids or regularizations to investigate their overall effects. The latter tolerance was chosen equal to the smallest one that could be obtained for the tensor decompositions.

$$\epsilon \equiv \frac{|\boldsymbol{u}^* - \boldsymbol{u}|}{|\boldsymbol{u}|} \,, \tag{III.46}$$

Accurate estimation of this error has also been argued in Subsection I.3, to be an important tool in balancing computational effort and accuracy, and stabilizing the topology optimization by allowing it to avoid inaccurate analyses and sensitivities. Hence, the tightness or error of this error estimate is also taken as a quantifier, in addition to the radius of convergence estimate that governs it.

Lastly, computational performance is another important quantifier. Regrettably, rigorously formulating a means to measure it was deemed too challenging, and

Case parameter	Specification
Load variable λ	Typically, $\lambda \in [0,\ 1+)$
Analysis order n (number of structural solves #S)	$n \geqslant 1$: Perturbed (n^{th}) $n \leqslant -1$: Bayesian ($\lvert n\rvert^{\text{th}}$) $\lvert n\rvert = 1$: Linear $n \Leftrightarrow \#S$: Newton-Raphson
Refinement (C-Beam)	Mesh refinement of the voxel grid on which the C-Beam design is defined, considering integer multiples of 10 by 10.
Void density $\underline{\varsigma}$	$\underline{\varsigma} = 0$: No voids $\underline{\varsigma} > 0$: Voids $\underline{\varsigma} \approx 10^{-9}$: Typical
EMDS threshold $\overline{\varsigma}$	$\overline{\varsigma} \equiv 0$: No EMDS $\overline{\varsigma} > 0$: EMDS $\overline{\varsigma} \approx 10^{-2}$: Typical
Density filter radius $\overline{\Delta}$	$\overline{\Delta} \leqslant L_e$: No filtering $\overline{\Delta} > L_e$: Filtering

Table III.1: List of **C-Beam analysis** case parameters and their specification for the structural analysis and topology optimization validation. Typical values are argued from literature or the results discussed in Section VII. No material penalization is considered for the C-Beam cases, meaning $\theta = 1$.

Case parameter	Specification
Error tolerance $\overline{\epsilon}$ (enforcing the error as estimated for NR, P and P)	$\overline{\epsilon} = \infty$: Inactive $\overline{\epsilon} < \infty$: Active Typically, $\overline{\epsilon} \in \left[10^{-3},\ 10^{-2}\right]$
Material penalization θ	$\theta = 1$: No penalization $\theta > 1$: Penalization Typically, $\theta \in [1,\ 3]$
Refinement	Mesh refinement of the voxel grid on which the design is optimized, typically close to 100 by 100.
Iterations	Maximum or enforced amount of design optimization iterations, typically close to 100.

Table III.2: List of **Topology Optimization** case parameters and their specification for the structural optimization validation, in addition to those specified in Table III.1. Typical values are argued from literature or the results discussed in Section VII.

left for future work. Instead, the number of iterations for each method is taken as a quantifier, equal to the order n, or amount of solves #S, at least providing a solid ground for speculation based on the nature and prior investment of each method's solves. As another crude quantifier of computational effort, shear runtime of the analysis is considered. It must be noted that this serves as a very rough indicator of the trends to be expected, as the proposed method is still in its conceptual stage, and the straightforward implementations of all compared analysis methods within the optimization framework are far from optimized in terms of computational efficiency.

A more detailed account of the investigated C-Beam study cases is presented within Section V. For each case, its subgoal with respect to the other case studies and the main goal of this work is briefly emphasized. Then, the fixed and swept case parameters, and relevant quantifiers, are listed and argued, followed directly by the results and notable observations.

The second and third parts of the validation concern actual density-based structural topology optimization, particularly a beam of minimized compliance, a force inverter and a micro gripper. Still using load-controlled structural analysis, the standard Newton-Raphson (NR) and linear analysis are compared to the proposed perturbed MacLaurin (P) and Bayesian-enhanced (B) analysis. In these parts, however, the order and selection of performed study cases are not ordered chronologically or along incremental complexity, as done for the C-Beam analysis. Instead, they aim to summarize the most important findings in a concise but intuitive manner. Their particular goals and problem formulations are elaborated in their respective sections, Section V and Section VI.

Some additional case parameters are considered during the second and third part of topology optimization validation, as listed in Table III.1, with emphasis on the load variable λ, analysis order n, and error tolerance $\overline{\epsilon}$. Where λ directly governs structural non-linearity, n and $\overline{\epsilon}$ accommodate its analysis. The particular choice for B over P analysis, and the settings of other case parameters are duly elaborated in the respective sections containing all topology optimization case studies and their results.

IV C-Beam Analysis

As argued in Subsection III.6, this part I of the results aims to validate and compare the standard Newton-Raphson (NR) and Linear (L) analysis to the proposed Perturbed (P) MacLaurin analysis, and its Bayesian-enhanced (B) equivalent, through load-controlled structural analysis of a C-shaped compliant structure (*C-Beam*) (Yoon & Kim, 2005; van Dijk et al., 2014) through four case studies. The structural problem definition is captured in Figure III.6, stating the geometry, material, and boundary conditions. First, the effects and challenges of non-linearity are explored in Subsection IV.1, by increasing the load and analysis order, tracking deformations, error, and convergence characteristics. Second, a density-based setting is more closely emulated in Subsection IV.2, incrementally applying reg-

ularizations and mesh refinements. Third, an exhaustive quantification is performed, sweeping over a wide and dense range of case parameters, indicating some generally ideal values of regularization parameters, or relations between them. Lastly, the fourth case C-Beam case study entails a crude comparison of computational effort in Subsection IV.4, naively based on computational times. Throughout the present section, notable results and observations are briefly discussed in preparation for the general discussion in Section VII.

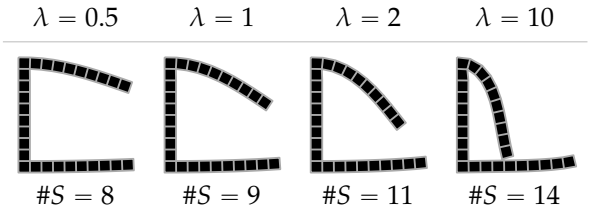

Figure IV.1: Deformed finite element model of the C-Beam according to nonlinear analysis for several load-scalars λ, using square 1 by 1 m bilinear finite elements. Here, $\#S$ denotes the required number of Newton-Raphson solves.[43]

IV.1 Non-Linearity and Error

The goal of this first C-Beam analysis case study is to gain some intuition on the effects and limitations of non-linearity and its analysis, respectively increased through load variable λ and accommodated by analysis order n. This is done by comparing the deformations based on Newton-Raphson (NR) analysis to those of Perturbed analysis using MacLaurin predictions (P), and its Bayesian enhanced equivalent (B). Furthermore, their errors and error estimates are graphed versus both λ and n. The specific case parameter specifications and sweeps are listed in Table IV.1. For several loads, the deformations based on a referential NR analysis are depicted in Figure IV.1, up to a normed relative residual of 10^{-10}. For several analysis orders, the deformations based on P and B are then depicted in Figure IV.2 and compared to the mentioned NR results. Lastly, a more thorough quantification of relative error versus λ and n or $\#S$ is performed[43], for all methods, validating their estimated or predicted behavior, qualities and limitations discussed in Subsection II.3 and III.4. For all methods of analysis, meaning NR, P, and B, true error ϵ is evaluated with respect to the referential NR analysis that has converged up to a normed relative residual of 10^{-10}.

Case parameter	Value (range)
Load variable λ	$[0,\ 10]$
(P, B) *Analysis order* n	$\{1,\ 2,\ \ldots,\ 50\}$
Void density $\underline{\varsigma}$	0 (no voids)
EMDS threshold $\overline{\underline{\varsigma}}$	0 (no EMDS)
Refinement	$\times 1$ (no refinement)
Density filter radius $\overline{\Delta}$	1 element (no filtering)

Table IV.1: List of **C-Beam analysis** case parameters and their studied value (range) for the first case study, exploring non-linearity and error. Recall that for all C-Beam case studies, no penalization was applied, meaning $\theta = 1$.

Inspecting the referential NR C-Beam deformations in Figure IV.1 reveals close agreement of the resulting deformations and required amount of solves $\#S$, with those reported in Yoon & Kim (2005) where an equivalent structural problem definition and tolerances were used. This validates structural model and nonlinear analysis based on the decomposed structural tensor reformulation, proposed in Section III. Furthermore, through NR analysis, both residual force and displacement error are predicted to decrease doubly exponentially versus the amount of solves, also referred to as quadratic convergence, as estimated in Appendix B.1 and reported in Bruns & Tortorelli (2001). Hence, a doubly exponentially increasing load should λ should require a linearly increasing amount of solves $\#S$, which can also very weakly be verified in Figure IV.1. Fortunately, much stronger evidence of the quadratic NR convergence can be seen in Figure IV.4c, as duly elaborated.

Concerning the perturbation-based deformations using MacLaurin extrapolations (P) in Figure IV.2a, practically all convergence characteristics predicted in Appendix B.2 can be readily confirmed. Figure IV.3 and IV.4b more precisely confirm the monomial n^{th} order error versus λ, and exponential error versus λ. Indeed, decreasing and increasing the load λ generally result in a decreasing or respectively increasing error. However, the order of both convergence and divergence are emphasized proportionately to the analysis order n. Depending on the fixed value for λ, an increased order n may either lead to (sub-) linear convergence or (super-) linear divergence of the deformation, compared to the referential NR-based result. This can be seen in Figure IV.4b. In other words, when λ is smaller or greater than some radius of convergence $\overline{\lambda}$, in this case estimated to be 1.15 using Equation B.2.5, the error decreases or respectively increases roughly exponentially versus n. While an emphasized convergence due to larger n is certainly desirable regarding accuracy, the equally emphasized divergence may be detrimental to the robustness within topology optimization.

Fortunately, the Bayesian-enhanced (B) deformations in Figure IV.2b seem to be of superior accuracy, despite the equal computational cost, compared to their respective pure MacLaurin counterparts of the same orders in Figure IV.2a. The assumption made

[43] Throughout this work, $\#S$ denotes the number of fully updated NR iterations, required to reduce the normed residual below 10^{-10} times the normed, scaled load.

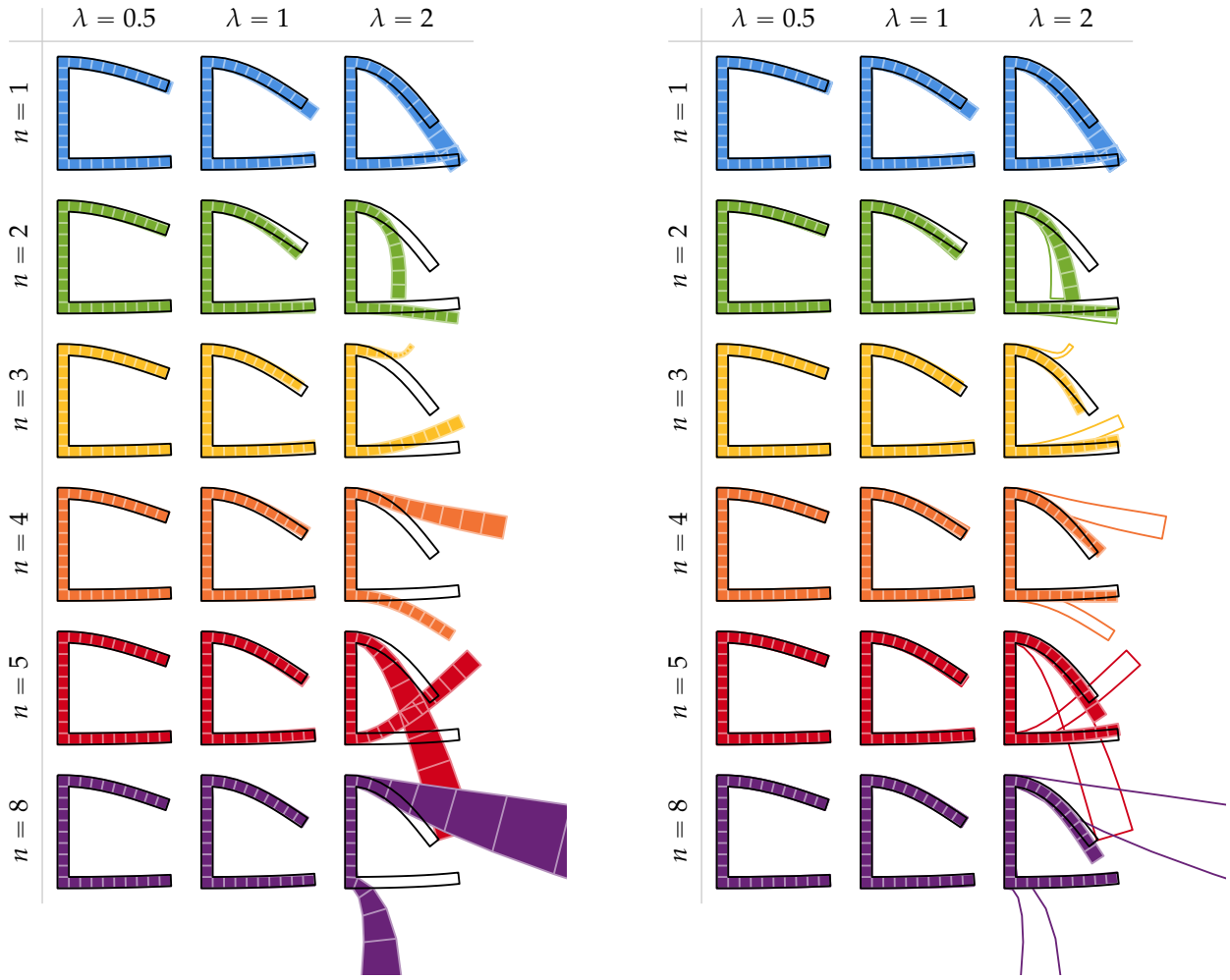

(a) Perturbed analysis (P), using n^{th}-order MacLaurin series. Also included in Figure IV.2b (**colored contour**) for reference.

(b) Perturbed analysis using the Bayesian average (B) (**colored**) of all the full 1^{st}- up to n^{th}-order MacLaurin series.

Figure IV.2: Deformed finite element model of the C-Beam according to approximate analysis (**colored solid**) and non-linear analysis (**black contour**), for several load-scalars λ and approximation orders n, using square 1 by 1 m bilinear finite elements.

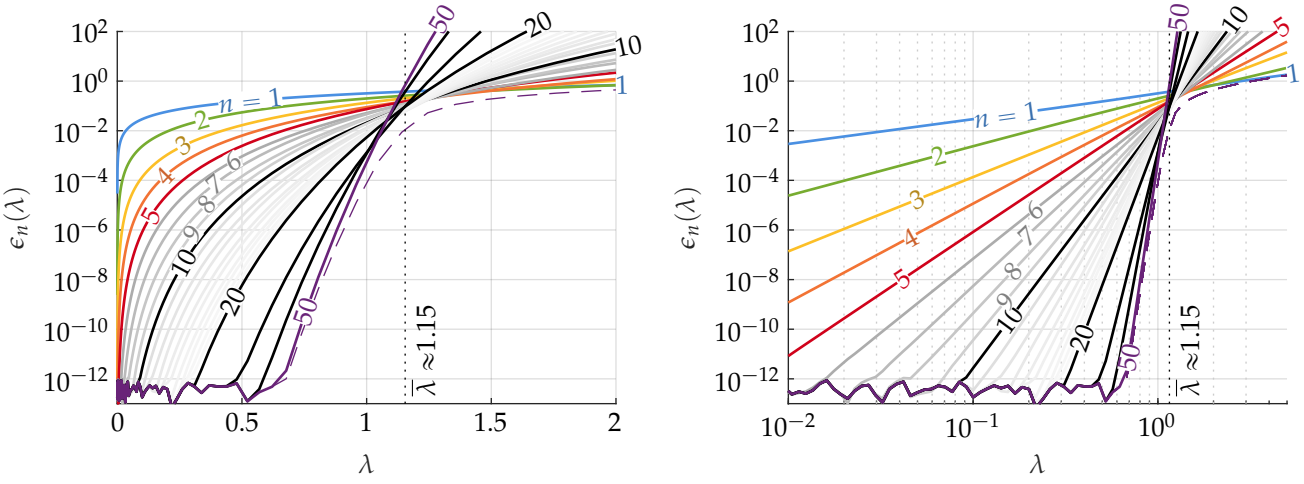

(a) Logarithmic $\epsilon_n(\lambda)$ versus linear λ-axis.

(b) Logarithmic $\epsilon_n(\lambda)$ versus logarithmic λ-axis.

Figure IV.3: Relative normed displacement errors $\epsilon_n(\lambda)$ of the deformed C-Beam versus load-scalar λ caused by perturbed analysis, for several n^{th}-order MacLaurin series (**solid graphs**), and their 50^{th}-order Bayesian average (**dashed graph**). Here, $\overline{\lambda}$ denotes the radius of convergence, as determined by Equation B.2.5.

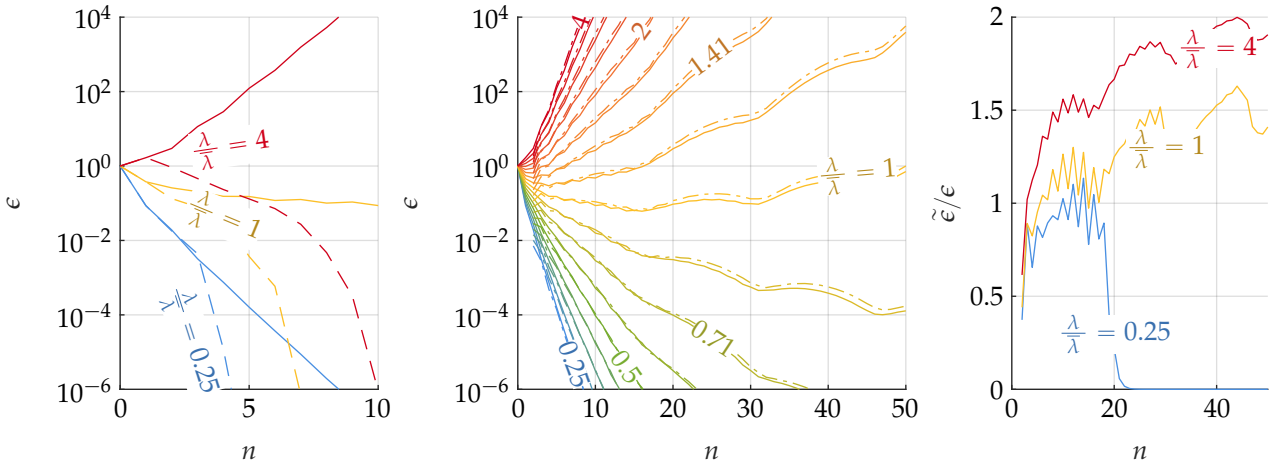

(a) True error ϵ using NR (– –) and P (—), for $\frac{\lambda}{\overline{\lambda}} = 0.25,\ 1,\ 4$.

(b) True error ϵ (—) and estimate $\tilde{\epsilon}$ (– · –) using P, for $\frac{\lambda}{\overline{\lambda}}$ logarithmically distributed from 0.25 to 4.

(c) True error ϵ relative to the estimate $\tilde{\epsilon}$ using P, for $\frac{\lambda}{\overline{\lambda}} = 0.25,\ 1,\ 4$.

Figure IV.4: Comparing the true and estimated relative normed displacement errors of the deformed C-Beam, versus the amount of structural solves $\#S \equiv n$ using Newton-Raphson (NR) and MacLaurin-based perturbed (P) analysis. For both methods, ϵ denotes their true relative error obtained through a referential NR analysis up to a normed relative residual of 10^{-10}. For P analysis, $\tilde{\epsilon}$ denotes its relative error estimate.

here is that practically all computational effort is spent on obtaining the governing set of displacement derivatives, and a negligible amount on constructing a continuous prediction from it. The B-enhanced deformations also appear in full agreement with the convergence characteristics predicted in Appendix C. For any λ and n, more accurate results are obtained compared to the pure MacLaurin extrapolations. Considering this particular structural problem, the most remarkable difference between P and B is emphasized for $\lambda = 2$. Most importantly, the divergence has been bounded to the first order versus λ for any n when $\lambda > \overline{\lambda}$, but benefits the full n^{th} order convergence as $\lambda \to 0$. This can be seen in Figure IV.3b, where the slopes indicate the order of convergence and divergence. Additionally, the resulting deformations given fixed λ and increasing n also seem to stabilize, meaning that while the predicted deformation remains equally inaccurate, they do not change. This facilitates a dynamically changing n - perhaps driven through a metric on error or computational cost - without risking discontinuity during topology optimization.

As a final remark on robustness, it appears that Newton-Raphson is able to ultimately converge for larger loads, judging from Figure IV.4a. Even when the first structural iteration yields an increased error, linear convergence appears to set on for a few iterations, followed by the expected quadratic terminal convergence. On the other hand, the perturbed analysis keeps linearly diverging when the considered load λ is beyond the critical value, or radius of convergence $\overline{\lambda}$. Conversely, where $\lambda < \overline{\lambda}$ predicts convergence of P or B analysis, it also seems to predict the rapid onset of quadratic convergence for NR analysis.

IV.2 Regularization and Refinement I

The goal of the presented second C-Beam analysis case study is to incrementally emulate aspects encountered during structural analysis within a typical density-based topology optimization. This mainly concerns the effects, limitations of regularization, and mesh refinement. Notably, elements of low and intermediate density are inevitable but problematic. Therefore, the aim is not to avoid them, but to remedy their effects. Hence this second case study explores the solid and void deformations and errors through the parameter sweep listed in Table IV.2, including density filtering. The corresponding results are captured in Figures IV.5 and IV.6. Ultimately, by the end of this case study and the more exhaustive one in Subsection IV.3, some ideal or sufficient values for void density $\underline{\varsigma}$ and EMDS threshold $\overline{\varsigma}$ are argued to minimize both the ramifications of other regularizations, but also their own.

Case parameter	Value (range)
Load variable λ	$[0,\ 10]$
(P, B) *Analysis order* n	5
Void density $\underline{\varsigma}$	$\{0,\ 10^{-9}\}$
EMDS threshold $\overline{\varsigma}$	$\{0,\ 0.01,\ 0.1,\ 0.5\}$
Refinement	$\{\times 1,\ \times 2,\ \times 4\}$
Density filter radius $\overline{\Delta}$	1 m, or effectively 1 element per refinement

Table IV.2: List of **CBeam analysis** case parameters and their studied value (range) for the second case study, exploring regularization and refinement.

The behavior of unregularized void elements with density $\underline{\varsigma} = 10^{-9}$ and their impact on NR analysis

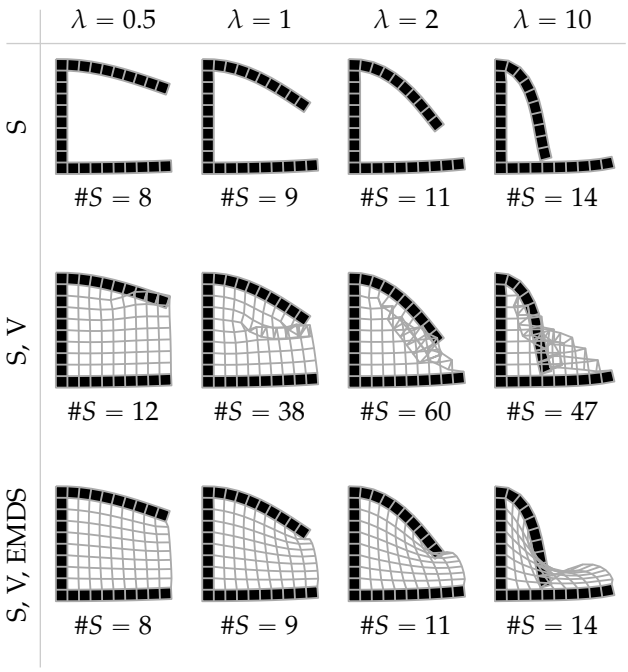

(a) Newton-Raphson analysis (NR). Here, #S denotes the number of Newton-Raphson solves required for a relative normed residual of 10^{-10}.

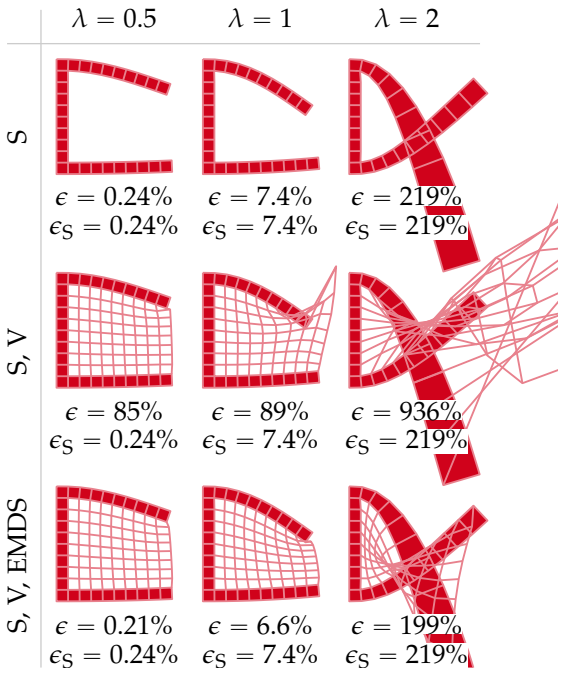

(b) Perturbed analysis (P) using a 5^{th}-order MacLaurin extrapolation.

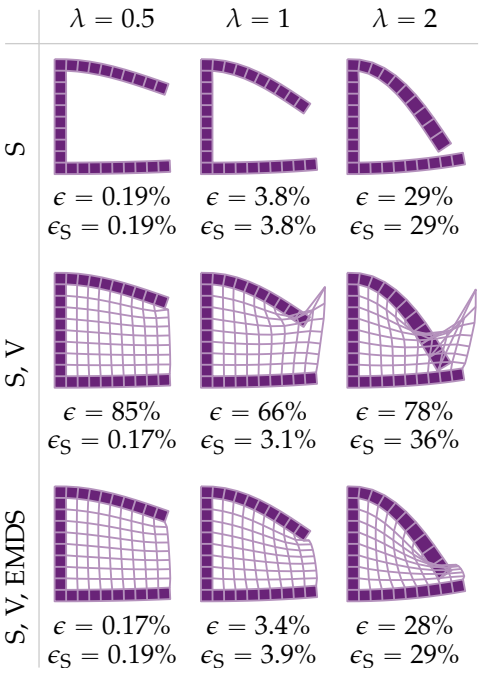

(c) Perturbed analysis using the Bayesian average (B) of all the full 1^{st}- up to 5^{th}-order MacLaurin series.

Figure IV.5: Deformed C-Beam according to Newton-Raphson and perturbed analysis, for several load variables λ and the inclusion of the following model options: **S)** Solid elements with $\rho = 1$; **V)** Void elements with $\underline{\varsigma} = 10^{-9}$; **EMDS)** *Element Material- and Displacement Scaling* with EMD threshold $\overline{\varsigma} = 10^{-2}$. Note that $\underline{\varsigma}$ and $\overline{\varsigma}$ are respectively zero, meaning excluded, otherwise. For the approximate analysis in Figure IV.5b and IV.5c, ϵ and ϵ_S denote the relative normed displacement errors over the full and solid domains respectively, as compared to their nonlinear counterparts in Figure IV.5a.

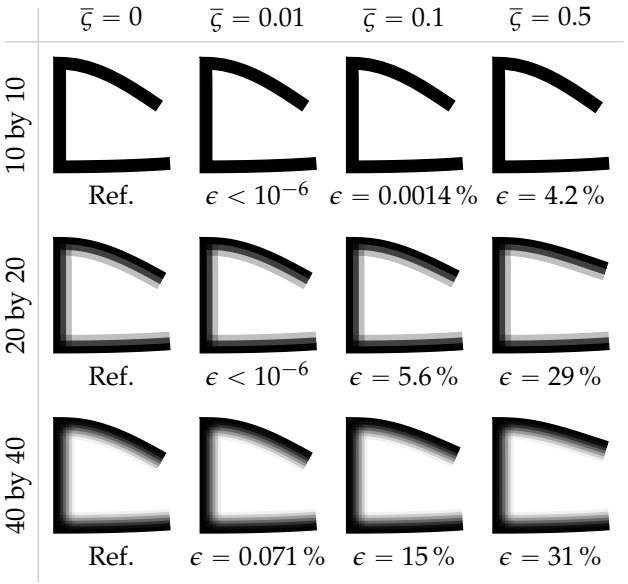

(a) Newton-Raphson analysis (NR). Here, ϵ denotes the relative displacement error with respect to the reference (Ref.) where $\overline{\varsigma} = 0$.

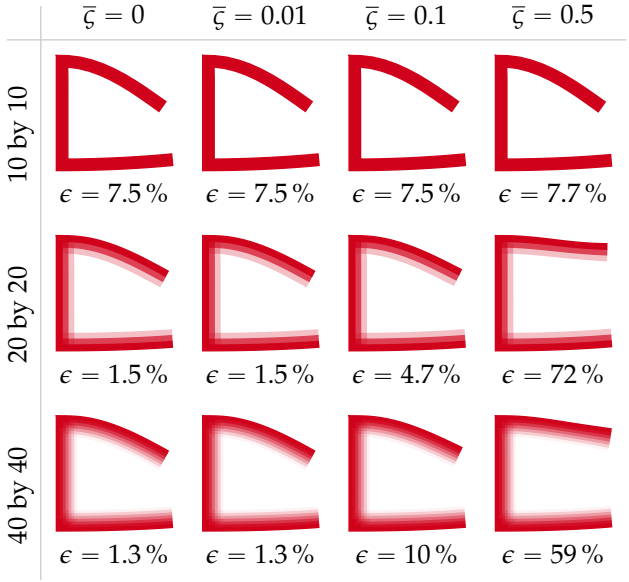

(b) Perturbed analysis (P) using a 5^{th}-order MacLaurin extrapolation.. Here, ϵ denotes the relative displacement error with respect to the nonlinear reference (Ref. in IV.6a) where $\overline{\varsigma} = 0$, given the same resolution.

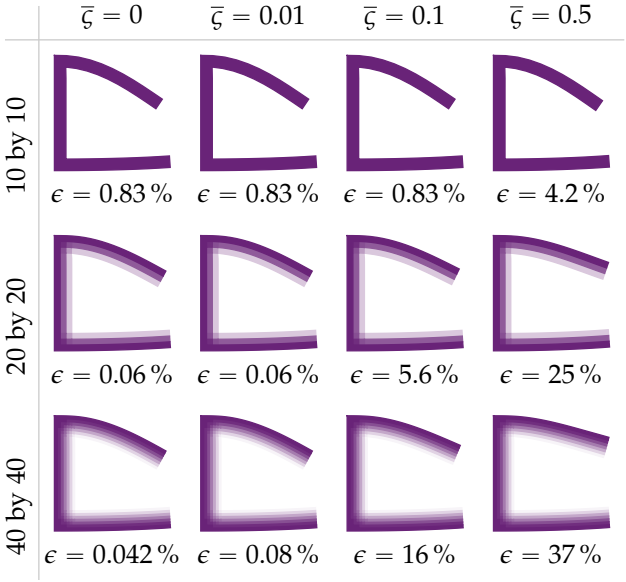

(c) Perturbed analysis using the Bayesian average (B) of all the full 1^{st}- up to 5^{th}-order MacLaurin series. Here, ϵ denotes the relative displacement error with respect to the NR reference (Ref. in IV.6a) where $\overline{\varsigma} = 0$, given the same resolution.

Figure IV.6: Deformed C-Beam according to Newton-Raphson and perturbed analysis with $\lambda = 1$, for several EMDS thresholds $\overline{\varsigma}$, and density-filtered mesh-refinements of the original 10 by 10 m structure (Figure III.6), with $\lambda = 1$ and $\underline{\varsigma} = 0$. A filter-radius of 1 m was used, spanning 10% of the domain. The minimum void density $\underline{\varsigma}$ was set to 0, and elements of this density were removed.

can be seen directly from Figure IV.5a. Note that the NR, P and B results without voids and EMDS (hence solid, or S) are respectively identical to Figure IV.1, Figure IV.2a and Figure IV.2b for $n = 5$. Concerning NR analysis including void regions (S, V), the latter appear crumbled in increasingly less unique ways versus the load λ. This may be explained by the many possible ways individual elements may deform, buckle or invert, relatively easily satisfying the imposed tolerance on the residual force for equilibrium, due to their low stiffness. The equilibrium curve, or one of the excessively many, not necessarily physical but closely bundled equilibrium branches, is very difficult to navigate using NR analysis, especially combined with the low-density induced ill-conditioning of the tangent stiffness. This is reflected through the increased amount of NR iterations, or solves $\#S$, required for convergence. Moreover, $\#S$ has been observed highly sensitive to small changes in the tolerance and void density $\underline{\varsigma}$, further testifying to the excess of local equilibria and resulting chaos within the NR procedure.

Void elements also compromise P and B analysis when unregularized, judging from Figure IV.5b and IV.5c. The higher order deformation predictions seem to suffer divergence, at least within the void regions. For P analysis (Figure IV.5b), there seems to be no further impact on the error of the solid regions ϵ_S compared to the voidless results, where the MacLaurin truncation error fully dominates. Concerning B analysis, the error on solid regions now seems increased due to including voids, rather than unaffected, despite remaining lower for all loads λ, compared to P analysis with and even without voids. The void-induced divergence is likely caused by the relatively small radius of convergence within the void elements. Currently, the B analysis measures this radius considering all degrees of deformation freedom and measures the extent of overall divergence without discriminating between components associated purely with void or solid elements. As a result, B analysis suppresses the higher-order contributions globally due to locally diverging predictions, despite them locally converging elsewhere. Effectively, localized divergence of void deformations causes B analysis to more quickly distrust higher-order contributions globally, despite the much more important localized convergence of solid deformations. Their higher-order information gets suppressed regardless, wasting the previously obtained accuracy within solid regions, increasing ϵ_S.

Remarkably, *Element Deformation Scaling* (EMDS) with threshold $\overline{\varsigma} = 0.01$ seems to completely remedy any of the previously mentioned issues due to void regions for NR and P analysis, reducing the solve count $\#S$ and solid error ϵ_S back to that of the unregularized, voidless structures. In other words, it remedies the excessive void deformations and associated computational burden reported by (Yoon & Kim, 2005; van Dijk et al., 2014). By linearizing the structural behavior of void elements, their radius of convergence tends towards infinity. Yet, a slight exception occurs for B analysis where $\lambda = 1$. Perhaps the local radius of convergence within void elements remains barely below that of the solid regions, as the non-zero EMDS threshold $\overline{\varsigma}$ is not sufficiently linearizing the structural behavior such as to compensate for the relatively excessive, thus non-linear, void-deformation. Alternatively, the current value of $\overline{\varsigma} = 0.01$ may have a direct but marginal effect on the solid region. Yet, this particular value for $\overline{\varsigma}$ shall be argued at the end of this section and the next, to minimally introduce structural model error, while maximally suppressing void-related issues. On account of the present and prior paragraph, a future recommendation is to augment Bayesian analysis with a local error estimator to make EMDS redundant and potentially increase the practical range of validity for λ. This is further elaborated in Subsection VII.4. Regardless, the B deformation accuracy when including voids and EMDS is practically equal to its voidless counterpart, and generally superior to the P deformations regardless of voids and EMDS, given the same load λ. Moreover, increased λ pronounces the superiority of B over P accuracy, also with and without voids or EMDS.

Finally, the effects of mesh refinement, EMDS, filtering[44] and intermediate densities can nearly be fully isolated through the results in Figure IV.6. Here, the density filtering radius $\overline{\Delta}$ is increased proportionally to the mesh refinement, particularly by 1 element per refinement. Then, some interesting EMDS thresholds $\overline{\varsigma}$. Figure IV.6 are considered. Furthermore, a fixed void density $\underline{\varsigma} = 10^{-9}$ is considered, and a load $\lambda = 1$ is taken, being close to the radius of convergence $\overline{\lambda} \approx 1.15$ for the unregularized and unrefined C-Beam.

EMDS is a density-based effect, as confirmed by all refined and filtered results in Figure IV.6. Therefore, it tends to increase with the simultaneous refinement and filtering, yielding larger errors when its threshold $\overline{\varsigma}$ is excessive, or smaller errors when the remedied void divergence is more prominent. Thresholds $\overline{\varsigma}$ of 0.1 and 0.5 especially, appear to have a linearization-induced stiffening effect now reaching the void regions. Obviously, the resulting error compared to when $\overline{\varsigma} = 0$ is not desirable. Fortunately, setting it to 0.01 results in a small error with respect to the referential NR result (Figure IV.6a), compared to those within the P and B predictions. Refinement and filtering effects are treated in the next case study and subsection, given the much denser and more elaborate parameter sweep.

[44]The density-filter used in this work is the same linear convolution-filter as used in the 99-line TO code by Sigmund (2001). It computes a current element's new density as the weighed average of that of all neighbouring elements within the filter-radius. The weight decays linearly as a function of the elements' distances to the current element, reaching exactly zero at the radius.

IV.3 Regularization and Refinement II

The goal of the third C-Beam analysis case study is to conclude trends and argue suitable values, based on the errors over a wide and dense sweep versus void density $\underline{\varsigma}$, EMDS threshold $\overline{\varsigma}$ and mesh refinement. While regularization-induced errors are undesirable on their own, a further risk would be their abuse by the structural design optimization. Therefore, a balance must be stricken between the problems they solve and those they introduce. The considered case parameters are listed in Table IV.3, and the full result is captured by the surface graphs within Figure IV.7. The left column of graphs serves as an important reference. It captures the error purely introduced by the considered parameters through NR analysis up to a relative normed residual of 10^{-10}, bounding the ultimate accuracy P or B analysis may ever obtain in predicting the same result using the same structural model and parameters. The right column serves as a generalized indicator of error for both P and B analysis, $\widetilde{\epsilon}_n(\lambda)$ and $\widetilde{\widetilde{\epsilon}}_n(\lambda)$ respectively, through the radius of convergence $\overline{\lambda}$ (Equation IV.1), as estimated using a 50^{th} order perturbed analysis. It allows the study of estimated error irrespective of the choice between B and P analysis, their order n, or applied load λ. Recall that both errors are estimated as:

$$\widetilde{\epsilon}_n(\lambda) = \beta^n \,, \qquad \widetilde{\widetilde{\epsilon}}_n(\lambda) = \sqrt{\frac{\beta^{2n} - \beta^{2n+2}}{1 - \beta^{2n}}} \,, \qquad \beta = \frac{\lambda}{\overline{\lambda}} \tag{IV.1}$$

Case parameter	Value (range)
Load variable λ	1
(P, B) *Analysis order* n	50
Void density $\underline{\varsigma}$	$\{0,\ [10^{-10},\ 1]\}$
EMDS threshold $\overline{\varsigma}$	$\{0,\ [0.01,\ 10]\}$
Refinement	$\{\times 1,\ \times 2,\ \ldots,\ \times 10\}$
Density filter radius $\overline{\Delta}$	1 m, or effectively 1 element $\times$ refinement

Table IV.3: List of **C-Beam analysis** case parameters and their studied value (range) for the third case study, performing an exhaustive quantification.

Starting with the referential NR analysis, ramifications introduced by voids and EMDS are concisely captured by Figure IV.7a. The additive property of their squared errors should indeed translate to somewhat of a smooth maximum property of their logarithmic errors, meaning typically only one of both dominates. When some higher value of one is required, a higher value of the other may as well be chosen without further increasing error. To illustrate, considering a void density $\underline{\varsigma}$ of 10^{-9} as often used throughout density-based structural analysis or topology optimization[45], one can choose the EMDS threshold $\overline{\varsigma}$ close to 0.1 but also very safely at 0.01 without having it worsen the error ϵ. Choosing it to be 0, however, re-introduces the computational problems for both NR, P and B analysis. The non-unique and parameter-sensitive NR solutions are reflected by the jaggedness versus $\underline{\varsigma}$ given $\overline{\varsigma} = 0$ in Figure IV.7a, indicating bad, and incidentally terrible convergence with respect to higher values for $\overline{\varsigma}$.

Moving on to P and B analysis, ramifications introduced by voids and EMDS are concisely captured by Figure IV.7b. Here, the result appears to suggest that $\underline{\varsigma}$ and $\overline{\varsigma}$ have a logarithmically additive (hence linearly multiplicative) effect on $\overline{\lambda}$, seemingly increasing versus both. While on its own a high radius of convergence $\overline{\lambda}$ or higher rate given some fixed λ may seem desirable, the result which is being converged to must not be affected by $\underline{\varsigma}$ or $\overline{\varsigma}$. Moreover, high values of either precisely result in high values of $\overline{\lambda}$ due to artificial stiffening effects of $\underline{\varsigma}$ and artificial linearization effects of $\overline{\varsigma}$. Fortunately, a few decades of smaller, non-zero values for either $\underline{\varsigma}$ or $\overline{\varsigma}$ at least circumvent the detrimental effect on $\overline{\lambda}$ with respect to choosing $\overline{\varsigma} = 0$, without noticeably affecting the structural model as verified through the referential NR analysis. Concretely, choosing $\underline{\varsigma} = 10^{-9}$ and $\overline{\varsigma} = 0.01$ safely mitigate void-related issues without affecting physical accuracy otherwise.

Refinement barely seems to have an effect on the referential NR analysis, judging from Figure IV.7a, IV.7c and IV.7e, meaning in that sense the structural model and filtering are properly regularizing with respect to it. However, a slight effect on P and B analysis can be seen from Figure IV.7a, IV.7c and IV.7e. More precisely, refinement seems to yield an initial reduction of $\overline{\lambda}$, most likely by relieving shear locking effects (Bathe, 2016) within the 4 noded elements. The latter would artificially increase stiffness, reducing deformations, and hence the effective non-linearity and perceived $\overline{\lambda}$. According to Azrar et al. (1993), $\overline{\lambda}$ should indeed not overly depend on refinement, with the apparent exception here stemming from an overly coarse mesh, causing associated shear locking. Beyond a certain level of refinement, no further decrease of $\overline{\lambda}$ seems to happen, except for when $\underline{\varsigma}$ is close to 1, likely causing a stress concentration and singularity in the deformation field. This overall mesh-independence of $\overline{\lambda}$ is a huge relief, as from algebraic geometry (Subsection II.4) it was learned that the degree of the equilibrium curve increases exponentially with the amount of considered variables, in this case freedom degrees. This increased degree might have implicated increased non-linearity thus decreased $\overline{\lambda}$ in non-obvious ways, such as additional complex singularities, despite the smooth equilibrium curve that should ultimately be converged towards. Fortunately, this is not the case, and the

[45] Some notable works using a void density of 10^{-9}, or effectively so after penalizing one of 10^{-3} to the third power, are Yoon & Kim (2005); Buhl et al. (2000a); Sigmund (2001); van Dijk et al. (2014).

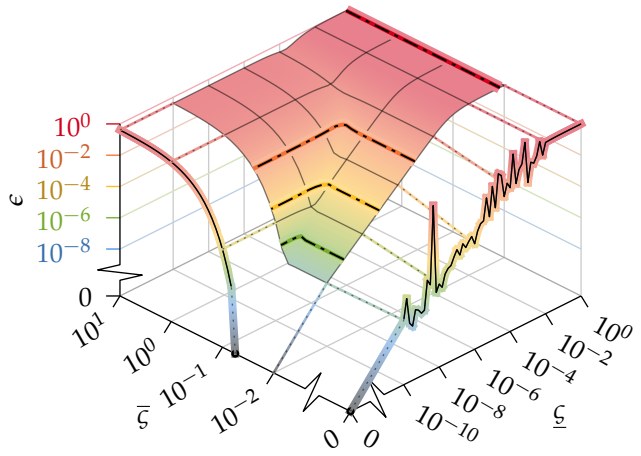

(a) Relative displacement error ϵ of NR analysis with $\lambda = 1$, calculated with respect to the result where $\underline{\varsigma} = 0$ and $\overline{\varsigma} = 0$. Furthermore, a refinement of $\times 10$ is used.

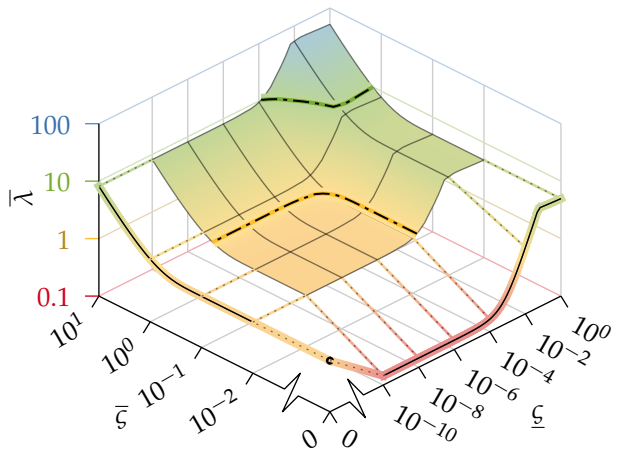

(b) Radius of convergence $\overline{\lambda}$ of P or B analysis, estimated with $n = 50$. Furthermore, a refinement of $\times 10$ is used.

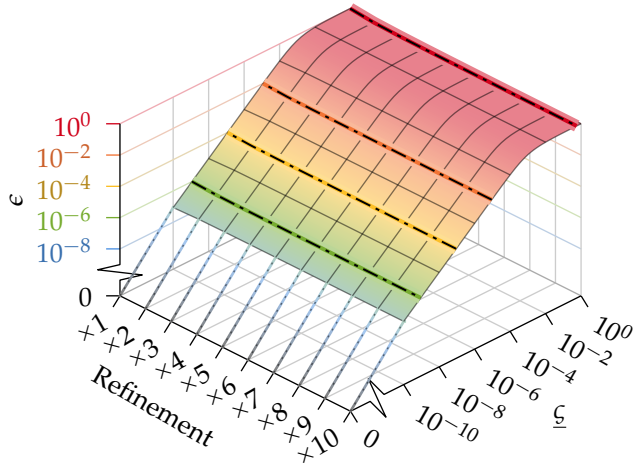

(c) Relative displacement error ϵ of NR analysis with $\lambda = 1$, calculated with respect to the result where $\underline{\varsigma} = 0$ for each refinement. Furthermore, $\overline{\varsigma}$ is set to 10^{-2}.

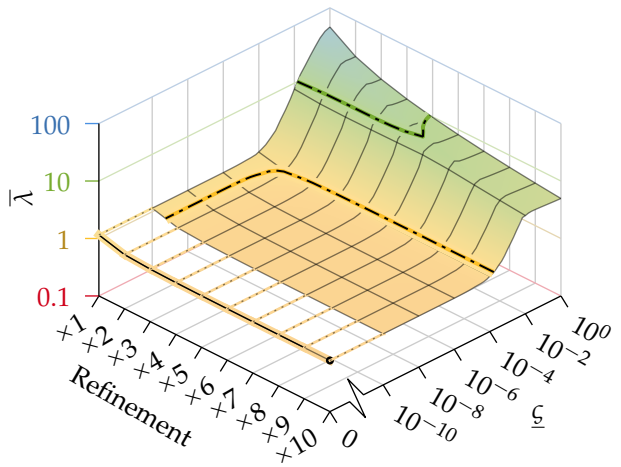

(d) Radius of convergence $\overline{\lambda}$ of P or B analysis, estimated with $n = 50$. Furthermore, $\overline{\varsigma}$ is set to 10^{-2}.

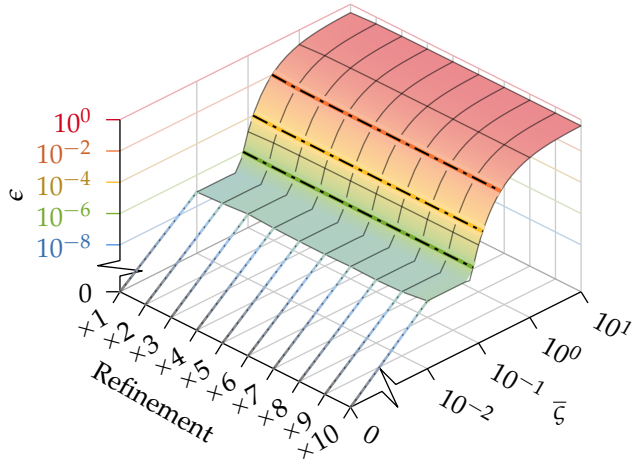

(e) Relative displacement error ϵ of NR analysis with $\lambda = 1$, calculated with respect to the result where $\overline{\varsigma} = 0$ for each refinement. Furthermore, $\underline{\varsigma}$ is set to 10^{-2}.

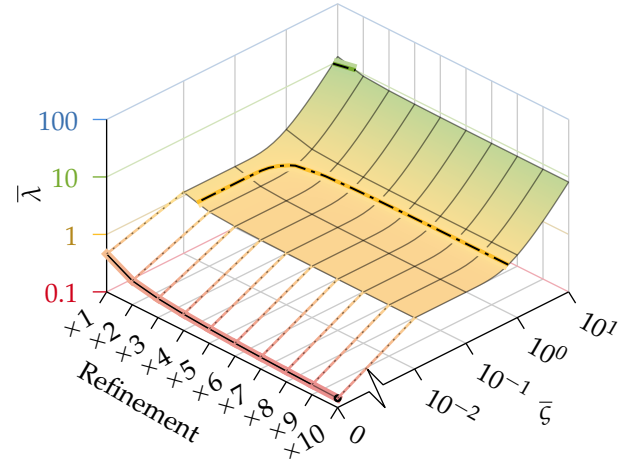

(f) Radius of convergence $\overline{\lambda}$ of P or B analysis, estimated with $n = 50$. Furthermore, $\overline{\varsigma}$ is set to 10^{-2}.

Figure IV.7: Relative normed displacement error ϵ (**left**) using NR analysis, and radius of convergence $\overline{\lambda}$ (**right**) using either P or B analysis, of the deformed C-Beam versus minimum void-density $\underline{\varsigma}$, EMDS threshold $\overline{\varsigma}$ and mesh refinements. Here, a filter-radius $\overline{\Delta} = 1\,\mathrm{m}$ is used. Furthermore, voids and EMDS are respectively removed for $\underline{\varsigma} = 0$ and $\overline{\varsigma} = 0$.

adopted regularizations seem mesh-independent beyond a minimal degree of coarseness.

IV.4 Computational Effort

Finally, this fourth CBeam analysis case study attempts a crude comparison of computational effort versus structural iteration count n and system size N, establishing the extent to which the trends sketched in Figure II.7 are followed. As mentioned at the top of this section IV, computational effort is naively measured through time, assuming it scales proportionally to the number of floating-point-operations, disregarding the wide range of unknown or uncontrollable factors. Due to the suboptimal or conceptual stage of the proposed perturbed analysis, and otherwise computationally suboptimal implementations, it is advised not to take the result from this case study at face value.

In order to obtain a meaningful quantification of computational time versus n and N, the simplified model in Equation IV.2 is argued for both NR and P. For most algorithms, computational time, complexity, or floating-point-operation count tends to follow a power law versus the system's scale, with the exponent roughly matching the depth level of nested loops. When applying Gaussian elimination to dense linear systems, the computational solve or decomposition time t expectedly requires some $\mathcal{O}(N^3)$ seconds, meaning $t \approx T \cdot N^3$ (Trefethen & Bau, 2022). The exponent is typically reduced through sparsity, preconditioning, prior decomposition, and particular iterative solution strategies alternative to Gaussian elimination (Trefethen & Bau, 2022). Considering the approximate NR analysis solve time $\tilde{t}_{\mathrm{NR}}$, each of the n iterations should take an equal amount of time $T^{(1)}_{\mathrm{NR}}$. The latter is typically dominated by the sparse structural solve, and less so by assembling the RHS (Right-Hand-Side) vector or residual force and tangent stiffness matrix (Aage & Lazarov, 2013). Considering P analysis time $\tilde{t}_{\mathrm{P}}$, however, a zeroth-, first-, and second-order component versus n can be argued respectively due to the initial Cholesky decomposition $T^{(0)}_{\mathrm{P}}$, a much cheaper structural solve $T^{(1)}_{\mathrm{P}}$ compared to NR, and the RHS construction $T^{(2)}_{\mathrm{P}}$ involving a nested sum versus order n. These components and their interpretation are summarised in Table IV.4.

The resulting computational time trends based on the model in Equation IV.2 are captured in Figure IV.8. Without going into too much detail on this crude case study, 13 C-beam refinements and 20 samples per refinement, each with a randomized load vector, have been performed in random order. First, polynomial regressions of time versus n were calculated for each N, followed by a linear regression of logarithmic time versus logarithmic N, obtaining $T^{(1)}_{\mathrm{NR}}$, $T^{(0)}_{\mathrm{P}}$, $T^{(1)}_{\mathrm{P}}$ and $T^{(2)}_{\mathrm{P}}$.

$$\begin{aligned} \tilde{t}_{\mathrm{NR}} &= T^{(1)}_{\mathrm{NR}} \cdot n \,, \\ \tilde{t}_{\mathrm{P}} &= T^{(0)}_{\mathrm{P}} + T^{(1)}_{\mathrm{P}} \cdot n + T^{(2)}_{\mathrm{P}} \cdot n^2 \,, \\ &\text{where} \quad T^{(k)} = \underline{T}^{(k)} \cdot N^{\overline{T}^{(k)}} \,, \end{aligned} \tag{IV.2}$$

Symbol	Unit	Interpretation
$T^{(1)}_{\mathrm{NR}}$	time / iteration	NR solve + RHS
$T^{(0)}_{\mathrm{P}}$	time	Cholesky
$T^{(1)}_{\mathrm{P}}$	time / iteration	P solve
$T^{(2)}_{\mathrm{P}}$	time / iteration^2	P RHS

Table IV.4: Interpretation of the coefficients estimating computational time for NR and P analysis, assuming a polynomial form versus the number of iterations n.

Considering the Newton-Raphson solve time $T^{(1)}_{\mathrm{NR}}$, Figure IV.8 suggests an unexpected trend. Moreover, as indicated by the slope of its regression, its order of growth versus N appears much closer to one than three, or even the expected value slightly above 2 for sparse systems (Trefethen & Bau, 2022). It must be noted, however, that Matlab chooses suitable algorithms under the hood, depending on the size and structure of the system matrix. Otherwise, this linear complexity can be attributed to other unknown overhead processes. The Cholesky solve time $T^{(0)}_{\mathrm{P}}$ shows a slightly more realistic yet unexpectedly low order of complexity. Fortunately, $T^{(0)}_{\mathrm{P}}$, and the resulting perturbed analysis solve time per iteration $T^{(1)}_{\mathrm{P}}$ respectively take three and ten times as little effort compared to $T^{(1)}_{\mathrm{NR}}$. This should give P analysis the expected head-start compared to NR analysis in terms of accuracy versus iteration count n, before NR and its quadratic convergence starts to increasingly dominate P analysis, ultimately bounded by linear convergence. Lastly, the RHS construction within P analysis, $T^{(2)}_{\mathrm{P}}$, does appear large enough not to be disregarded. With $T^{(0)}_{\mathrm{P}}$, $T^{(1)}_{\mathrm{P}}$ and $T^{(2)}_{\mathrm{P}}$ each separated a decade for nearly all N, it can be estimated that the growth of $\tilde{t}_{\mathrm{P}}$ becomes noticeably superlinear beyond $n = 10$, using the same theory that estimates the radius of convergence $\overline{\lambda}$ based on the geometric progression of $\boldsymbol{u}^{(1)}, \ldots, \boldsymbol{u}^{(n)}$.

While the regressed computational time models for NR and P analysis are currently based on N and n, a practically meaningful comparison can be made versus N and some identical error tolerance $\overline{\epsilon}$. Then again, this would introduce dependence on the extent of nonlinearity through $\lambda/\overline{\lambda} \equiv \epsilon_{\mathrm{L}}$. Interestingly, the latter can be factored out when considering a number of Newton-Raphson iterations n_{NR} and perturbed analysis order n_{P} separately, such that the corresponding estimated

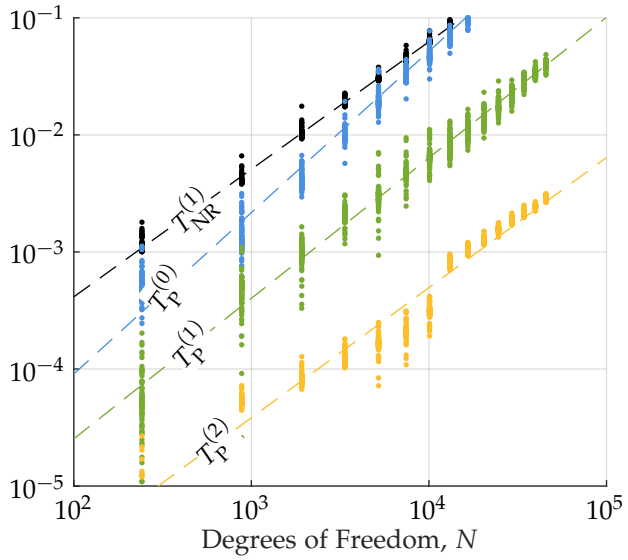

Figure IV.8: Logarithmic Regression of the polynomial coefficients of structural analysis time estimators $\tilde{t}_{NR}$ and $\tilde{t}_{P}$, as defined in Equation IV.2 and Table IV.4.

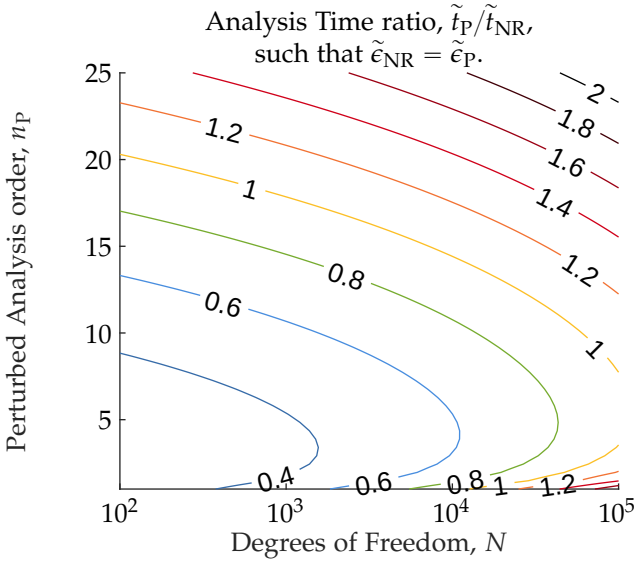

Figure IV.9: Analysis time ratio estimate, with Perturbed (P) analysis time $\tilde{t}_P$ over Newton-Raphson (NR) analysis time $\tilde{t}_P$ for several refinements thus degrees of freedom N, and Perturbed analysis orders n_P. The amount of Newton-Raphson iterations n_{NR} is chosen such that both the NR and P error estimates are equal, meaning $\tilde{\epsilon}_{NR} = \tilde{\epsilon}_P$.

errors[46] are the same. Setting the NR error estimator $\tilde{\epsilon}_{NR} = \epsilon_L^{2^{n_{NR}}-1}$ equal to the P error estimator $\tilde{\epsilon}_P = \epsilon_L^{n_P}$, yields $n_{NR} = \log_2(n_P + 1)$. The corresponding time ratio is graphed in Figure IV.9.

Over a moderate range versus degrees of freedom N and perturbed analysis orders n_P, Figure IV.9 suggests that P analysis can be more than twice as efficient as NR analysis given the same error tolerance. Yet, both Figure IV.9 and IV.8 imply diminished relative efficiency versus N, contrary to the increased relative efficiency predicted in Subsection II.3. To clarify, the required computational effort of structural solves without Cholesky decomposition should typically grow faster versus N, rather than slower. Certainly, the Cholesky factorization proves useful by reducing the structural solve time over tenfold, comparing $T_P^{(1)}$ to $T_{NR}^{(1)}$, even if this reduction is not growing but mildly shrinking versus N. Overall, the respective growths of $T_P^{(1)}$ and $T_{NR}^{(1)}$ versus N, seems inaccurately reflected in the case study presented here. Particularly, the nearly linear growth of $T_{NR}^{(1)}$ versus N contradicts established literature, predicting orders slightly beyond two (Trefethen & Bau, 2022) for sparse systems. The discrepancy may be caused by a wide range of unknowns within the custom Matlab implementation, such as an insufficiently large range of N, and the lack of control or knowledge over hidden parameters and other sources of computational overhead. The apparent discontinuity of the data behind the trends in Figure IV.8 further testifies to this.

[46] Recall that the error estimators for NR and P analysis are derived in Appendix B.

V Compliance Minimization

This part II of the results resumes the validation of the proposed and state-of-the-art non-linear structural analysis methods, now integrated into density-based, load-controlled topology optimization. The present section covers the well-known compliance minimization, studied in (Buhl et al., 2000a; Pedersen et al., 2001; Chen et al., 2019b). First, the structural and optimization problems are formally defined in Subsection V.1, including a list of relevant case parameters. Then, the effects and limitations of non-linearity on the various analysis methods are explored through the results within Subsection V.2. Lastly, a more thorough comparative study of attainable design performance and optimization robustness is presented in Subsection V.3, sweeping over a wide and dense range of case parameters, and indicating some ideal regularization parameter values. Similarly to the results in part I, notable observations are briefly discussed throughout the results presented here, in preparation for the general discussion in Section VII.

V.1 Problem Formulation

The compliance minimization problem studied within this section is formally defined here, imposing a volume and error constraint. Figure V.1 illustrates the design domain's geometry, material, and applied bound-

ary conditions. The negative null form of the optimization problem is then defined for Newton-Raphson (NR) analysis in Equation V.1, and Bayesian (B) analysis in Equation V.2. Details such as the bounds on $\boldsymbol{x}$, the higher-order residual-, or adjoint equations and explicit functional depencence on λ are omitted here, as they would obscure more relevant aspects and are already covered within Subsection III.5 through Equation III.36. The volume-constrained, NR-based compliance minimization is formulated as:

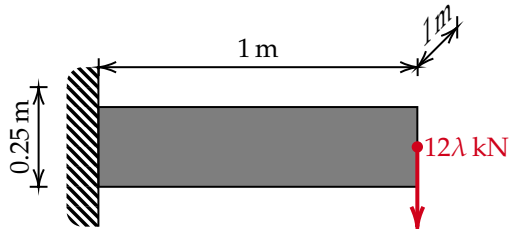

Figure V.1: Geometry, material, and boundary conditions of the compliance minimization problem, as studied within this section and defined in Equation V.1 and V.2. An isotropic, linear elastic material is assumed, with Young's Modulus $E = 3\,\text{GPa}$ and Poison's ratio $\nu = 0.4$ under plane-strain condition, in accordance with Buhl et al. (2000a).

$$\text{(NR)} \qquad \underset{\boldsymbol{x}}{\text{minimize}} \quad \lambda \boldsymbol{p} \bullet \boldsymbol{u}_{\boldsymbol{x}} \,, \qquad \text{(V.1)}$$
$$\text{subject to} \quad V_{\boldsymbol{x}} \leqslant \eta \overline{V} \,,$$

where $\boldsymbol{u}_{\boldsymbol{x}}$ denotes the deformation given some design $\boldsymbol{x}$ and applied load $\lambda \boldsymbol{p}$ using NR analysis. Then, a maximum volume-fraction η is imposed, with $\overline{V}$ the design-domain's volume (see Figure V.1) and $V_{\boldsymbol{x}}$ the structure's volume, defined here as $\sum_{e=1}^{M} \rho_e / M$. The additionally error-constrained B-based compliance minimization is then formulated as:

$$\text{(B)} \qquad \underset{\boldsymbol{x}}{\text{minimize}} \quad \lambda \boldsymbol{p} \bullet \tilde{\tilde{\boldsymbol{u}}}_{\boldsymbol{x}} \,, \qquad \text{(V.2)}$$
$$\text{subject to} \quad V_{\boldsymbol{x}} \leqslant \eta \overline{V} \,,$$
$$\tilde{\tilde{\epsilon}}_{\boldsymbol{x}} \leqslant \overline{\epsilon} \,,$$

where $\tilde{\tilde{\boldsymbol{u}}}_{\boldsymbol{x}}$ denotes the deformation given some design $\boldsymbol{x}$ and applied load $\lambda \boldsymbol{p}$ using B analysis, and $\tilde{\tilde{\epsilon}}_{\boldsymbol{x}}$ the corresponding normed, relative error-estimate, constrained at or below the tolerance $\overline{\epsilon}$.

Over the remaining subsection, a series of case studies sweeps over the case parameters specified in Table V.1. In particular, the effects and limitations of non-linearity on the error, robustness, and attainable structural performance are investigated through λ, n, and $\overline{\epsilon}$. Regularization parameters such as void density $\underline{\varsigma} = 10^{-9}$ and EMDS threshold $\overline{\varsigma} = 0.01$ are readily argued as reasonably ideal or sufficient in Subsection IV.3. Notably, the optimized designs, required amount of iterations and resulting trends were deemed too sensitive to some design convergence criterion, impacting the clarity of those results and trends. Hence, for all methods, loads, and analysis orders, a fixed number of 200 design iterations is performed here.

Case parameter	Value (range)
Load variable λ	$\{1,\ 5,\ 12,\ 20\}$
(B) *Analysis order* n	$\{1,\ 5,\ 20\}$
Error tolerance $\overline{\epsilon}$	10^{-3}
Material penalization θ	1 ++0.05, up to 3
Void density $\underline{\varsigma}$	10^{-9}
EMDS threshold $\overline{\varsigma}$	0.01
Density filter radius $\overline{\Delta}$	1.5 elements
Refinement	20 by 80 elements
Optimization iterations	200
Volume fraction η	0.5

Table V.1: List of compliance minimization case parameters and their value (range) studied in this subsection. Here, ++ denotes the increment per design iteration.

V.2 Non-linearity and Error

The goal of this first compliance minimization case study is to demonstrate the implications and limitations of non-linearity, through increased loads λ and analysis orders n. This is done by comparing the optimized designs, their compliances, and errors, based on Newton-Raphson (NR) and Bayesian-enhanced Perturbed (B) analysis. The specific case parameter specifications and sweeps are listed in Table V.1. The corresponding results are summarized in Figure V.2, showing their deformed state, indicating their error and optimality. In this case study, all optimizations based on higher-order perturbed analysis are governed by constraining their error-estimate $\tilde{\tilde{\epsilon}}$ below a tolerance $\overline{\epsilon} = 10^{-3}$, whose importance and effects shall be demonstrated in the second and third case studies. For all results, their true errors ϵ, and true compliance C in kJ, are evaluated at the last design iteration based on a referential Newton-Raphson analysis up to a normed relative residual of 10^{-10}.

Some observations regarding non-linearity can be made in preparation for the general discussion in Section VII. For all loads $\lambda = 5$, 12 and 20, the obtained Newton-Raphson-based optimization results presented in Figure V.2 are very similar to those of Buhl et al. (2000a, Table 1) in terms of their final design and compliance. Moreover, the small load for $\lambda = 1$ yields a practically identical result when based on Newton-Raphson (NR), Bayesian analysis ($n > 1$), each with an end-compliance $C = 0.19\,\text{kJ}$, and identical

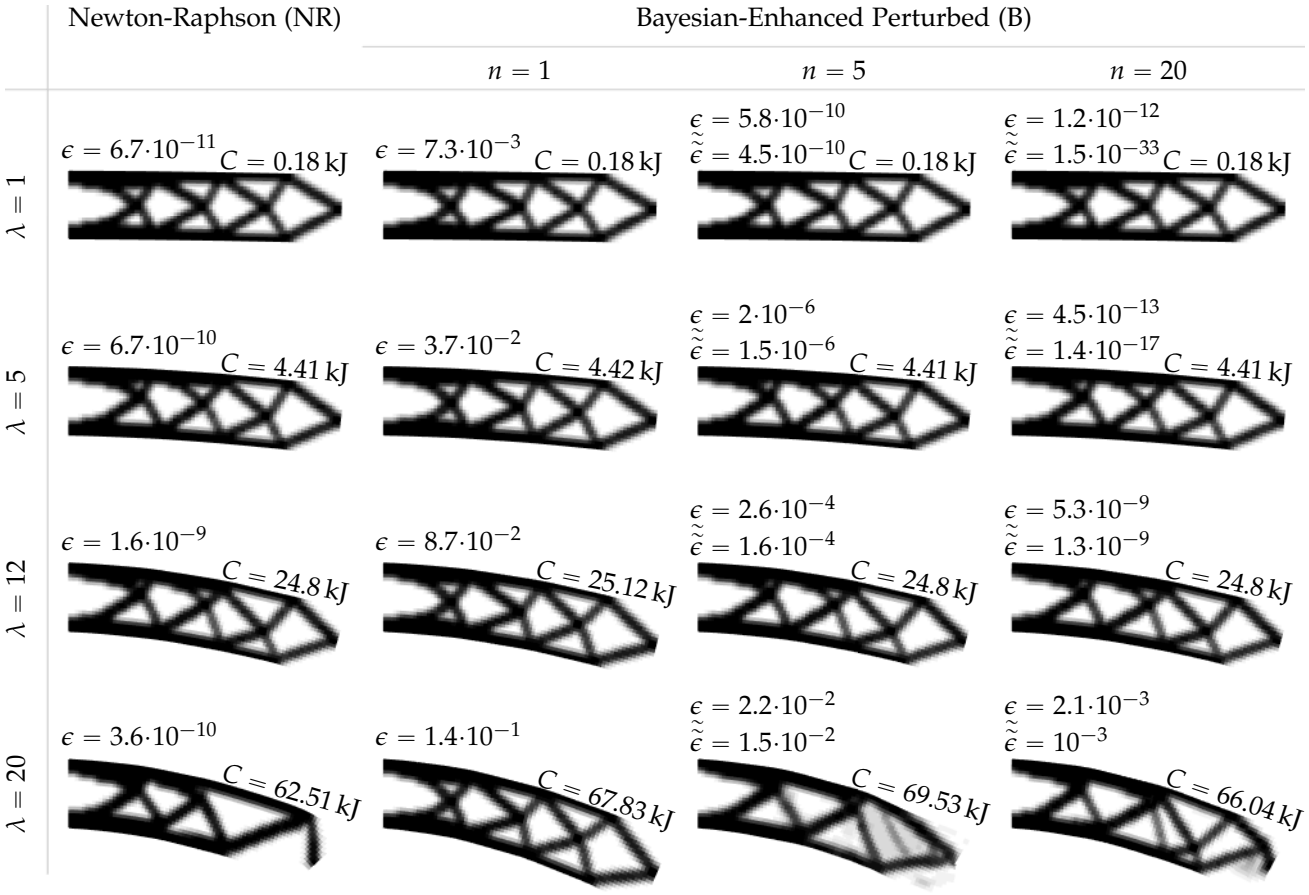

Figure V.2: Resulting compliance minimization designs, optimized through Newton-Raphson (NR) and Bayesian-enhanced perturbed (B) structural analysis, ranging over several loads λ and analysis orders n, after 200 iterations, subject to a tolerance $\overline{\epsilon} = 10^{-3}$ on the relative normed displacement error estimates for NR, and B with $n > 1$. Recall that $n = 1$ effectively represents linear analysis. Other applied regularization steps, geometry and material are stated at the beginning of this section. Here, ϵ and $\tilde{\epsilon}$ respectively denote the true and estimated errors, and C the true compliance as measured through the referential NR analysis up to a relative normed residual of 10^{-10}. All presented deformations are based on the same referential NR analysis.

to the corresponding result of Buhl et al. (2000a, Table 1). As the load approaches zero, the actual structural problem practically becomes linear, and the boundary conditions purely (anti-) symmetrical, explaining the symmetrical design. On the other hand, taking $n = 1$ assumes the structural problem to be linear about the load of zero. As a result, dependence on λ can be factored out of the energy or compliance equation, and the design that minimizes this energy minimizes any of its scalar multiples. Hence, linear analysis ($n = 1$) or small loads ($\lambda \to 0$) all yield the same compliance-minimizing design.

As a brief sidenote on performance, higher orders B analysis generally seems to result in lower compliance, as desired. For the mildly non-linear case where $\lambda = 12$ in Figure V.2, the much cheaper optimization based on 5^{th} order B analysis achieves the same design and performance compared to the much more expensive NR based design. For the nearly critical load case where $\lambda = 20$, however, the designs for $n = 5$ and 20 have not entirely converged. Regardless, for $n = 20$ a compliance of 66.04 kJ has been achieved, lying below the 66.52 kJ obtained by Buhl et al. (2000a). This may be due to slight implementation differences, and the presented NR design for $\lambda = 20$ in Figure V.2 provides a more trustworthy reference. Interestingly, it more closely matches the design obtained by (Buhl et al., 2000a) for $\lambda = 12$.

Higher loads seem to result in designs close to their buckling limit, or otherwise increase the extent of non-linearity. In a load-controlled analysis versus λ, the buckling limit forms a hard upper bound on the radius of convergence $\overline{\lambda}$ for P and B, associated with an infinite slope of displacement versus λ. Hence, P and B are unable to capture (post-) buckling behavior, as their higher-order prediction error increases (super) linearly beyond this point. However, NR has the ability to converge beyond a load limit. As a result, even when this occurs subtly, in void regions, or intermediate designs, NR-based optimizations can possibly reach

feasible designs that are unreachable to P- or B-based optimizations. This may explain why the latter were unable to produce the unsupported slender filament connecting the loaded tip to the rest of the structure, and consistently so for a wide range of other tried case parameters that are not explicitly documented here.

In nearly all cases, the estimated and true errors seem to agree within an order of magnitude or even closer. Of course, when errors smaller than 10^{-10} are predicted, the true error based on the referential Newton-Raphson analysis is going to be dominated either by its tolerance of 10^{-10}, or by that of the structural tensors decomposed up to the same error tolerance. For small to moderate loads, in this case when $\lambda \leqslant 12$, the order of the Bayesian error estimate $\tilde{\tilde{\epsilon}}$ also appears proportionate to n, as predicted by Equation III.23. However, the highest load $\lambda = 20$ seems close to some critical value for the Bayesian-based structural optimization. Judging from the results given $n = 5$ and $n = 20$, the optimization appears actively constrained or guided such that the error estimate $\tilde{\tilde{\epsilon}}$ remains bounded by $\bar{\epsilon} = 10^{-3}$. Not only is the true error ϵ still close to its desired tolerance, but the Method of Moving Asymptotes (MMA) seems capable of handling the constraint on $\tilde{\tilde{\epsilon}}$.

V.3 Design Performance and Robustness

In the end, the previously studied analysis error is a crucial, yet indirect measure for the arguably much more important optimization robustness, and attainable objective values, unbiased through approximation or perturbation error. Hence, in this second study case, a more exhaustive parameter sweep is performed as listed in Table V.2, mainly concerning the analysis order n, load variable λ and error tolerance $\bar{\epsilon}$, with half the previous mesh refinement to manage computational times. The aim is to study the conditions for, and ultimate extent of, design convergence, by measuring compliance and error. To get a more detailed understanding of the error constraint and its role during perturbed analysis, the true and estimated error and compliance are graphed versus the design iteration number in Figure V.3, considering two different error tolerances. Then, sweeping over all mentioned case parameters, Newton-Raphson (NR), Perturbed (P), and Bayesian-enhanced (B) analysis are compared in terms of final error and compliance through Figure V.4, as determined through a referential NR analysis up to a normed relative residual tolerance of 10^{-10}.

From the optimization iteration profiles in Figure V.3, the role and effect of the imposed error constraint and gradual material penalization can be seen. Over the first five iterations, the optimizer is able to quickly reduce compliance, most likely exploiting the initially unpenalized intermediate densities. Soon after, until the 40$^{\text{th}}$ iteration, the penalty exponent θ increments from 1 to 3, visibly penalizing compliance but also challenging the optimizer in maintaining an error $\tilde{\tilde{\epsilon}}$ below the imposed tolerance $\bar{\epsilon}$. Most likely, the penalization enforces a black-and-white solution, featuring slender filaments more prone to buckling and hence a decreased radius of convergence $\bar{\lambda}$. After a more moderate initial breach of the error constraint, the optimizer stabilizes and maintains a slighter breach. While in both cases the true error ϵ is safely overestimated by $\tilde{\tilde{\epsilon}}$ throughout the optimization, this does not occur in general and depends mostly on the estimator's qualities. More notably, the true relative compliance c does appear consistently underestimated by $\tilde{\tilde{c}}$, supplied to the optimizer, arguably exploiting error. To clarify, despite the barely visible difference between both resulting designs, a greater error tolerance $\bar{\varepsilon}$ appears to result in a lower estimated compliance $\tilde{\tilde{c}}$, at greater expense of the true objective, yielding larger c. This trend is more rigorously demonstrated in Figure V.4.

Case parameter	Value (range)
Load variable λ	$[1,\ 24]$
(P, B) *Analysis order* n	$\{1,\ 2,\ \ldots,\ 30\}$
Error tolerance $\bar{\epsilon}$	$\{1,\ 0.1,\ 0.01,\ 10^{-3}\}$
Material penalization θ	1 ++0.05, up to 3
Void density $\underline{\varsigma}$	10^{-9}
EMDS threshold $\overline{\underline{\varsigma}}$	0.01
Density filter radius $\overline{\Delta}$	1.25 elements
Refinement	10 by 40 elements
Optimization iterations	100
Volume fraction η	0.5

Table V.2: List of compliance minimization case parameters and their value (range) studied for the performance and robustness quantification. Here, ++ denotes the increment per design iteration.

Comparing P and B analysis, Figure V.4 suggests the latter is generally superior, up to the high initiation sensitivity and other subtle chaotic components inherent to large-scale non-convex optimization. The compliance minimization using B analysis is able to stay below the imposed error more frequently, which becomes especially apparent for higher loads λ and smaller tolerances $\bar{\epsilon}$ restricting the feasible design domain. When the optimization does converge for both P and B given the same parameters, the compliance difference is more subtle but still generally lower for the latter. Overall, B analysis appears more robust towards non-linearity than pure MacLaurin-based P analysis within topology optimization, yielding better designs more frequently.

Comparing both P and B to NR analysis, the latter appears more capable when faced with non-linearity or high λ, considering a reasonably low tolerance $\bar{\epsilon}$. In this case, the design domain is not constrained through

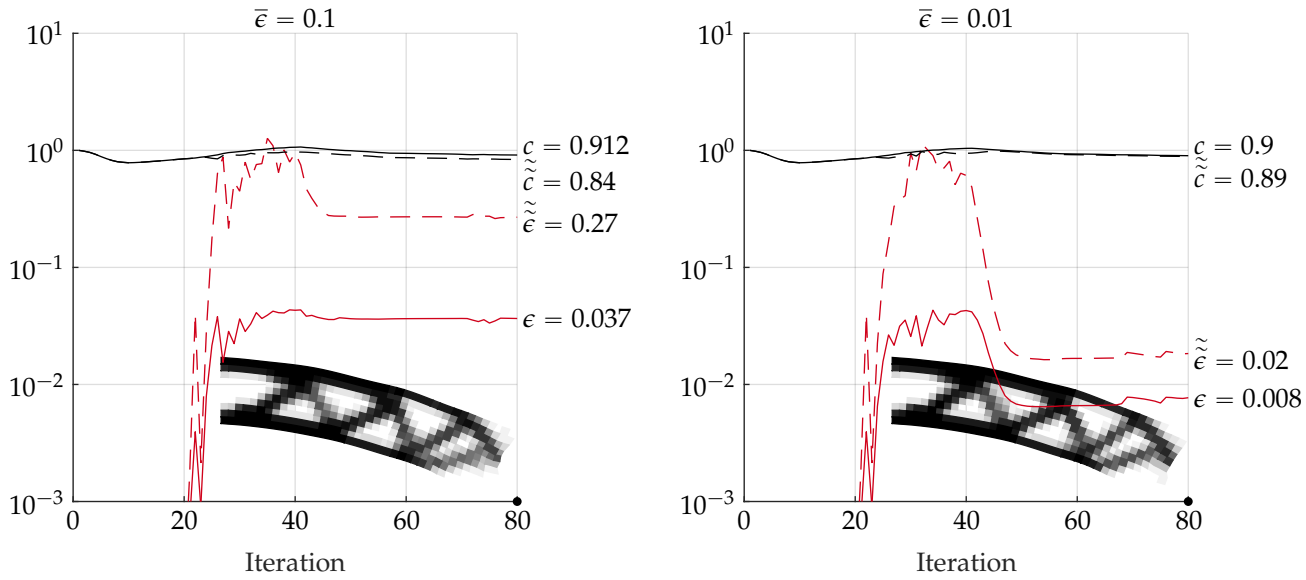

Figure V.3: Response iteration profiles of two compliance minimization cases, including deformed design at the final iteration, optimized through Bayesian-enhanced perturbed analysis subject to different error tolerances $\bar{\epsilon}$. Furthermore, ϵ and $\tilde{\tilde{\epsilon}}$ denote the true and estimated error. Likewise, c and $\tilde{\tilde{c}}$ denote the true and estimated compliance, relative to the true compliance at the first iteration.

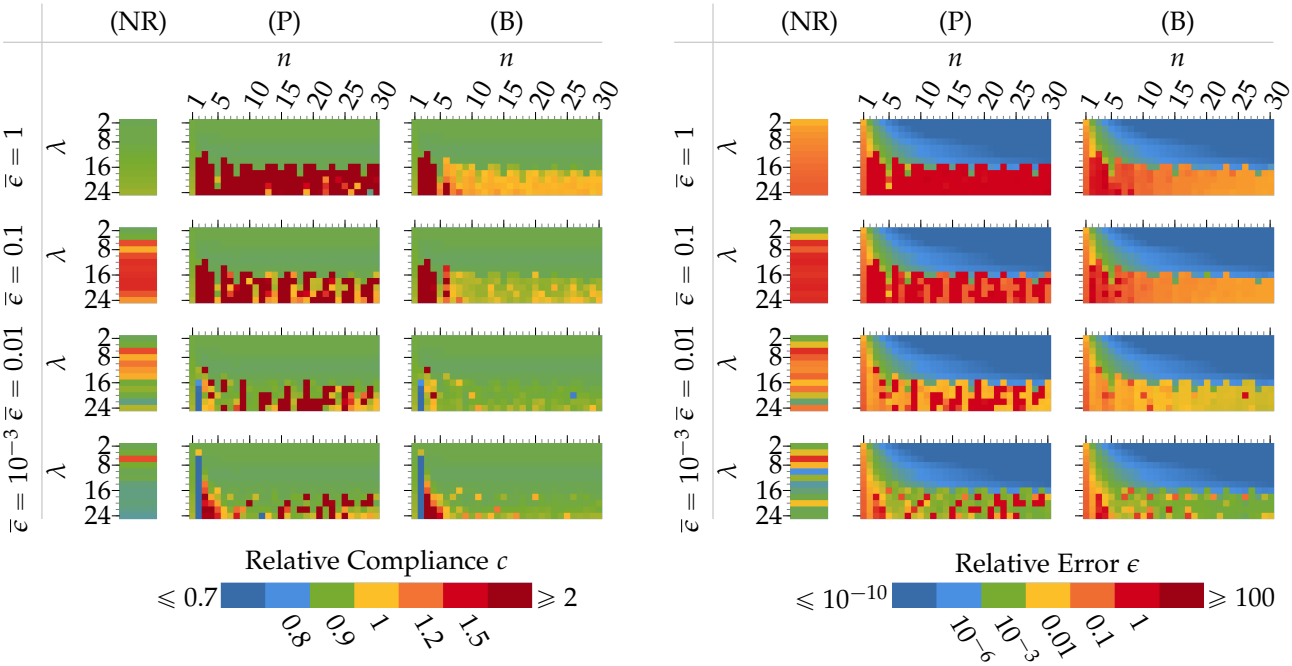

(a) Relative compliance c, denoting the compliance at the final design iteration with respect to the first, both of which are evaluated using a referential NR analysis.

(b) Relative error ϵ, evaluated using a referential NR analysis.

Figure V.4: Resulting true compliances and errors, after optimization through Newton-Raphson (NR), MacLaurin-based perturbed (P), and Bayesian-enhanced perturbed (B) structural analysis, over a dense range of load variables λ, analysis orders n, and several error tolerances $\bar{\epsilon}$, after 100 iterations. Recall that this tolerance only applies to P and B for $n > 1$, both of which reduce to linear analysis for $n = 1$.

an error estimate, allowing designs that feature greater non-linearity. This is ultimately facilitated by the ability of NR analysis to converge for greater λ than B and P analysis.

Considering the imposed error tolerance $\overline{\epsilon}$, values much greater than 0.01 seem to affect its utility and the robustness of the structural optimization. The excessive tolerance of $\overline{\epsilon} = 1$ allows NR to terminate after a single iteration, rendering it equivalent to linear analysis, and also B and P for all other tolerances given $n = 1$. Interestingly, this promotes robustness by preventing divergence, ironically yielding superior designs compared to a slightly lower tolerance and related issues that can only be remedied by even lower tolerances. However, when the optimizer is limited by linear analysis, the true extent of non-linearity, error, feasibility, or optimality cannot be estimated cheaply as done in higher-order P or B analysis. Overall, error estimation becomes less accurate, meaningful, and useful for larger values of $\overline{\epsilon}$, and impossible when only a single structural iteration is performed, meaning non-linearity is poorly accounted for in either case.

Somewhat ironically, reducing the error tolerance $\overline{\epsilon}$ does not always necessarily result in superior design performance, at least given fixed perturbed analysis order n. This is indirectly demonstrated within Figure V.2 for the higher loads λ, where increasingly higher orders of perturbed analysis result in compliance close to the one obtained through NR. An activate error constraint effectively imposes a minimum radius of convergence $\overline{\lambda}$, that necessarily grows for smaller n and smaller $\overline{\epsilon}$. To clarify using the MacLaurin-based perturbed analysis error estimate:

$$\epsilon = \left(\frac{\lambda}{\overline{\lambda}}\right)^n \leqslant \overline{\epsilon}, \quad \Longleftrightarrow \quad \overline{\lambda} \geqslant \lambda \overline{\epsilon}^{-\frac{1}{n}} \,. \tag{V.3}$$

Moreover, the feasible design space that can accommodate larger $\overline{\lambda}$ shrinks, potentially excluding designs of superior performance. This effect may dominate the otherwise increased attainable performance through the increased accuracy by which the optimizer perceives design performance. In order not to compromise the feasible design space by constraining error, thus effectively $\overline{\lambda}$, the P analysis order n must change with the imposed error tolerance ϵ as:

$$\frac{n_2}{n_1} = \frac{\log \overline{\epsilon}_2}{\log \overline{\epsilon}_1} \,, \tag{V.4}$$

as derived from Equation V.3. A similar reasoning but slightly more complex derivation applies to B analysis.

Additional computational efficiency may be achieved by conditionally terminating perturbed analysis when the error constraint is satisfied, or limiting the order regardless. In fact, conditional termination is a very common, straightforward, and presently adopted approach using NR analysis. However, as the convergence of P or B analysis is not guaranteed versus the number of structural solves, hence analysis order n, convergence is controlled instead through the design by constraining its error estimate. Nevertheless, given low non-linearity or small λ, Figure V.4b indicates that computational effort is wasted when the error constraint is inactive, reducing the error far below the imposed tolerance. On the other hand, the first five to ten solves appear to yield the highest returns of accuracy and design performance, especially with respect to the initial computational cost of Cholesky factorization, and super-linearly increasing cost per future solve. Arguably, perturbed analysis suits its purpose best when the error constraint is active anyway, requiring the maximum number of solves to exploit the maximum extent of structural non-linearity. The presently studied compliance minimization is an exceptional case where deformation, and perhaps non-linearity as an indirect consequence, are minimized.

VI Force Inverter and Micro Gripper

Finally, part II of the results is concluded by validating the proposed and state-of-the-art non-linear structural analysis methods, applied to more practical topology optimization problems that much rather tend to exploit, than minimize structural non-linearity. This is to conduct a more nuanced discussion on the balance between, and effect of, non-linearity, analysis order, and imposed error tolerance. To this end, a classical force-inverter and micro gripper are optimized here, inspired by the works of Buhl et al. (2000a). Pedersen et al. (2001) and Eschenauer & Olhoff (2001). Similarly to the previous section, the structural and optimization problems are formally defined in Subsection VI.1. Then, Subsection VI.2 follows with a range of resulting designs, deformations, analysis errors, and design performances.

VI.1 Problem Formulations

The force inverter and micro gripper design optimizations studied within this section are formally defined here. Figure VI.1 illustrates their design domain's geometry, material, and applied boundary conditions, which are notably similar. Black and white regions are maintained respectively solid and void throughout the design optimization. Moreover, their optimization problem definitions are identical, as formulated in Equation VI.1 for Newton-Raphson (NR) analysis, and Equation VI.2 for Bayesian (B) analysis. The NR formulation reads:

$$\text{(NR)} \qquad \underset{\boldsymbol{x}}{\text{minimize}} \quad (\boldsymbol{u}_x)_\text{o} \,, \qquad \text{(VI.1)}$$

$$\text{subject to} \quad (\boldsymbol{u}_x)_\text{i} \leqslant \overline{u} \,,$$
$$V_x \leqslant \eta \overline{V} \,,$$

where $\boldsymbol{u}_x$ denotes the deformation given some design $\boldsymbol{x}$ and applied load variable λ using NR analysis, and $(\boldsymbol{u}_x)_\text{o} \equiv u_\text{o}$ the output displacement. This time, the input displacement $(\boldsymbol{u}_x)_\text{i} \equiv u_\text{i}$ is also constrained. The error-constrained B formulation then reads:

$$\text{(B)} \qquad \underset{\boldsymbol{x}}{\text{minimize}} \quad (\tilde{\tilde{\boldsymbol{u}}}_x)_\text{o} \,, \qquad \text{(VI.2)}$$

$$\text{subject to} \quad (\tilde{\tilde{\boldsymbol{u}}}_x)_\text{i} \leqslant \overline{u} \,,$$
$$V_x \leqslant \eta \overline{V} \,,$$
$$\tilde{\tilde{\epsilon}}_x \leqslant \overline{\epsilon} \,,$$

where $(\tilde{\tilde{\boldsymbol{u}}}_x)_\text{i} \equiv \tilde{\tilde{u}}_\text{i}$ and $(\tilde{\tilde{\boldsymbol{u}}}_x)_\text{o} \equiv \tilde{\tilde{u}}_\text{o}$ respectively denote the input and output displacements using B analysis. Again, $\tilde{\tilde{\epsilon}}_x$ denotes corresponding normed, relative error-estimate, constrained at or below the tolerance $\overline{\epsilon}$.

The next subsection presents the results that are obtained through the parameter sweep specified in Table VI.1. Again, the effects and limitations of nonlinearity on the error, robustness, and attainable structural performance are investigated mostly through λ, while comparing NR to linear and 5$^{\text{th}}$-order B analysis. This time, a fixed error tolerance $\overline{\epsilon} = 10^{-3}$ is imposed. It is deemed a reasonably ideal value regarding optimization robustness and response accuracy based on the results and discussion within Section V.

Case parameter	Value (range)
Load variable λ	[1, 50]
(B) *Analysis order* n	{1, 5}
Error tolerance $\overline{\epsilon}$	10^{-3}
Material penalization θ	1 ++0.1, up to 3
Void density $\underline{\varsigma}$	10^{-9}
EMDS threshold $\overline{\varsigma}$	0.01
Density filter radius Δ	1.6 mm (1.72 elements)
Refinement	36 by 72 elements
Optimization iterations	200
Volume fraction η	0.2

Table VI.1: List of force inverter and micro gripper optimization case parameters, and their value (range) studied in this section. Here, ++ denotes the increment per design iteration.

As a side note, the original problem formulations within Pedersen et al. (2001) and Eschenauer & Olhoff (2001) are rescaled here to facilitate laser-cut, handheld prototypes for future testing and demonstrational purposes. Both optimization problems originally concern a 300 μm by 300 μm design domain of thickness 7 μm, assuming isotropic, linearly elastic silicon with $E = 180$ GPa and $\nu = \frac{1}{3}$ under plane-strain condition, $p = 1$ mN. Furthermore, for the inverter $\overline{u} = 2\,\mu$m and $\kappa = 200$ N/m, and for the gripper $\overline{u} = 5\mu$m and $\kappa = 1000$ N/m. Through dimensionless groups, these quantities, excluding ν, have been transformed into those presented in Figure VI.1, such that nearly identical relative displacement fields and designs are obtained, but on a handheld, rather than microscopical scale.

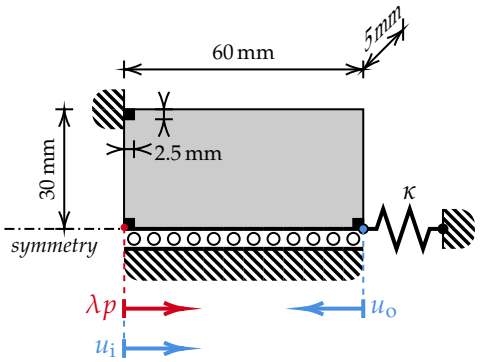

(a) Force inverter definition, scaled but similar to the one studied by (Pedersen et al., 2001) and Eschenauer & Olhoff (2001). Here, $p = 2.31$ N, $u_\text{i} \leqslant \overline{u} = \frac{1}{3}$ mm and $\kappa = 2.78$ kN/m.

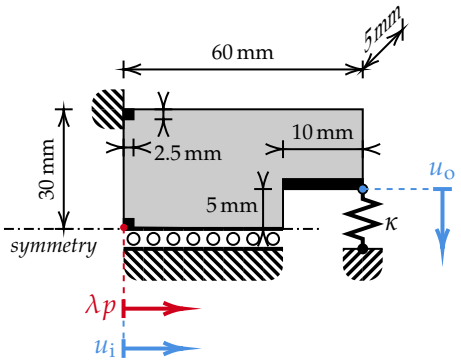

(b) Micro gripper definition, scaled but similar to the one studied by Pedersen et al. (2001) and Eschenauer & Olhoff (2001). Here, $p = 2.31$ N, $u_\text{i} \leqslant \overline{u} = \frac{5}{6}$ mm and $\kappa = 13.9$ kN/m.

Figure VI.1: Geometry, material, and boundary conditions of the force inverter (VI.1a) and micro gripper (VI.1b) problems, as studied within this section and defined in Equation VI.1 and VI.2. An isotropic, linear elastic material is assumed, with Young's Modulus $E = 3$ GPa and Poison's ratio $\nu = 0.4$ under plane-strain condition.

VI.2 Performance and Error

The optimized force inverters and micro grippers are visualized in their deformed state in Figure VI.2 and Figure VI.3, including their estimated and final error and output displacements. Apparently, all force inverter and micro gripper designs are very similar versus the analysis method and order n, but change

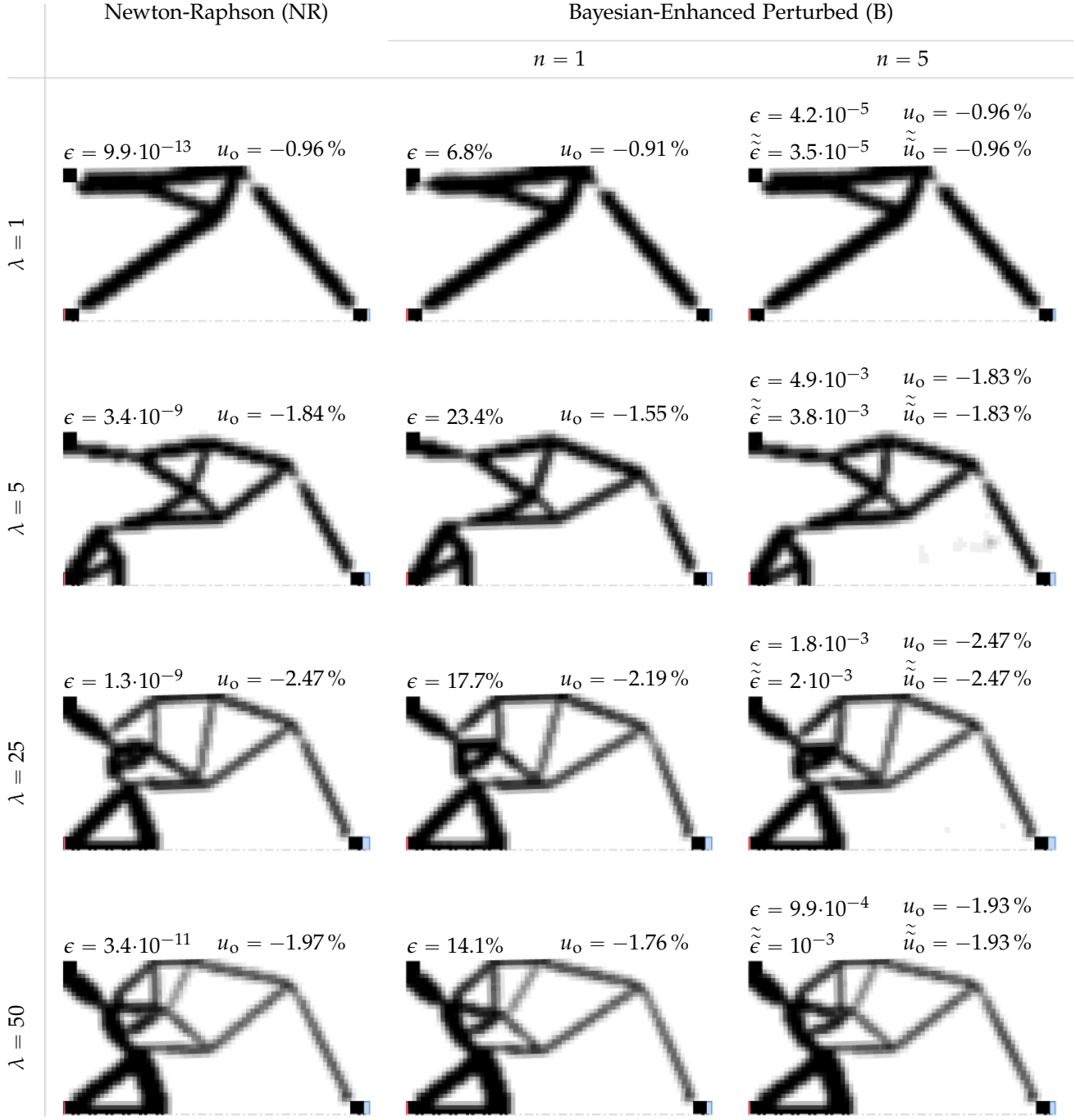

Figure VI.2: Resulting force inverter designs, optimized using Newton-Raphson (NR) and Bayesian-enhanced perturbed (B) structural analysis, ranging over several loads λ and analysis orders n, given 200 iterations and a target tolerance $\bar{\epsilon} = 10^{-3}$ on the relative normed displacement error estimates for NR, and B with $n > 1$. Other applied regularization steps, geometry and material are stated at the beginning of this section. Here, ϵ and $\tilde{\tilde{\epsilon}}$ respectively denote the true and estimated errors. Correspondingly, u_o and $\tilde{\tilde{u}}_o$ respectively denote the true and Bayesian-predicted tip displacements, relative to the design domain's width. All true values, and the presented deformations, are based on a referential NR analysis up to a relative normed residual of 10^{-10}.

more drastically versus the load λ. Nevertheless, nonlinearity remains arguably low, judging from the modest errors resulting from linear analysis $n = 1$, and the designs' similarity resulting from higher order B or non-linear NR analysis. The designs are mostly changing to accommodate the imposed maximum input displacement.

Despite the apparent linearity of all designs, nonlinearity is seemingly exploited in most cases, and efficiently so using B analysis. To clarify, for all loads λ greater than 1, the force inverter designs resulting from 5^{th}-order B analysis feature a relative displacement er-

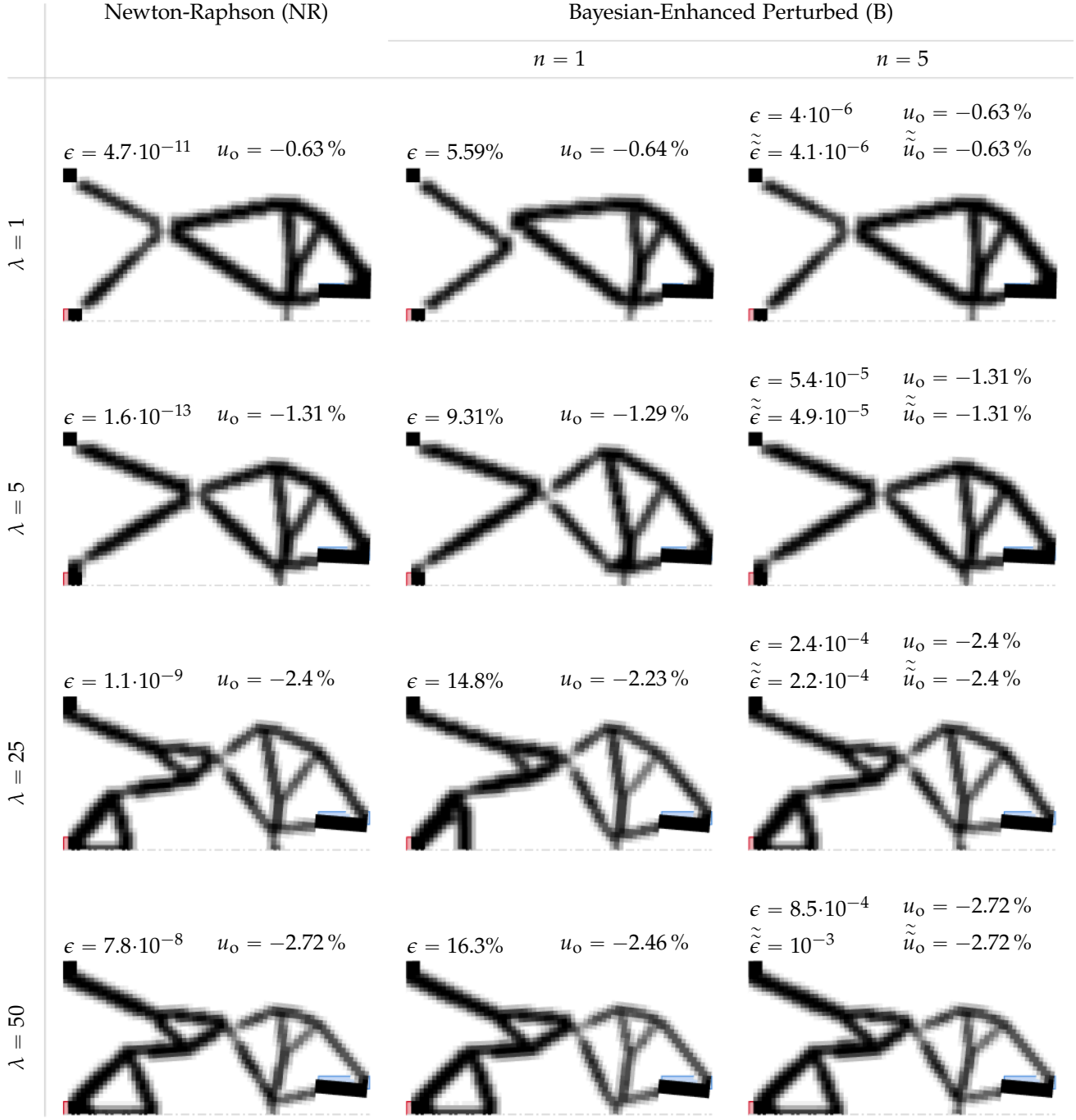

Figure VI.3: Resulting micro gripper designs, optimized using Newton-Raphson (NR) and Bayesian-enhanced perturbed (B) structural analysis, ranging over several loads λ and analysis orders n, given 200 iterations and a target tolerance $\overline{\epsilon} = 10^{-3}$ on the relative normed displacement error estimates for NR, and B with $n > 1$. Other applied regularization steps, geometry and material are stated at the beginning of this section. Here, ϵ and $\tilde{\tilde{\epsilon}}$ respectively denote the true and estimated errors, and C the true compliance as measured through the referential NR analysis up to a relative normed residual of 10^{-10}. All presented deformations are based on the same referential NR analysis.

ror $\tilde{\tilde{\epsilon}}$ very close to the imposed tolerance $\overline{\epsilon} = 10^{-3}$. The same applies to the micro gripper when the load λ approaches 50. The active error constraint suggests the optimizer prefers designs close to their limiting $\overline{\lambda}$. Comparing the designs resulting from both NR and 5$^{\text{th}}$-order B analysis to linear analysis, a nearly identical performance increase can be seen despite the subtle difference in topology. Strikingly, the design optimizations based on NR analysis required 6 to 7 structural iterations, each of which is much more expensive than the 5 required by the optimizations based on B analysis, including Cholesky factorization.

While the resulting designs, but especially their final performance or output displacement u_o, closely match those of Buhl et al. (2000b), larger deformations would be more interesting to study. Occasionally, considerably larger deflections of around 15 % were obtained by reducing the output stiffness κ and increasing the maximum input displacement $\overline{u}$. Regrettably, design optimization convergence based on NR, P and B analysis was often compromised, leaving random clouds of material or large regions of intermediate densities. While heaviside projection (Guest et al., 2004) may have remedied this, its implementation was opted out due to the additional time and complexity it would add to the presented work.

VII Discussion

Due to the elaborate discussion conducted throughout the results, the present section aims to mainly summarize, interpret, and generalize it further beyond the particularly studied cases of structural analysis and optimization. Overall contributions and benefits of the proposed Bayesian-enhanced perturbed structural analysis are discussed in Subsection VII.1, and compared to state-of-the-art linear and Newton-Raphson analysis within structural topology optimization. Correspondingly, the major limitations are critically examined in Subsection VII.2. Then, Subsection VII.3 follows up with a very brief practical guide on recommended use, balancing benefits and limitations. It mainly argues sufficient or ideal parameter values and existing tools regarding regularization, optimization, and tensor decomposition. Finally, Subsection VII.4 concludes the discussion, recommending future work extending current benefits and remedying current limitations of perturbed analysis, within and without structural analysis or topology optimization.

VII.1 Contributions

Arguing from the mathematical method and numerical results, the novel Bayesian-enhanced perturbed structural analysis appears to have extended the powerful design capabilities of topology optimization with much of the qualitative aspects of non-linearity, without as much of the computational ramifications associated with state-of-the-art Newton-Raphson analysis. Its *five* major contributions and benefits are summarized and clarified in the following paragraphs.

1) Perturbed structural analysis provides a *continuous* non-linear extrapolation of deformation $\widetilde{\boldsymbol{u}}(\lambda)$ or $\widetilde{\widetilde{\boldsymbol{u}}}(\lambda)$ versus load λ. The continuous extrapolation especially benefits the computational efficiency of responses based on multiple equilibrium points, or integrations along the equilibrium curve. As discussed in Subsection VII.4, perturbed analysis may be straightforwardly generalized towards multiple expansion points other than the undeformed state considered in the present work.

2) Particularly the Bayesian-enhanced equivalent to the pure MacLaurin-based perturbed analysis provides a *stable* means of deformation extrapolation $\widetilde{\boldsymbol{u}}(\lambda)$, with predictable error. Some n^{th} order extrapolation features n^{th} order convergence towards the true deformation as λ approaches the expansion point. On the other hand, it ultimately diverges only linearly as λ exceeds the radius of convergence $\overline{\lambda}$ with respect to the expansion point, benefitting the robustness of the structural optimization. Considering some fixed λ, $\widetilde{\widetilde{\boldsymbol{u}}}(\lambda)$ respectively features linear convergence and divergence versus n, within and without the radius of convergence. This is derived in Appendix C and demonstrated in Section IV.

3) More specifically, the deformation extrapolation $\widetilde{\widetilde{\boldsymbol{u}}}(\lambda)$ is paired with an *accurate* posterior error estimator including its design sensitivity, at negligible computational cost. It has been demonstrated as a reliable tool to enforce some desired tolerance throughout the design optimization in Section V and VI. This ensures a certain degree of accuracy of the predicted design performance and feasibility, but more importantly, it improves the design optimization robustness.

4) By exploiting a decomposed tensor reformulation of the non-linear structural equations, computational effort and memory storage required for internal force and tangent stiffness evaluations can be reduced even below that using Bathe's traditional formulation 2016, as elaborated in Appendix A. The structural tensors fully take care of domain integration inherent to the finite element method, by factoring out the multilinear deformation dependence of energy, force, stiffness, and higher-order equivalents. Moreover, their expensive decomposition can be performed on the element level, and tabulated off-line, to be cheaply recycled for all elements throughout all future topology optimizations, given that their structural models are linearly related.

5) Most importantly, the proposed Bayesian-enhanced perturbed analysis has shown computational efficiency conditionally superior to Newton-Raphson analysis, given the same error tolerance, while often yielding nearly identical design performance improvements compared to using linear analysis. Admittedly, Newton-Raphson converges quadratically versus the number of structural solves, when provided with tangent stiffness matrix updates. While perturbed analysis converges linearly at the same initial rate, it does not require tangent stiffness updates and can hence exploit a relatively cheap Cholesky factorization. The resulting cost per solve is significantly lower, especially considering more degrees of freedom. This equips perturbed analysis with a much greater initial accuracy gain versus computational effort compared to Newton-

Raphson analysis, as visualized in Figure II.7. Up to moderate perturbed analysis orders, the cost of higher-order tensor contractions involved in constructing the necessary right-hand-side vectors remains negligible. Moreover, higher orders of perturbed structural analysis yield severely diminishing returns of accuracy versus computational effort anyway, being the focal point of its remaining limitations and recommended future work discussed next.

One of two minor, more arguable contributions worth addressing is the custom element deformation scaling proposed in Subsection III.5. Judging from Subsection IV.2, it appears to successfully remedy issues related to void elements for both Newton-Raphson and perturbed analysis, such as poor convergence and excessive deformations. However, this approach hardly differs from F. Wang et al.'s (2014), and may even become redundant when implementing an element- or degree-of-freedom-specific error estimator into the Bayesian-enhanced perturbed analysis, as recommended in Subsection VII.4.

Lastly, an arguable contribution may be the provided explanation for the effectiveness of rational extrapolation, including a more robust formulation compared to Cochelin, Damil, & Potier-Ferry's 1994. The algebraic analysis (Subsection II.4) and Bayesian-averaging (Appendix C) both provide a strong argument for Padé-like or rational extrapolation from different perspectives, particularly using a shared denominator of all deformation and load components (El Kihal et al., 2022). Perhaps this contributes an explanation for the reportedly mysterious effectiveness (Noor & Peters, 1983) of more traditional Padé extrapolations. Moreover, the spurious poles or divergence encountered in other works (Cochelin, 1994; De Boer & Van Keulen, 1997; El Kihal et al., 2022), are inherently prevented through the Bayesian-averaged MacLaurin extrapolation proposed in Subsection III.4, simply being a continuously weighted average of polynomials. In fact, it was the very attempt to optimize robustness and minimize estimated error, that turned the original set of MacLaurin series into a vectorial Padé-like extrapolant. It is as if algebraic problems truly desire rational solutions, even if by means of a substantially truncated degree compared to the astronomically high but finite degree[47] of some rational parametric formulation perfectly tracing a branch of the equilibrium curve.

VII.2 Limitations

Despite its merits and potential discussed in the previous subsection, perturbed analysis is an unpolished, double-edged sword. There is much room for improvement regarding its effectiveness, efficiency, scaling, and user-friendliness, within pure structural analysis and topology optimization. Its *five* major limitations are summarized and clarified in the following paragraphs.

1) The radius of convergence $\overline{\lambda}$ appears to be the dominant barrier to improved accuracy and efficiency of perturbed analysis. Given some error tolerance, increasing the order and computational effort only asymptotically increases the allowable extent of non-linearity λ, ultimately limited by the radius of convergence. Typically, accuracy only gets worse beyond this radius, but better within it, with both effects pronounced the further away from this radius. From another perspective, increasing this radius roughly exponentially reduces the required effort for some given error tolerance for both the pure MacLaurin-based analysis and its Bayesian-enhanced version. As further discussed in Subsection VII.4, the radius of convergence strongly depends on the chosen parameterization of both displacement $\widetilde{\boldsymbol{u}}(a)$ and load variable $\widetilde{\lambda}(a)$ in terms of some path parameter a (Najah et al., 1998; Cochelin, Damil, & Potier-Ferry, 1994). Arguably, the presently adopted load-controlled analysis $\lambda = a$ is the worst choice, inherently forcing load limits to be singularities, bounding the radius of convergence.

2) The adopted load-controlled formulation directly limits the utility of perturbed analysis, extending the previous argument. It prevents the analysis, hence design, of strongly non-linear mechanics such as multi-stability or (near-)zero actuation stiffness. Then again, a parametric formulation where displacement $\widetilde{\boldsymbol{u}}(a)$ and load variable $\widetilde{\lambda}(a)$ are both functions of some path parameter a is much less difficult to obtain. Much more so is finding a particular parametric formulation that actually increases the radius of convergence. While not documented in this work, an experimental parametric extension of the proposed perturbed analysis has been obtained. Here, the newly introduced coefficients within $\widetilde{\lambda}(a)$ were resolved by imposing a constant path-rate of $(\widetilde{\boldsymbol{u}}(a), \widetilde{\lambda}(a))$ versus a. While this parameterization is capable of passing load limits, its radius of convergence generally appeared no larger than that of the load-controlled formulation when further away from load limits.

3) Scaling up the order, degree of non-linearity, or number of freedom degrees for a structural element may be problematic to perturbed analysis and tensor formulation, especially considering the tensor decomposition. This pertains to higher-order strain models, shape functions, three spatial dimensions, or even worse, non-polynomial or non-conservative energy models. The presently adopted two-dimensional, conservative elasto-mechanics with quadratic Green-Lagrange strain model may have played a large role in the methodology's apparent feasibility, especially the decomposed tensor formulations which readily posed one of the most difficult challenges encoun-

[47] Recall that Subsection II.4 argues the existence and degree of the perfect rational parametric solution to a set of algebraic equations.

tered throughout the present work. The curse of dimensionality certainly applies to the *np-hard* tensor decomposition (Comon et al., 2008). Moreover, the tensor rank exponentially increases versus the degree of non-linearity, and at least super-linearly versus the element's number of freedom degrees, based on Equation II.7. Potential remedies are discussed in Subsection VII.4. Then again, the decomposition needs to be carried out once and for all, while the resulting efficiency of future contractions remains to be investigated. Even if the tensorial reformulation of any polynomial model proves the most efficient in terms of floating-point operations and memory, given a minimal decomposition, obtaining the latter remains a far from trivial topic of ongoing academic research (Ge & Ma, 2022; Hopkins & Shi, 2019; Battaglino et al., 2018; Rabanser et al., 2017).

4) Implementing and using perturbed analysis is much less straightforward than Newton-Raphson or linear analysis, affecting its accessibility. This concerns obtaining and decomposing the elemental structural tensors, the recursive higher-order analysis itself, formulating responses based on it, and their (adjoint) sensitivity analysis. It currently requires in-depth knowledge on the workings behind the methodology. It adds to the readily increased complexity inherent to responses based on non-linearity, such as critical load (Baguet & Cochelin, 2002).

5) The facilitated control of a displacement-based error estimator may still be loose on the residual force. When the displacement error of fixed magnitude aligns with stiffer eigendeformations, greater residual forces may be observed. However, residual evaluations, and especially their design sensitivities, are much more expensive than the displacement error estimators as proposed in this work for perturbed analysis. Depending on the desired structural performance, indirect rather than direct residual control might be problematic.

While not exactly a limitation, the proposed element deformation scaling and Bayesian enhancement of the perturbed analysis played a much smaller role in the optimization robustness, than the greatly increased accuracy for larger loads seems to suggest (see Figure IV.2 and IV.5). In fact, most robustness seems to be derived directly from the imposed error constraint, as without it the optimizer promptly diverges as soon as the estimated error breaches about one to ten percent. Even then, the error constraint had to be complemented with a trust region, restricting a design change of $\boldsymbol{x}$ such that any of its components never exceeds some small number. Most results obtained in this work converged consistently imposing a maximum design change of 0.1. Admittedly, the slightly increased radius of convergence due to Bayesian averaging likely contributed to robustness through the increased feasible design domain, in addition to the attenuated divergence of the analysis beyond the radius of convergence.

VII.3 Recommended Parameter Values

In order to exploit the benefits of perturbed geometrically non-linear analysis within topology optimization of compliant mechanisms, a brief parameter guide is provided here. Notably, for all newly introduced tunable regularization and optimization parameters, ideal values can be argued without considering the particular structural optimization problem. Provided a functional implementation of perturbed analysis, most regularization parameters can be chosen to more than sufficiently improve the structural analysis and optimization robustness, without noticeably sacrificing the structural model and analysis accuracy, or regularity of the optimized results. Lastly, some advice is given on some potential implementation difficulties or choices towards a functional perturbed structural analysis.

Starting with the regularization parameters of the solid isotropic material penalization and custom element material deformation scaling, their ideal values (Table VII.1) can be argued directly from the results in Section IV and the literature. The material penalization exponent θ has produced satisfactory results when slowly incremented from 1 towards 3, in the present work but also that of others (Deaton & Grandhi, 2014). When the desired black-white projection is still insufficient, Heaviside projection filtering (Deaton & Grandhi, 2014) is advised much rather than further increasing θ. As for the minimum void density $\underline{\varsigma}$, the (effective) value of 10^{-9} is not uncommon (Yoon & Kim, 2005; Buhl et al., 2000a; Sigmund, 2001; van Dijk et al., 2014). Moreover, values up to 10^{-6} resulted in a physical error below one percent of the C-Beam analysis (Figure IV.7a), meaning the duly discussed error tolerance $\overline{\epsilon}$ typically results in dominant effects. Choosing $\underline{\varsigma}$ much lower than 10^{-10}, however, may affect the conditioning of structural solves. Corresponding to this range of void densities, an EMDS threshold $\overline{\varsigma}$ around 0.01 perfectly remedies the effect of voids on the robustness and convergence of both Newton-Raphson and perturbed analysis, without introducing any physical error (Figure IV.7a). Lastly, the effect of density filtering changes least with the element refinement, when choosing the radius $\overline{\Delta}$ equal to one, plus some constant proportional to the refinement. Whatever this constant is, may still very much depend on the desired minimal structural feature size or personal preference, as long as it is non-zero to prevent checkerboarding and single-noded hinges (Sigmund & Petersson, 1998).

Moving on to the optimization parameters, the ideal value of the analysis order n and normed relative error tolerance $\overline{\epsilon}$ is more nuanced (Table VII.2). Assuming convergence, increasing n yields exponentially di-

Regularization parameter	Value (range)
Material penalization θ	1 ++0.05, up to 3
Void density $\underline{\varsigma}$	$\left[10^{-10},\ 10^{-6}\right]$
EMDS threshold $\overline{\underline{\varsigma}}$	0.01
Density filter radius $\overline{\Delta}$	$1 + \overline{\overline{\Delta}}$, with $\overline{\overline{\Delta}} \geqslant 0$ proportional to refinement for regularity of filtered structural design.

Table VII.1: List of reasonably ideal or sufficient regularization parameters, based on the present work.

minished returns of accuracy versus ultimately super-linearly increased computational cost. Moreover, the direct effect of analysis error on the response surfaces, and most importantly the locations of their minima or roots versus the design $\boldsymbol{x}$, is hard to predict. Without a doubt, however, the feasible design domain and potentially attainable performance grow and shrink directly with the effective allowable load λ, resulting from the analysis order n and imposed error tolerance $\overline{\epsilon}$. In this sense, maximizing n and $\overline{\epsilon}$ is desirable. Still, recalling the diminishing returns versus n, some value up to 20 should take a total solve time close to the order of magnitude of the initial Cholesky decomposition while yielding most of the attainable accuracy. Some sufficiently robust $\overline{\epsilon}$ of 0.001, 0.01 or 0.1, respectively translates to an allowable load $\lambda/\overline{\lambda}$ of 0.71, 0.86 or 0.89, using $\lambda/\overline{\lambda} = \overline{\epsilon}^{1/n}$, rewritten from Equation B.2.7. While further work is needed to pinpoint the ideal tolerance $\overline{\epsilon}$, values much greater than 0.01 primarily affect the optimization robustness, next to causing a less predictable performance loss resulting from response inaccuracy. Yet, values much smaller than 0.01 may yield a much more detrimental performance loss by restricting the design domain, unless n is increased proportionally to $\log \overline{\epsilon}$.

Optimization parameter	Value (range)
Error tolerance $\overline{\epsilon}$	0.001 to 0.1
Analysis order n	5 to 20. Change proportionally to $\log \overline{\epsilon}$ for regularity of feasible design domain.

Table VII.2: List of reasonably ideal or sufficient optimization parameters, based on the present work.

As a final remark on truncating the perturbed analysis order, the gain in computational efficiency is not expected entirely worth the introduced discontinuity of $\overline{\lambda}$, $\widetilde{\epsilon}$ or $\widetilde{\overline{\epsilon}}$, denoting the convergence radius, MacLaurin extrapolation and Bayesian error estimators. As demonstrated in Figure V.3, when the error constraint becomes active, it remains active throughout most of the optimization requiring the maximum analysis order. A notable exception is during problem formulations inherently avoiding deformation, thus arguably non-linearity, such as during compliance minimization. This should become apparent during a quick initial optimization attempt, and n could be reduced accordingly without truncating the analysis dynamically based on the error criterion. Regardless, any potential user is encouraged to experiment.

VII.4 Recommended Future Work

In order to remedy the current limitations and further exploit or apply the benefits of perturbed geometrically non-linear analysis more generally, future work is recommended here, divided into *seven* groups. Notably, the radius of convergence and algebraic analysis are discussed first, addressing limitations 1) and 2) of perturbed analysis, as listed in Subsection VII.2. Then, some alternative extensions of (Bayesian-enhanced) perturbed analysis are discussed, such as partially inverting the internal force function, using multiple expansion points, incorporating zeroth-order information, combining multiple approximation methods, and further exploiting the continuous nature of the perturbed analysis prediction.

1a) The first and foremost future recommendation is to extend the radius of convergence or range of validity of the perturbation method, particularly through parametric and algebraic analysis. The choice of parameterizing the equilibrium curve prediction has been noted as highly influential on the radius of convergence. Particularly rational or Padé-like extrapolation has been observed to result in spectacular improvements upon polynomial extrapolation (Cochelin, Damil, & Potier-Ferry, 1994; De Boer & Van Keulen, 1997; Najah et al., 1998). Reportedly, this could increase the radius of convergence up to tenfold, although this likely paints an optimistic picture. At any rate, an explicit or load-controlled formulation directly limits the extent to which a generally strongly non-linear curve can be accurately described. However, any arbitrary means of formulating both displacement and load non-linearly or even rationally versus some path parameter may still not directly yield the desired increased radius of convergence. Therefore, it is recommended to consult or employ an algebraic geometer, as the following clarification and approach of algebraic analysis may still be vague or insufficient.

1b) Perturbed algebraic analysis embraces the algebraic nature of the structural equations, to which a perfect (piecewise) rational parametric formulation of the solution exists, as elaborated in Subsection II.4. Where parametric analysis includes a non-linear formulation of displacement and load, algebraic analysis includes yet another variable[48], assuming it and the

[48]This additional variable could be considered a homogenization variable, homogenizing the governing set of algebraic structural

former as polynomials:

$$\begin{cases} \widetilde{\boldsymbol{u}}(a) = \dfrac{\boldsymbol{U}(a)}{Z(a)} \\ \widetilde{\lambda}(a) = \dfrac{\Lambda(a)}{Z(a)} \end{cases} \quad : \quad \boldsymbol{f}\big(\widetilde{\boldsymbol{u}}(a)\big) = \widetilde{\lambda}(a)\boldsymbol{p} \ , \qquad \text{(VII.1)}$$

with the components of $\boldsymbol{U}(a)$, $\Lambda(a)$, and $Z(a)$ being univariate polynomials of degree up to 3^N given N degrees of freedom and a fourth-order multivariate polynomial model of strain energy. The additional freedom within the parameterization of this new variable $Z(a)$ can then be exploited directly to maximize a current estimate of the radius of convergence. Moreover, the true radius of convergence using this formulation is argued as infinite in Subsection II.4, since an astronomically high but finite order of perturbed algebraic analysis should perfectly trace the local branch of the equilibrium curve. Rather than using incrementally higher-order polynomials, algebraic analysis aims to approximate the algebraic equilibrium curve using other, incrementally higher-order algebraic curves.

1c) As a final addition to the robustness and accuracy of perturbed algebraic analysis, Bayesian averaging of all obtained predictions up to the current order could be applied. This step hardly differs from the proposed Bayesian enhancement of the pure MacLaurin-based perturbed analysis in this work. The required error estimate should be straightforward as well, by starting with the error estimate of all involved numerator and denominator polynomials, applying the same reasoning as in Appendix B.2. Moreover, this Bayesian enhancement of perturbed algebraic analysis should preserve the rational nature and shared denominator among all load and displacement components, hopefully featuring the associated range of validity reported in Cochelin, Damil, & Potier-Ferry (1994); De Boer & Van Keulen (1997); Najah et al. (1998); El Kihal et al. (2022), in addition to the increased robustness as validated in the present work for MacLaurin predictions.

2) Applying algebraic analysis on the element level, and considering a multivariate load variable $\boldsymbol{\lambda}$ scaling (orthogonal) loads, may lead to an effective, partial inverse of the internal force function. To clarify, applying a pure translational or rotational force to an unconstrained element yields an infinite or undefined deformation. Instead, by considering perturbed analysis along all eigendeformations at the undeformed state, or eigenvectors of the initial stiffness matrix associated with nonzero eigenvalues in $\boldsymbol{V}$, the following structural equation can be solved for:

$$\boldsymbol{f}\big(\widetilde{\boldsymbol{u}}(a)\big) = \boldsymbol{V} \bullet \widetilde{\boldsymbol{\lambda}}(a) \qquad \text{(VII.2)}$$

assuming a rational description of $\big(\widetilde{\boldsymbol{u}}(a),\ \widetilde{\boldsymbol{\lambda}}(a)\big)$ versus a. As a starting point, a MacLaurin-based or Bayesian-enhanced perturbed analysis could be considered instead, being readily developed throughout the present work. In order to apply this analysis, one could first assume the rigid body deformation of a particular element and then apply the approximate inverse. This cycle then repeats by updating the assumed rigid body deformation through some Newton-Raphson or perturbed analysis, or heuristically. Essentially, most of the non-linear analysis would be carried out cheaply through forward application of this approximate inverse, leaving only the rigid body deformations to traditional solution methods. This may be especially efficient for higher-order elements, as the number of rigid body modes always remains three or six, respectively considering two and three spatial dimensions of kinetic freedom.

3a) Including multiple expansion points in addition to the undeformed state, is one of two ways (Bayesian-enhanced) perturbed analysis may be extended much more straightforwardly than by using algebraic geometry. This would involve consecutive higher-order predictions requiring little to no corrections[49]. This is still distinct from some higher-order or modified Newton-Raphson approach, as it does not involve corrections. The obtained separate predictions and their respective error estimators may be smoothly and stably unified, or interpolated, through Bayesian averaging, yielding a single continuous prediction rather than a piece-wise one. In fact, this approach to accurately and robustly unifying separate extrapolations was the inspiration behind the proposed Bayesian-enhanced perturbed analysis, where multiple expansions in a single point were smoothly combined instead. An additional advantage is that the posterior error estimation could lead to an automatized posterior step-size selection. This could balance computational effort versus estimated error per unit of user-defined arc length, based on some user-specified tolerance.

3b) Complementary to the previous lateral extension of Bayesian-enhanced perturbed analysis, one could incorporate zeroth-order information into the Bayesian average[50]. To clarify, the zeroth-order prediction $\widetilde{\boldsymbol{u}}_0(\lambda) = \boldsymbol{0}$ may actually improve the accuracy of $\widetilde{\widetilde{\boldsymbol{u}}}_n(\lambda)$ at $\lambda = \overline{\lambda}$ where all predictors are equally (in)accurate, and especially for $\lambda > \overline{\lambda}$ where all other predictors diverge. However, one may argue some qualitative benefits of having $\widetilde{\widetilde{\boldsymbol{u}}}_n(\lambda)$ tend to $\widetilde{\boldsymbol{u}}_1(\lambda)$ rather than the quantitatively more accurate $\widetilde{\boldsymbol{u}}_0(\lambda) = \boldsymbol{0}$ as λ increases beyond $\overline{\lambda}$.

4) Higher-order or even non-polynomial structural element models need not be entirely prohibitive to per-

equations to a single multivariate monomial.

[49] The low need for corrections using higher-order prediction stems from the inherent possibility to strongly prevent and predict error, where linear analysis minimally prevents and cannot predict error.

[50] Regrettably there was no more available time to incorporate and study a zeroth-order prediction in the present work.

turbed analysis and a decomposed tensor formulation, when using a lower-order polynomial approximation of this element model. This may address the scaling limitation of the perturbed analysis and tensor decomposition discussed in Subsection VII.2. For instance, the approximation may feature a certain extent of accuracy up to some percentage of normed strain, or perfect first-order accuracy near the undeformed state and rotational invariance as desired. Moreover, rather than finding the required structural tensors, one could directly optimize for their decomposition. At times, approximating the governing equation rather than its solution may be much more feasible in terms of efficiency and accuracy. The quadratic Green-Lagrange strain approximation is a prime example of how the corresponding global structural equilibrium solutions remain more than sufficiently useful, despite some higher-degree or even non-polynomial strain model being more physically accurate.

5) By estimating the error's value and its rate of convergence or divergence locally, rather than globally, meaning for each respective element or node, two benefits may be obtained. Firstly, locally converging predictions versus analysis order n need not be wasted in the attempt to suppress divergence within that of other elements or degrees of freedom. Secondly, the proposed EMDS (Element Material and Deformation Scaling) becomes redundant. To clarify, EMDS preventively linearizes structural behavior and hence divergence, based on the local density, while Bayesian analysis does so based directly on the local extent of divergence. Ultimately, the latter is what truly matters, but whether the overall implementation and computational difficulties increase or decrease remains to be tested. The Bayesian error estimate response $\widetilde{\widetilde{e}}_{\boldsymbol{x}}(\lambda)$ and its design sensitivity do become more complex and potentially more expensive, respectively turning into a vector and matrix of dimensions equal to the number of elements or degrees of freedom.

6a) Preconditioning, orthogonalizing or otherwise exploiting a transformed set of higher-order displacement derivatives, may improve the gained accuracy to effort ratio of the resulting higher-order prediction. A Gramm-Schmidt orthogonalization of the basis $\left\{\boldsymbol{u}^{(1)}, \ldots, \boldsymbol{u}^{(n)}\right\}$ has already been used by Najah et al. (1998) to precondition his Padé-approximant, but may further enforce the independence of contributions or errors as assumed during the Bayesian averaging proposed in the present work. In addition, the many multilinear forms involved in the higher-order residual calculations may be mathematically and numerically simplified by orthogonalizing the higher-order displacement derivatives. Moreover, principal component analysis of this basis typically reveals that most information resides within the first few derivative vectors (Imazatène et al., 2001). Even more, higher-order derivatives seem to ultimately fall into a precisely repeating pattern, as indicated by their inner product in Figure VII.1 for the C-Beam analysis up to the 50^{th} order. This further suggests the finity of their combined information, and perhaps may lead to a way of extracting a disproportionately high or even maximal order prediction, from a relatively small number of derivatives. A quick, undocumented experiment was conducted, fitting a linear map from the last three derivatives to a new one. Fitting this map on some first $n \geqslant 15$ derivatives, yielded an accurate recursive prediction of the next n derivatives before the normed relative error exceeded 0.01, at negligible cost compared to a structural solve.

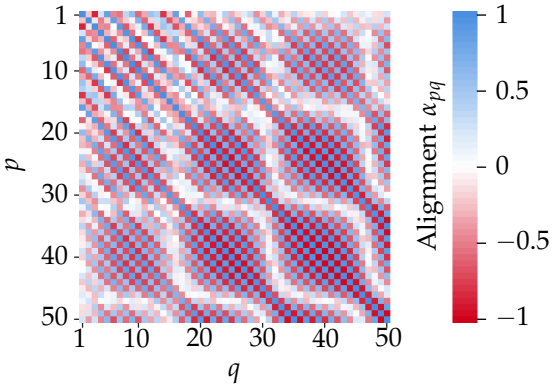

Figure VII.1: Alignment α_{pq} of the p^{th} and q^{th} displacement derivatives from the C-Beam analysis in Subsection IV.1, for $p, q = 1, \ldots, 50$. Here, $\alpha_{pq} \equiv \dfrac{\boldsymbol{u}^{(p)}}{|\boldsymbol{u}^{(p)}|} \bullet \dfrac{\boldsymbol{u}^{(q)}}{|\boldsymbol{u}^{(q)}|}$

7) Reduced-order modeling (ROM) may become especially feasible when combined with perturbed analysis and topology optimization. Among others, Noor & Peters (1983) and Imazatène et al. (2001) have demonstrated the potential of ROM using perturbed analysis of fixed designs, while Gogu (2015) has done so using linear analysis within large-scale topology optimization. Finally, L. Zhang et al. (2023) extended the latter to non-linear analysis, although the sensitivity analysis proved computationally impractical, requiring its approximation. However, the proposed perturbed analysis nearly directly provides a reduced solution basis. As argued in recommendation 6a), a small number of displacement derivatives may readily span most of the solution space, which may be cheaply orthogonalized using a Gramm-Schmidt procedure. Moreover, the adjoint sensitivity formulation of responses based on the original basis of displacement derivatives has also been demonstrated to be computationally efficient. In addition, the decomposed tensorial reformulation proposed in this work may remedy the prohibitive cost of the many involved residual force evaluations, or their higher-order derivatives in this case, when updating the ROM "on-the-fly" (Gogu, 2015) throughout the op-

timization. Alternatively, one could construct a small basis through low-order perturbed analysis, and complete the structural analysis by applying higher-order perturbed, or even Newton-Raphson analysis, within the reduced basis.

8) Exploiting the continuous nature of the predicted equilibrium curve is the last, but certainly not least important recommendation for future work. Regrettably, there was no more time for its implementation and validation within the present work. This would further validate the first major contribution of perturbed analysis within structural optimization, mentioned in Subsection VII.1. When responses are based on multiple points on, or integrals along the equilibrium curve, the utility and computational efficiency of perturbed analysis is expectedly further emphasized over Newton-Raphson analysis. Notable applications are designing biomedical devices featuring multi-stability (Parenti-Castelli & Sancisi, 2013; Zhu et al., 2020), non-linear path generators (Megaro et al., 2017) and frequency multipliers (MacHekposhti et al., 2018), as mentioned in Section I. Polynomial predictions are particularly suited for analytical integration, and numerical integration through Gauss quadrature. Moreover, even rational predictions are still manageable through quadrature rules, and a Gauss-type quadrature rule exists that can even exactly integrate rationals (Gautschi, 1993). This further facilitates integration-based responses for the currently undeveloped algebraic analysis.

VIII Conclusion

In order to address the rapidly increasing demand for compliant mechanisms of superior performance, the impact and challenges of non-linearity have been demonstrated and tackled in this work. Using the established powerful design capabilities of topology optimization, a novel means of non-linear structural analysis is developed as an alternative to the most popular but arguably lacking Newton-Raphson procedure. While the much lesser-known perturbed or asymptotic structural analysis has been extensively studied since even before the notable works of Thompson & Walker (1968); Noor & Peters (1983) and Cochelin (1994), it has not been implemented into a structural optimization setting[51] until the work of Hoevenaars (2021), albeit a finite difference version. The present work furthers their independent efforts. It extends topology optimization with a modified, Bayesian-enhanced perturbed structural analysis, error estimator, custom element deformation scaling, and an adjoint design sensitivity analysis of responses based on the former. The required higher-order displacement derivatives are obtained through an exact multivariate polynomial reformulation of the structural equations, and the higher-order tensor contractions are mediated through prior integrated and decomposed element tensors. Admittedly, the current state of perturbed analysis is that of an unpolished, double-edged sword.

On its sharp end, the proposed Bayesian-enhanced structural analysis appears to be a conditionally superior and generally more versatile alternative to both linear and Newton-Raphson analysis, within structural design optimization. Especially considering higher loads, accounting for non-linearity has yielded increased performance during all topology optimization case studies. To clarify, Bayesian-enhanced perturbed analysis often achieved identical designs thus performance improvements, using noticeably less computational effort, compared to Newton-Raphson analysis subjected to the same displacement-based error tolerance.

Perturbed analysis should become especially efficient and useful compared to Newton-Raphson analysis, due to the continuous nature of its equilibrium prediction and analytically available higher-order structural derivatives. This entails design responses based on more than a single equilibrium point, or definite integrals along the equilibrium curve, including all analytically available elastic energy derivatives such as internal force, tangent stiffness, stiffening, and higher-order equivalents. Moreover, it would be wasteful not to employ such responses that exploit structural non-linearity to the fullest extent. Notably, recall the examples of biomedical devices featuring multi-stability (Parenti-Castelli & Sancisi, 2013; Zhu et al., 2020), hand-held tools featuring near-zero actuation stiffness (Lourdes Thomas et al., 2021), non-linear path generators (Megaro et al., 2017) and frequency multipliers (MacHekposhti et al., 2018) mentioned in Section I.

Currently, perturbed analysis is mostly limited by its radius of convergence, partially through the load- or displacement-controlled formulation. Ultimately, this restricts the extent of non-linearity within error-constrained design optimization, and hence the feasible design domain and expected attainable performance. In some of the highest load cases, still positive yet smaller performance gains were observed through Bayesian analysis[52]. In such cases, it is suspected that the active error constraint either slows the design's convergence or restricts its domain of feasibility. It does testify to the functionality of the implemented error constraint, bounding the true structural analysis error often within 50 percent relative to some desired tolerance. This is decidedly vital in preventing divergence of the analysis and optimization, more so than just reinforcing confidence in the predicted performance

[51] To clarify, no clear documentation has been found on load-perturbations, not to be confused with design-perturbations.

[52] On a single occasion, the Bayesian-enhanced perturbed analysis for $n = 5$ and $\lambda = 20$ yielded a performance worse than linear analysis in the compliance minimization study case, as can be seen in Figure V.2).

of a particular design. The radius of convergence may never be breached without severe loss of accuracy, hence the radius must be increased to facilitate superior design performance.

A particularly interesting but speculative prospect of perturbed analysis, may be its combination with reduced order modeling (Noor & Peters, 1983; Imazatène et al., 2001), potentially constructed and updated *"on-the-fly"* throughout the structural optimization (Gogu, 2015), but without impractically expensive sensitivity analysis (L. Zhang et al., 2023). Although this does not directly remedy the limiting radius of convergence of perturbed analysis, it may further increase its computational efficiency.

Regarding the potential of perturbed analysis for non-linear analysis in general, the foremost recommendation based on the present work is to increase the radius of convergence, particularly by embracing vectorial, rational extrapolation and algebraic geometry. To clarify, in subsection II.4 it was first learned that a rational parametric form exists with a shared denominator among all components, that perfectly traces a curve governed by an algebraic set of equations. Considering a set of low-degree Taylor extrapolations of the solution instead, their Bayesian average of minimized expected truncation error as proposed in Subsection III.4 again results in a vectorial Padé, hence rational extrapolation. Thirdly, rational and particularly vectorial, diagonal Padé extrapolations have been noted to feature a surprising accuracy and ranges of validity (Najah et al., 1998; Cochelin, Damil, & Potier-Ferry, 1994; Imazatène et al., 2001; El Kihal et al., 2022), although it should hardly be surprising at this point. Augmenting Bayesian-enhanced perturbed analysis with algebraic geometry, as further argued in Subsection VII.4, would certainly address the radius of convergence that currently bottlenecks the proposed error-constrained topology optimization framework.

Much more exciting than the potential contributions stemming from perturbed analysis to structural optimization, is the wide range of non-linear problems within and without the field of structural engineering, where it may prove useful. The author hopes to draw the attention of mathematicians and engineers specialized in algebraic geometry and numerical analysis, so that perhaps they can ultimately turn the inevitable hurdle of non-linear analysis into a more efficient, accurate, robust, and accessible tool throughout the fields of applied and theoretical science.

2

Bibliography

Aage, N., & Lazarov, B. S. (2013). Parallel framework for topology optimization using the method of moving asymptotes. *Structural and Multidisciplinary Optimization*, *47*(4), 493–505. doi: 10.1007/s00158-012-0869-2

Agarwal, P., Akbar, M., Nawaz, R., & Jleli, M. (2021). Solutions of system of Volterra integro-differential equations using optimal homotopy asymptotic method. *Mathematical Methods in the Applied Sciences*, *44*(3), 2671–2681. doi: 10.1002/mma.6783

Ambrose, S. H. (2001, 3). Paleolithic Technology and Human Evolution. *Science*, *291*(5509), 1748–1753. Retrieved from `https://www.science.org/doi/10.1126/science.1059487` doi: 10.1126/science.1059487

Andreassen, E., Clausen, A., Schevenels, M., Lazarov, B. S., & Sigmund, O. (2011). Efficient topology optimization in MATLAB using 88 lines of code. *Structural and Multidisciplinary Optimization*, *43*(1), 1–16. doi: 10.1007/s00158-010-0594-7

Ayane, R., Hamdaoui, A., Braikat, B., Tounsi, N., & Damil, N. (2019, 12). An improved Padé approximant in the ANM algorithm: Application to the post-buckling of shells. *Finite Elements in Analysis and Design*, *167*, 103330. Retrieved from `https://linkinghub.elsevier.com/retrieve/pii/S0168874X19302756` doi: 10.1016/j.finel.2019.103330

Azrar, L., Cochelin, B., Damil, N., & Potier-Ferry, M. (1993). An asymptotic-numerical method to compute the postbuckling behaviour of elastic plates and shells. *International Journal for Numerical Methods in Engineering*, *36*(8), 1251–1277. doi: 10.1002/nme.1620360802

Bader, B. W., & Kolda, T. G. (2007). Efficient MATLAB computations with sparse and factored tensors. *SIAM Journal on Scientific Computing*, *30*(1), 205–231. doi: 10.1137/060676489

Baguet, S., & Cochelin, B. (2002). Stability of thin-shell structures and imperfection sensitivity analysis with the Asymptotic Numerical Method. *Revue Europeenne des Elements*, *11*(2-4), 493–509. doi: 10.3166/reef.11.493-509

Bathe, K.-J. (2016). *Finite element procedures, 2nd edition*. Klaus-Jurgen Bathe.

Battaglino, C., Ballard, G., & Kolda, T. G. (2018). A practical randomized CP tensor decomposition. *SIAM Journal on Matrix Analysis and Applications*, *39*(2), 876–901. doi: 10.1137/17M1112303

Bejan, A. (2000). *Shape and structure, from engineering to nature*. Cambridge university press.

Bendsøe, M. P. (1989). Optimal shape design as a material distribution problem. *Structural Optimization*, *1*(4), 193–202. doi: 10.1007/BF01650949

Bendsøe, M. P., & Kikuchi, N. (1988). Generating optimal topologies in structural design using a homogenization method. *Computer Methods in Applied Mechanics and Engineering*, *71*(2), 197–224. doi: 10.1016/0045-7825(88)90086-2

Bernardi, A., Brachat, J., Comon, P., & Mourrain, B. (2013). General tensor decomposition, moment matrices and applications. *Journal of Symbolic Computation*, *52*, 51–71. Retrieved from `http://dx.doi.org/10.1016/j.jsc.2012.05.012` doi: 10.1016/j.jsc.2012.05.012

Brachat, J., Comon, P., Mourrain, B., & Tsigaridas, E. (2010). Symmetric tensor decomposition. *Linear Algebra and Its Applications*, *433*(11-12), 1851–1872. Retrieved from `http://dx.doi.org/10.1016/j.laa.2010.06.046` doi: 10.1016/j.laa.2010.06.046

Bruns, T. E., & Tortorelli, D. A. (2001, 3). Topology optimization of non-linear elastic structures and compliant mechanisms. *Computer Methods in Applied Mechanics and Engineering*, *190*(26-27), 3443–3459. Retrieved from `https://linkinghub.elsevier.com/retrieve/pii/S0045782500002784` doi: 10.1016/S0045-7825(00)00278-4

Buhl, T., Pedersen, C. B., & Sigmund, O. (2000a). Stiffness design of geometrically nonlinear structures using topology optimization. *Structural and Multidisciplinary Optimization*, *19*(2), 93–104. doi: 10.1007/s001580050089

Buhl, T., Pedersen, C. B., & Sigmund, O. (2000b). Stiffness design of geometrically nonlinear structures using topology optimization. *Structural and Multidisciplinary Optimization*, *19*(2), 93–104. doi: 10.1007/s001580050089

Carroll, S. B. (2001, 2). Chance and necessity: the evolution of morphological complexity and diversity. *Nature*, *409*(6823), 1102–1109. Retrieved from `http://www.nature.com/articles/35059227` doi: 10.1038/35059227

Cattelain, P. (1997). Hunting during the upper paleolithic: bow, spearthrower, or both? In *Projectile technology* (pp. 213–240). Springer.

Charpentier, I. (2008). Sensitivity of solutions computed through the Asymptotic Numerical Method. *Comptes Rendus - Mecanique*, *336*(10), 788–793. Retrieved from `http://dx.doi.org/10.1016/j.crme.2008.09.003` doi: 10.1016/j.crme.2008.09.003

Chen, G., Ma, F., Hao, G., & Zhu, W. (2019a). Modeling large deflections of initially curved beams in compliant mechanisms using chained beam constraint model. *Journal of Mechanisms and Robotics*, *11*(1). doi: 10.1115/1.4041585

Chen, G., Ma, F., Hao, G., & Zhu, W. (2019b). Modeling large deflections of initially curved beams in compliant mechanisms using chained beam constraint model. *Journal of Mechanisms and Robotics*, *11*(1). doi: 10.1115/1.4041585

Cochelin, B. (1994). A path-following technique via an asymptotic-numerical method. *Computers and Structures*, *53*(5), 1181–1192. doi: 10.1016/0045-7949(94)90165-1

Cochelin, B., Damil, N., & Potier-Ferry, M. (1994). The asymptotic-numerical method: An efficient perturbation technique for nonlinear structural mechanics. *Revue Europeenne des Elements*, *3*(2), 281–297. doi: 10.1080/12506559.1994.10511124

Cochelin, B., Damil, N., & Potier-Ferry, M. (1994). Asymptotic–numerical methods and Pade approximants for non-linear elastic structures. *International Journal for Numerical Methods in Engineering*, *37*(7), 1187–1213. doi: 10.1002/nme.1620370706

Comon, P., Golub, G., Lim, L.-h., & Mourrain, B. (2008, 1). Symmetric Tensors and Symmetric Tensor Rank. *SIAM Journal on Matrix Analysis and Applications*, *30*(3), 1254–1279. Retrieved from `http://epubs.siam.org/doi/10.1137/060661569` doi: 10.1137/060661569

Comon, P., & Luciani, X. (2009). Tensor Decompositions , Alternating Least Squares and other Tales To cite this version : Tensor Decompositions , Alternating Least Squares and other Tales. *Journal of Chemometrics*, *23*, 393–405. Retrieved from https://hal.archives-ouvertes.fr/hal-00410057

Courant, R. (1943). *Variational methods for the solution of problems of equilibrium and vibrations* (Vol. 49) (No. 1). doi: 10.1090/S0002-9904-1943-07818-4

Crisfield, M. A. (1997). *Non-linear finite element analysis of solids and structures: Volume 2: Advanced topics*. Wiley.

Damil, N., & Potier-Ferry, M. (1990). A New method to compute perturbed bifurcations: Application to the buckling of imperfect elastic structures. *International Journal of Engineering Science*, *28*(9), 943–957. doi: 10.1016/0020-7225(90)90043-I

Deaton, J. D., & Grandhi, R. V. (2014). A survey of structural and multidisciplinary continuum topology optimization: Post 2000. *Structural and Multidisciplinary Optimization*, *49*(1), 1–38. doi: 10.1007/s00158-013-0956-z

Debeurre, M., Grolet, A., Cochelin, B., & Thomas, O. (2023). Finite element computation of nonlinear modes and frequency response of geometrically exact beam structures. *Journal of Sound and Vibration*, *548*(September 2022), 117534. Retrieved from https://doi.org/10.1016/j.jsv.2022.117534 doi: 10.1016/j.jsv.2022.117534

De Boer, H., & Van Keulen, F. (1997, 7). Padé approximants applied to a non-linear finite element solution strategy. *Communications in Numerical Methods in Engineering*, *13*(7), 593–602. Retrieved from https://onlinelibrary.wiley.com/doi/10.1002/(SICI)1099-0887(199707)13:7%3C593::AID-CNM104%3E3.0.CO;2-V doi: 10.1002/(SICI)1099-0887(199707)13:7<593::AID-CNM104>3.0.CO;2-V

De Borst, R., Crisfield, M. A., Remmers, J. J., & Verhoosel, C. V. (2012). *Nonlinear finite element analysis of solids and structures*. John Wiley & Sons.

de Buhan, P., Bleyer, J., & Hassen, G. (2017). The Homogenization Approach: Reinforced Materials as Macroscopically Homogeneous Anisotropic Media. *Elastic, Plastic and Yield Design of Reinforced Structures*, 39–92. doi: 10.1016/b978-1-78548-205-2.50002-5

Demanet, L., & Townsend, A. (2019). Stable Extrapolation of Analytic Functions. *Foundations of Computational Mathematics*, *19*(2), 297–331. doi: 10.1007/s10208-018-9384-1

El Kihal, C., Askour, O., Hamdaoui, A., Braikat, B., Damil, N., & Potier-Ferry, M. (2022). Convergence acceleration by Padé approximants in the ANM algorithm for large strain elasto-plasticity. *Finite Elements in Analysis and Design*, *212*(July), 103853. Retrieved from https://doi.org/10.1016/j.finel.2022.103853 doi: 10.1016/j.finel.2022.103853

Eschenauer, H. A., & Olhoff, N. (2001). Topology optimization of continuum structures: A review. *Applied Mechanics Reviews*, *54*(4), 331–390. doi: 10.1115/1.1388075

Gautschi, W. (1993). Gauss-type Quadrature Rules for Rational Functions. *Numerical Integration IV*, 111–130. doi: 10.1007/978-3-0348-6338-4{_}9

Ge, R., & Ma, T. (2022). On the optimization landscape of tensor decompositions. *Mathematical Programming*, *193*(2), 713–759. doi: 10.1007/s10107-020-01579-x

Gogu, C. (2015, 1). Improving the efficiency of large scale topology optimization through on-the-fly reduced order model construction. *International Journal for Numerical Methods in Engineering*, *101*(4), 281–304. Retrieved from http://onlinelibrary.wiley.com/doi/10.1002/nme.3279/fullhttps://onlinelibrary.wiley.com/doi/10.1002/nme.4797 doi: 10.1002/nme.4797

Greenstein, D. S. (1965). Interpolation and approximation (philip j. davis). *SIAM Review*, *7*(1), 151.

Guest, J. K., Prévost, J. H., & Belytschko, T. (2004). Achieving minimum length scale in topology optimization using nodal design variables and projection functions. *International Journal for Numerical Methods in Engineering*, *61*(2), 238–254. doi: 10.1002/nme.1064

Haisler, W. E., Stricklin, J. A., & Stebbins, F. J. (1972). Development and evaluation of solution procedures for geometrically nonlinear structural analysis. *AIAA Journal*, *10*(3), 264–272. doi: 10.2514/3.50089

Han, Y., Xu, B., & Liu, Y. (2021). An efficient 137-line MATLAB code for geometrically nonlinear topology optimization using bi-directional evolutionary structural optimization method. *Structural and Multidisciplinary Optimization*, *63*(5), 2571–2588. doi: 10.1007/s00158-020-02816-9

Hartshorne, R. (2013). *Algebraic geometry* (Vol. 52). Springer Science & Business Media.

He, J. (1998). An approximate solution technique depending on an artificial parameter: A special example. *Communications in Nonlinear Science and Numerical Simulation*, *3*(2), 92–97. doi: 10.1016/S1007-5704(98)90070-3

Hoeting, J. A., Madigan, D., Raftery, A. E., & Volinsky, C. T. (1999). Bayesian Averaging Models: A Tutorial. *Statistical Science*, *14*(4), 382–417.

Hoevenaars, J. (2021). *Approximate geometric non-linear analysis in topology optimization [unpublished]* (Master's thesis, Delft University of Technology, Delft, The Netherlands). Retrieved from `http://resolver.tudelft.nl/uuid:c0511489-318e-490d-b756-37b395dce070`

Hopkins, S. B., & Shi, J. (2019). A Robust Spectral Algorithm for Overcomplete Tensor Decomposition. , *99*(1), 1–40.

Howell, L. L. (2013). *Compliant mechanisms*. Springer. doi: 10.1007/978-1-4471-4510-3_3

Howell, L. L., & Midha, A. (1994). A method for the design of compliant mechanisms with small-length flexural pivots. *Journal of Mechanical Design, Transactions of the ASME*, *116*(1), 280–290. doi: 10.1115/1.2919359

Imazatène, A., Cadou, J. M., Zahrouni, H., & Potier-Ferry, M. (2001). A new reduced basis method for non-linear problems. *Revue Européenne des Éléments Finis*, *10*(1), 55–76. doi: 10.1080/12506559.2001.11869239

Koiter, W. (1945). On the stability of elastic equilibrium (thesis). *Delft. Univ*. Retrieved from `https://apps.dtic.mil/sti/pdfs/AD0704124.pdf`

Kolda, T. G., & Bader, B. W. (2009, 8). Tensor Decompositions and Applications. *SIAM Review*, *51*(3), 455–500. Retrieved from `http://epubs.siam.org/doi/10.1137/07070111X` doi: 10.1137/07070111X

Kota, S., Joo, J., Li, Z., Rodgers, S. M., & Sniegowski, J. (2001). Design of compliant mechanisms: Applications to MEMS. *Analog Integrated Circuits and Signal Processing*, *29*(1-2), 7–15. doi: 10.1023/A:1011265810471

Kota, S., Lu, K. J., Kreiner, Z., Trease, B., Arenas, J., & Geiger, J. (2005). Design and application of compliant mechanisms for morphing aircraft structures. *Journal of Biomechanical Engineering*, *127*(6), 981–989. doi: 10.1115/1.2056561

Liao, S. (2004). On the homotopy analysis method for nonlinear problems. *Applied Mathematics and Computation*, *147*(2), 499–513. doi: 10.1016/S0096-3003(02)00790-7

Liao, S. (2010). An optimal homotopy-analysis approach for strongly nonlinear differential equations. *Communications in Nonlinear Science and Numerical Simulation*, *15*(8), 2003–2016. Retrieved from `http://dx.doi.org/10.1016/j.cnsns.2009.09.002` doi: 10.1016/j.cnsns.2009.09.002

Liu, J., Gaynor, A. T., Chen, S., Kang, Z., Suresh, K., Takezawa, A., ... To, A. C. (2018). Current and future trends in topology optimization for additive manufacturing. *Structural and Multidisciplinary Optimization*, *57*(6), 2457–2483. doi: 10.1007/s00158-018-1994-3

Lourdes Thomas, T., Kalpathy Venkiteswaran, V., Ananthasuresh, G. K., & Misra, S. (2021). Surgical Applications of Compliant Mechanisms: A Review. *Journal of Mechanisms and Robotics*, *13*(2). doi: 10.1115/1.4049491

MacHekposhti, D. F., Herder, J. L., Semon, G., & Tolou, N. (2018). A Compliant Micro Frequency Quadrupler Transmission Utilizing Singularity. *Journal of Microelectromechanical Systems*, *27*(3), 506–512. doi: 10.1109/JMEMS.2018.2825442

Megaro, V., Zehnder, J., Bächer, M., Coros, S., Gross, M., & Thomaszewski, B. (2017). A computational design tool for compliant mechanisms. *ACM Transactions on Graphics*, *36*(4). doi: 10.1145/3072959.3073636

Merriam, E. G., Jones, J. E., Magleby, S. P., & Howell, L. L. (2013). Monolithic 2 DOF fully compliant space pointing mechanism. *Mechanical Sciences*, *4*(2), 381–390. doi: 10.5194/ms-4-381-2013

Midha, A., Norton, T. W., & Howell, L. L. (1992, 9). On the Nomenclature and Classification of Compliant Mechanisms: Abstractions of Mechanisms and Mechanism Synthesis Problems. In *22nd biennial mechanisms conference: Flexible mechanisms, dynamics, and analysis* (Vol. 47). American Society of Mechanical Engineers. Retrieved from https://asmedigitalcollection.asme.org/IDETC-CIE/proceedings/DETC92/09419/225/1105587 doi: 10.1115/DETC1992-0385

Miyata, M., Robinson, R. C., Uyeda, T. Q., Fukumori, Y., Fukushima, S. i., Haruta, S., ... Wakabayashi, K. i. (2020). Tree of motility – A proposed history of motility systems in the tree of life. *Genes to Cells*, *25*(1), 6–21. doi: 10.1111/gtc.12737

Najah, A., Cochelin, B., Damil, N., & Potier-Ferry, M. (1998, 3). A critical review of asymptotic numerical methods. *Archives of Computational Methods in Engineering*, *5*(1), 31–50. Retrieved from http://link.springer.com/10.1007/BF02736748 doi: 10.1007/BF02736748

Noor, A. K., & Peters, J. M. (1983). Recent advances in reduction methods for instability analysis of structures. *Computers and Structures*, *16*(1-4), 67–80. doi: 10.1016/0045-7949(83)90148-7

Parenti-Castelli, V., & Sancisi, N. (2013). *Synthesis of Spatial Mechanisms to Model Human Joints*. doi: 10.1007/978-1-4471-4510-3{_}3

Pedersen, C. B. W., Buhl, T., & Sigmund, O. (2001). Topology synthesis of large-displacement compliant mechanisms. *International Journal for Numerical Methods in Engineering*, *50*(12), 2683–2705. Retrieved from http://link.springer.com/10.1007/BF01743537https://onlinelibrary.wiley.com/doi/10.1002/nme.148 doi: 10.1002/nme.148

Poincare, H. (1992). *New Methods of Celestial Mechanics* (1st ed.; D. Goroff, Ed.). Melville, NY.

Powell, M. J. D. (1964, 2). An efficient method for finding the minimum of a function of several variables without calculating derivatives. *The Computer Journal*, *7*(2), 155–162. Retrieved from https://academic.oup.com/comjnl/article-lookup/doi/10.1093/comjnl/7.2.155 doi: 10.1093/comjnl/7.2.155

Powell, M. J. D. (1981). *Approximation theory and methods*. Cambridge University Press. doi: 10.1017/CBO9781139171502

Rabanser, S., Shchur, O., & Günnemann, S. (2017, 11). Introduction to Tensor Decompositions and their Applications in Machine Learning. *arXiv preprint arXiv:1711.10781*, 1–13. Retrieved from http://arxiv.org/abs/1711.10781

Rajih, M., Comon, P., & Harshman, R. A. (2008, 1). Enhanced Line Search: A Novel Method to Accelerate PARAFAC. *SIAM Journal on Matrix Analysis and Applications*, *30*(3), 1128–1147. Retrieved from http://epubs.siam.org/doi/10.1137/06065577 doi: 10.1137/06065577

Rus, D., & Tolley, M. T. (2015). Design, fabrication and control of soft robots. *Nature*, *521*(7553), 467–475. doi: 10.1038/nature14543

Sendra, J. R., Winkler, F., & Pérez-Díaz, S. (2008). Rational algebraic curves. *Algorithms and Computation in Mathematics*, *22*.

Shuib, S., Ridzwan, M. I., & Kadarman, A. H. (2007). Methodology of compliant mechanisms and its current developments in applications: A review. *American Journal of Applied Sciences*, *4*(3), 160–167. doi: 10.3844/ajassp.2007.160.167

Sigmund, O. (1997). On the design of compliant mechanisms using topology optimization. *Mechanics of Structures and Machines*, *25*(4), 493–524. doi: 10.1080/08905459708945415

Sigmund, O. (2001). A 99 line topology optimization code written in matlab. *Structural and Multidisciplinary Optimization*, *21*(2), 120–127. doi: 10.1007/s001580050176

Sigmund, O., & Petersson, J. (1998). Numerical instabilities in topology optimization: A survey on procedures dealing with checkerboards, mesh-dependencies and local minima. *Structural Optimization*, *16*(1), 68–75. doi: 10.1007/BF01214002

Stewart, J. (2016). *Calculus: early transcendentals 8th edition*. Cengage Learning.

Sturmfels, B. (2016). Tensors and their eigenvectors. *Notices of the AMS*, *63*(6).

Svanberg, K. (1987). The method of moving asymptotes—a new method for structural optimization. *International Journal for Numerical Methods in Engineering*, *24*(2), 359–373. doi: 10.1002/nme.1620240207

Thompson, J. M., & Walker, A. C. (1968). The non-linear perturbation analysis of discrete structural systems. *International Journal of Solids and Structures*, *4*(8), 757–768. Retrieved from `http://dx.doi.org/10.1016/0020-7683(68)90054-1` doi: 10.1016/0020-7683(68)90054-1

Trefethen, L. N., & Bau, D. (2022). *Numerical linear algebra* (Vol. 181). Siam.

Turner, M. J., Dill, E. H., Martin, H. C., & Melosh, R. J. (1960, 2). Large Deflections of Structures Subjected to Heating and External Loads. *Journal of the Aerospace Sciences*, *27*(2), 97–106. Retrieved from `https://arc.aiaa.org/doi/10.2514/8.8412` doi: 10.2514/8.8412

van Dijk, N. P., Langelaar, M., & van Keulen, F. (2014). Element deformation scaling for robust geometrically nonlinear analyses in topology optimization. *Structural and Multidisciplinary Optimization*, *50*(4), 537–560. doi: 10.1007/s00158-014-1145-4

Wang, C., Zhao, Z., Zhou, M., Sigmund, O., & Zhang, X. S. (2021). *A comprehensive review of educational articles on structural and multidisciplinary optimization* (Vol. 64) (No. 5). Springer Berlin Heidelberg. Retrieved from `https://doi.org/10.1007/s00158-021-03050-7` doi: 10.1007/s00158-021-03050-7

Wang, F., Lazarov, B. S., Sigmund, O., & Jensen, J. S. (2014, 7). Interpolation scheme for fictitious domain techniques and topology optimization of finite strain elastic problems. *Computer Methods in Applied Mechanics and Engineering*, *276*, 453–472. Retrieved from `https://linkinghub.elsevier.com/retrieve/pii/S0045782514001078` doi: 10.1016/j.cma.2014.03.021

Williamson, F. (1980). Richard courant and the finite element method: A further look. *Historia Mathematica*, *7*, 369–378. doi: 10.1016/0315-0860(80)90001-4

Wurm, E., Jüttler, B., & Kim, M.-S. (2005). Approximate Rational Parameterization of Implicitly Defined Surfaces. In *Lecture notes in computer science (including subseries lecture notes in artificial intelligence and lecture notes in bioinformatics)* (Vol. 3604 LNCS, pp. 434–447). Retrieved from `http://link.springer.com/10.1007/11537908_26` doi: 10.1007/11537908{_}26

Yoon, G. H., & Kim, Y. Y. (2005, 4). Element connectivity parameterization for topology optimization of geometrically nonlinear structures. *International Journal of Solids and Structures*, *42*(7), 1983–2009. Retrieved from `https://linkinghub.elsevier.com/retrieve/pii/S0020768304004962` doi: 10.1016/j.ijsolstr.2004.09.005

Yu, J., Li, S., Su, H. j., & Culpepper, M. L. (2011). Screw theory based methodology for the deterministic type synthesis of flexure mechanisms. *Journal of Mechanisms and Robotics*, *3*(3). doi: 10.1115/1.4004123

Zhang, L., Zhang, Y., & van Keulen, F. (2023). Topology optimization of geometrically nonlinear structures using reduced-order modeling. *Computer Methods in Applied Mechanics and Engineering*, *416*, 116371. Retrieved from https://doi.org/10.1016/j.cma.2023.116371 doi: 10.1016/j.cma.2023.116371

Zhang, X., & Zhu, B. (2018). *Topology optimization of compliant mechanisms*. doi: 10.1007/978-981-13-0432-3

Zhou, M., & Rozvany, G. (1991, 8). The COC algorithm, Part II: Topological, geometrical and generalized shape optimization. *Computer Methods in Applied Mechanics and Engineering*, *89*(1-3), 309–336. Retrieved from https://linkinghub.elsevier.com/retrieve/pii/0045782591900469 doi: 10.1016/0045-7825(91)90046-9

Zhu, B., Zhang, X., Zhang, H., Liang, J., Zang, H., Li, H., & Wang, R. (2020). Design of compliant mechanisms using continuum topology optimization: A review. *Mechanism and Machine Theory*, *143*. doi: 10.1016/j.mechmachtheory.2019.103622

ZHU, J., ZHOU, H., WANG, C., ZHOU, L., YUAN, S., & ZHANG, W. (2021). A review of topology optimization for additive manufacturing: Status and challenges. *Chinese Journal of Aeronautics*, *34*(1), 91–110. Retrieved from https://doi.org/10.1016/j.cja.2020.09.020 doi: 10.1016/j.cja.2020.09.020

Zu, M.-l. (1885). Mittheilung, einen von König Oscar II gestifteten mathematischen Preis betreffend. *Acta Mathematica*, *7*(1), I-VI. Retrieved from http://projecteuclid.org/euclid.acta/1485888287 doi: 10.1007/BF02402191

Appendices

A

Finite Element Tensor Formulation

The structural equations are fundamental to modeling and analyzing the non-linear relation between applied load and deformation. They are used to provide a numerical indication of a structure's expected performance in practice. The structural model adopted in the present work is founded on the seminal procedures of Bathe (2016, Chapter 6). This first appendix aims to provide supplementary details on the methodology elaborated in Section III, mainly considering the structural equations on the element level. First, Appendix A.1 elaborates Bathe's canonical form of internal energy, internal force, and tangent stiffness. Then, Appendix A.2 extends their formulation using even higher-order displacement-derivatives, facilitating a multivariate, tensorial formulation and the perturbed structural analysis. Finally, Appendix A.3 shows how to decompose the involved structural tensors, turning the otherwise computationally impractical form even more efficient than the canonical form. Note that each subappendix concludes with a floating-point operation count for the internal force $\boldsymbol{f}(\boldsymbol{u})$ and tangent stiffness $\boldsymbol{\mathcal{K}}(\boldsymbol{u})$, respectively through their canonical, dense tensorial, and decomposed tensorial forms.

A.1 Canonical Structural Equations

Recall from Section III that the density-based structural design is modeled using a regular grid of tiny structural elements of varying stiffness, after subdividing design-domain Ω (Figure III.1) into some M corresponding element-domains. Design vector $\boldsymbol{x} \in \mathbb{R}^M$ then contains for each element a continuous scalar between zero and one, controlling these stiffnesses, effectively defining the total structure's design and consequently its structural energetic and kinematic behavior. The latter is characterized by the (non-linear) relation between the deformation- and applied pressure fields, such that the total potential is minimized, and the boundary conditions are satisfied. Both fields and their boundary conditions are mediated through work-equivalent nodal quantities, *deformation*-vector $\boldsymbol{u} \in \mathbb{R}^N$ and *applied force*-vector $\boldsymbol{p} \in \mathbb{R}^N$ respectively, with N as the amount of deformation freedom degrees among the nodes. Since structural assembly and coordinate mapping have readily been covered in Subsection III.5, the presented derivations of the structural equations concern only a single structural element over its natural coordinates for simplicity.

Consider the single, two-dimensional, four-noded structural element e in its deformed state in Figure A.1.1. Let its initial or material coordinates be denoted by ${}^0\boldsymbol{\xi} \in {}^0\ \Omega_e \subset \mathbb{R}^2$, with the material domain ${}^0\Omega_e$ taken as the square between ± 1 along both coordinates. The material, hence the initial material coordinates ${}^0\boldsymbol{\xi}$, may arbitrarily *deform* towards some other ${}^t\boldsymbol{\xi} = {}^0\ \boldsymbol{\xi} + \boldsymbol{u}^*({}^0\boldsymbol{\xi}) \in \mathbb{R}^2$, where $\boldsymbol{u}^*({}^0\boldsymbol{\xi}) \in \mathbb{R}^2$ denotes the local material displacement. However, considering the element as a very small but finite part of a continuous structure, this deformation may be accurately approximated by interpolating the nodal displacements, accommodating finite computational power. The remainder of

this subappendix shall elaborate on the mentioned displacement interpolation, the elastic energy stored within this deformed element, and its displacement derivatives required to find structural equilibrium, according to the seminal procedures of Bathe (2016, Chapter 6).

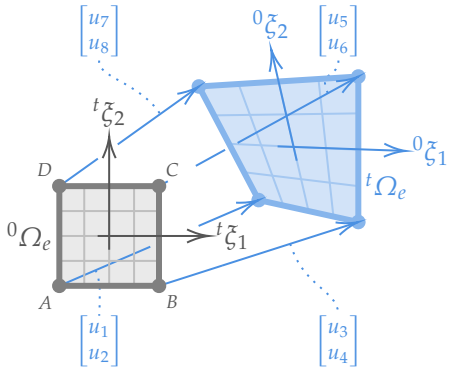

Figure A.1.1: Coordinate mapping diagram for some element e. w.r.t. global frame of reference: a. w.r.t. local spatial coordinates: ${}^t a$. w.r.t. local deformed material coordinates: ${}^0 a$

The elastic potential, or internally stored energy $\mathcal{E}_e$ (Equation A.1.1) of the deformed elastic element e (Figure A.1.1), is modeled using bilinear nodal interpolation of deformation, and Green-Lagrange strain through a total Lagrangian approach, assuming isotropic linear elasticity. In essence, local strain-energy is integrated over the element's undeformed material domain $\Omega_e \equiv {}^0\Omega_e$, based on nodally interpolated deformations and corresponding strains, elaborated duly:

$$\mathcal{E}_e = \iint\limits_{\xi \in \Omega_e} \tfrac{1}{2} \gamma_m \underbrace{D_{mn} \gamma_n}_{\tau_m} \mathrm{d}\Omega_e \ , \qquad \begin{matrix} m = 1,\ 2,\ 3\ , \\ n = 1,\ 2,\ 3\ , \end{matrix} \tag{A.1.1}$$

where $\Omega_e = \{(\xi_1,\ \xi_2) : -1 \leqslant \xi_1 \leqslant 1 \wedge -1 \leqslant \xi_2 \leqslant 1\}$ denotes the undeformed element's domain, γ_m the Green-Lagrange strains in Voigt-notation (Equation A.1.2), τ_m the Second Piola-Kirchhoff stresses in Voigt-notation, and D_{mn} the constant elastic moduli that map strains γ_n to stresses τ_m:

$$\boldsymbol{\tau} \equiv \begin{bmatrix} \tau_{11} \\ \tau_{22} \\ \tau_{12} \end{bmatrix} = \boldsymbol{D}\boldsymbol{\gamma}\ , \qquad \tau_m = D_{mn}\gamma_n\ , \qquad \boldsymbol{\gamma} \equiv \begin{bmatrix} \gamma_{11} \\ \gamma_{22} \\ 2\gamma_{12} \end{bmatrix}\ , \quad \gamma_{ij} = \tfrac{1}{2}(F_{ki}F_{kj} - \delta_{ij})\ , \quad \begin{matrix} i = 1,\ 2\ , \\ j = 1,\ 2\ , \\ k = 1,\ 2\ , \end{matrix} \tag{A.1.2}$$

where γ_{ij} denote the Green-Lagrange strains in Tensor-notation, F_{ij} the deformation gradient (Equation A.1.3), and $\delta_{ij} = 1 \Leftrightarrow i = j$ while $\delta_{ij} = 0 \Leftrightarrow i \neq j$. The deformation gradient F_{ij} is then based on the bilinearly interpolated displacement field $u_i^* = H_{ik}u_k$:

$$\boldsymbol{F} \equiv \begin{bmatrix} F_{11} \\ F_{12} \\ F_{21} \\ F_{22} \end{bmatrix}\ , \qquad F_{ij} \equiv \frac{\mathrm{d}({}^t\xi_i)}{\mathrm{d}({}^0\xi_j)} = \frac{\mathrm{d}\left(\xi_i + H_{ik}u_k\right)}{\mathrm{d}\xi_j} = \delta_{ij} + \frac{\mathrm{d}H_{ik}}{\mathrm{d}\xi_j}u_k\ , \quad \begin{matrix} i = 1,\ 2\ , \\ j = 1,\ 2\ , \\ k = 1,\ ...,\ 8\ , \end{matrix} \tag{A.1.3}$$

where u_k denote the independent nodal displacements and H_{ik} the bilinear interpolation functions:

$$\boldsymbol{H} \equiv \begin{bmatrix} h_A & 0 & h_B & 0 & h_C & 0 & h_D & 0 \\ 0 & h_A & 0 & h_B & 0 & h_C & 0 & h_D \end{bmatrix}\ , \qquad \text{with} \tag{A.1.4}$$

$$\boldsymbol{h} \equiv \begin{bmatrix} h_A \\ h_B \\ h_C \\ h_D \end{bmatrix} \equiv \frac{1}{4}\begin{bmatrix} (\xi_1 - 1)(\xi_2 - 1) \\ (\xi_1 - 1)(\xi_2 + 1) \\ (\xi_1 + 1)(\xi_2 + 1) \\ (\xi_1 + 1)(\xi_2 - 1) \end{bmatrix}\ , \qquad \frac{\mathrm{d}\boldsymbol{h}}{\mathrm{d}\boldsymbol{\xi}} = \frac{1}{4}\begin{bmatrix} \xi_2 - 1 & \xi_1 - 1 \\ -\xi_2 + 1 & -\xi_1 - 1 \\ \xi_2 + 1 & \xi_1 + 1 \\ -\xi_2 - 1 & -\xi_1 + 1 \end{bmatrix}\ ,$$

where the components of $\boldsymbol{h}$ denote the actual nodal shapefunctions, simply rearranged into $\boldsymbol{H}$ to facilitate a more compact definition of the deformation gradient F_{ij}.

Recall that the structural equations relate applied force and deformation, through minimum total

potential, in case of a conservative system. Hence, the goal is to find the deformation for which the derivative of the total potential versus deformation equals zero. Using a Newton-Raphson approach, even the second-order derivative of the total potential is required. Recall from II.2 that the total potential equals the internally stored elastic energy, minus externally exerted work. Since the present appendix only concerns the internal energy $\mathcal{E}$ on the element level, its first- and second-order derivative versus displacement shall be elaborated next, respectively denoted as the internal force vector $\boldsymbol{f}$ and tangent stiffness matrix $\boldsymbol{\mathcal{K}}$. Furthermore, subscript e denoting the element number, and left-hand superscript 0 denoting the initial undeformed state, will be omitted from here on out for simplicity. A convenient consequence of the Total Lagrangian Approach, is that functional dependence on nodal displacements $\boldsymbol{u} = [u_1,\ ...,\ u_8]^\top \in \mathbb{R}^8$ and material coordinates $\boldsymbol{\xi} = [\xi_1,\ \xi_2]^\top \in \mathbb{R}^2$ has become separate. In other words, $\boldsymbol{u}$ and $\boldsymbol{\xi}$ are independent, thus differentiation and integration with respect to either may be performed in arbitrary order:

$$\mathcal{E}(\boldsymbol{u}) \equiv \int_\Omega \tfrac{1}{2}\gamma_m(\boldsymbol{u}) D_{mn} \gamma_n(\boldsymbol{u})\, \mathrm{d}\Omega \ , \tag{A.1.5a}$$

$$f_i(\boldsymbol{u}) \equiv \frac{\mathrm{d}\mathcal{E}}{\mathrm{d}u_i} = \int_\Omega \underbrace{\frac{\mathrm{d}\gamma_m}{\mathrm{d}u_i}}_{\left(\mathbf{B}_\mathrm{L}(\boldsymbol{u})\right)_{mi}} \underbrace{D_{mn}\gamma_n(\boldsymbol{u})}_{\tau_m(\boldsymbol{u})}\, \mathrm{d}\Omega \ , \tag{A.1.5b}$$

$$\mathcal{K}_{ij}(\boldsymbol{u}) \equiv \frac{\mathrm{d}^2\mathcal{E}}{\mathrm{d}u_i\,\mathrm{d}u_j} = \int_\Omega \underbrace{\frac{\mathrm{d}\gamma_m}{\mathrm{d}u_i} D_{mn} \frac{\mathrm{d}\gamma_n}{\mathrm{d}u_j}}_{\left(\frac{\mathrm{d}}{\mathrm{d}\Omega}\boldsymbol{\mathcal{K}}_\mathrm{L}(\boldsymbol{u})\right)_{ij}} + \underbrace{\frac{\mathrm{d}^2\gamma_m}{\mathrm{d}u_i\,\mathrm{d}u_j} D_{mn}\gamma_n(\boldsymbol{u})}_{\left(\frac{\mathrm{d}}{\mathrm{d}\Omega}\boldsymbol{\mathcal{K}}_\mathrm{NL}(\boldsymbol{u})\right)_{ij}}\, \mathrm{d}\Omega \ , \tag{A.1.5c}$$

$$\text{where} \quad \left(\tfrac{\mathrm{d}}{\mathrm{d}\Omega}\boldsymbol{\mathcal{K}}_\mathrm{NL}(\boldsymbol{u})\right)_{ij} = \underbrace{\frac{\mathrm{d}F_p}{\mathrm{d}u_i}}_{\left(\mathbf{B}_\mathrm{NL}(\boldsymbol{u})\right)_{pi}} \underbrace{\left(\frac{\partial^2\gamma_m}{\partial F_p \partial F_q}\tau_m(\boldsymbol{u})\right)}_{\left(\boldsymbol{\mathcal{T}}(\boldsymbol{u})\right)_{pq}} \underbrace{\frac{\mathrm{d}F_q}{\mathrm{d}u_j}}_{\left(\mathbf{B}_\mathrm{NL}(\boldsymbol{u})\right)_{qj}} \ ,$$

where $\mathbf{B}_\mathrm{L} \in \mathbb{R}^{(3\times 8)}$ and $\mathbf{B}_\mathrm{NL} \in \mathbb{R}^{(4\times 8)}$ can be recognized as the canonical *'linear'* and *'non-linear'* strain-displacement matrices[1] from Bathe (2016) and De Borst et al. (2012):

$$\mathbf{B}_\mathrm{L} \equiv \frac{\mathrm{d}\boldsymbol{\gamma}}{\mathrm{d}\boldsymbol{u}} = \begin{bmatrix} F_{11}\frac{\mathrm{d}h_A}{\mathrm{d}\xi_1} & F_{21}\frac{\mathrm{d}h_A}{\mathrm{d}\xi_1} & \cdots & F_{11}\frac{\mathrm{d}h_D}{\mathrm{d}\xi_1} & F_{21}\frac{\mathrm{d}h_D}{\mathrm{d}\xi_1} \\ F_{12}\frac{\mathrm{d}h_A}{\mathrm{d}\xi_2} & F_{22}\frac{\mathrm{d}h_A}{\mathrm{d}\xi_2} & \cdots & F_{12}\frac{\mathrm{d}h_D}{\mathrm{d}\xi_2} & F_{22}\frac{\mathrm{d}h_D}{\mathrm{d}\xi_2} \\ F_{11}\frac{\mathrm{d}h_A}{\mathrm{d}\xi_2} + F_{21}\frac{\mathrm{d}h_A}{\mathrm{d}\xi_1} & F_{21}\frac{\mathrm{d}h_A}{\mathrm{d}\xi_2} + F_{22}\frac{\mathrm{d}h_A}{\mathrm{d}\xi_1} & \cdots & F_{11}\frac{\mathrm{d}h_D}{\mathrm{d}\xi_2} + F_{21}\frac{\mathrm{d}h_D}{\mathrm{d}\xi_1} & F_{21}\frac{\mathrm{d}h_D}{\mathrm{d}\xi_2} + F_{22}\frac{\mathrm{d}h_D}{\mathrm{d}\xi_1} \end{bmatrix} , \tag{A.1.6}$$

$$\mathbf{B}_\mathrm{NL} \equiv \frac{\mathrm{d}\boldsymbol{F}}{\mathrm{d}\boldsymbol{u}} = \begin{bmatrix} \frac{\mathrm{d}h_A}{\mathrm{d}\xi_1} & 0 & \frac{\mathrm{d}h_B}{\mathrm{d}\xi_1} & 0 & \frac{\mathrm{d}h_C}{\mathrm{d}\xi_1} & 0 & \frac{\mathrm{d}h_D}{\mathrm{d}\xi_1} & 0 \\ \frac{\mathrm{d}h_A}{\mathrm{d}\xi_2} & 0 & \frac{\mathrm{d}h_B}{\mathrm{d}\xi_2} & 0 & \frac{\mathrm{d}h_C}{\mathrm{d}\xi_2} & 0 & \frac{\mathrm{d}h_D}{\mathrm{d}\xi_2} & 0 \\ 0 & \frac{\mathrm{d}h_A}{\mathrm{d}\xi_1} & 0 & \frac{\mathrm{d}h_B}{\mathrm{d}\xi_1} & 0 & \frac{\mathrm{d}h_C}{\mathrm{d}\xi_1} & 0 & \frac{\mathrm{d}h_D}{\mathrm{d}\xi_1} \\ 0 & \frac{\mathrm{d}h_A}{\mathrm{d}\xi_2} & 0 & \frac{\mathrm{d}h_B}{\mathrm{d}\xi_2} & 0 & \frac{\mathrm{d}h_C}{\mathrm{d}\xi_2} & 0 & \frac{\mathrm{d}h_D}{\mathrm{d}\xi_2} \end{bmatrix} . \tag{A.1.7}$$

Lastly, The Voigt-like reshape of the deformation gradient, $\boldsymbol{F}$, and the matrix containing the Second Piola-Kirchhoff stresses, $\boldsymbol{\mathcal{T}}$, may then compactly be calculated as:

[1] Note that both the linear and non-linear strain-displacement matrices $\mathbf{B}_\mathrm{L}$ and $\mathbf{B}_\mathrm{NL}$ are in-fact *quadratic*, thus non-linear, in both $\boldsymbol{u}$ and $\boldsymbol{\xi}$. When $\boldsymbol{u} = \mathbf{0}$ however, $\mathbf{B}_\mathrm{L}$ does equal the strain-displacement matrix as derived in *linear* FEM, while $\mathbf{B}_\mathrm{NL}$ vanishes.

$$\boldsymbol{F} = \begin{bmatrix} \frac{\mathrm{d}h_A}{\mathrm{d}\xi_1}u_1 + \frac{\mathrm{d}h_B}{\mathrm{d}\xi_1}u_3 + \frac{\mathrm{d}h_C}{\mathrm{d}\xi_1}u_5 + \frac{\mathrm{d}h_D}{\mathrm{d}\xi_1}u_7 + 1 \\ \frac{\mathrm{d}h_A}{\mathrm{d}\xi_2}u_1 + \frac{\mathrm{d}h_B}{\mathrm{d}\xi_2}u_3 + \frac{\mathrm{d}h_C}{\mathrm{d}\xi_2}u_5 + \frac{\mathrm{d}h_D}{\mathrm{d}\xi_2}u_7 \\ \frac{\mathrm{d}h_A}{\mathrm{d}\xi_1}u_2 + \frac{\mathrm{d}h_B}{\mathrm{d}\xi_1}u_4 + \frac{\mathrm{d}h_C}{\mathrm{d}\xi_1}u_6 + \frac{\mathrm{d}h_D}{\mathrm{d}\xi_1}u_8 \\ \frac{\mathrm{d}h_A}{\mathrm{d}\xi_2}u_2 + \frac{\mathrm{d}h_B}{\mathrm{d}\xi_2}u_4 + \frac{\mathrm{d}h_C}{\mathrm{d}\xi_2}u_6 + \frac{\mathrm{d}h_D}{\mathrm{d}\xi_2}u_8 + 1 \end{bmatrix} , \tag{A.1.8}$$

$$\boldsymbol{\mathcal{T}} \equiv \boldsymbol{\tau} \bullet \frac{\mathrm{d}^2\boldsymbol{\gamma}}{\mathrm{d}\boldsymbol{F}^{\overset{2}{\otimes}}} = \begin{bmatrix} \tau_{11} & \tau_{12} & 0 & 0 \\ \tau_{12} & \tau_{22} & 0 & 0 \\ 0 & 0 & \tau_{11} & \tau_{12} \\ 0 & 0 & \tau_{12} & \tau_{22} \end{bmatrix} . \tag{A.1.9}$$

To finalize this subappendix on the canonical form of an element's internal force $\boldsymbol{f}$ and tangent stiffness $\boldsymbol{\mathcal{K}}$, their calculation and floating-point operation count are elaborated through the diagram in Figure A.1.2. Admittedly, the resulting numbers may still overestimate those of an optimized implementation. Still, all quantities are implemented as derived in this subappendix, and the number of floating-point operations accounts for addition and multiplication. Note that the numbers of flops for the domain-derivatives, $\mathrm{d}\boldsymbol{f}/\mathrm{d}\Omega$, $\mathrm{d}\boldsymbol{f}/\mathrm{d}\Omega$ and $\mathrm{d}\boldsymbol{f}/\mathrm{d}\Omega$, are approximated assuming dense matrix multiplication. For all other quantities, the number of flops are determined through their explicit minimal forms as shown in this subappendix.

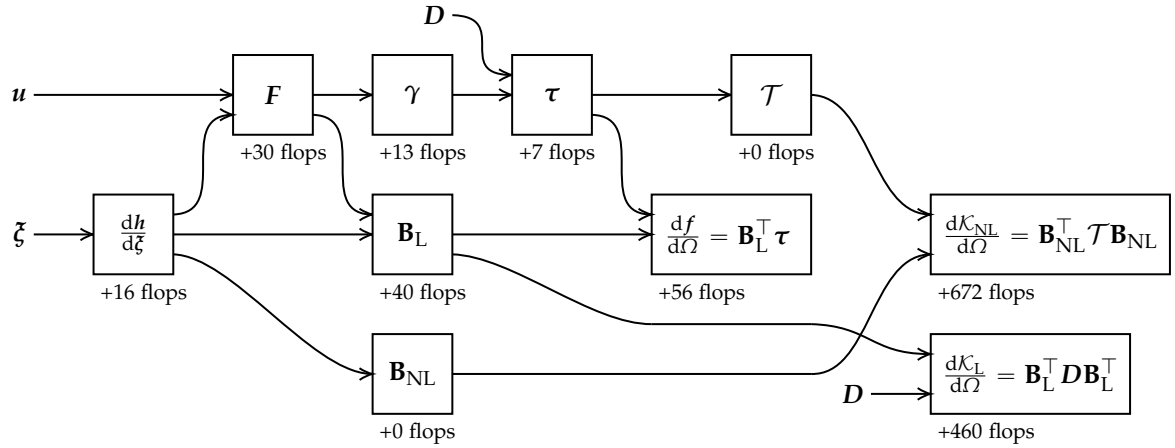

Figure A.1.2: Calculation diagram, including the number of floating-point operations (flops), regarding intermediate quantities required for the canonical formulation and calculation of internal force $\boldsymbol{f}$ and tangent stiffness $\boldsymbol{\mathcal{K}}$ for a single structural element. Note that the instances of +0 flops involve the rearrangement of known quantities.

The total number of flops required for $\boldsymbol{f}$ and $\boldsymbol{K}$ are determined, assuming exact integration through a 3 by 3 Gauss quadrature rule (Bathe, 2016) to accomodate their fourth-order polynomial nature versus the respective components of $\boldsymbol{\xi}$:

$$I \equiv \int_{\boldsymbol{\xi}\in\Omega} \iota(\boldsymbol{\xi})\,\mathrm{d}\Omega = \sum_{i=1}^{3}\sum_{j=1}^{3} \iota(\boldsymbol{\xi}_{ij})w_{ij} \,. \tag{A.1.10}$$

Adding all numbers of flops required for $\mathrm{d}\boldsymbol{f}/\mathrm{d}\Omega$ yields a total of 162. Then, repeating this for all 9 integration points yields a total of 1458. Finally, incorporating all weights and additions of the quadrature rule, yields a total of 1594 flops in order to calculate the internal force $\boldsymbol{f}$, for a single structural element. Likewise, adding all numbers of flops required for $\mathrm{d}\boldsymbol{\mathcal{K}}/\mathrm{d}\Omega$ yields a total of 1302, without exploiting symmetry, or assuming that the quantities required for $\mathrm{d}\boldsymbol{f}/\mathrm{d}\Omega$ have readily been calculated. Again, repeating this for all 9 integration points yields a total of 11 718 flops. Finally, incorporating all weights and additions of the quadrature rule, yields a grand total of 12 806 flops in order to calculate the tangent stiffness $\boldsymbol{\mathcal{K}}$, for a single structural element. These values are sumarized in

Table A.3.1.

A.2 Tensor Reformulation

In order to perform perturbed structural analysis about some particular (equilibrium) point, ultimately all local higher-order displacement derivatives of the elastically stored energy $\mathcal{E}(\boldsymbol{u})$ are required through the chain rule. These evaluated higher-order displacement derivatives essentially extend the internal force $\boldsymbol{f}(\boldsymbol{u})$ and tangent stiffness $\boldsymbol{\mathcal{K}}(\boldsymbol{u})$ as obtained in the previous Appendix A.1, but notably no further than the fourth-order. To clarify, higher-order derivatives vanish, as $\mathcal{E}(\boldsymbol{u})$ is ultimately bilinear in $\boldsymbol{\gamma}$, which itself is bilinear in $\boldsymbol{u}$, meaning that $\mathcal{E}(\boldsymbol{u})$ is ultimately quartic in $\boldsymbol{u}$:

$$\mathcal{E}(\boldsymbol{u}) = \int_\Omega \tfrac{1}{2}\gamma_m(\boldsymbol{u}) D_{mn} \gamma_n(\boldsymbol{u}) \,\mathrm{d}\Omega \ , \tag{A.2.1a}$$

$$f_i(\boldsymbol{u}) \equiv \frac{\mathrm{d}\mathcal{E}}{\mathrm{d}u_i} = \int_\Omega \underbrace{\frac{\mathrm{d}\gamma_m}{\mathrm{d}u_i}}_{\left(\mathbf{B}_\mathrm{L}(\boldsymbol{u})\right)_{mi}} \underbrace{D_{mn}\gamma_n(\boldsymbol{u})}_{\tau_m(\boldsymbol{u})} \mathrm{d}\Omega \ , \tag{A.2.1b}$$

$$\mathcal{K}_{ij}(\boldsymbol{u}) \equiv \frac{\mathrm{d}^2\mathcal{E}}{\mathrm{d}u_i\,\mathrm{d}u_j} = \int_\Omega \underbrace{\frac{\mathrm{d}\gamma_m}{\mathrm{d}u_i} D_{mn} \frac{\mathrm{d}\gamma_n}{\mathrm{d}u_j}}_{\left(\frac{\mathrm{d}}{\mathrm{d}\Omega}\boldsymbol{\mathcal{K}}_\mathrm{L}(\boldsymbol{u})\right)_{ij}} + \underbrace{\frac{\mathrm{d}^2\gamma_m}{\mathrm{d}u_i\,\mathrm{d}u_j} D_{mn}\gamma_n(\boldsymbol{u})}_{\left(\frac{\mathrm{d}}{\mathrm{d}\Omega}\boldsymbol{\mathcal{K}}_\mathrm{NL}(\boldsymbol{u})\right)_{ij}} \mathrm{d}\Omega \ , \tag{A.2.1c}$$

$$\text{where} \quad \left(\tfrac{\mathrm{d}}{\mathrm{d}\Omega}\boldsymbol{\mathcal{K}}_\mathrm{NL}(\boldsymbol{u})\right)_{ij} = \underbrace{\frac{\mathrm{d}F_p}{\mathrm{d}u_i}}_{\left(\mathbf{B}_\mathrm{NL}(\boldsymbol{u})\right)_{pi}} \underbrace{\left(\frac{\partial^2\gamma_m}{\partial F_p \partial F_q}\tau_m(\boldsymbol{u})\right)}_{\left(\boldsymbol{\mathcal{T}}(\boldsymbol{u})\right)_{pq}} \underbrace{\frac{\mathrm{d}F_q}{\mathrm{d}u_j}}_{\left(\mathbf{B}_\mathrm{NL}(\boldsymbol{u})\right)_{qj}} \ ,$$

$$\mathcal{S}_{ijk}(\boldsymbol{u}) \equiv \frac{\mathrm{d}^3\mathcal{E}}{\mathrm{d}u_i\,\mathrm{d}u_j\,\mathrm{d}u_k} = \int_\Omega \underbrace{\frac{\mathrm{d}^2\gamma_m}{\mathrm{d}u_i\,\mathrm{d}u_j} D_{mn} \frac{\mathrm{d}\gamma_n}{\mathrm{d}u_k}}_{\left(\frac{\mathrm{d}}{\mathrm{d}\Omega}\boldsymbol{\mathcal{S}}_\mathrm{NL}(\boldsymbol{u})\right)_{ijk}} + \underbrace{\frac{\mathrm{d}^2\gamma_m}{\mathrm{d}u_i\,\mathrm{d}u_k} D_{mn} \frac{\mathrm{d}\gamma_n}{\mathrm{d}u_j}}_{\left(\frac{\mathrm{d}}{\mathrm{d}\Omega}\boldsymbol{\mathcal{S}}_\mathrm{NL}(\boldsymbol{u})\right)_{ikj}} + \underbrace{\frac{\mathrm{d}^2\gamma_m}{\mathrm{d}u_j\,\mathrm{d}u_k} D_{mn} \frac{\mathrm{d}\gamma_n}{\mathrm{d}u_i}}_{\left(\frac{\mathrm{d}}{\mathrm{d}\Omega}\boldsymbol{\mathcal{S}}_\mathrm{NL}(\boldsymbol{u})\right)_{jki}} \mathrm{d}\Omega \ , \tag{A.2.1d}$$

$$\mathcal{Q}_{ijkl}(\boldsymbol{u}) \equiv \frac{\mathrm{d}^4\mathcal{E}}{\mathrm{d}u_i\,\mathrm{d}u_j\,\mathrm{d}u_k\,\mathrm{d}u_l} = \int_\Omega \underbrace{\frac{\mathrm{d}^2\gamma_m}{\mathrm{d}u_i\,\mathrm{d}u_j} D_{mn} \frac{\mathrm{d}^2\gamma_n}{\mathrm{d}u_k\,\mathrm{d}u_l}}_{\left(\frac{\mathrm{d}}{\mathrm{d}\Omega}\boldsymbol{\mathcal{Q}}_\mathrm{NL}\right)_{ijkl}} + \underbrace{\frac{\mathrm{d}^2\gamma_m}{\mathrm{d}u_i\,\mathrm{d}u_k} D_{mn} \frac{\mathrm{d}^2\gamma_n}{\mathrm{d}u_j\,\mathrm{d}u_l}}_{\left(\frac{\mathrm{d}}{\mathrm{d}\Omega}\boldsymbol{\mathcal{Q}}_\mathrm{NL}\right)_{ikjl}} + \underbrace{\frac{\mathrm{d}^2\gamma_m}{\mathrm{d}u_j\,\mathrm{d}u_k} D_{mn} \frac{\mathrm{d}^2\gamma_n}{\mathrm{d}u_i\,\mathrm{d}u_l}}_{\left(\frac{\mathrm{d}}{\mathrm{d}\Omega}\boldsymbol{\mathcal{Q}}_\mathrm{NL}\right)_{jkil}} \mathrm{d}\Omega \ . \tag{A.2.1e}$$

Note that all of these instantaneous structural tensors are symmetrical, as the order of differentiation does not matter assuming smoothness of the differentiated functions. In order to obtain and manage these quantities, using a symbolic toolbox is strongly advised.

The multivariate polynomial, or tensorial reformulation of the internal energy $\mathcal{E}(\boldsymbol{u})$ may be obtained without loss of accuracy, through its own MacLaurin expansion about the undeformed state, where $\boldsymbol{u} = \boldsymbol{0}$. Moreover, all of its higher-order local displacement derivatives are analogously reformulated with perfect accuracy through:

$$\mathcal{Q}_{ijkl}(\boldsymbol{u}) = Q_{ijkl} \ , \tag{A.2.2a}$$

$$\mathcal{S}_{ijk}(\boldsymbol{u}) = S_{ijk} + Q_{ijkl}u_l \ , \tag{A.2.2b}$$

$$\mathcal{K}_{ij}(\boldsymbol{u}) = K_{ij} + S_{ijk}u_k + \tfrac{1}{2}Q_{ijkl}u_k u_l \ , \tag{A.2.2c}$$

$$f_i(\boldsymbol{u}) = K_{ij}u_j + \tfrac{1}{2}S_{ijk}u_j u_k + \tfrac{1}{6}Q_{ijkl}u_j u_k u_l \ , \tag{A.2.2d}$$

$$\mathcal{E}(\boldsymbol{u}) = \tfrac{1}{2}K_{ij}u_i u_j + \tfrac{1}{6}S_{ijk}u_i u_j u_k + \tfrac{1}{24}Q_{ijkl}u_i u_j u_k u_l \ , \tag{A.2.2e}$$

with respectively defined coefficient tensors $K_{ij} \equiv \mathcal{K}_{ij}(\boldsymbol{0}) \in \mathrm{Sym}\left(\mathbb{R}^{8^2}\right)$, $S_{ijk} \equiv \mathcal{S}_{ijk}(\boldsymbol{0}) \in \mathrm{Sym}\left(\mathbb{R}^{8^3}\right)$ and $Q_{ijkl} \equiv \mathcal{Q}_{ijkl}(\boldsymbol{0}) \in \mathrm{Sym}\left(\mathbb{R}^{8^4}\right)$.

In order to demonstrate why the decomposition of these structural tensors is vital, the corresponding numbers of flops required to calculate the internal force $\boldsymbol{f}(\boldsymbol{u})$ and tangent stiffness $\mathcal{K}(\boldsymbol{u})$ are loosely argued here. For some multilinear form $\boldsymbol{A} \underset{d}{\bullet} \boldsymbol{u}^{\overset{d}{\otimes}}$ with $\boldsymbol{A} \in \mathrm{Sym}\left(\mathbb{R}^{8^{b+d}}\right)$ and $\boldsymbol{u} \in \mathbb{R}^8$, it is more efficient to successively contract $\boldsymbol{A}$ with $\boldsymbol{u}$, for a number of d times. Each fiber contraction then requires 8 multiplications and 7 additions, meaning 15 flops. The number of flops of the d successive contractions then totals at $8^{b+d-1} \cdot 15 + 8^{b+d-2} \cdot 15 + \cdots + 8^b \cdot 15$.

In the case of $\boldsymbol{f}$, including the 16 flops of adding the multilinear forms, an excessive total of 9976 flops is required. This is over six times the amount compared to the canonical form. Interestingly, for $\mathcal{K}$ one fewer contraction is required, making it slightly cheaper than $\boldsymbol{f}$. Including the 128 flops of adding the multilinear forms, $\mathcal{K}$ requires a total of 9792 flops, which is incidentally slightly lower compared to the canonical form as well. These values are summarized in Table A.3.1.

A.3 Tensor Decomposition

While the tensorial structural reformulation cannot be avoided for perturbed analysis, its computational ramifications can be remedied. Arguably, a minimal form may be achieved through tensor decomposition. Canonical Polyadic decomposition (Kolda & Bader, 2009) transforms some multilinear form, typically involving an excessive amount of cross terms, to a minimal sum of scalar products of pure linear forms. The remainder of this appendix elaborates on what this means, and then directly justifies the decomposition through a floating-point operation count and comparison with the canonical and dense tensorial formulations. Finally, a brief account is given of the process of actually obtaining the decompositions, which admittedly posed a substantial challenge within this work overall.

Tensor decomposition can be understood as a higher-order generalization of the spectral or eigen decomposition, singular value decomposition, or factorization otherwise, of matrices (Kolda & Bader, 2009; Bernardi et al., 2013). A possible decomposition of the element's structural tensors could be:

$$\boldsymbol{K} \in \mathrm{Sym}\left(\mathbb{R}^{8^2}\right) \ , \qquad \boldsymbol{K} = \sum_{r=1}^{8} \kappa_r \cdot \boldsymbol{\phi}_r^{\overset{2}{\otimes}} \ , \tag{A.3.1}$$

$$\boldsymbol{S} \in \mathrm{Sym}\left(\mathbb{R}^{8^3}\right) \ , \qquad \boldsymbol{S} = \sum_{r=1}^{R} \boldsymbol{s}_r \otimes \boldsymbol{q}_r^{\overset{2}{\otimes}} \ , \tag{A.3.2}$$

$$\boldsymbol{Q} \in \mathrm{Sym}\left(\mathbb{R}^{8^4}\right) \ , \qquad \boldsymbol{Q} = \sum_{r=1}^{R} \boldsymbol{q}_r^{\overset{4}{\otimes}} \ , \tag{A.3.3}$$

where the decomposition of $\boldsymbol{K}$ is notably just a spectral or eigen decomposition, with eigenvalues κ_r and eigen deformations $\boldsymbol{\phi}_r$ visualized in Figure A.3.1. The symmetric decomposition of higher-order tensors is loosely visualized in Figure A.3.2. Technically, the vectors $\boldsymbol{q}_r$ are not eigenvectors of $\boldsymbol{Q}$, and their scalar multiplications have been absorbed into the vectors to reduce storage. Moreover, $\boldsymbol{S}$ is asymmetrically decomposed in order to recycle a part of the decomposition of $\boldsymbol{Q}$. This allows future contractions with either tensor to be recycled as well, promoting efficiency. Needless to say, there is a lot of freedom on how to formulate the desired decomposition, while numerically finding such decomposition is an entirely different challenge.

Before elaborating on how to achieve the challenging tensor decomposition, their use is justified with a final flop count comparison. Starting with the internal force:

$$\boldsymbol{f}(\boldsymbol{u}) = \boldsymbol{K} \bullet \boldsymbol{u} + \sum_{r=1}^{R} \left(\tfrac{1}{2} \boldsymbol{s}_r \cdot (\boldsymbol{q}_r \bullet \boldsymbol{u})^2 + \tfrac{1}{6} \boldsymbol{q}_r \cdot (\boldsymbol{q}_r \bullet \boldsymbol{u})^3 \right) \ , \tag{A.3.4}$$

where for some r, the calculation of $(\boldsymbol{q}_r \bullet \boldsymbol{u})$ require 8 multiplications and 7 additions each, totalling at 15 flops. Then, $(\boldsymbol{q}_r \bullet \boldsymbol{u})^2$ and $(\boldsymbol{q}_r \bullet \boldsymbol{u})^3$ are obtained through a single multiplication each, raising the total to 17 flops. Then, both terms within the sum are obtained through scalar multiplication and addition of the pre-calculated and stored vectors $\frac{1}{2}\boldsymbol{s}_r$ and $\frac{1}{6}\boldsymbol{q}_r$, adding 24 flops. Repeating these 41 flops R times, and adding them to the first term $\boldsymbol{K} \bullet \boldsymbol{u}$, raises the total to $49R$. With $\boldsymbol{K} \bullet \boldsymbol{u}$ requiring 40 flops of its own, yields a total of $49R + 40$ flops to calculate $\boldsymbol{f}$. Also considering that the maximal symmetric rank R of

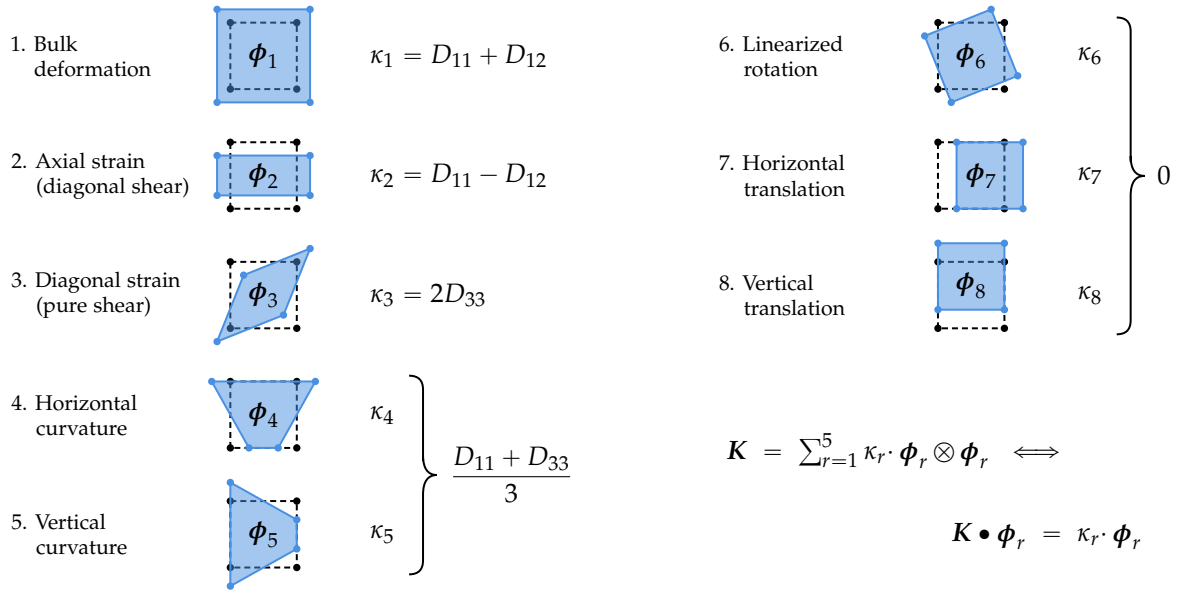

Figure A.3.1: Eigendecomposition of the two-way, eight-dimensional elemental stiffness tensor $\mathbf{K}$, with eigen deformations $\boldsymbol{\phi}_r$ and corresponding eigenstiffnesses κ_r for $r = 1, \ldots, 8$.

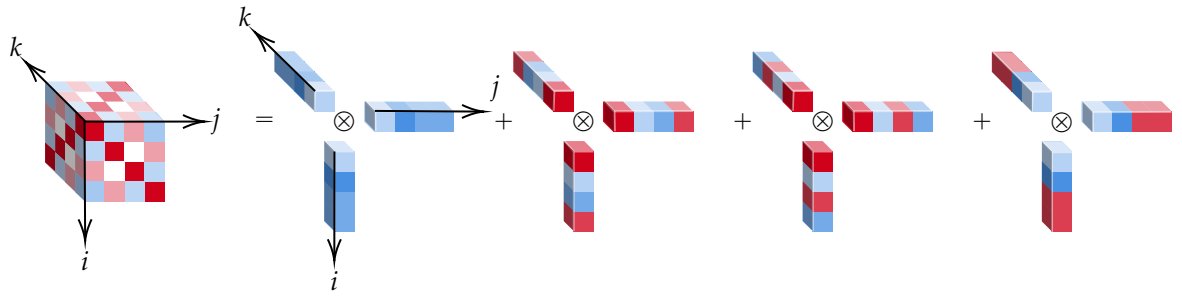

Figure A.3.2: *Canonical Polyadic* (CP) decomposition of some arbitrary tree-way four-dimensional symmetric tensor of symmetric rank four.

$\boldsymbol{Q}$ could never exceed 21, as elaborated in Subsection II.1, a total of 1069 flops is required to calculate $\boldsymbol{f}$, which is roughly two-thirds compared to the canonical formulation, and one-tenth compared to the dense tensorial formulation.

The flop count for the elemental tangent stiffness matrix is very similar to that of the internal force:

$$\boldsymbol{\mathcal{K}}(\boldsymbol{u}) = \boldsymbol{K} + \sum_{r=1}^{R} \left(\boldsymbol{s}_r \otimes \boldsymbol{q}_r (\boldsymbol{q}_r \bullet \boldsymbol{u}) + \tfrac{1}{2} \boldsymbol{q}_r^{\overset{2}{\otimes}} \cdot (\boldsymbol{q}_r \bullet \boldsymbol{u})^2 \right) , \tag{A.3.5}$$

where for some r, the calculation of $(\boldsymbol{q}_r \bullet \boldsymbol{u})$ requires 15 flops, and that of $(\boldsymbol{q}_r \bullet \boldsymbol{u})^2$ an additional one. Then, both terms within the sum are obtained through scalar multiplication and addition of the pre-calculated and stored matrices $\boldsymbol{s}_r \otimes \boldsymbol{q}_r$ and $\frac{1}{2} \boldsymbol{q}_r^{\overset{2}{\otimes}}$, each containing 64 components, hence requiring 128 multiplications and 64 additions. Repeating these 208 flops R times, and adding them to the first term $\boldsymbol{K}$, requires a total of $208R + 64$ flops. Again, considering that R could never exceed one, a total of 4432 flops is required to calculate $\boldsymbol{\mathcal{K}}$, which is one-third compared to the canonical formulation.

To compare the decomposed to the dense tensorial and canonical formulation, their respective flop counts are summarized in Table A.3.1. Much more importantly, however, less memory storage and transfer are required using the decomposed tensorial form. This is arguably a more limiting aspect than flops in modern computing Battaglino et al. (2018). In fact, the decomposed form arguably involves a nearly minimal amount of storage and floating point operations regarding the evaluation of all structural quantities and derivatives, compared to other exact formulations. To clarify, the adopted structural model is inherently multivariate polynomial, and the minimal sum-product of linear forms

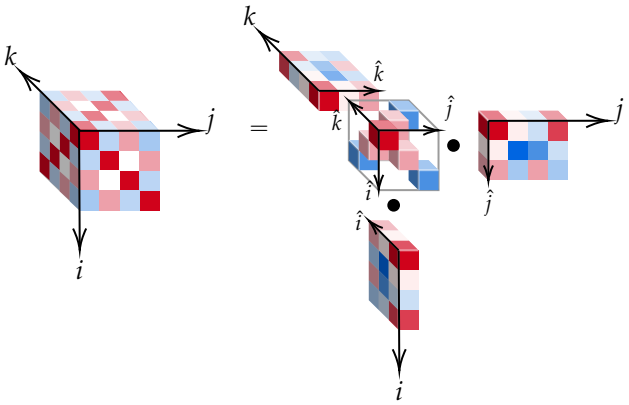

Figure A.3.3: *Tucker* decomposition of some arbitrary tree-way four-dimensional symmetric tensor of symmetric rank 4 and inner dimensionality 3 (i.e. nullity 1).

cannot be reduced any further. However, further improvements may be obtained by enforcing sparsity or optimizing data movement of some kind, which can be a future project on its own.

	Canonical	Tensorial (Dense)	Tensorial (Decomposed)
$\boldsymbol{f}(\boldsymbol{u})$	1 594	9 976	1 069
$\boldsymbol{\mathcal{K}}(\boldsymbol{u})$	12 807	9 792	4 432

Table A.3.1: Required number of floating-point operations (flops) in order to calculate the elemental internal force vector $\boldsymbol{f}(\boldsymbol{u})$, and tangent stiffness matrix $\boldsymbol{\mathcal{K}}(\boldsymbol{u})$, using their canonical, dense tensorial and decomposed tensorial forms, as derived over the present Appendix A.

The idea behind tensor decomposition often involves a least-squares approach:

$$\min_{\{\boldsymbol{q}_1,\,\ldots,\,\boldsymbol{q}_R\}} \left|\left| \boldsymbol{Q} - \sum_{r=1}^{R} \boldsymbol{q}_r^{\overset{4}{\otimes}} \right|\right|_{\mathcal{F}}^2 , \tag{A.3.6}$$

where the *Frobenious norm* $||\circ||_{\mathcal{F}}^2$ indicates the sum of all components squared, and R denotes the rank of $\boldsymbol{Q}$. Sadly, there is no finite algorithm for determining this rank, no less the decomposition. However, a fairly successful and popular method is the *Alternating Least-Squares* approach (Kolda & Bader, 2009), where in subsequent minimization proplems, all but one of the factors $\boldsymbol{q}_r$ is fixed:

$$\min_{\{\boldsymbol{q}_1,\,\ldots,\,\boldsymbol{q}_R\}} \left|\left| \boldsymbol{Q} - \sum_{r=1}^{R} \widehat{\boldsymbol{q}}_r^{\overset{3}{\otimes}} \otimes \boldsymbol{q}_r \right|\right|_{\mathcal{F}}^2 , \tag{A.3.7}$$

where $\widehat{\boldsymbol{q}}_r$ denotes the factor fixed in the current optimization subproblem.

Regardless, the problem remains ill-posed, and the obtained decompositions are often necessarily non-orthogonal, non-unique, or just locally optimal leaving a large error. Without specialized regularization (or penalty terms of the objective to be minimized), these problems persist, with saddle points or factor degeneracy slowing down or halting the least-squares solution approach. Moreover, convergence highly depends on the initialization guess (Battaglino et al., 2018). Fortunately, in this work, a decomposition needs to be obtained only once given some unique material model up to a scalar multiplication of the Young's modulus, and several approaches led to a successful decomposition of $\boldsymbol{Q}$ and $\boldsymbol{S}$.

For instance, an enhanced line search along an initially found gradient-descent direction yielded a major improvement in convergence speed and robustness (Rajih et al., 2008). Ultimately, a Barzilai-Borwein method was employed, being a gradient descent method with a heuristically determined step size based on previous steps. This allows the approximate use of second-order information, without the computational draw-backs of a true second-order optimization method. Even more, a second-order optimization method is much more prone to get stuck in bad local optima during tensor decomposition, than a first-order method.

Then, a prior Tucker decomposition (Kolda & Bader, 2009) greatly improved the sparsity of the

initial decomposition problem, which is essentially a change of coordinates from the original $\mathbb{R}^8$ to the basis spanned by the first six eigenmodes of $\boldsymbol{K}$ (Figure A.3.1). To clarify, projecting $\boldsymbol{K}$ onto this basis diagonalizes it, effectively functioning as a CP decomposition as well. While it does not necessarily diagonalize higher-order tensors that are physically related to $\boldsymbol{K}$, it does introduce a great extent of scarcity within both $\boldsymbol{S}$ and $\boldsymbol{Q}$, as visualized in Figure A.3.3. Moreover, it filters out redundant dimensions, turning the tensors six-dimensional without loss of information, which is possible due to the translational invariance of energy and all of its displacement derivatives. This greatly sped up the CP decomposition process.

B

Error and Convergence Estimation

Approximation often means accepting error in favor of computational efficiency, although this is rarely an equal trade-off. For an increased computational cost, the error often diminishes decreasingly or sometimes even diverges excessively. Therefore, error analysis is vital to balancing this trade-off given a desired tolerance or desired computational effort, or avoiding designs altogether where no acceptable balance can be reached. To this end, the present appendix argues and derives the metric that was implemented to validate the perturbed structural analysis, being an approximation, extrapolation, or prediction of the non-linear equilibrium curve from the undeformed state. First, an error and convergence estimation is derived for its state-of-the-art competitor, Newton-Raphson analysis, in Appendix B.1. Then, the same estimators are derived for perturbed analysis in Appendix B.2. Ultimately, this facilitates a means to actively steer the topology optimization, ensuring the accuracy of the analysis and, more importantly, improving the optimization robustness.

B.1 Newton-Raphson Analysis

Newton-Raphson analysis is used to solve a non-linear set of equations, by sequentially solving its local linearization, until the error due to this linearization has converged sufficiently towards zero. In this appendix, the corresponding conditions and rate will be analyzed, considering a single load-step from the undeformed state.

Consider the residual force $\boldsymbol{r} \in \mathbb{R}^N$ as a function of some displacement $\boldsymbol{u} \in \mathbb{R}^N$ and load-scalar $\lambda \in \mathbb{R}$. Moreover, λ is assumed given, and the local linearization is taken with respect to $\boldsymbol{u} = \underline{\boldsymbol{u}} + \Delta\boldsymbol{u}$, where $\underline{\boldsymbol{u}}$:

$$\boldsymbol{r}(\underline{\boldsymbol{u}} + \Delta\boldsymbol{u},\ \lambda) = \lambda\boldsymbol{p} - \boldsymbol{f}(\underline{\boldsymbol{u}} + \Delta\boldsymbol{u}) = \lambda\boldsymbol{p} - \boldsymbol{f}(\underline{\boldsymbol{u}}) - \underbrace{\left.\frac{\partial \boldsymbol{f}(\boldsymbol{u})}{\partial \boldsymbol{u}}\right|_{\boldsymbol{u}=\underline{\boldsymbol{u}}}}_{\boldsymbol{\mathcal{K}}(\underline{\boldsymbol{u}})} \bullet \Delta\boldsymbol{u} + \boldsymbol{\mathcal{O}}\left(|\Delta\boldsymbol{u}|^2\right) = \boldsymbol{0}\,. \tag{B.1.1}$$

By disregarding the current truncation-error $\boldsymbol{\mathcal{O}}\left(|\Delta\boldsymbol{u}|^2\right)$, a linear system of equations remains that implies the correction-step $\Delta\boldsymbol{u} \in \mathbb{R}^N$, approximately solving the original equation. Here, $f(u) = \mathcal{O}\big(g(u)\big)$ is equivalent to $f(u) \leqslant M \cdot g(u)$ for some finite $M \in \mathbb{R}$. The Newton-Raphson sequence of solutions is then obtained by denoting the new solution $\boldsymbol{u}_{k+1} = \underline{\boldsymbol{u}} + \Delta\boldsymbol{u}$, in terms of the previous solution $\boldsymbol{u}_k = \underline{\boldsymbol{u}}$, with $\boldsymbol{u}_0 = \boldsymbol{0}$:

$$\boldsymbol{u}_{k+1} = \boldsymbol{u}_k - \Big[\boldsymbol{\mathcal{K}}(\boldsymbol{u}_k)\Big]^{-1} \bullet \Big(\boldsymbol{f}(\boldsymbol{u}_k) - \lambda\boldsymbol{p}\Big)\,, \qquad \text{with} \quad \boldsymbol{u}_0 = \boldsymbol{0}\,. \tag{B.1.2}$$

Assuming a true solution $\boldsymbol{u}$ exists that satisfies Equation B.1.1, $\boldsymbol{u}_k$ converges to this solution as $k \to \infty$, under certain conditions. Before analyzing this convergence, some convenient definitions are made:

$$\lambda \boldsymbol{p} \equiv \boldsymbol{f}_\infty \equiv \boldsymbol{f}(\boldsymbol{u}_\infty) \,, \qquad \boldsymbol{K}_\infty \equiv \boldsymbol{\mathcal{K}}(\boldsymbol{u}_\infty) \,, \qquad \boldsymbol{S}_\infty \equiv \boldsymbol{\mathcal{S}}(\boldsymbol{u}_\infty) \,, \tag{B.1.3}$$

respectively denoting the zeroth-, first- and second-order derivatives of internal the force $\boldsymbol{f}$ versus displacement $\boldsymbol{u}$, at the converged solution $\boldsymbol{u}_\infty$. Furthermore, let $\Delta \boldsymbol{u}_k$ denote the distance of the k^{th} solution towards the true solution:

$$\Delta \boldsymbol{u}_k \equiv \boldsymbol{u}_k - \boldsymbol{u}_\infty \,. \tag{B.1.4}$$

Convergence of $\boldsymbol{u}_k$ may then be accurately analyzed by considering the local second-order Taylor expansion of $\boldsymbol{f}(\boldsymbol{u}_k)$ and its derivative $\boldsymbol{\mathcal{K}}(\boldsymbol{u}_k)$:

$$\boldsymbol{f}(\boldsymbol{u}_k) = \boldsymbol{f}_\infty + \boldsymbol{K}_\infty \bullet \Delta \boldsymbol{u}_k + \tfrac{1}{2} \boldsymbol{S} \underset{2}{\bullet} \Delta \boldsymbol{u}_k^{\overset{2}{\otimes}} + \boldsymbol{\mathcal{O}}\Big(|\Delta \boldsymbol{u}_k|^3\Big) \,. \tag{B.1.5a}$$

$$\boldsymbol{\mathcal{K}}(\boldsymbol{u}_k) = \boldsymbol{K}_\infty + \boldsymbol{S}_\infty \bullet \Delta \boldsymbol{u}_k + \boldsymbol{\mathcal{O}}\Big(|\Delta \boldsymbol{u}_k|^2\Big) \,, \tag{B.1.5b}$$

and then substituting these expansions back into the recursive Newton-Raphson sequence defined in Equation B.1.2:

$$\begin{aligned}
\Delta \boldsymbol{u}_{k+1} &= \Delta \boldsymbol{u}_k - \Big[\boldsymbol{\mathcal{K}}(\boldsymbol{u}_k)\Big]^{-1} \bullet \Big(\boldsymbol{f}(\boldsymbol{u}_k) - \lambda \boldsymbol{p}\Big) \\
&= \Big[\boldsymbol{\mathcal{K}}(\boldsymbol{u}_k)\Big]^{-1} \bullet \Big(\Big[\boldsymbol{\mathcal{K}}(\boldsymbol{u}_k)\Big] \bullet \Delta \boldsymbol{u}_k + \boldsymbol{f}(\boldsymbol{u}_k) - \lambda \boldsymbol{p}\Big) \\
&= \Big[\boldsymbol{K}_\infty + \boldsymbol{S}_\infty \bullet \Delta \boldsymbol{u}_k + \boldsymbol{\mathcal{O}}\Big(|\Delta \boldsymbol{u}_k|^2\Big)\Big]^{-1} \bullet \\
&\qquad \underbrace{\Big(\Big[\boldsymbol{K}_\infty + \boldsymbol{S}_\infty \bullet \Delta \boldsymbol{u}_k + \boldsymbol{\mathcal{O}}\Big(|\Delta \boldsymbol{u}_k|^2\Big)\Big] \bullet \Delta \boldsymbol{u}_k - \boldsymbol{K}_\infty \bullet \Delta \boldsymbol{u}_k - \tfrac{1}{2} \boldsymbol{S} \underset{2}{\bullet} \Delta \boldsymbol{u}_k^{\overset{2}{\otimes}} + \boldsymbol{\mathcal{O}}\Big(|\Delta \boldsymbol{u}_k|^3\Big)\Big)}_{\tfrac{1}{2} \boldsymbol{S} \underset{2}{\bullet} \Delta \boldsymbol{u}_k^{\overset{2}{\otimes}} + \boldsymbol{\mathcal{O}}\Big(|\Delta \boldsymbol{u}_k|^3\Big)} \,.
\end{aligned} \tag{B.1.6}$$

Assuming convergence, meaning $|\Delta \boldsymbol{u}_k| \to 0$ as $k \to \infty$, all factors tend towards their lowest-order non-vanishing terms. This greatly simplifies Equation B.1.6 to:

$$|\Delta \boldsymbol{u}_{k+1}| \approx \left| \Big(\tfrac{1}{2} \boldsymbol{K}_\infty^{-1} \bullet \boldsymbol{S}_\infty\Big) \underset{2}{\bullet} \Delta \boldsymbol{u}_k^{\overset{2}{\otimes}} \right| = \boldsymbol{\mathcal{O}}\Big(|\Delta \boldsymbol{u}_k|^2\Big) \,, \tag{B.1.7}$$

hence the order of convergence is *quadratic*. To clarify the right-hand-side result of Equation B.1.7, the behavior of $|\Delta \boldsymbol{u}_k| \to 0$ as $k \to \infty$ may be argued through the following tensor-decomposition:

$$\tfrac{1}{2} \boldsymbol{K}_\infty^{-1} \bullet \boldsymbol{S}_\infty \equiv \sum_{r=1}^{R} \boldsymbol{\phi}_r \otimes \boldsymbol{\psi}_r^{\overset{2}{\otimes}} \,, \qquad \text{with} \quad \boldsymbol{\phi}_r \in \mathbb{R}^N \,,\ \boldsymbol{\psi}_r \in \mathbb{R}^N \,. \tag{B.1.8}$$

Regarding the asymmetry, note that $\boldsymbol{S}_\infty$ is symmetric among all three ways. However, the resulting three-way tensor is obtained through a left-hand contraction with $\frac{1}{2} \boldsymbol{K}_\infty^{-1}$, effectively transforming the first way of $\boldsymbol{S}_\infty$. The resulting magnitude in Equation B.1.8 may then be upper-bounded as:

$$\left| \tfrac{1}{2} \Big(\boldsymbol{K}_\infty^{-1} \bullet \boldsymbol{S}_\infty\Big) \underset{2}{\bullet} \Delta \boldsymbol{u}_k^{\overset{2}{\otimes}} \right| = \left| \sum_{r=1}^{R} \boldsymbol{\phi}_r (\boldsymbol{\psi}_r \bullet \Delta \boldsymbol{u}_k)^2 \right| \leqslant \left(\sum_{r=1}^{R} |\boldsymbol{\phi}_r| |\boldsymbol{\psi}_r|^2 \right) |\Delta \boldsymbol{u}_k|^2 = \boldsymbol{\mathcal{O}}\Big(|\Delta \boldsymbol{u}_k|^2\Big) \,, \tag{B.1.9}$$

using both the triangle inequalities $|\Sigma_i a_i| \leqslant \Sigma_i |a_i|$ and $|\boldsymbol{a} \bullet \boldsymbol{b}| \leqslant |\boldsymbol{a}||\boldsymbol{b}|$. Finally, the relative normed error with respect to the true solution may then be approximated using Equation B.1.7, and upper-bounded using Equation B.1.9:

$$\epsilon_{k+1} \equiv \frac{|\Delta \boldsymbol{u}_{k+1}|}{|\boldsymbol{u}_\infty|} \approx \frac{\left| \Big(\tfrac{1}{2} \boldsymbol{K}_\infty^{-1} \bullet \boldsymbol{S}_\infty\Big) \underset{2}{\bullet} \Delta \boldsymbol{u}_k^{\overset{2}{\otimes}} \right|}{|\boldsymbol{u}_\infty|} \leqslant \beta \frac{|\Delta \boldsymbol{u}_k|^2}{|\boldsymbol{u}_\infty|^2} = \beta \epsilon_k^2 \,, \tag{B.1.10}$$

where β denotes some positive scalar that depends on the structural design, load-case and true solution $\boldsymbol{u}_\infty$, but is constant with respect to k. A necesary *condition* for convergence is readilly implied here:

$$\lim_{k\to\infty} \frac{\epsilon_{k+1}}{\epsilon_k} = \lim_{k\to\infty} \beta\epsilon_k < 1 \,, \tag{B.1.11}$$

where a sufficient condition would mean that $\beta\epsilon_k < 1$ for all $k \geqslant 0$.

In explicit form, the relative error after some n Newton-Raphson correction-steps may then be obtained by recursively substituting $\epsilon_{k+1} \leqslant \beta\epsilon_k^2$ into itself for $k = 1, \ldots, n$:

$$\epsilon_n \leqslant \beta\epsilon_{n-1}^2 \leqslant \beta\left(\beta\epsilon_{n-2}\right)^2 \leqslant \beta\left(\beta\left(\beta\cdots\beta\left(\beta\epsilon_0\right)^2\cdots\right)^2\right)^2 \tag{B.1.12}$$

$$= \beta\cdot\beta^2\cdot\beta^4\cdots\beta^{2^{n-1}}\cdot\epsilon_0^{2^n} = \beta^{\sum_{j=0}^{n-1}2^j} = \beta^{2^n-1}\cdot\epsilon_0^{2^n} \,, \tag{B.1.13}$$

$$\text{where} \quad \sum_{j=0}^{n-1} 2^j = 2\left(\sum_{j=0}^{n-1} 2^j\right) - \left(\sum_{j=0}^{n-1} 2^j\right) = \left(\sum_{j=1}^{n} 2^j\right) - \left(\sum_{j=0}^{n-1} 2^j\right) = 2^n - 1 \,. \tag{B.1.14}$$

Note that $\epsilon_0 = 1$ as $\Delta\boldsymbol{u}_0 = \boldsymbol{u}_\infty$, using the definition in Equation B.1.9. Furthermore, ϵ_1 then approximately reduces to β, the former of which exactly equals the relative normed displacement error ϵ_L as obtained through linear FEM:

$$\epsilon_L \equiv \epsilon_1 = \frac{|\boldsymbol{u}_1 - \boldsymbol{u}_\infty|}{|\boldsymbol{u}_\infty|} \,, \qquad \text{where} \quad \boldsymbol{u}_1 = \Big[\underbrace{\boldsymbol{\mathcal{K}}(\boldsymbol{0})}_{\boldsymbol{K}}\Big]^{-1} \bullet \left(\lambda\boldsymbol{p}\right) . \tag{B.1.15}$$

Substituting $\epsilon_0 = 1$ and $\epsilon_1 = \epsilon_L$ into the inequality Equation B.1.12 then finally yields an estimator:

$$\widetilde{\epsilon}_n \approx \epsilon_L^{2^n-1} \,. \tag{B.1.16}$$

which is notably a double exponential function versus n, as tabulated in Table B.1.1. In-fact, although each pair of consecutive terms ϵ_k may be related by a polynomial, the explicit sequence generally tends to a double exponential. Only when the relation is linear, such as for perturbed analysis (Appendix B.2), the explicit sequence tends to a regular exponential.

n	0	1	2	3	4	5
$\widetilde{\epsilon}_n$	1	ϵ_L	ϵ_L^3	ϵ_L^7	ϵ_L^{15}	ϵ_L^{31}

Table B.1.1: Relative displacement error estimator $\widetilde{\epsilon}_n$ where n denotes the number of Newton-Raphson iterations starting at the undeformed state. Note that $\epsilon_L \equiv \epsilon_1$ is obtained after a single Newton-Raphson iteration, which is exactly equivalent to linear FEM.

To conclude, the following observations can be made regarding the Newton-Raphson convergence behavior in non-linear structural analysis. Its order is confirmed to be quadratic (Equation B.1.9), thus superlinear. Where the linear convergence yields a constant rate, being the error-ratio of consecutive iterations, super-linear convergence yields an exponentially increasing rate. The condition for convergence, however, depends both on the initial error $\Delta\boldsymbol{u}_k$ from the true solution, and the upper-bound estimate of scalar β that depends on the function's local behavior. In other words, while $\epsilon_L < 1$ is a necessary condition for convergence, smaller ϵ_L still indicate improved odds of convergence.

B.2 Perturbed Analysis

Perturbed analysis, used for Taylor extrapolation to be more precise, is used to solve a non-linear set of equations in the neighborhood of some known solution point. In this work, the undeformed state, being the origin, was considered for simplicity. Rather than solving the non-linear equation in multiple points, it solves higher-order derivatives of this equation versus some path parameter, evaluated in a single point. This implies a recursive sequence of higher-order solution derivatives versus the path

parameter, with the solution and path parameter respectively considered as the structural displacement and applied load variable.

Formulating the approximate structural analysis through an explicit power series allows for some useful assumptions and simplifications on the convergence rate and conditions that affect it. First, recall the n^{th}-order power, Taylor, or MacLaurin series that approximates displacement versus load-scalar λ in the neighbourhood of $\lambda = 0$:

$$\widetilde{\boldsymbol{u}}_n(\lambda) \equiv \sum_{p=1}^{n} \frac{\boldsymbol{u}^{(p)}\lambda^p}{p!} \,. \tag{B.2.1}$$

Then, consider its associated *true relative displacement error* $\epsilon_n(\lambda)$, being a straightforward scalar measure, approximately indicating the relative error of the predicted solution:

$$\epsilon_n(\lambda) \equiv \frac{|\widetilde{\boldsymbol{u}}_n(\lambda) - \boldsymbol{u}(\lambda)|}{|\boldsymbol{u}(\lambda)|} \,. \tag{B.2.2}$$

Note that $\epsilon_n(\lambda)$ has been defined to depend on the true solution $\boldsymbol{u}(\lambda)$, which requires an iterative solver that likely exceeds the cost of the approximate analysis itself. Hence, an estimator for $\epsilon_n(\lambda)$ was derived and implemented instead.

The truncation error of a power series such as $\widetilde{\boldsymbol{u}}_n(\lambda)$ is bounded (Stewart, 2016), given that $|\lambda|$ remains within the *radius of convergence* $\overline{\lambda}$, as will be elaborated shortly:

$$\left|\widetilde{\boldsymbol{u}}_p(\lambda) - \boldsymbol{u}(\lambda)\right| \leqslant M_p \cdot \lambda^{p+1} \,, \tag{B.2.3a}$$

$$\text{where} \quad M_p \approx \frac{|\boldsymbol{u}^{(p+1)}|}{(p+1)!} \,. \tag{B.2.3b}$$

In-fact, M_p equals the normed maximum of the $p+1^{\text{st}}$-order derivative of $\widetilde{\boldsymbol{u}}_p(\lambda)$ within the range $|\lambda| \leqslant \overline{\lambda}$ (Greenstein, 1965; Powell, 1981). Moreover, when λ is small, M_p may be considered approximately maximized at zero Equation B.2.3b, supported by Powell's 1981 statement that the error of Taylor series is often dominated by their first truncated term. Additionally, this may be tied to the fact that the error of any convergent, alternating sequence is upper bounded by their first truncated term (Stewart, 2016), considering that terms of Taylor series tend to oscillate in magnitude and sign as well. In either case, Equation B.2.3b is an excellent estimator for M_p.

Another useful, closely related fact is that Taylor series behave very similarly to geometric series, and accordingly often show approximate linear convergence or divergence. Hence, the magnitudes of the terms of $\widetilde{\boldsymbol{u}}_n(\lambda)$ were assumed to follow an exponential trend:

$$\left|\frac{\boldsymbol{u}^{(p)}\lambda^p}{p!}\right| \approx \beta \cdot \left|\frac{\boldsymbol{u}^{(p-1)}\lambda^{p-1}}{(p-1)!}\right| \approx \beta^{p-1} \cdot \left|\boldsymbol{u}^{(1)}\lambda\right| \,, \tag{B.2.4a}$$

$$\text{hence} \quad \beta \equiv \left(\frac{|\boldsymbol{u}^{(n)}|}{n!|\boldsymbol{u}^{(1)}|}\right)^{\frac{1}{n-1}} |\lambda| \,, \tag{B.2.4b}$$

where some positive β represents the average ratio's estimate, whose logarithm represents the *rate of divergence*, accounting for all n terms of $\widetilde{\boldsymbol{u}}_n(\lambda)$ to ensure accuracy.

Using these assumptions, the radius of convergence was estimated in terms of λ. A geometric series converges if and only if the ratio among consecutive terms $\beta < 1$ (Stewart, 2016). This condition was directly applied to Equation B.2.4, yielding:

$$|\lambda| < \left(n!\frac{|\boldsymbol{u}^{(1)}|}{|\boldsymbol{u}^{(n)}|}\right)^{\frac{1}{n-1}} \equiv \overline{\lambda}_n \,, \tag{B.2.5a}$$

$$\text{hence} \quad \beta = \frac{|\lambda|}{\overline{\lambda}_n} \,, \tag{B.2.5b}$$

where $\overline{\lambda}_n$ defines the *radius of convergence estimate*, whose supreme limit tends towards the true radius of convergence $\overline{\lambda}$ as $n \to \infty$ (Powell, 1981).

Finally, an estimator was derived for $\epsilon_n(\lambda)$ (Equation B.2.2), assuming $|\lambda| < \overline{\lambda}$ where the series of $\widetilde{\boldsymbol{u}}_n(\lambda)$ converge, and simplifying its denominator $|\boldsymbol{u}(\lambda)|$ to $|\boldsymbol{u}^{(1)}\lambda|$. Although Equation B.2.3b could be substituted directly by taking $p = n$, this would require an additional solve for $\boldsymbol{u}^{(n+1)}$, which may as well be used to obtain $\widetilde{\boldsymbol{u}}_{n+1}(\lambda)$. Instead, $\epsilon_p(\lambda)$ was considered, substituting Equation B.2.3b by taking $p = n - 1$, and then extrapolated a single step using Equation B.2.4:

$$\epsilon_n(\lambda) \approx \frac{\beta \cdot \left| \dfrac{\boldsymbol{u}^{(n)}\lambda^n}{n!} \right|}{\left|\boldsymbol{u}^{(1)}\lambda\right|} \approx \beta^n = \left(\frac{\lambda}{\overline{\lambda}_n}\right)^n \equiv \widetilde{\epsilon}_n(\lambda) \,, \tag{B.2.6}$$

defining the *relative displacement error estimate* $\widetilde{\epsilon}_n(\lambda)$, as implemented within the approximate structural analysis and corresponding topology optimizations.

Still, the ramifications of $|\lambda| > \overline{\lambda}$ must be considered for the error estimator, where the series of $\widetilde{\boldsymbol{u}}_n(\lambda)$ diverges. While $\widetilde{\boldsymbol{u}}_n(\lambda)$ may become meaningless due to excessive error, a robust and accurate error estimator should still be able to guide the topology optimization toward a design that leads to less inaccuracy, through larger $\overline{\lambda}$. In the case of large λ, it can be argued through Equation II.28 that displacements $|\boldsymbol{u}(\lambda)|$ approximately scale with $\lambda^{\frac{1}{3}}$, while $|\widetilde{\boldsymbol{u}}_n(\lambda) - \boldsymbol{u}(\lambda)|$ simply tends to scale with λ^n. Overall, the error $\epsilon_n(\lambda)$ scales with $\lambda^{n-\frac{1}{3}}$, which nearly agrees with the estimated λ^n. To which extent this holds true in practice, is verified in Section IV and V. Regardless, reducing the error estimate is equivalent to increasing the radius of convergence $\overline{\lambda}$, whose estimate $\overline{\lambda}_n$ appeared to be a smooth response of the structural design during the topology optimizations performed in this work.

In conclusion, a relative displacement error estimator $\widetilde{\epsilon}_n(\lambda)$ of approximate displacement $\widetilde{\boldsymbol{u}}_n(\lambda)$ is derived and implemented, in terms of the corresponding radius of convergence $\overline{\lambda}_n$ (Equation B.2.7). Furthermore, it is expected to be accurate for $|\lambda|$ up to, and possibly beyond $\overline{\lambda}$, and capable of guiding the optimizer towards more accurate designs, regardless of excessively large error or small $\overline{\lambda}$.

$$\widetilde{\epsilon}_n(\lambda) \equiv \left(\frac{\lambda}{\overline{\lambda}_n}\right)^n \,, \quad \text{with} \quad \overline{\lambda}_n \equiv \left(n! \frac{|\boldsymbol{u}^{(1)}|}{|\boldsymbol{u}^{(n)}|}\right)^{\frac{1}{n-1}} \,, \tag{B.2.7}$$

which is notably similar to the error estimator used by Cochelin (1994), Cochelin, Damil, & Potier-Ferry (1994), and other related works adopting a polynomial asymptotic numerical method of structural analysis. Furthermore, first-order perturbed analysis is equivalent to linear analysis, meaning that the approximate normed relative error of linear analysis $\epsilon_L \equiv \widetilde{\epsilon}_1(\lambda) = \beta$, yielding a definition of β similar to that for Newton-Raphson analysis in Appendix B.1

C

Bayesian Taylor Averaging

From statistics, it is widely known that the error of some average measurement decreases with the sample count when the individual errors are independent and of similar magnitude. When used correctly, more information generally leads to better prediction. In the case of the initially proposed perturbed structural analysis, only the derivatives were used, but their error estimators were not. Here, rather than just considering the highest-order MacLaurin expansion, all lower-orders and corresponding error estimators will be exploited as well. For each value of the load-scalar λ, a weighted average of all partial MacLaurin expansions will be taken, such that their combined error is minimal and coincidentally below all individual errors. The application of weighted averaging according to each component's variance, called *Bayesian Model Averaging*, is supported by considerable amounts of empirical evidence of improved model stability and accuracy (Hoeting et al., 1999).

C.1 Derivation

Up to this point, the best attempt at approximating the ground truth of interest $\boldsymbol{u}$ given some λ, involves using the highest available order MacLaurin-expansion $\boldsymbol{u}_n \equiv \widetilde{\boldsymbol{u}}_n(\lambda)$ as in Equation C.1.1a. Compared to $\boldsymbol{u}_1$ up to $\boldsymbol{u}_{n-1}$, this indeed yields the lowest error within the radius of convergence $\overline{\lambda}$ as estimated in Equation C.1.1b. On the other hand, it yields a maximal error outside of it, directly affecting the responses, their design sensitivities, and consequently the effectiveness of the overall optimization. Recall the MacLaurin approximant $\widetilde{\boldsymbol{u}}_p(\lambda)$ and its associated relative error-estimator[1] $\widetilde{\epsilon}_p(\lambda)$ for $p = 1, \ldots, n$:

$$\boldsymbol{u}_p \equiv \widetilde{\boldsymbol{u}}_p(\lambda) = \sum_{q=1}^{p} \frac{\boldsymbol{u}^{(q)}}{q!} \lambda^q \,, \tag{C.1.1a}$$

$$\epsilon_p \equiv \widetilde{\epsilon}_p(\lambda) = \left(\frac{\lambda}{\overline{\lambda}_n} \right)^p \,. \tag{C.1.1b}$$

The key principle behind an improved predictor $\boldsymbol{\theta} = \widetilde{\widetilde{\boldsymbol{u}}}(\lambda)$ of $\boldsymbol{u}$ given some λ and approximations $\boldsymbol{u}_p$ for $p = 1, \ldots, n$, is treating $\boldsymbol{\theta}$ and $\boldsymbol{u}_p$ as samples from stochastic vectors $\boldsymbol{U}$ and $\boldsymbol{U}_p$ respectively. Moreover, consider the following linear combination:

$$\boldsymbol{\theta} \equiv \sum_{p=1}^{n} \omega_p \boldsymbol{u}_p \,, \qquad \Longleftrightarrow \qquad \boldsymbol{U} = \sum_{p=1}^{n} \omega_p \boldsymbol{U}_p \tag{C.1.2}$$

[1] Recall that any relative error or -estimator is consistently denoted using the symbol ϵ_p, dividing the normed error of some approximant by the normed solution from linear FEM.

where the weights ω_p will be chosen such that the expected value $\mathbb{E}(\boldsymbol{U}) = \boldsymbol{u}$ and the variance $\mathbb{V}(\boldsymbol{U})$ is minimal. Note that while the *direction* of the true error $\boldsymbol{u}_p - \boldsymbol{u}$ is unknown, its magnitude with respect to $\boldsymbol{u}_1$ is accurately estimated by ϵ_p. Hence, it is assumed that this direction is uniformly distributed, meaning $\mathbb{E}(\boldsymbol{U}_p) = \boldsymbol{u}$, while $|\mathbb{V}(\boldsymbol{U}_p)|$ is proportional to ϵ_p^2. Furthermore, $\boldsymbol{U}_p$ is assumed independently distributed for distinct p. Considering the variance and expected value of $\boldsymbol{U}$:

$$\mathbb{E}(\boldsymbol{U}) = \sum_{p=1}^{n} \omega_p \mathbb{E}(\boldsymbol{U}_p) = \boldsymbol{u} \sum_{p=1}^{n} \omega_p = \boldsymbol{u} \,, \qquad \Longleftrightarrow \qquad \sum_{p=1}^{n} \omega_p = 1 \,, \tag{C.1.3a}$$

$$\mathbb{V}(\boldsymbol{U}) = \sum_{p=1}^{n} \omega_p^2 \mathbb{V}(\boldsymbol{U}_p) \,, \qquad \Longleftrightarrow \qquad \epsilon^2 = \sum_{p=1}^{n} \omega_p^2 \epsilon_p^2 \,, \tag{C.1.3b}$$

the optimal choice for the weights ω_p may be obtained by minimizing ϵ^2 such that $\sum_{p=1}^{n} \omega_p = 1$. Since this is a constrained optimization problem, consider the following augmented Lagrangian $\mathcal{L}(\omega_p, \, \Lambda)$ with Lagrangian multiplier Λ:

$$\mathcal{L}(\omega_p, \, \Lambda) \equiv \left(\sum_{p=1}^{n} \omega_p^2 \right) - \Lambda \left(\sum_{p=1}^{n} \omega_p - 1 \right) \tag{C.1.4}$$

Minimizing $\mathcal{L}(\omega_p, \, \Lambda)$ versus the weights ω_p yields:

$$\frac{\partial \mathcal{L}(\omega_p, \, \Lambda)}{\partial \omega_p} = 2\omega_p \epsilon_p^2 - \Lambda = 0 \,, \qquad \text{hence} \quad \omega_p = \frac{\frac{1}{2}\Lambda}{\epsilon_p^2} \,. \tag{C.1.5}$$

Then, minimizing $\mathcal{L}(\omega_p, \, \Lambda)$ versus Λ is equivalent to satisfying the constraint, substituting ω_p for the right-hand-side of Equation C.1.5:

$$\frac{\partial \mathcal{L}(\omega_p, \, \Lambda)}{\partial \Lambda} = \sum_{p=1}^{n} \omega_p - 1 = \sum_{p=1}^{n} \frac{\frac{1}{2}\Lambda}{\epsilon_p^2} - 1 = 0 \,, \qquad \text{hence} \quad \tfrac{1}{2}\Lambda = \frac{1}{\sum_{p=1}^{n} \frac{1}{\epsilon_p^2}} \,. \tag{C.1.6}$$

Next, the weights ω_p that minimize the variance of $\boldsymbol{U}$ about the ground-truth $\boldsymbol{u}$ are obtained by substituting Λ for the right-hand-side of Equation C.1.6

$$\omega_p = \frac{\frac{1}{\epsilon_p^2}}{\sum_{q=1}^{n} \frac{1}{\epsilon_q^2}} \,. \tag{C.1.7}$$

Finally, the improved predictor $\tilde{\tilde{\boldsymbol{u}}}_n(\lambda)$ as a function of λ can be written as:

$$\tilde{\tilde{\boldsymbol{u}}}_n(\lambda) \equiv \frac{\sum_{p=1}^{n} \left(\frac{1}{\tilde{\epsilon}_p(\lambda)} \right)^2 \tilde{\boldsymbol{u}}_p(\lambda)}{\sum_{p=1}^{n} \left(\frac{1}{\tilde{\epsilon}_p(\lambda)} \right)^2} \,, \tag{C.1.8}$$

which is simplified as a rational of type $(2n-1)$ over $(2n-2)$ in the following Appendix C.2, by multiplying the numerator and denominator with $\tilde{\epsilon}_n^2(\lambda)$. Its associated error-estimator $\tilde{\tilde{\epsilon}}_n(\lambda)$ can then be obtained by combining the expression for weights ω_p with the premised squared error in Equation C.1.3b:

$$\tilde{\tilde{\epsilon}}_n(\lambda) \equiv \sqrt{\frac{1}{\sum_{p=1}^{n} \left(\frac{1}{\tilde{\epsilon}_p(\lambda)} \right)^2}} \,, \tag{C.1.9}$$

which may notably be recognized as the smooth minimum of $\widetilde{\epsilon}_p(\lambda)$ for all $p = 1, \ldots, n$.

In conclusion, this novel approximant $\widetilde{\widetilde{\boldsymbol{u}}}_n(\lambda)$ is expectedly more accurate than any MacLaurin approximant $\widetilde{\boldsymbol{u}}_p(\lambda)$ for any $\lambda \in \mathbb{R}$ and $p \leqslant n$. Of course, the validity of the previous and following statements depends on the accuracy of the error estimators $\widetilde{\epsilon}_p(\lambda)$ through the radius of convergence estimate $\overline{\lambda}_n$, from which the weights $\omega_p(\lambda)$ were argued to minimize the true error of $\widetilde{\widetilde{\boldsymbol{u}}}_n(\lambda)$. For some fixed $|\lambda| < \overline{\lambda}$ and increased n, $\widetilde{\widetilde{\boldsymbol{u}}}_n(\lambda)$ converges at least as fast as $\widetilde{\boldsymbol{u}}_n(\lambda)$, as the error of $\widetilde{\widetilde{\boldsymbol{u}}}_n(\lambda)$ is bounded by that of $\widetilde{\boldsymbol{u}}_p(\lambda)$ for any $p \leqslant n$ as $\lambda \to 0$. Interestingly, the fact that $|\widetilde{\widetilde{\boldsymbol{u}}}_n(\lambda) - \boldsymbol{u}(\lambda)| \leqslant |\widetilde{\boldsymbol{u}}_n(\lambda) - \boldsymbol{u}(\lambda)| = \mathcal{O}(\lambda^{n+1})$ implies that all lower order terms, hence all derivatives of $\widetilde{\widetilde{\boldsymbol{u}}}_n(\lambda)$, exactly match that of the true $\boldsymbol{u}(\lambda)$ at $\lambda = 0$. Therefore, the proposed Bayesian approach coincidentally yields $\widetilde{\widetilde{\boldsymbol{u}}}_n(\lambda)$ as a *vectorial* Padé-type approximant (El Kihal et al., 2022), albeit without its typical downside of spurious poles (Cochelin, 1994; Cochelin, Damil, & Potier-Ferry, 1994; De Boer & Van Keulen, 1997). More importantly, for $|\lambda| > \overline{\lambda}$, $\widetilde{\widetilde{\boldsymbol{u}}}_n(\lambda)$ *does not* diverge beyond $\widetilde{\boldsymbol{u}}_1(\lambda)$. As a result, a higher-order n for $\widetilde{\widetilde{\boldsymbol{u}}}_n(\lambda)$ maximally improves its accuracy within the radius of convergence, without worsening the divergence elsewhere. While divergence versus λ cannot be prevented, its rate is strongly bounded below that of linear FEM. What is more, divergence versus n is successfully eliminated. This should greatly improve the odds of the topology optimization to recover from inaccurate responses and sensitivities, and perhaps decrease the odds of derailing in the first place.

C.2 Stable Simplified Implementation

In order to conveniently implement and stably evaluate the Bayesian-enhanced predictor, the involved weights, and error estimator, the present appendix derives their simplification. Throughout this appendix, functional dependence on λ has been omitted for readability.

Denoting the n^{th} order Bayesian prediction as $\widetilde{\widetilde{\boldsymbol{u}}}$, Equation C.1.8 may be rewritten as:

$$\widetilde{\widetilde{\boldsymbol{u}}} \equiv \underbrace{\left[\boldsymbol{u}^{(1)}, \ldots, \boldsymbol{u}^{(n)}\right]}_{\boldsymbol{U}} \bullet \underbrace{\begin{bmatrix} \lambda & \lambda & \cdots & \lambda \\ & \frac{1}{2}\lambda^2 & \cdots & \frac{1}{2}\lambda^2 \\ & & \ddots & \vdots \\ & & & \frac{1}{n!}\lambda^n \end{bmatrix}}_{\boldsymbol{\Lambda}} \bullet \underbrace{\begin{bmatrix} \omega_1 \\ \omega_2 \\ \vdots \\ \omega_n \end{bmatrix}}_{\boldsymbol{\omega}} = \boldsymbol{U} \bullet \boldsymbol{\Lambda} \bullet \boldsymbol{\omega} \,, \tag{C.2.1}$$

where $\boldsymbol{U} \bullet \boldsymbol{\Lambda}$ produces a matrix whose columns equal the first- up to n^{th}-order MacLaurin predictions, $[\widetilde{\boldsymbol{u}}_1, \ldots, \widetilde{\boldsymbol{u}}_n]$. The remainder of this appendix aims to simplify the weights in $\boldsymbol{\omega}$:

$$\omega_p \equiv \frac{\beta^{-2p}}{\sum_{q=1}^{n} \beta^{-2q}} \,, \qquad \text{with} \quad \beta \equiv \frac{\lambda}{\overline{\lambda}} \,, \tag{C.2.2}$$

where ω_0 notably produces the expression for the Bayesian error estimate $\widetilde{\widetilde{\epsilon}}^2$, as formulated in Equation C.1.9. This will be convenient for the sensitivity analysis in the next Appendix D.

Multiplying the numerator and denominator of Equation C.2.2 by β^{2n} prevents the numerically unstable zero-pole cancelation, by explicitly factoring out the highest order pole:

$$\omega_p = \frac{\beta^{2n-2p}}{\sum_{q=1}^{n} \beta^{2n-2q}} = \frac{\beta^{2n-2p}}{\sum_{q=0}^{n-1} \beta^{2q}} \,, \tag{C.2.3}$$

where the sum in the denominator has also been simplified. Noting that $(1-\beta^2)\sum_{q=0}^{n-1} \beta^{2q} = 1 - \beta^{2n}$, Equation C.2.3 may be even further simplified to:

$$\omega_p = \frac{1-\beta^2}{1-\beta^{2n}} \beta^{2n-2p} \,. \tag{C.2.4}$$

D

Sensitivity Analysis

The present appendix is supplementary to the adjoint formulation argued and mostly elaborated in Subsection III.5. Hence, it reiterates the adjoint response formulation and its sensitivity in Appendix D.1. Then, the displacement-based *Adjoint Forces* and error estimate sensitivities are derived over the remaining subappendices, concerning both pure MacLaurin-based perturbed analysis, and its Bayesian-enhanced version. Finally, the last missing component of the adjoint formulation, the *Adjoint Stiffness*, is derived in detail within Appendix D.6. Throughout this appendix, functional dependence on λ is omitted for readability. Likewise, the subscript $\boldsymbol{x}$ originally present throughout Subsection III.5, denoting design dependence, is also dropped.

D.1 Adjoint Response Formulation

Recall the *Adjoint* Formulation (Bendsøe & Kikuchi, 1988) that casts some original response $g(\boldsymbol{x},\ \boldsymbol{u})$ into its *Lagrange* form $\mathcal{L}$, with Lagrange multipliers in $\boldsymbol{M} \in \mathbb{R}^{N\times n}$ and inherently satisfied constraints $\boldsymbol{R} \in \mathbb{R}^{N\times n}$ with $\boldsymbol{R} = \boldsymbol{0}$:

$$\mathcal{L} \equiv g(\boldsymbol{x},\ \boldsymbol{u}) + \underbrace{\sum_{p=1}^{n} \boldsymbol{\mu}^{(p)} \bullet \boldsymbol{r}^{(p)}}_{\boldsymbol{M} \underset{2}{\bullet} \boldsymbol{R} = 0}\ , \quad \begin{cases} g(\boldsymbol{x},\ \boldsymbol{u}) = \mathcal{L}\ , \\ \dfrac{\mathrm{d}g(\boldsymbol{x},\ \boldsymbol{u})}{\mathrm{d}\boldsymbol{x}} = \dfrac{\mathrm{d}\mathcal{L}}{\mathrm{d}\boldsymbol{x}}\ . \end{cases} \quad \forall \boldsymbol{M} \in \mathbb{R}^{N\times n} \tag{D.1.1}$$

Here $g(\boldsymbol{x},\ \boldsymbol{u})$ denotes a general response based directly on structural design $\boldsymbol{x}$, and its deformation $\boldsymbol{u}$. The latter is hereafter replaced by its MacLaurin and Bayesian predictions $\widetilde{\boldsymbol{u}}$ and $\widetilde{\widetilde{\boldsymbol{u}}}$ respectively, both directly dependent on load variable λ and the higher order displacement derivatives at the undeformed state, $\boldsymbol{U} \equiv \left[\boldsymbol{u}^{(1)},\ \ldots,\ \boldsymbol{u}^{(n)}\right]$. Furthermore, these displacement derivatives are obtained so as to satisfy the higher-order residual equations, $\boldsymbol{R} \equiv \left[\boldsymbol{r}^{(1)},\ \ldots,\ \boldsymbol{r}^{(n)}\right] = \boldsymbol{0}$, as elaborated in Subsection III.4. Lastly, the Lagrange multipliers $\boldsymbol{M} \equiv \left[\boldsymbol{\mu}^{(1)},\ \ldots,\ \boldsymbol{\mu}^{(n)}\right]$, also referred to as the *Adjoint Solutions*, may be chosen freely in $\mathbb{R}^{N\times n}$, and are hence conveniently chosen such that some expensive terms within the design sensitivity cancel out. The reader is referred back to Subsection III.5 for further clarification.

The resulting response design sensitivity, and adjoint solutions, can be obtained through:

$$\frac{\mathrm{d}g(\boldsymbol{x},\,\boldsymbol{u})}{\mathrm{d}\boldsymbol{x}} = \frac{\partial g(\boldsymbol{x},\,\boldsymbol{u})}{\partial \boldsymbol{x}} + \sum_{p=1}^{n} \boldsymbol{\mu}^{(p)} \bullet \frac{\partial \boldsymbol{r}^{(p)}}{\partial \boldsymbol{x}} \,, \tag{D.1.2}$$

$$\text{given that} \quad \boldsymbol{K} \bullet \boldsymbol{\mu}^{(p)} = \boldsymbol{\Gamma}^{(p)} - \sum_{q=p+1}^{n} \boldsymbol{K}^{(q,\,p)} \bullet \boldsymbol{\mu}^{(q)} \quad \text{for} \quad p = n,\, n-1,\, \ldots,\, 1 \,.$$

Here, the second line denotes the higher-order *Adjoint Structural Equations*. Over the remainder of this appendix, the adjoint forces $\boldsymbol{\Gamma}^{(p)}$ and adjoint stiffness $\boldsymbol{K}^{(p,\,q)}$ are derived for $p,\, q = 1,\, \ldots,\, n$, given MacLaurin-based perturbed analysis, and its Bayesian-enhanced version.

D.2 Adjoint MacLaurin Force

The goal of this appendix is to obtain the partial state derivatives of the general response based on the MacLaurin displacement prediction, which may be plugged directly into the adjoint formulation, copied in Appendix D.1 from Subsection III.5. They are defined as $\boldsymbol{G} \equiv \left[\boldsymbol{\Gamma}^{(1)},\, \ldots,\, \boldsymbol{\Gamma}^{(n)}\right] = \partial g(\boldsymbol{x},\, \widetilde{\boldsymbol{u}})/\partial \widetilde{\boldsymbol{u}} \bullet \partial \widetilde{\boldsymbol{u}}/\partial \boldsymbol{U}$, where g denotes the general displacement based response function, and $\widetilde{\boldsymbol{u}}$ the n^{th}-order MacLaurin displacement prediction.

Recall the n^{th}-order MacLaurin displacement prediction $\widetilde{\boldsymbol{u}}$. It can be rewritten as:

$$\widetilde{\boldsymbol{u}} \equiv \underbrace{\left[\boldsymbol{u}^{(1)},\, \ldots,\, \boldsymbol{u}^{(n)}\right]}_{\boldsymbol{U}} \bullet \underbrace{\begin{bmatrix} \lambda \\ \frac{1}{2}\lambda^2 \\ \vdots \\ \frac{1}{n!}\lambda^n \end{bmatrix}}_{\boldsymbol{\lambda}} = \boldsymbol{U} \bullet \boldsymbol{\lambda} \,. \tag{D.2.1}$$

The adjoint MacLaurin forces can then be obtained directly as:

$$\underbrace{\left[\boldsymbol{\Gamma}^{(1)},\, \ldots,\, \boldsymbol{\Gamma}^{(n)}\right]}_{\boldsymbol{G}} \equiv \frac{\partial g(\boldsymbol{x},\, \widetilde{\boldsymbol{u}})}{\partial \widetilde{\boldsymbol{u}}} \bullet \frac{\mathrm{d}\widetilde{\boldsymbol{u}}}{\mathrm{d}\boldsymbol{U}} = \frac{\partial g(\boldsymbol{x},\, \widetilde{\boldsymbol{u}})}{\partial \widetilde{\boldsymbol{u}}} \otimes \boldsymbol{\lambda} \,. \tag{D.2.2}$$

D.3 MacLaurin Error Estimate

The present appendix derives the sensitivities of the MacLaurin error estimator $\widetilde{\epsilon}$, and the radius of convergence $\overline{\lambda}$, exploiting the chain rule. More precisely, their state derivatives are obtained, meaning they are differentiated versus the higher order displacement derivatives $\boldsymbol{U}$. The respective design sensitivities of these responses may then be obtained by plugging their state derivatives directly into the adjoint formulation, copied in Appendix D.1 from Subsection III.5.

$$\widetilde{\epsilon} = \beta^n \,, \qquad \text{with} \quad \beta \equiv \frac{\lambda}{\overline{\lambda}} \,, \qquad \text{and} \quad \overline{\lambda} \equiv \left(n! \frac{|\boldsymbol{u}^{(1)}|}{|\boldsymbol{u}^{(n)}|} \right)^{\frac{1}{n-1}} \,. \tag{D.3.1}$$

$$\frac{\mathrm{d}\widetilde{\epsilon}}{\mathrm{d}\boldsymbol{U}} = \frac{\mathrm{d}\widetilde{\epsilon}}{\mathrm{d}\beta} \cdot \frac{\mathrm{d}\beta}{\mathrm{d}\overline{\lambda}} \cdot \frac{\mathrm{d}\overline{\lambda}}{\mathrm{d}\boldsymbol{U}} \,, \tag{D.3.2}$$

$$\text{where} \quad \frac{\mathrm{d}\widetilde{\epsilon}}{\mathrm{d}\beta} = n\beta^{n-1} \,, \qquad \frac{\mathrm{d}\beta}{\mathrm{d}\overline{\lambda}} = -\frac{\lambda}{\overline{\lambda}^2} \,, \qquad \text{and} \quad \frac{\mathrm{d}\overline{\lambda}}{\mathrm{d}\boldsymbol{U}} = \left[\frac{\mathrm{d}\overline{\lambda}}{\mathrm{d}\boldsymbol{u}^{(1)}},\, \boldsymbol{0},\, \ldots,\, \boldsymbol{0},\, \frac{\mathrm{d}\overline{\lambda}}{\mathrm{d}\boldsymbol{u}^{(n)}} \right] \,. \tag{D.3.3}$$

Redefining $\overline{\lambda}$ implicitly from Equation D.3.1, facilitates a more convenient implicit differentiation, from which ultimately the desired state derivatives of $\overline{\lambda}$ can be isolated. Starting with its implicit redefinition:

$$\frac{\overline{\lambda}^{n-1}}{n!} = \frac{|\boldsymbol{u}^{(1)}|}{|\boldsymbol{u}^{(n)}|} \,. \tag{D.3.4}$$

Differentiating both sides with respect to $\boldsymbol{u}^{(p)}$ yields:

$$\frac{(n-1)\overline{\lambda}^{n-2}}{n!}\frac{\mathrm{d}\overline{\lambda}}{\mathrm{d}\boldsymbol{u}^{(p)}} = \frac{\mathrm{d}}{\mathrm{d}\boldsymbol{u}^{(p)}}\left(\frac{|\boldsymbol{u}^{(1)}|}{|\boldsymbol{u}^{(n)}|}\right) = \begin{cases} \dfrac{\boldsymbol{u}^{(1)}}{|\boldsymbol{u}^{(1)}||\boldsymbol{u}^{(n)}|}\,, & p = 1\,, \\ -\dfrac{|\boldsymbol{u}^{(1)}|\boldsymbol{u}^{(n)}}{|\boldsymbol{u}^{(n)}|^3}\,, & p = n\,. \end{cases} \tag{D.3.5}$$

Hence, the state derivative of the radius of convergence equals:

$$\frac{\mathrm{d}\overline{\lambda}}{\mathrm{d}\boldsymbol{U}} = \frac{n!}{(n-1)\overline{\lambda}^{n-2}}\left[\frac{\boldsymbol{u}^{(1)}}{|\boldsymbol{u}^{(1)}||\boldsymbol{u}^{(n)}|},\ \boldsymbol{0},\ \ldots,\ \boldsymbol{0},\ -\frac{|\boldsymbol{u}^{(1)}|\boldsymbol{u}^{(n)}}{|\boldsymbol{u}^{(n)}|^3}\right]. \tag{D.3.6}$$

D.4 Adjoint Bayesian Force

The goal of this appendix is to obtain the partial state derivatives of the general response based on the Bayesian displacement prediction, which may be plugged directly into the adjoint formulation, copied in Appendix D.1 from Subsection III.5. They are defined as $\boldsymbol{G} \equiv \left[\boldsymbol{\Gamma}^{(1)},\ \ldots,\ \boldsymbol{\Gamma}^{(n)}\right] = \partial g(\boldsymbol{x},\ \widetilde{\widetilde{\boldsymbol{u}}})/\partial\widetilde{\widetilde{\boldsymbol{u}}} \bullet \partial\widetilde{\widetilde{\boldsymbol{u}}}/\partial\boldsymbol{U}$, where g denotes the general displacement based response function, and $\widetilde{\widetilde{\boldsymbol{u}}}$ the n^{th}-order Bayesian-enhanced displacement prediction.

Starting with the n^{th}-order Bayesian-enhanced displacement prediction $\widetilde{\widetilde{\boldsymbol{u}}}$, its simplified expression from Equation C.2.1 reads:

$$\widetilde{\widetilde{\boldsymbol{u}}} \equiv \underbrace{\left[\boldsymbol{u}^{(1)},\ \ldots,\ \boldsymbol{u}^{(n)}\right]}_{\boldsymbol{U}} \bullet \underbrace{\begin{bmatrix} \lambda & \lambda & \cdots & \lambda \\ & \frac{1}{2}\lambda^2 & \cdots & \frac{1}{2}\lambda^2 \\ & & \ddots & \vdots \\ & & & \frac{1}{n!}\lambda^n \end{bmatrix}}_{\boldsymbol{\Lambda}} \bullet \underbrace{\begin{bmatrix} \omega_1 \\ \omega_2 \\ \vdots \\ \omega_n \end{bmatrix}}_{\boldsymbol{\omega}} = \boldsymbol{U} \bullet \boldsymbol{\Lambda} \bullet \boldsymbol{\omega}\,. \tag{D.4.1}$$

Most complexity lies within the weight vector $\boldsymbol{\omega}$. Its simplified expression from Equation C.2.3, extended with the squared Bayesian error estomator $\omega_0 \equiv \widetilde{\widetilde{\epsilon}}^2$, reads:

$$\begin{bmatrix} \widetilde{\widetilde{\epsilon}}^2 \\ \cdots \\ \boldsymbol{\omega} \end{bmatrix} \equiv \begin{bmatrix} \omega_0 \\ \cdots \\ \omega_1 \\ \omega_2 \\ \vdots \\ \omega_n \end{bmatrix} = \begin{bmatrix} \beta^{2n} \\ \cdots\cdots \\ \beta^{2n-2} \\ \beta^{2n-4} \\ \vdots \\ 1 \end{bmatrix} \frac{1-\beta^2}{1-\beta^{2n}}\,, \qquad \text{recalling that} \quad \beta \equiv \frac{\lambda}{\overline{\lambda}}\,, \tag{D.4.2}$$

highlighting that $\boldsymbol{\omega}$ and $\widetilde{\widetilde{\epsilon}}$ ultimately depend on the higher-order displacement derivatives $\boldsymbol{U}$ through the radius of convergence $\overline{\lambda}$. The state derivative of $\boldsymbol{\omega}$ is obtained in the following Appendix D.5.

Finally, the adjoint Bayesian forces can be obtained as:

$$\begin{aligned} \underbrace{\left[\boldsymbol{\Gamma}^{(1)},\ \ldots,\ \boldsymbol{\Gamma}^{(n)}\right]}_{\boldsymbol{G}} &\equiv \frac{\partial g(\boldsymbol{x},\ \widetilde{\widetilde{\boldsymbol{u}}})}{\partial\widetilde{\widetilde{\boldsymbol{u}}}} \bullet \frac{\mathrm{d}\widetilde{\widetilde{\boldsymbol{u}}}}{\mathrm{d}\boldsymbol{U}} \\ &= \frac{\partial g(\boldsymbol{x},\ \widetilde{\widetilde{\boldsymbol{u}}})}{\partial\widetilde{\widetilde{\boldsymbol{u}}}} \otimes (\boldsymbol{\Lambda} \bullet \boldsymbol{\omega}) + \frac{\partial g(\boldsymbol{x},\ \widetilde{\widetilde{\boldsymbol{u}}})}{\partial\widetilde{\widetilde{\boldsymbol{u}}}} \bullet \left(\boldsymbol{U} \bullet \boldsymbol{\Lambda} \bullet \frac{\mathrm{d}\boldsymbol{\omega}}{\mathrm{d}\beta}\right) \cdot \frac{\mathrm{d}\beta}{\mathrm{d}\overline{\lambda}} \cdot \frac{\mathrm{d}\overline{\lambda}}{\mathrm{d}\boldsymbol{U}}\,. \end{aligned} \tag{D.4.3}$$

Note that $\mathrm{d}\beta\,/\,\mathrm{d}\overline{\lambda}$ and $\mathrm{d}\overline{\lambda}\,/\,\mathrm{d}\boldsymbol{U}$ have been derived in the previous Appendix D.3. The Bayesian weights $\boldsymbol{\omega}$, and by extension the Bayesian error estimate $\widetilde{\widetilde{\epsilon}}$, are differentiated in the following Appendix D.5.

D.5 Bayesian Weights and Error Estimate

The present appendix derives the sensitivities of Bayesian weights ω_p and error estimator $\tilde{\tilde{\epsilon}}$ exploiting the chain rule. More precisely, they are differentiated versus β, whose state derivative, $\mathrm{d}\beta\,/\,\mathrm{d}\boldsymbol{U}$ has readily been derived in Appendix D.3. The respective design sensitivities of ω_p and $\tilde{\tilde{\epsilon}}$ may be then be obtained by plugging their state derivatives directly into the adjoint formulation, copied in Appendix D.1 from Subsection III.5.

Consider again the p^{th} weight ω_p from Equation C.2.4, which may be rewritten as:

$$(1-\beta^{2n})\omega_p = \beta^{2n-2p} - \beta^{2n+2-2p}\,. \tag{D.5.1}$$

This formulation facilitates an intermediate implicit differentiation step with respect to β. Ultimately, this will yield an expression for the desired derivative of ω_p with respect to β in terms of β and ω_p itself, saving some mathematical and computational labor. Hence, differentiating both sides of Equation D.5.1 with respect to β results in:

$$\begin{aligned}(1-\beta^{2n})\frac{\mathrm{d}\omega_p}{\mathrm{d}\beta} - 2n\beta^{2n-1}\omega_p &= (2n-2p)\beta^{2n-2p-1} - (2n+2-2p)\beta^{2n-2p+1} \\ &= (2n-2p)\left(1-\frac{2n+2-2p}{2n-2p}\beta^2\right)\beta^{2n-2p-1}\,.\end{aligned} \tag{D.5.2}$$

Isolating $\mathrm{d}\omega_p\,/\,\mathrm{d}\beta$ then yields:

$$\frac{\mathrm{d}\omega_p}{\mathrm{d}\beta} = \frac{2n\beta^{2n-1}\omega_p + (2n-2p)\left(1-\frac{2n+2-2p}{2n-2p}\beta^2\right)\beta^{2n-2p-1}}{1-\beta^{2n}}\,. \tag{D.5.3}$$

Moving on to the Bayesian error estimator $\tilde{\tilde{\epsilon}}$, it can also be conveniently obtained through implicit differentiation of $\tilde{\tilde{\epsilon}}^2 = \omega_0$:

$$\frac{\mathrm{d}\omega_0}{\mathrm{d}\beta} = 2\tilde{\tilde{\epsilon}}\frac{\mathrm{d}\tilde{\tilde{\epsilon}}}{\mathrm{d}\beta}\,, \qquad \text{hence} \quad \frac{\mathrm{d}\tilde{\tilde{\epsilon}}}{\mathrm{d}\beta} = \frac{1}{2\tilde{\tilde{\epsilon}}}\frac{\mathrm{d}\omega_0}{\mathrm{d}\beta}\,. \tag{D.5.4}$$

As the final step connecting the previous derivatives to the adjoint formulation, the state derivative $\mathrm{d}\beta\,/\,\mathrm{d}\boldsymbol{U}$ is obtained. Recalling that $\beta \equiv \lambda/\overline{\lambda}$:

$$\frac{\mathrm{d}\beta}{\mathrm{d}\boldsymbol{U}} = \frac{\mathrm{d}\beta}{\mathrm{d}\overline{\lambda}}\cdot\frac{\mathrm{d}\overline{\lambda}}{\mathrm{d}\boldsymbol{U}} = -\frac{\lambda}{\overline{\lambda}^2}\frac{\mathrm{d}\overline{\lambda}}{\mathrm{d}\boldsymbol{U}}\,, \tag{D.5.5}$$

where the state derivative of the radius of convergence, $\mathrm{d}\overline{\lambda}\,/\,\mathrm{d}\boldsymbol{U}$, can be taken from Equation D.3.6, in a previous section D.3.

D.6 Adjoint Stiffness

This final sensitivity analysis appendix derives the family of adjoint stiffness matrices, which are actually the higher order residual's state derivatives. Note that index notation is still adopted here, as this derivation has been worked out in an early stage of the project. The adjoint stiffnesses are defined for all $p,\ s \in \{0,\ \ldots,\ n\}$, as:

$$\begin{aligned}K_{im}^{(p,\,s)} \equiv \frac{\partial r_i^{(p)}}{\partial u_m^{(s)}} &= K_{ij}\frac{\partial u_j^{(p)}}{\partial u_m^{(s)}} + \frac{1}{2}S_{ijk}\frac{\partial v_{jk}^{(p)}}{\partial u_m^{(s)}} + \frac{1}{6}Q_{ijkl}\frac{\partial w_{jkl}^{(p)}}{\partial u_m^{(s)}} \\ &= \binom{p}{p-s}\mathcal{K}_{im}(\boldsymbol{u}^{(p-s)}) = \begin{cases} 0\,, & s > p\,, \\ K_{im}\,, & s = p\,, \\ \binom{p}{p-s}K_{im}^{(p-s,\,0)}\,, & s < p\,, \end{cases}\end{aligned} \tag{D.6.1}$$

recalling the higher order residual equation:

$$r_i^{(p)} = K_{ij}u_j^{(p)} + \frac{1}{2}S_{ijk}v_{jk}^{(p)} + \frac{1}{6}Q_{ijkl}w_{jkl}^{(p)} - \lambda^{(p)}p_i = 0\,, \qquad u_i^{(p)} = 0\,, \tag{D.6.2}$$

$$\text{where} \quad v_{ij}^{(p)} = u_i^{(1)}u_j^{(p-1)} + \sum_{q=1}^{p-2}\left(\frac{\partial v_{ij}^{(p-1)}}{\partial u_k^{(q)}}u_k^{(q+1)}\right), \qquad v_{ij}^{(0)} = 0\,, \tag{D.6.3}$$

$$\text{and} \quad w_{ijk}^{(p)} = u_i^{(1)}v_{jk}^{(p-1)} + \sum_{q=1}^{p-3}\left(\frac{\partial w_{ijk}^{(p-1)}}{\partial u_l^{(q)}}u_l^{(q+1)}\right), \qquad w_{ijk}^{(0)} = 0\,. \tag{D.6.4}$$

To elaborate, the case for $s = p$ can be worked out by noting that $v_{jk}^{(p)}$ and $w_{jkl}^{(p)}$ are functions of $u_i^{(1)}$ up to $u_i^{(p-1)}$ and $u_i^{(2)}$ up to $u_i^{(p-2)}$ respectively, leaving only $K_{im}^{(p,\,p)} = K_{ij}\partial u_j^p/\partial u_m^p = K_{im}$. Similarly, for $s > p$ everything vanishes. However, the case for $s < p$ is more complex as only the first term of Equation D.6.1 vanishes. Yet, for fixed difference $p - s$ all $K_{im}^{(p,s)}$ appear identical up to a scalar multiplication, hence requiring only $n - 1$, rather than $n(n-1)/2$ separate adjoint stiffness matrix constructions, excluding the trivial cases of $s \geqslant p$.

Moving on to the cases for $s < p$, consider $\partial v_{jk}^{(p)}/\partial u_m^{(s)}$ within the second term of Equation D.6.1, substituting $v_{jk}^{(p)}$ from Equation D.6.2:

$$\frac{\partial v_{jk}^{(p)}}{\partial u_m^{(s)}} = \binom{p}{s}\frac{\partial u_j^{(s)}}{\partial u_m^{(s)}}u_k^{(p-s)} + \binom{p}{p-s}u_j^{(p-s)}\frac{\partial u_k^{(s)}}{\partial u_m^{(s)}} = \binom{p}{p-s}\left(\delta_{jm}u_k^{(p-s)} + u_j^{(p-s)}\delta_{km}\right), \tag{D.6.5}$$

where the terms in $v_{jk}^{(p)}$ from Equation D.6.2 vanish upon differentiation for all q excluding $q = s$ and $q = p - s$. Within the third term of Equation D.6.1, consider $\partial w_{jkl}^{(p)}/\partial u_m^{(s)}$ with $w_{jkl}^{(p)}$ from **??**:

$$\frac{\partial w_{jkl}^{(p)}}{\partial u_m^{(s)}} = \sum_{q=0}^{p}\binom{p}{q}\left(v_{jk}^{(q)}\frac{\partial u_l^{(p-q)}}{\partial u_m^{(s)}} + \frac{\partial v_{jk}^{(q)}}{\partial u_m^{(s)}}u_l^{(p-q)}\right), \tag{D.6.6a}$$

$$\text{where} \quad \sum_{q=0}^{p}\binom{p}{q}v_{jk}^{(q)}\frac{\partial u_l^{(p-q)}}{\partial u_m^{(s)}} = \binom{p}{p-s}v_{jk}^{(p-s)}\delta_{lm}\,, \tag{D.6.6b}$$

$$\text{and} \quad \sum_{q=0}^{p}\binom{p}{q}\frac{\partial v_{jk}^{(q)}}{\partial u_m^{(s)}}u_l^{(p-q)} = \sum_{q=s}^{p}\binom{p}{q}\binom{q}{q-s}\left(\delta_{jm}u_k^{(q-s)} + u_j^{(q-s)}\delta_{km}\right)u_l^{(p-q)}\,. \tag{D.6.6c}$$

Note that in Equation D.6.6b, the terms vanish for all q excluding $q = p - s$, while in Equation D.6.6c they vanish for all $q < s$. Furthermore, $\partial v_{jk}^{(q)}/\partial u_m^{(s)}$ in Equation D.6.6c is substituted from Equation D.6.5. Next, Equation D.6.6c may be conveniently rewritten to explicitly depend on p and $p - s$ by substituting $r = q - s$. As for the binomial coefficients in Equation D.6.6c:

$$\binom{p}{q}\binom{q}{p-s} = \binom{p}{s+r}\binom{s+r}{s} = \frac{p!(s+r)!}{(s+r)!(p-s-r)!s!r!} = \frac{p!}{s!(p-s)!}\frac{(p-s)!}{r!(p-s-r)!} = \binom{p}{p-s}\binom{p-s}{r}. \tag{D.6.7}$$

Substituting these into Equation D.6.6c, and then *it* and Equation D.6.6b into Equation D.6.6a yields $\partial w_{jkl}^{(p)}/\partial u_m^{(s)}$:

$$\begin{aligned}\frac{\partial w_{jkl}^{(p)}}{\partial u_m^{(s)}} &= \binom{p}{p-s}\left(v_{jk}^{(p-s)}\delta_{lm} + \sum_{r=0}^{p-s}\binom{p-s}{r}\left(\delta_{jm}u_k^{(r)} + u_j^{(r)}\delta_{km}\right)u_l^{(p-s-r)}\right)\\ &= \binom{p}{p-s}\left(v_{jk}^{(p-s)}\delta_{lm} + v_{kl}^{(p-s)}\delta_{jm} + v_{jl}^{(p-s)}\delta_{km}\right)\,.\end{aligned} \tag{D.6.8}$$

Finally, the adjoint stiffness matrix for $s < p$ reduces to:

$$\begin{aligned} K_{im}^{(p,\,s)} &= \frac{1}{2} S_{ijk} \binom{p}{p-s} \left(\delta_{jm} u_k^{(p-s)} + u_j^{(p-s)} \delta_{km} \right) \\ &\quad + \frac{1}{6} Q_{ijkl} \binom{p}{p-s} \left(v_{jk}^{(p-s)} \delta_{lm} + v_{kl}^{(p-s)} \delta_{jm} + v_{jl}^{(p-s)} \delta_{km} \right) \\ &= \binom{p}{p-s} \underbrace{\left(S_{imk} u_k^{(p-s)} + \frac{1}{2} Q_{imkl} v_{kl}^{(p-s)} \right)}_{K_{im}^{(p-s,\,0)}}, \end{aligned} \tag{D.6.9}$$

concluding the proof for Equation D.6.1. In fact, the simplicity of the final expression suggests there may be a much simpler and more elegant proof involving combinatorics, but the result is obtained nonetheless.